19 September 2008 | $10

Science

AAAS

Volume 321, Issue 5896

COVER

A cotton bollworm larva (*Helicoverpa armigera*) feeds on a cotton boll. Transgenic Bt cotton was designed to resist this and other caterpillar pests. See page 1676.

Image: Nigel Cattlin/Visuals Unlimited Inc.

DEPARTMENTS

EDITORIAL

NEWS OF THE WEEK

NEWS FOCUS

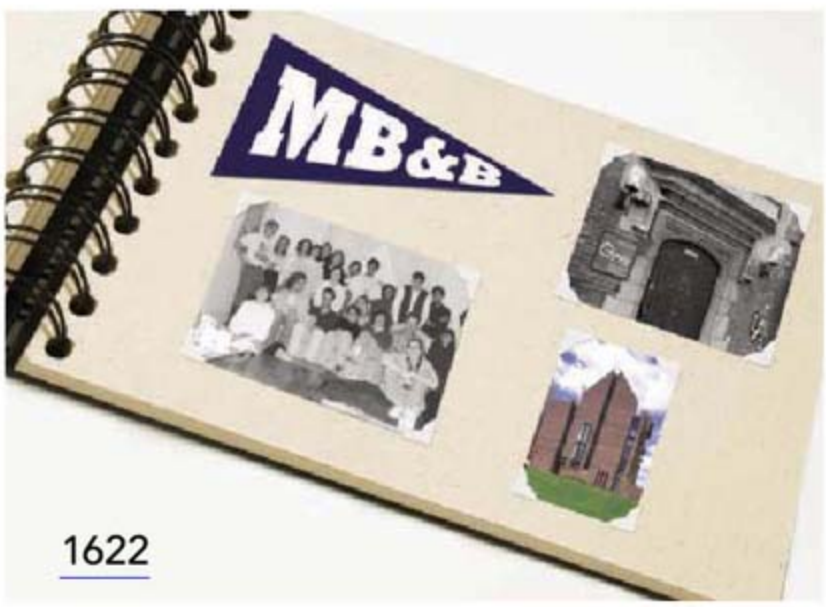

1622

LETTERS

BOOKS *ET AL.*

POLICY FORUM

PERSPECTIVES

1636

CONTENTS continued >>

Science

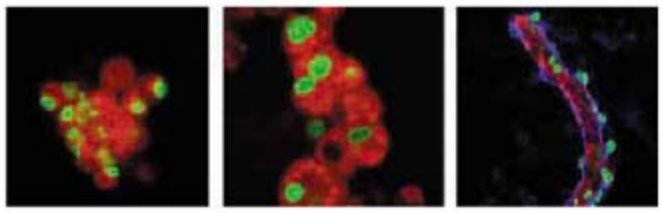

SCIENCE EXPRESS

www.sciencexpress.org

PHYSICS

A High Phase-Space-Density Gas of Polar Molecules
K.-K. Ni et al.
Raman laser irradiation can cool a cloud of KRb molecules to ultralow translational, vibrational, and rotational temperatures, a step toward forming molecular condensates.
10.1126/science.1163861

IMMUNOLOGY

Innate Immunity in *Caenorhabditis elegans* Is Regulated by Neurons Expressing NPR-1/GPCR
K. L. Styer et al.
In the nematode *Caenorhabditis elegans*, sensory neurons surprisingly can inhibit innate immune responses, in part through the mitogen-activated prtoein kinase signaling pathway.
10.1126/science.1163673

CELL BIOLOGY

White Fat Progenitor Cells Reside in the Adipose Vasculature
W. Tang et al.
Adipocytes (fat cells) originate from precursor cells that reside within the walls of the blood vessels that feed fat tissue.
10.1126/science.1156232

CHEMISTRY

Catalytic Conversion of Biomass to Monofunctional Hydrocarbons and Targeted Liquid-Fuel Classes
E. L. Kunkes et al.
A set of two reactors, one that breaks down biomass sugars and a second that directs chain formation, can synthesize various hydrocarbon fuels.
10.1126/science.1159210

TECHNICAL COMMENT ABSTRACTS

GEOLOGY

BREVIA

CLIMATE CHANGE

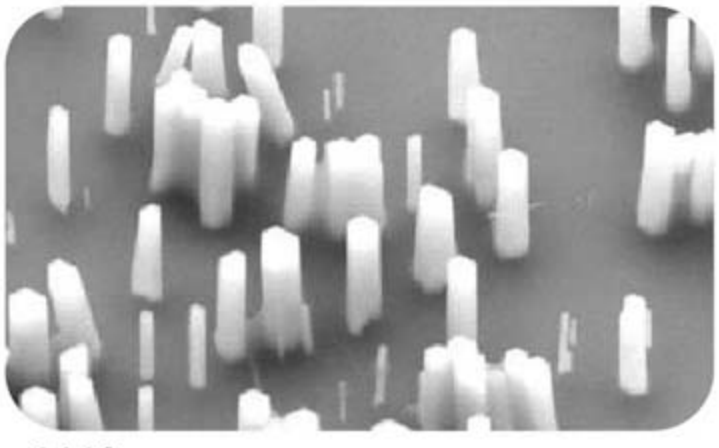

1660

REPORTS

PHYSICS

PHYSICS

CHEMISTRY

MATERIALS SCIENCE

MATERIALS SCIENCE

CONTENTS continued >>

REPORTS *CONTINUED...*

CREDIT: COREY ARNOLD

AAAS

ADVANCING SCIENCE, SERVING SOCIETY

SCIENCE (ISSN 0036-8075) is published weekly on Friday, except the last week in December, by the American Association for the Advancement of Science, 1200 New York Avenue, NW, Washington, DC 20005. Periodicals Mail postage (publication No. 484460) paid at Washington, DC, and additional mailing offices. The title SCIENCE is a registered trademark of the AAAS. Domestic individual membership and subscription (51 issues): $144 ($74 allocated to subscription). Domestic institutional subscription (51 issues): $770; Foreign postage extra: Mexico, Caribbean (surface mail) $55; other countries (air assist delivery) $85. First class, airmail, student, and emeritus rates on request. Canadian rates with GST available upon request, GST #1254 88122. Publications Mail Agreement Number 1069624. SCIENCE is printed on 30 percent post-consumer recycled paper. **Printed in the U.S.A.**

Change of address: Allow 4 weeks, giving old and new addresses and 8-digit account number. **Postmaster:** Send change of address to AAAS, P.O. Box 96178, Washington, DC 20090–6178. **Single-copy sales:** $10.00 current issue, $15.00 back issue prepaid includes surface postage; bulk rates on request. **Authorization to photocopy** material for internal or personal use under circumstances not falling within the fair use provisions of the Copyright Act is granted by AAAS to libraries and other users registered with the Copyright Clearance Center (CCC) Transactional Reporting Service, provided that $20.00 per article is paid directly to CCC, 222 Rosewood Drive, Danvers, MA 01923. The identification code for *Science* is 0036-8075. *Science* is indexed in the *Reader's Guide to Periodical Literature* and in several specialized indexes.

Printed on 30% post-consumer recycled paper.

CONTENTS continued >>

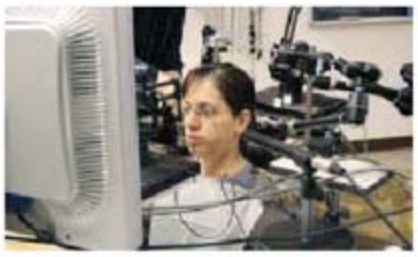

Mouthful.

SCIENCE**NOW**

www.sciencenow.org

HIGHLIGHTS FROM OUR DAILY NEWS COVERAGE

Speaking Without Sound
Facial muscles tell us whether we are pronouncing words correctly.

No Glee for Grandma?
Brains of the young and old process rewards in different ways.

China Quake No Stress Reliever
Temblor last May could have activated adjoining fault lines.

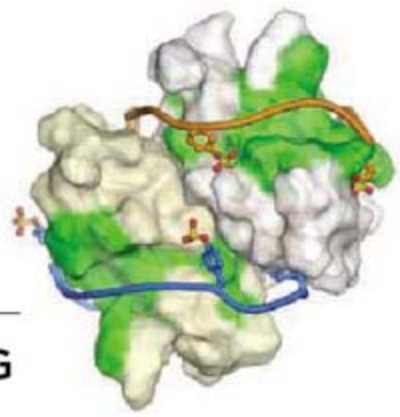

SDF-1 bound to CXCR4.

SCIENCE **SIGNALING**

www.sciencesignaling.org

THE SIGNAL TRANSDUCTION KNOWLEDGE ENVIRONMENT

RESEARCH ARTICLE: Structural Basis of CXCR4 Sulfotyrosine Recognition by the Chemokine SDF-1/CXCL12
C. T. Veldkamp, C. Seibert, F. C. Peterson, N. B. De la Cruz, J. C. Haugner III, H. Basnet, T. P. Sakmar, B. F. Volkman
The structure of SDF-1 bound to an extracellular domain of CXCR4 illustrates how chemokines recognize receptor sulfotyrosines and helps to identify an inhibitor of leukocyte chemotaxis.

PROTOCOL: Analysis of Signaling Events by Combining High-Throughput Screening Technology with Computer-Based Image Analysis
M. Kodiha, C. M. Brown, U. Stochaj
High-throughput screening and MetaXpress software modules can be adapted to quantify the subcellular localization of fluorescently labeled molecules.

PRESENTATION: Dynamic Visualization of Signaling Activities in Living Cells
M. D. Allen, L. M. DiPilato, B. Ananthanarayanan, R. H. Newman, Q. Ni, J. Zhang
Engineered fluorescent reporters allow researchers to follow subcellular activities of signaling components in real time in live cells.

Program officers get a panoramic view of science.

SCIENCE **CAREERS**

www.sciencecareers.org/career_development

FREE CAREER RESOURCES FOR SCIENTISTS

Special Feature: Working as a Program Officer
K. Travis
Program officers may not work at the bench, but they are at the leading edge of science.

Steering Science From a High Altitude
S. Carpenter
Scientific program officers take a big-picture view of science to determine research funding.

Become a Program Officer Your Own Way
E. Pain
There is no typical way of becoming a program officer.

In Person: A European Career Tour From Research to Research Management
A. Di Trapani
A science officer at the European Science Foundation describes her journey.

SCIENCE**PODCAST**

www.sciencemag.org/multimedia/podcast

FREE WEEKLY SHOW

Download the 19 September *Science* Podcast to hear about traces of the inner solar system from the Stardust mission, trust in the World Wide Web, a survey of Yale graduates, and more.

Separate individual or institutional subscriptions to these products may be required for full-text access.

EDITED BY STELLA HURTLEY

<< Toward Antibiotic Development

The identification of new antibiotics and potential microbe-specific targets remains a critical goal of much microbiological research (see the Perspective by **Payne**). Microorganisms must have menaquinone for respiration. *Escherichia coli* synthesizes menaquinone from chorismate using seven enzymes. There are no traces of orthologs of these enzymes in several pathogens, yet these bacteria and some archea synthesize menaquinone. **Hiratsuka *et al.*** (p. 1670) traced an alternative pathway in the nonpathogenic organism *Streptomyces coelicolor* using a combination of bioinformatics and biochemistry to identify functions for uncharacterized genes. Because humans and certain intestinal commensals, notably lactobacilli, lack this alternative pathway, it represents an attractive target for the development of antibiotics. Antibiotics that block bacterial cell division are lacking. **Haydon *et al.*** (p. 1673) have synthesized a small molecule that binds to the bacterial cell division protein FtsZ and inhibits cell division. The molecule appears to bind to the bacterial protein at a site equivalent to the taxol binding site of tubulin. When injected into mice that had been given a lethal dose of *Staphylococcus aureus*, nontoxic doses of the molecule prevented the animals' death.

Tracking Electronic Phase Transitions

In solid-state systems, correlated electron effects can cause the electrons to behave collectively, forming large-scale ordered states. How these states form dynamically and influence, or are influenced by, other processes are of great current interest. Below a transition temperature, TbTe3, forms a charge density wave where the electrons order spontaneously into regions of low and high charge density. Using a time- and angle-resolved photoemission technique, **Schmitt *et al.*** (p. 1649, published online 14 August) can track the transient melting of the charge density as it is excited by a laser pulse and show how it affects the underlying electronic state of the system. Such a technique will be invaluable in studying many-body correlated effects in modern condensed-matter physics.

Fine-Point Lithographic Printing

The advantages of two low-cost approaches for creating patterns with molecular inks on surfaces have been combined in a method that **Huo *et al.*** (p. 1658, published online 14 August) call polymer pen lithography. Like microcontact printing, an elastomeric stamp is inked with molecules such as 16-mercaptohexanioc acid and transferred to a gold surface. Like dip-pen lithography, ink is delivered on individual tips to create nanoscale dots, but on soft polymer tips without the use of individual cantilever control. The array can be leveled relative to the surface optically, and the size of the features formed can be controlled from 90 nanometers to hundreds of micrometers by varying the force and time over which the stamp is in contact with the surface.

CREDITS (TOP TO BOTTOM): PROLYSIS LIMITED; NOLTE *ET AL.*

Nanoparticle Shape Shifting

Heterogeneous catalysts often consist of metal nanoparticles absorbed on oxide supports, and the size and shape of these nanoparticles are likely to be affected by conditions in the reactor such as temperature and oxidation state. However, such changes are not readily observed experimentally because many methods require vacuum conditions. **Nolte *et al.*** (p. 1564) were able to examine the changes to rhodium nanoparticles on a MgO surface using high-resolution in situ x-ray diffraction, as well as transmission election microscopy. At elevated temperatures (570 K), these pyramid-shaped nanoparticles became flatter upon exposure to oxygen, which causes the formation of a surface oxide. The nanoparticles returned to their original shape after exposure to CO, which causes reduction of the surface.

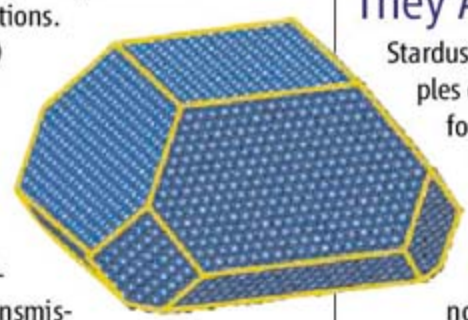

Exotic Superconducting Magnetism

Superconductivity and magnetic ordering are usually considered to be competing processes, the two being mutually exclusive, or seen only in a small region of the phase diagram for inhomogeneous materials. CeCoIn5 is an extremely clean material that can be prepared with high crystal quality. A so-called exotic superconductor, it exhibits many similar properties to the more complex high-temperature superconducting cuprates. **Kenzelmann *et al.*** (p. 1652, published online 21 August) use neutron scattering to probe the magnetic ordering in this material at low temperature and high magnetic field, and find evidence of magnetic ordering that is stabilized by, and coexistent with, superconducting behavior.

They Are Stardust...

Stardust recently returned our first direct samples of a comet. Comets are thought to have formed toward the outer part of the solar system. Early analysis provided some evidence for a few high temperature grains that may be from the inner solar system. **Nakamura *et al.*** (p. 1664) now find that the comet also contains material similar to chondrules, which are abundant in the most primitive meteorites, which are also thought to be from the inner solar system. Thus, mixing seems to have been widespread in the inner solar system and chondrules, or similar material, may have been distributed throughout it.

Political Baggage

Political attitudes have been thought to be shaped only by experiences and environment, but research is now beginning to show that some of

Continued on page 1603

Continued from page 1601

our responses to events may be "hard wired" **Oxley *et al.*** (p. 1667) found that individuals who had the strongest eye and skin responses to unexpected noises or threatening pictures (such as the picture of a spider crawling on a person's eyeball) also tended to endorse political positions that were interpreted as protective of social groups.

Collateral Help

For some years, farmers in China have been using cotton plants engineered to express the insecticidal toxin Bt. **Wu *et al.*** (p. 1676; cover) have now analyzed data from 1997 to 2007 about the planting of Bt-cotton, as well as other crops, and have compared these observations with data about the occurrence of pests. The target pest, the cotton bollworm, has indeed declined over this same period. Furthermore, as might have been hoped, these reductions in pest populations locally carry collateral benefits for non–Bt-expressing crops that this pest would tend to attack.

Activity Around Plaques

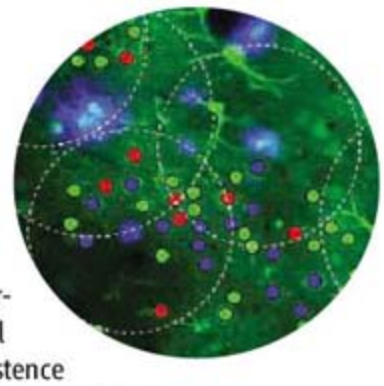

Identifying the underlying cellular mechanisms of cortical dysfunction in amyloid-depositing mammalian brains should hopefully generate leads in the search for effective treatments for Alzheimer's disease. **Busche *et al.*** (p. 1686) used in vivo two-photon calcium imaging of cortical networks to monitor Ca^{2+} signaling of individual layer 2/3 cortical neurons in a mouse model of Alzheimer's disease. Fifty percent of cortical neurons in diseased mice exhibited impaired functional properties. A class of "hyperactive" neurons were identified, whose existence was not predicted from previous in situ or functional imaging data. The hyperactive neurons were located exclusively in peri-plaque regions and their presence correlated with impairment of cognitive behavior. This synaptically-driven hyperactivity of peri-plaque regions may underlie the increased incidence of epileptic seizures in Alzheimer's disease patients.

Fish Lore

Amid increasing concerns about food security is the fear that our ocean fisheries are in imminent danger of collapse. **Costello *et al.*** (p. 1678; see the news story by **Stokstad**) contend that if fishermen have the exclusive and guaranteed right to harvest a given quantity of fish in a particular fishery at any time during the fishing season, they will have the incentive to manage the stock sustainably and collapse will be averted. The problem with rolling out this approach has been measuring the success of recently implemented schemes in the absence of data. By collating the available harvest data from all known fisheries, encouragingly, the authors conclude that rights-based fishing halves the chances of economic collapse.

Expensive Sons

Shags are large fish-eating seabirds that nest on rocky shores and are vulnerable to fish-borne anisakid nematode parasites. After ingestion, the worms migrate systemically, triggering physiologically costly inflammatory responses, and finally colonize the birds' guts, where the parasites compete with their host for nutrients. **Reed *et al.*** (p. 1681, published online 7 August) found that parasitism impeded the ability of mothers to rear sons. Male chicks grow larger and more quickly than female chicks, and thus need more food. Female shags that had been treated with ivermectin to remove worms could forage at sea for longer and consequently were able to rear more sons than those that had not been treated. A similar effect of parasitism probably operates in many seasonally breeding birds.

May the Force Be with You

Apoptosis, or programmed cell death, not only removes unnecessary cells to shape embryonic development and maintain adult homeostasis, but also serves as a source of forces that contributing to tissue movements during embryogenesis. **Toyama *et al.*** (p. 1683; see the Perspective by **Davidson**) measured the mechanical forces provided by the ongoing process of cellular apoptosis and removal during *Drosophila*'s dorsal closure, a model system for wound healing and cell sheet morphogenesis during development. Suppressing apoptosis slowed dorsal closure, while enhancing apoptosis speeded-up dorsal closure relative to wild-type embryos. Thus it appears that organisms can co-opt apoptotic force for development, metamorphosis, and wound healing.

CREDIT: BUSCHE ET AL.

Norman R. Augustine is retired chairman and chief executive officer of Lockheed Martin Corporation and was chairman of the U.S. National Academies committee that produced *The Gathering Storm* report.

Scilence

MORE THAN HALF OF THE INCREASE IN U.S. GROSS DOMESTIC PRODUCT (GDP) HAS BEEN attributed to advancements in science, technology, and innovation. The solution to many of America's, and the world's, greatest challenges depends on advancements in science and technology—including providing energy, preserving the environment, supplying food and water, ensuring physical security, providing health care, and improving the global standard of living.

But there are a few problems. The United States ranks 16th and 20th among nations in college and high-school graduation rates, respectively; 60th in the proportion of college graduates receiving natural science and engineering degrees; and 23rd in the fraction of GDP devoted to publicly funded nondefense research. The number of U.S. citizens receiving Ph.D.s in engineering and the physical sciences has dropped by 22% in a decade. U.S. high-school students rank near the bottom in math and science.

Three years ago, a U.S. National Academies committee recommended (in the report *The Gathering Storm*) doubling federal investment in basic research in math, the physical sciences, and engineering while, at a minimum, protecting the health sciences against inflation (the cost of which, in math, the physical sciences, and engineering, equals the amount by which the nation's expenditure on health care increases every 7 weeks).

Much has been accomplished since *The Gathering Storm* was published. A new research university was established, with an opening endowment equal to what the Massachusetts Institute of Technology amassed after 142 years. Next year, over 200,000 students will study abroad, mostly pursing science or engineering degrees, often under government scholarships. Government investment in R&D is set to increase by 25%. An initiative is under way to create a global nanotechnology hub. An additional $10 billion dollars is being devoted to K-12 education, with emphasis on math and science. And a $3 billion dollar add-on to the nation's research budget is in process. Of course, these actions are taking place in Saudi Arabia, China, the United Kingdom, India, Brazil, and Russia, respectively.

What about in the United States? After the U.S. Congress authorized funding to implement many of *The Gathering Storm*'s recommendations, the needed funds were lost in an impasse over the Appropriations Act. As a result, one leading national laboratory began to impose mandatory 2-day-per-month "unpaid holidays" on its science staff, several laboratories began laying off researchers, the U.S. portion of the international program to develop plentiful energy through nuclear fusion was reduced to "survival mode," America's firms continued to spend three times more on litigation than research, and many young would-be scientists presumably began reconsidering their careers. Meanwhile, a $3 trillion dollar federal budget was approved and a $152 billion dollar economic stimulus package (much of which is likely to be spent on products made in China) whisked through Congress along with 12,000 earmarks that found their way into the Appropriations Act.

Where were the voices of those who understand the dire consequences of these actions? During the past two presidential campaigns, efforts were made by the science and engineering communities to engage candidates in a "user-friendly" science policy conversation not designed to be a debate (questions were to be provided in advance and "contentious" issues were off limits). Every candidate declined to participate. Imagine this happening to invitations from the American Bar Association or American Medical Association! Ironically, there are five times as many people in the United States with a degree in science or engineering currently working in those fields than there are either practicing lawyers or medical doctors. The "scilence" is deafening.

Of the 535 members of the U.S. Congress, only 8 list themselves as engineers or scientists. Of the 9 senior leaders in China, 8 hold such degrees. How can America's political leaders be expected to make sound policy decisions in a world of increasingly complex science and technology if the most qualified individuals in those fields remain absent from the field of play? If current trends persist, the United States may well be on its way to becoming "America, the land of the free and the home of the unemployed."

– Norman R. Augustine

10.1126/science.1162924

EDITED BY GILBERT CHIN AND JAKE YESTON

BIOMEDICINE

Revisiting a Premature Aging Drug

Children with the rare disorder Hutchinson-Gilford progeria syndrome (HGPS) develop a constellation of health problems typically seen in the geriatric population, including severe atherosclerosis and osteoporosis, and most affected individuals die as teenagers. The disease-causing mutation lies in the *LMNA* gene, which encodes the nuclear scaffold protein lamin A, and it results in the production of an unprocessed form of lamin A that aberrantly retains a farnesyl lipid anchor and induces structural changes in the cell nucleus. The observations that farnesyltransferase inhibitors (FTIs: drugs that inhibit the enzyme that attaches the farnesyl tail to proteins) partially reversed the nuclear changes in cultured cells and ameliorated disease symptoms in mouse models of HGPS, led to the initiation of a clinical trial to test these drugs in children with the disease.

New results suggest that the concept motivating this clinical trial may require revision. To test the hypothesis that the HGPS-associated lamin A is toxic because of its farnesyl group, Yang *et al.* generated mice expressing a mutant version of lamin A that contained not only the disease-causing mutation but an additional mutation that prevented the protein from being farnesylated. Surprisingly, these mice developed the same spectrum of HGPS-like phenotypes as did mice expressing the farnesylated protein, albeit in a milder form. Thus, farnesylation of lamin A is unlikely to be a major contributor to the pathogenesis of HGPS, and the mechanism underlying the therapeutic efficacy of FTIs in the earlier preclinical studies remains unclear. — PAK

J. Clin. Invest. **118**, 10.1172/JCI35876 (2008).

IMMUNOLOGY

Responding with Restraint

Eating and breathing are essential activities, but both allow foreign substances and pathogens access to internal epithelial environments—the gut and the lungs. The immune system is poised to launch an effective attack against pathogens in the respiratory tract, yet the response must be limited to avoid collateral damage to airway tissue. Snelgrove *et al.* report that in mice, this delicate balance is maintained in part by alveolar macrophages in the lower respiratory tract; these cells express a high level of the receptor for CD200, a ligand that coats airway epithelial cells. Binding of CD200 to its receptor inhibits the secretion of inflammatory cytokines. Macrophage receptor expression normally increases during infection of lungs with influenza virus. Mice lacking CD200 showed an increase in alveolar macrophages expressing the cognate receptor, but the resolution of lung inflammation was delayed during a bout of influenza, and these animals eventually died, despite viral clearance from the lungs. Treatment with a soluble form of CD200 did not compromise viral clearance, but limited damaging inflammation. This receptor-ligand pair may be relevant to the search for drugs that dampen inflammation in respiratory conditions, such as asthma and chronic obstructive pulmonary disease, without interfering with responses that control infection. — LC

Nat. Immunol. **9**, 1074 (2008).

NEUROSCIENCE

Faced with Emotion

Humans are especially interested in faces, as a means of sending signals—witness the sizeable arc of somatosensory cortex devoted to representation of one's own face—and as a substrate for social cognition. Pitcher *et al.* describe results supporting theories of embodied cognition and emotion, which posit cognition and emotion as being shaped by our bodily movements and perceptions. They used repetitive transcranial magnetic stimulation (rTMS) to interfere with neural activity in the face areas of the somatosensory cortex while people discriminated the emotional expressions of faces (happy, sad, surprised, fearful, angry, and disgusted) and found that accuracy dropped significantly, as it also did when the occipital face area was similarly stimulated. The temporal sequence of neural processing was then delineated using double-pulse TMS, showing that the occipital area acted in the time window from 60 to 100 ms after the face stimulus was shown, whereas the somatosensory area was active a bit later, between 100 and 170 ms. — GJC

J. Neurosci. **28**, 8929 (2008).

CLIMATE SCIENCE

Waters of Life

River discharge transports nutrients such as nitrate to the sea, fueling the primary production that removes carbon dioxide from the atmosphere and thereby helps to regulate climate. Some of the atmospheric carbon dioxide fixed by this production is effectively diverted from the active carbon cycle and buried in sediments on the sea floor in a process referred to as

CREDITS (TOP TO BOTTOM): HULTON-DEUTSCH COLLECTION/CORBIS; YANG ET AL., *J. CLIN. INVEST.* 118, 10.1172/JCI35876 (2008)

the "biological pump." It has been shown that river discharge causes significant carbon sequestration in the shelf areas near the mouths of rivers, yet it remains unclear whether its influence extends much further from the coast.

Subramaniam *et al.* report that the Amazon River plume stimulates a great deal of carbon fixation in the open ocean far off the coast, largely by stimulating diazotrophy (fixation of atmospheric nitrogen by bacteria) in surface waters. They estimate that the amount of organic carbon produced through this pathway is nearly three times as much as that resulting from the near-shore production that is supported by nitrate, and they speculate that this could be an important effect of rivers worldwide. Because river runoff is influenced by climate, this aspect of the biological pump could be affected by anthropogenic climate change as well. — HJS

Proc. Natl. Acad. Sci. U.S.A. **105**, 10460 (2008).

CHEMISTRY

A Window into Cyclization

Few carbon-based compounds absorb light in the visible portion of the spectrum. Organic photochemical reactions therefore largely rely on irradiation in the ultraviolet, which is expensive to implement on a large scale and often introduces substantial excess energy into the system, which limits selectivity. At the same time, there is a multitude of metal-bearing molecules that

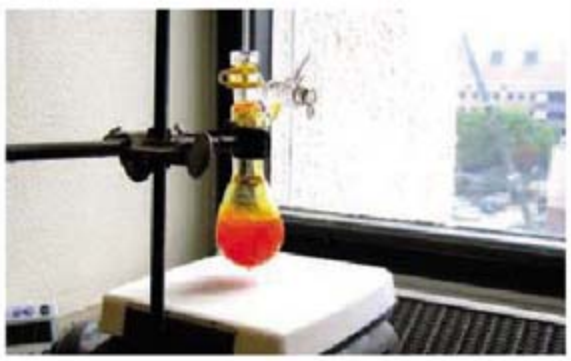

CREDIT: TEHSHIK YOON

absorb efficiently in the visible and have been studied thoroughly in the context of electron-transfer chemistry.

Ischay *et al.* applied one such compound, a ruthenium (Ru) complex bearing three bipyridyl ligands, toward the catalysis of enone cyclization. The substrates are two tethered C=C-C(O)-R moieties, where at least one R group must be a phenyl ring (the other can be an alkyl, alkoxy, or amide group). Upon absorbing blue light, the Ru complex can undergo an electron-transfer cycle that lends an electron to the substrate, accelerating formation of a bicyclic product via bond formation between the olefins. Placing the reaction flask by the window is sufficient for ordinary sunlight to drive the process. — JSY

J. Am. Chem. Soc. **130**, 10.1021/ja805387f (2008).

PHYSICS

Combs with Tunable Teeth

The generation of optical combs—broadband light made up of individual frequency components, equally spaced and spanning many orders of magnitude—has revolutionized metrology and spectroscopy because it provides an exact ruler with which to compare and mea sure wavelengths and spectroscopic signals. The spacing between the teeth of these optical combs, however, tends to be fixed for the system being used for light generation.

Savchenkov *et al.* introduce a generation method that allows the frequency spacing to be tuned. Using a calcium fluoride optical whispering-gallery–mode resonator, which sustains a family of resonant modes, they show that the nonlinear interaction of the laser light pumped into the cavity of the resonator generates a comb of equally spaced frequencies. By tuning the frequency of the pump laser with a particular resonant mode of the resonator, the frequency spacing of the output light comb can be shifted in a controlled manner, thereby providing an additional degree of flexibility in the generation of bespoke light. — ISO

Phys. Rev. Lett. **101**, 93902 (2008).

GENETICS

Just One Copy

Most model plant species have undergone at least one whole-genome duplication event relative to their nearest well-studied relative. The occurrence of a duplicated genome in the history of the species, even if not retained in the extant species, can confound estimates of molecular evolution. Wang *et al.* have investigated the relative rates of molecular evolution in a conserved syntenic sequence in members of the *Solanaceae* family (eggplant, pepper, petunia, potato, and tomato) that have undergone no genome-wide duplication events since they diverged, which from this study was estimated to have been ~30 million years ago. Although some regions were duplicated within individual species, the authors were able to analyze genes and regions that have, more or less, been evolving as a single copy within the genome. They identified small-scale differences in the location of insertions and deletions, lineage-specific selection, gene content, order, and orientation, and estimated that approximately one-third of the examined regions is under selection and two-thirds of the sequences under selection are outside of genes and not associated with domestication. — LMZ

Genetics **179**, 10.1534/genetics.108.087981 (2008).

www.sciencemag.org

Science

1200 New York Avenue, NW
Washington, DC 20005
Editorial: 202-326-6550, FAX 202-289-7562
News: 202-326-6581, FAX 202-371-9227
Bateman House, 82-88 Hills Road
Cambridge, UK CB2 1LQ
+44 (0) 1223 326500, FAX +44 (0) 1223 326501

Subscription Services For change of address, missing issues, new orders and renewals, and payment questions: 866-434-AAAS (2227) or 202-326-6417, FAX 202-842-1065. Mailing addresses: AAAS, P.O. Box 96178, Washington, DC 20090-6178 or AAAS Member Services, 1200 New York Avenue, NW, Washington, DC 20005

Institutional Site Licenses please call 202-326-6755 for any questions or information

Reprints: Author Inquiries 800-635-7181
Commercial Inquiries 803-359-4578

Permissions 202-326-7074, FAX 202-682-0816

Member Benefits AAAS/Barnes&Noble.com bookstore www.aaas.org/bn; AAAS Online Store http://www.apisource.com/aaas/ code MKB6; AAAS Travels: Betchart Expeditions 800-252-4910; Apple Store www.apple/eppstore/aaas; Bank of America MasterCard 1-800-833-6262 priority code FAA3YU; Cold Spring Harbor Laboratory Press Publications www.cshlpress.com/affiliates/aaas.htm; GEICO Auto Insurance www.geico.com/landingpage/go51.htm?logo=17624; Hertz 800-654-2200 CDP#343457; Office Depot https://bsd.officedepot.com/portalLogin.do; Seabury & Smith Life Insurance 800-424-9883; Subaru VIP Program 202-326-6417; VIP Moving Services http://www.vipmayflower.com/domestic/index.html; Other Benefits: AAAS Member Services 202-326-6417 or www.aaasmember.org.

science_editors@aaas.org (for general editorial queries)
science_letters@aaas.org (for queries about letters)
science_reviews@aaas.org (for returning manuscript reviews)
science_bookrevs@aaas.org (for book review queries)

Published by the American Association for the Advancement of Science (AAAS), *Science* serves its readers as a forum for the presentation and discussion of important issues related to the advancement of science, including the presentation of minority or conflicting points of view, rather than by publishing only material on which a consensus has been reached. Accordingly, all articles published in *Science*—including editorials, news and comment, and book reviews—are signed and reflect the individual views of the authors and not official points of view adopted by AAAS or the institutions with which the authors are affiliated.

AAAS was founded in 1848 and incorporated in 1874. Its mission is to advance science, engineering, and innovation throughout the world for the benefit of all people. The goals of the association are to: enhance communication among scientists, engineers, and the public; promote and defend the integrity of science and its use; strengthen support for the science and technology enterprise; provide a voice for science on societal issues; promote the responsible use of science in public policy; strengthen and diversify the science and technology workforce; foster education in science and technology for everyone; increase public engagement with science and technology; and advance international cooperation in science.

Information for Authors
See pages 634 and 635 of the 1 February 2008 issue or access www.sciencemag.org/about/authors

Fire Out of Africa

Just when our ancestors began lighting their own fires rather than letting nature do it is one of archaeology's burning questions.

In 2004, Israeli archaeologists at the ancient hominid site of Gesher Benot Ya'aqov (GBY) in Israel, first occupied 790,000 years ago, convinced many experts that hominids living there had mastered fire, pushing back previously accepted dates by a half-million years (*Science*, 30 April 2004, p. 663). Now a member of that team has evidence that fire was controlled during the entire 100,000-year occupation of GBY.

Nira Alperson-Afil of The Hebrew University of Jerusalem analyzed the distribution of burned and unburned pieces of flint from eight occupational levels, looking for evidence of "phantom hearths": fireplaces obliterated by time but whose locations are indicated by debitage from the toolmakers who gathered around them.

Although only about 2% of the flint at the site is burned, Alperson-Afil found clusters where at least half the flint was burnt—revealed by pinhead-sized bubbles called "potlidding"—in each of the eight levels, she reports online this month in *Quaternary Science Reviews*.

The GBY hominids made tools belonging to the Acheulian cultural tradition, which arose in Africa about 1.6 million years ago. Ralph Rowlett, a prehistorian at the University of Missouri, Columbia, says that the study offers persuasive evidence that not only tools but mastery of fire was probably part of the "cultural package" of hominids who settled in the Near East after migrating from Africa.

A Win for Greenpeace

Aided by testimony from U.S. climate guru James Hansen, six Greenpeace activists last week were found not guilty of causing more than $60,000 worth of damage to a coal-fired power plant last year. The accused were in the process of painting "Gordon, bin it" (a message to U.K. Prime Minister Gordon Brown) on the plant's chimney when they were arrested.

The case was brought by the energy company E.ON, owner of the Kingsnorth power station in Kent, where there are plans to build the first of a new generation of coal-fired plants. But after an 8-day criminal trial, the jury agreed with Hansen, who argued that the miscreants had a "lawful excuse"—that they were trying to protect "property of greater value (the Earth!) from the impact of climate change." Hansen has called for a moratorium on all coal-fired plants.

Geologist Nigel Woodcock of the University of Cambridge says that the court's acceptance of the "just-war" argument "potentially opens the way for other direct actions by environmentalists who feel that their voice is not being heard."

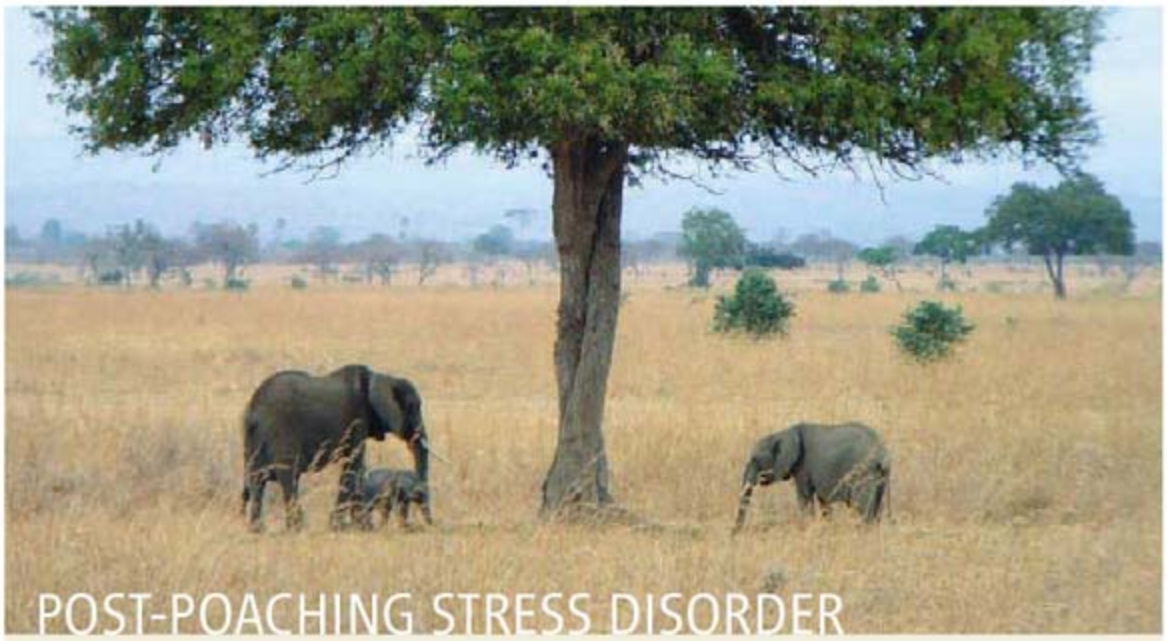

POST-POACHING STRESS DISORDER

Until a 1989 ban on ivory trading, the elephant population in Tanzania's Mikumi National Park was being ravaged by poaching. Now, almost 20 years later, more than 1000 elephants remain, but the past trauma continues to take a toll. "It disrupted the elephants' intricate social structure" and with it their breeding patterns, says Kathleen Gobush, lead author of a study in the current online issue of *Conservation Biology*, who is now at the U.S. Fish and Wildlife Service in Hawaii.

Normally, old females, known as matriarchs, guide groups of female relatives. But many families lost their matriarchs and older females, leaving younger ones adrift. Today, some 30% of adult Mikumi females are alone, and many are calfless despite being in their reproductive prime. Such lonely individuals have a rough go of it, say Gobush and her colleagues, who analyzed hormones in the elephants' dung. "They have very high stress hormone levels," which have apparently hampered their reproductive success, she says. "It may require another full generation or two before they fully recover."

The study "confirms that elephants are profoundly affected by the loss of older matriarchs and by deaths and disruptions in their families," says elephant researcher Cynthia Moss of the Amboseli Trust for Elephants in Nairobi, Kenya. "The more we know about their sensitivity to loss and disruptions, the more we have to consider the ethics of what we do to them," such as culling and translocations.

Bee Bottoms Up

Sort of like the "wave" that fans generate at football games, there's a "shimmer" that ripples through African honey bee hives. But unlike the fans, the bees have a serious purpose: warding off predators.

Bees create their ripple by doing a headstand and flipping their abdomens upward. One bee's flip triggers movement by its neighbor, says Gerald Kastberger, an ethologist at the University of Graz in Austria. The changing reflection of light from the bees' wings creates a shimmer across the surface of the hive. Kastberger and colleagues studied films of 450 shimmers frame by frame and discovered that the bees shimmered whenever a hornet or wasp drifted too close to the hive, causing would-be attackers to retreat. They reported their findings 10 September in *PLoS One*.

Michael Breed, an animal behaviorist at the University of Colorado, Boulder, says the work clinches the purpose of shimmering: "The most analogous thing is when large groups of fish get together. Once a predator is spotted, there's a lot of visual disruption, which makes it harder to catch individual prey."

CREDITS (TOP TO BOTTOM): KATHLEEN GOBUSH; NAAMA GOREN-INBAR; GERALD KASTBERGER

EDITED BY YUDHIJIT BHATTACHARJEE

Three Q's >>

At 38, **Joseph DeRisi** already has an impressive resume that includes co-developing the ViroChip, the DNA microarray used in 2003 to identify the SARS virus that plagued Asia. Last week, the University of California, San Francisco, scientist won this year's $250,000 award for Technology, the Economy and Employment from the Heinz Family Foundation. The full list of awards is at heinzawards.net.

Q: Why haven't you tried to patent ViroChip or any of your other inventions?
It's a sense of fairness. If we really want to push the endeavor of researching human health forward, we're going to need to disseminate technology faster and into more people's hands simultaneously rather than simply making it available to only those who can pay.

Q: Are there any situations in which you think patenting technology is appropriate?
Sure. I'd patent the iPhone. But publishing scientific progress and keeping the methods secret, … that's not okay. Or keeping something secret when it would slow public health advancement, that's a problem, too.

Q: Can you give an example in which open sharing of research has led to faster development of a tangible health benefit?
Two companies that do genetic testing to predict the likelihood of a recurrence of breast cancer, Genomic Health and Agendia, have products based on microarray gene expression experiments that used the open-access platform we gave away. If we had kept those things secret, maybe those experiments wouldn't have been done, and [someone] wouldn't know what their risk of recurrence of breast cancer is.

Celebrities >>

ROW, ROW. As a postdoc at the University of Oxford in the U.K., geochemist Joshua West is in the opening stages of what he hopes will be a long and successful career in science. But the 31-year-old American has already reached the summit in his other career: Last month, he won an Olympic silver medal in rowing, competing for Great Britain in its eight-man boat.

Born and raised in Santa Fe, New Mexico, West has dual U.S.–U.K. citizenship. He came to attend graduate school at the University of Cambridge in 1998 and joined the British rowing team in 2001. After years of balancing both sports and his study of Earth's chemical weathering, he left the lab for the year running up to the games because "trying to train at that level and keep a career going is a tough lifestyle."

Competing in Beijing was "a fantastic opportunity," he says. Now that he's back to the daily grind of research, he's not sure which is tougher. "While it's definitely not physically as taxing as a training session, research certainly has its own intensity," he says.

MOVERS

FORESHADOWING. British plasma physicist Steven Cowley is the new director of the Culham Science Centre in the United Kingdom. The center is home to the Joint European Torus (JET), which will be the world's largest fusion reactor until ITER comes online in 10 years in southern France. "I started out in fusion," says Cowley, 49, who in recent years has been pondering the origins of the universe's magnetic field through a joint position at the University of California, Los Angeles, and Imperial College London. "It'll be good to be thrown back into it."

JET, which set the fusion world record back in 1997 by generating 16 megawatts of power, is being refitted as an ITER test bed with an interior lining and radio-frequency heating antenna similar to that of its bigger cousin. "We have to learn a lot of things from JET about ITER," he says. But it's not all about preparing for the next big thing. After JET's upgrade is finished in 2010, "we'll put some tritium in and break all the world records again," Cowley promises.

Got a tip for this page? E-mail people@aaas.org

Cowley takes over from Chris Llewellyn Smith, who is retiring after 5 years at the helm.

AWARDS

BIOMEDICAL STARS. Four scientists have won the prestigious Lasker Awards for research on RNAs that opened up a new world of gene regulation and for discovering the first statin drug that lowers cholesterol.

Victor Ambros, 54, of the University of Massachusetts Medical School in Worcester, Gary Ruvkun, 56, of Massachusetts General Hospital in Boston, and David Baulcombe, 56, of the University of Cambridge, U.K., will share the $300,000 basic research award for their RNA work, which began in the early 1980s when Ambros and Ruvkun were postdoctoral fellows in the same lab at the Massachusetts Institute of Technology in Cambridge. Their discovery of tiny RNA molecules controlling development in worms was seen as having limited impact until Baulcombe found small RNAs in plants that also controlled gene expression. That "really lit up a dry tinder," says Ruvkun. Since then, hundreds of small RNAs have been identified in many species, including humans.

Separately, the $300,000 Lasker Award for clinical research goes to Akira Endo, 74, of Biopharm Research Laboratories in Tokyo. Endo speculated that substances in fungi might be able to lower cholesterol, and, after exhaustive testing, he found one in 1973. Statin drugs today are taken by millions of people.

CREDITS (TOP TO BOTTOM): NIH; GETTY IMAGES; UKAEA/CULHAM SCIENCE CENTRE

A better way to manage fisheries
1619

More delay for climate satellites
1620

MUSEUMS

California Academy Practices What It Preaches About Sustainable Living

SAN FRANCISCO—When Pritzker Prize–winning architect Renzo Piano set out 8 years ago to design a new building here for the California Academy of Sciences, he envisioned lifting up a piece of the city's famous Golden Gate Park and slipping the academy's museum underneath it. Now, tucked under an undulating 1-hectare living roof, Piano's vision is ready for visitors. It houses a colony of African penguins, a four-story rainforest, and the deepest coral reef tank in the world. When the building opens to the public 27 September, it will mark a milestone for the 155-year-old academy, which closed the doors on its old museum, aquarium, planetarium, and research buildings in the park nearly 5 years ago, eschewing relatively modest repairs and seismic retrofitting in favor of a more dramatic transformation.

The new building is green, literally and figuratively. The roof mimics the city's rolling hills and is covered with native plants to provide habitat for birds, butterflies, and other insects. Skylights, solar panels, and a host of other eco-friendly features should qualify the museum as the largest public space in the world to earn the U.S. Green Building Council's highest rating for Leadership in Energy and Environmental Design. "It's a fantastic building," says Leonard Krishtalka, director of the University of Kansas Natural History Museum and Biodiversity Research Center in Lawrence. "It practices what natural history museums are preaching, that we need to live in harmony with biodiversity and harm the environment as little as possible."

The new building also unites the academy's research collections and scientists, who were previously scattered across a 12-building campus. The academy's new dean of science and research collections, evolutionary biologist David Mindell, says the move will help foster greater collaboration among the various disciplines. "This is intended to be a new beginning," Mindell says.

The academy's move has roots in the 1989 Loma Prieta earthquake, which damaged several of the old buildings. During the dot-com gold rush of the late 1990s, San Francisco was booming, and the academy's then-director, Patrick Kociolek, saw an opportunity to tap into public goodwill to build a more inspiring museum (*Science*, 30 April 2004, p. 669). Although a few planned features proved unfeasible, "it is remarkable that the vision we had back in those days actually did turn out pretty much as we'd described it," says Kociolek, now the director of the University of Colorado Museum of Natural History in Boulder.

The vision came with a hefty price tag. The entire project, including the transfer of about 300 academy staffers and 20 million specimens to a temporary location during the construction, cost approximately $488 million. So far, the academy has raised about $465 million: about $152 million from city, state, and federal funds, and the rest from individual, corporate, and foundation contributions.

The new museum, which incorporates the once-separate planetarium and aquarium, puts a new face on the academy's public spaces. Old standbys like the Africa hall have been enlivened: The dioramas are still there, but now a video system projects a troop of elephants trudging along on the horizon behind the stuffed zebras and oryx. Live African penguins preen and splash behind a large window.

In the rainforest dome, an underwater tunnel takes visitors below the surface of a flooded Amazon forest, and a ramp takes them up through exhibits of flora and fauna native to other rainforests of the world, including Madagascar—a case study in habitat destruction—and Costa Rica—where large swaths of rainforest have been preserved. The goal is to present the natural world in the context of the scientific issues of our times, such as climate change, extinction, and evolution, says the academy's executive director, Gregory Farrington. "It's not just a series of cases of stuffed lemurs."

The living roof is itself an exhibit and an opportunity to teach visitors about sustainable architecture, says

New digs. Topped with a living roof (*inset*), the eco-friendly California Academy of Sciences building opens its doors next week.

CREDITS: TIM GRIFFITH

10 years after the Ph.D.
1622

Sunnier outlook for new Australian crops
1629

senior botany curator Frank Almeda. In addition to providing insulation, the roof's plants absorb storm water to reduce runoff, and its hills funnel air into the museum's central piazza, providing natural ventilation.

The academy also hopes to breathe fresh air into its research programs with new hires, including Mindell, who left the University of Michigan, Ann Arbor, to join the academy in July, and Zeresenay Alemseged, a 39-year-old Ethiopian-born paleoanthropologist who joined the academy in May as its anthropology chair. Mindell says he hopes to hire several more young researchers like Alemseged, a rising star recognized for his discovery of the earliest known skeleton of a hominid child (*Science*, 22 September 2006, p. 1716). Mindell also aims to foster more collaborations with scientists at Bay Area universities.

Expanding the academy's research into microbial biodiversity and the phylogenetic relationships among viruses, bacteria, and other microscopic life forms is also part of the plan. "Natural history museums have traditionally been unconcerned with those taxa because they were relatively unknown at the time when the large research museums were formed, yet they represent the vast majority of the tree of life," Mindell says.

"It's a huge world waiting for exploration," agrees Michael Novacek, provost of science at the American Museum of Natural History (AMNH) in New York City. Novacek says AMNH was the first museum to appoint a microbial curator in 2004, but it's an idea that seems to be catching on. By virtue of the expeditions they mount to sample diverse environments and their expertise in building and maintaining collections, natural history museums can play an important role in microbiology, Novacek points out.

The work of reinventing the academy is just beginning, says Farrington. "Our goal is really simple: We want to do our very best to define what it means to be an institution of this sort for this century," he says. "Opening day is the starting line."

–GREG MILLER

MUSEUMS

Smithsonian Takes the Plunge With Ocean Exhibit

The right whale hanging from the new Sant Ocean Hall at the Smithsonian National Museum of Natural History (NMNH) is only half the size of the iconic blue whale featured at the American Museum of Natural History in New York City. But she's much more "alive." The 14-meter-long, 1043-kilogram replica is modeled after 21-year-old Phoenix, one of 400 remaining North Atlantic right whales, and one that researchers have tracked since birth thanks to her signature tail and fin shape and birthmarks. Visitors can retrace her maritime travels in a new permanent exhibit opening next week that showcases the popular Washington, D.C., museum's expanding presence in marine research.

"The new ocean hall will really make a difference," says marine ecologist Larry Crowder of the Duke University Marine Lab in Beaufort, North Carolina. Adds NMNH advisory board member Rita Colwell of the University of Maryland, College Park, "It gets millions of visitors a year; you can get the message across in an exceptional way."

Phoenix joins the hall's 674 specimens, including two giant squid, a live coral reef, and fossil trilobites and shark jaws, along with an 8-meter Native American canoe and a surfboard. Their new surroundings are a response to a call 5 years ago for the 160-year-old institution to take stock of its strengths and focus on a few research areas (sciencenow.sciencemag.org/cgi/content/full/2003/107/4). In addition to an exhibit, NMNH is hiring curators with a marine bent. It also plans to set up a Web portal that will provide ocean education and outreach over the Internet in conjunction with other leading oceanographic and marine research institutions.

Calamari, anyone? The museum required special fluid to exhibit its giant squids.

Five years ago, very little exhibit space dealt with the marine realm, despite its importance to the evolution of life and to humans, past and present. Yet 80 million of the museum's 124 million specimens and artifacts came from the sea. Dozens of curators study some aspect of the marine world—from undersea volcanoes to fish systematics—but not in any cohesive way. Several other Smithsonian research centers also concern themselves with marine studies.

Congress gave $22 million to the National Oceanic and Atmospheric Administration toward the 2137-square-meter, $49 million museum exhibit. In addition to displaying sea life and human maritime culture, the new hall will highlight "why science matters" and how science works, says NMNH Director Cristián Samper: "This is not a hall just about fish. We're trying to look at oceans from every discipline." A $15 million endowment from Washington, D.C., philanthropist and Smithsonian Regents adviser Roger Sant and his wife, Victoria, will ensure that the exhibits are kept up-to-date. The Sants also donated $10 million for an endowed position in ocean research, the centerpiece for an expanded program in marine science, now filled by marine biologist Nancy Knowlton.

"It is critical that the Smithsonian be a convener rather than just another research program competing for the same dollars and projects," says oceanographer Andrew Rosenberg of the University of New Hampshire, Durham. "It needs to be a linking institution—linking together researchers from around the country and the world, linking research to public education and education and research to public policy."

–ELIZABETH PENNISI

CREDIT: SMITHSONIAN

ECOLOGY

Privatization Prevents Collapse of Fish Stocks, Global Analysis Shows

Two years ago, a team of researchers took a broad look at the world's commercial fisheries and predicted that excessive harvesting would cause them all to collapse by 2048. Now, three other scientists have taken an equally broad look at how fisheries are managed and come up with a more hopeful view.

On page 1678, the trio—Christopher Costello and Steven Gaines of the University of California, Santa Barbara, and John Lynham, now at the University of Hawaii, Manoa—shows that stocks are much less likely to collapse if fishers own rights to fish them, called catch shares. If implemented worldwide, they say, this kind of market-based management could reverse a destructive global trend. Says David Festa of the Environmental Defense Fund in San Francisco, California, "This gives definitive, concrete proof that this tool does end overfishing."

In the bank. Transferable quotas helped save the halibut fishery in Alaska, which was threatened by overfishing in the early 1990s.

CREDIT: PAUL A. SOUDERS/CORBIS

The new paper was inspired by a dismal report by Boris Worm of Dalhousie University in Halifax, Canada, and his colleagues (*Science*, 3 November 2006, p. 745). Worm's team had analyzed all the large marine ecosystems in the world and found that those with declining biodiversity tended to have more collapsed fisheries, defined as yields less than 10% of historical maximums. Costello, Gaines, and Lynham wanted to know if allotting catch shares—a kind of equity in the ecosystem—might provide a solution. "It's like having shares in a company," Costello explains. "It gives fishermen an incentive not to overharvest."

There was anecdotal evidence for optimism. Fishing for halibut in Alaska, for example, used to be a dangerous, inefficient race. Competitors rushed to fill their holds before the industry reached its quota. They often overshot the quota, so regulators shortened the season to just a few days—prompting all the boats to go to sea no matter how bad the weather. When they returned en masse, they promptly flooded the market with a year's worth of fish.

Business became better—and safer—after a system of catch shares was implemented in 1995. Each fisher was allocated a number of individual transferable quotas (ITQs), which they can use to catch fish or sell to others. The quotas are a percentage of the total allowable catch, which is set by regulators each year. The catch varies from year to year, based on scientific assessment of the health of the fishery. The result: Captains could plan when to fish without worrying about weather or being beaten, regulators have extended the season, and prices for halibut have climbed.

Australia, New Zealand, and Iceland, among others, claimed success with this approach, but no one had done a comprehensive analysis. Costello, Gaines, and Lynham examined more than 11,135 fisheries worldwide. Only 14% of the 121 fisheries using ITQs or similar methods had collapsed, compared with the 28% collapsed among fisheries without ITQs. Had all the world's fisheries implemented catch-share management in 1970, the researchers found, only 9% would have collapsed by 2003. The findings are conservative, Costello explains, because most ITQ systems have been put into place fairly recently; each year of rights-based management makes a collapse 0.5% less likely.

Jeremy Prince, a consultant in fisheries ecology in Perth, Australia, says that further research could help reveal how to tailor catch-share management schemes to particular fisheries. Meanwhile, he says, the new findings could help win over skeptical fishing communities. Most important, Prince says, the study highlights the impact of rights-based management. "It comes down to a long-term choice about having sustainable fishery or not."

–ERIK STOKSTAD

SCIENCESCOPE

Aussie Science Review

CANBERRA—Australia's approach to funding R&D needs a major revamp, says a review released here last week. The report, commissioned by science minister Kim Carr, highlights a fundamental flaw in the system, researchers say. Whereas funding agencies in the United States cover about a third of research project overhead, Australian government bodies fund as little as 20% of overhead costs such as electricity and lab maintenance. "We're running down our physical infrastructure and milking international students," says Michael Gallagher, CEO of the Group of Eight Universities, which represents Australia's research-intensive universities.

The review, led by industrialist Terry Cutler of Cutler & Co., calls on the government to boost R&D spending by $1.7 billion a year to $6.8 billion per year. The increase should be used in part to fully fund overhead, the report says. John Mattick, director of the Institute for Molecular Bioscience at the University of Queensland in Brisbane, applauds the proposals, because more funds for overhead "will eliminate the cross-subsidization of research by teaching [fees]," he says. Carr's office calls the report "timely and important" and says the government will respond by year's end.

–ELIZABETH FINKEL

NIH to Get New Look

The push to merge some of the 27 institutes and centers at the sprawling U.S. National Institutes of Health (NIH) is back on the agenda. Last week, Director Elias Zerhouni announced that a panel drawn from inside and outside NIH will be charged with examining its structure and looking for ways to improve efficiency. With biomedicine becoming more complex, "NIH must respond nimbly and strategically," Zerhouni said in a press release.

Observers have long complained that NIH is bogged down by a heavy superstructure created over the years at the behest of patient advocacy groups and Congress. Former NIH director Harold Varmus once said that there should be just six institutes, and a 2003 Institute of Medicine report suggested some specific consolidations. The 21 members of the new panel, the NIH Scientific Management Review Board, which includes Varmus, will reexamine these ideas. Chair Norman Augustine, former head of Lockheed Martin Corp., says he's optimistic that the panel will have clout because it was mandated by Congress in the 2006 NIH Reform Act. "It's a question of how compelling the arguments are," Augustine says. NIH has not yet scheduled the board's first meeting.

–JOCELYN KAISER

EARTH MONITORING

Troubled U.S. Satellite Program Runs Into Additional Hurdles

Problems with a key sensor could further delay the first flight of a troubled $12.5 billion U.S. weather and climate satellite program. *Science* has learned that the technical problems not only threaten the planned June 2010 inaugural launch of the National Polar-orbiting Operational Environmental Satellite System (NPOESS) but also could imperil the satellites' ability to collect reliable climate measurements during the next decade.

NPOESS is a planned fleet of five satellites, launched sequentially, that would gather environmental data continuously from every inch of Earth. The latest problems concern the troubled Visible Infrared Imaging Radiometer Suite (VIIRS), one of four instruments aboard the first proof-of-concept satellite. The three agencies that jointly manage the program—NASA, the National Oceanic and Atmospheric Administration (NOAA), and the U.S. Department of Defense—must decide by the end of the month whether to delay the 2010 launch, which could have a snowball effect on the program's schedule and cost.

NPOESS is no stranger to adversity (*Science*, 2 June 2006, p. 1296). Begun in 1994, the program was to cost $6.5 billion and send up its first satellite in 2008. The date was later pushed back to 2013. Two years ago, a mandatory Pentagon review led to the removal of five crucial climate sensors, three of which have since been restored.

Hazy picture. VIIRS sensor hopes to measure climate variables such as dust over land.

Raytheon Space and Airborne Systems, which is building VIIRS, calls it "the most sophisticated weather sensor ever developed for space." But the $153 million instrument, which can measure 23 environmental variables, has also created a multitude of headaches. One problem has been getting the latches that secure its radiator to work properly, a problem that engineers have been unable to resolve for months. NASA engineers are also worried that the instrument may have been damaged during a July test in which it was exposed to an electromagnetic field roughly 10 times stronger than the level NASA terms a safe operating limit.

The biggest fear among climate scientists is that electrical noise between segments of the VIIRS sensor has not been eliminated. Northrop Grumman says the sensors meet specifications, but NASA's James Gleason, the head scientist on the preliminary mission, says tests on that specific part "were not quantitative, as we would have liked." An upcoming test should determine whether the noise levels are low enough to allow measurements precise enough to detect climate trends.

If the levels are too high, it may not be possible to fix the problem. In June, the Pentagon said any further projected cost increases could force a return to lower specifications for data quality that scientists say could make climate measurements impossible. NASA and NOAA officials oppose such a move, but the Pentagon has threatened to cut off its share of funding for the program if the three agencies cannot agree on an overall budget and schedule. A 31 August deadline for such an agreement, already 4 years late, has passed. At presstime, officials said the agreement was in "final sign off."

–ELI KINTISCH

EPIDEMIOLOGY

Lower Malaria Numbers Reflect Better Estimates and a Glimmer of Hope

At first glance, a new report by the World Health Organization (WHO) appears to herald good news in the global battle against malaria: The number of cases is down from the 350 million to 500 million WHO estimated in 2005 to 247 million, and deaths from more than 1 million to 881,000. But the report's authors say that the drop isn't a sign we're winning the battle, just that the methodology of gathering data is better. Among other things, WHO has a better way to estimate the true number of malaria cases from the figures reported by governments—which are known to be inaccurate.

The study does have some truly good news, however: In endemic areas, the number of people who sleep under insecticide-treated bed nets and have access to a new generation of effective drugs called artemisinin combination therapies (ACTs) has gone up rapidly. Plummeting malaria rates in Eritrea, Rwanda, São Tomé and Príncipe (a country off Africa's West Coast), and Zanzibar, which led the way in introducing these interventions, suggest they hold great promise.

Determining the burden of malaria is notoriously hard because many patients don't seek or receive medical attention, and even if they do their case may not be lab-confirmed or entered into government statistics. One result is that WHO's numbers have huge error bars: For instance, the estimate for Kenya ranges from 5 million to 19 million cases.

The uncertainty also leads to controversy. Malaria epidemiologist Robert Snow of the University of Oxford, U.K. and the Kenya Medical Research Institute in Nairobi says that WHO still relies too heavily on weak government data, resulting in too rosy a picture. Based on his own work, Snow believes the actual numbers are at least 50% higher than WHO's. But Nicholas White, a malaria researcher at Mahidol University in Bangkok, Thailand, says the report is "reasonably robust" given the difficulties.

In any case, says report co-author Mac Otten, the key news is that ACTs and bed nets have more than halved the malaria burden since 2000 in the areas that led the way with intervention. White agrees. "I think we can be confident that we're having an impact," he says—and that should translate into numbers dropping in many countries in the years to come. But Peter Agre, head of the Johns Hopkins Malaria Research Institute in Baltimore, Maryland, says that will happen only if donors keep up the funding that makes scaling up the interventions possible. **–MARTIN ENSERINK**

CREDIT: AP PHOTO/PAUL HELLSTERN

SCHOLARLY PUBLISHING

House Weighs Proposal to Block Mandatory 'Open Access'

A controversial policy requiring researchers to make their papers freely available to the public at a U.S. National Institutes of Health (NIH) Web site is facing a potential roadblock. Last week, members of a powerful House committee held the first-ever congressional hearing on the policy and floated a proposal to overturn it.

Three years ago, NIH began asking grantees to send the agency copies of their accepted, peer-reviewed manuscripts so that it can post them in its full-text PubMed Central archive within 12 months after they are published. But compliance was so poor that proponents of the idea persuaded the House and Senate appropriations committees to tell NIH to make the policy mandatory (*Science*, 18 January, p. 266). Many publishers protested, complaining that the "public access" policy infringes on their copyrights and will put them out of business by cutting into their subscription base.

These critics have now found allies on the House Judiciary Committee. Last week at a 2-hour review of the policy, members of its Subcommittee on Courts, the Internet, and Intellectual Property grumbled that by changing copyright rules, appropriators had overstepped their jurisdiction. Members heard testimony from both sides of the debate.

NIH Director Elias Zerhouni argued that NIH simply wants to "maximize the return of our investment" of $400,000 per research grant. He emphasized that PubMed Central is enhancing the papers by linking them to other databases. "The real value is in the full connectivity," not "the passive document" in archives, he said. He noted that compliance with NIH's rule has risen since it took effect in April: Submissions are on track to reach 56% of the 80,000 eligible papers per year, many submitted directly by journals (see graph, above). "There is no evidence that this has been harmful" to publishers, he argued. Open Access advocate Heather Joseph of the Scholarly Publishing and Academic Resources Coalition in Washington, D.C., agreed. She argued that journals lose little by posting "old" papers 12 months after publication and noted that the policy applies to only NIH-funded studies.

Others disagreed. Law professor Ralph Oman of George Washington University in Washington, D.C., argued that NIH's policy is a "dilution of the rights of the copyright owners" and "will destroy the commercial market" for science and technology journals.

A bill introduced by Judiciary Committee Chair John Conyers (D–MI) would bar any federal agency from requiring "the transfer or license" to the government of a work that has been produced in part with nongovernment funds or to which value has been added by the publisher through peer review. The Fair Copyright in Research Works Act (HR 6845) would mean grantees could not be required to submit accepted papers to a free archive.

Congress is not expected to act on the legislation before it adjourns later this month. Jonathan Band, a Washington, D.C., attorney who represents the American Library Association, which favors open access, says the bill is fatally flawed because of its sweeping provisions. "It goes far beyond the NIH policy. It limits a lot of what the federal government can do," he says. But Allan Adler, legal affairs director for the Association of American Publishers, which supports the bill, expects that both the House and Senate Judiciary Committees will examine the issue again next year. "This is really the beginning," Adler says.

–JOCELYN KAISER

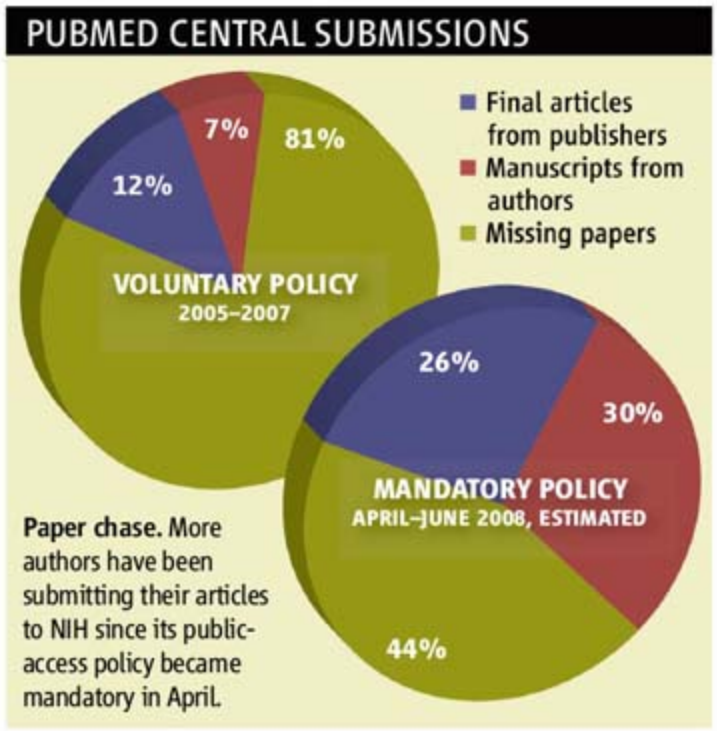

Paper chase. More authors have been submitting their articles to NIH since its public-access policy became mandatory in April.

SOURCE: NIH; CREDIT: NASA

Physicists Support Conservation of Energy

"Energy efficiency is one of America's great hidden energy reserves," declares a new report by the American Physical Society released this week. To better tap that mother lode, the authors call for big increases in basic research funding, establishment of an agile, high-risk research agency modeled after DARPA, and a commitment to what they call "critical longer term applied research," such as developing advanced windows and ventilation. (The U.S. Department of Energy often favors deploying technologies already on the shelf, the report says.) In order to persuade both consumers and industries to save kilowatts, the report calls for new kinds of electric power metering to support plug-in hybrid vehicles, tougher commercial and residential building standards, and fuel-efficiency standards of 50 miles per gallon by 2030. (Current standards call for 35 mpg by 2020.)

By coincidence, on the same day a coalition of unions, energy companies, environmentalists, and industry groups called on the federal government and states to prioritize efficiency. They believe tax incentives for companies and households, job training programs, and the appointment of a National Energy Efficiency Advocate at the White House can make efficiency "the essential starting point in meeting demand for additional U.S. power supply."

–ELI KINTISCH

Cravin' MAVEN

A new mission to Mars aims to provide the first in-depth probe of the Red Planet's atmosphere, NASA announced this week. The Mars Atmosphere and Volatile Evolution (MAVEN) spacecraft will be designed to orbit the planet for a year and collect data on features of the atmosphere such as the electromagnetic composition of solar winds that bombard the planet. Previous Mars missions have shown that the planet's atmosphere has thinned considerably over the past 4 billion years, and MAVEN will quantify the planet's gas loss to enable researchers to analyze that impact on climate change. "I see this as exploring the nature of martian habitability," says principal investigator Bruce Jakosky, an atmospheric scientist at the University of Colorado, Boulder. With a price tag estimated at $485 million, MAVEN is set to launch in November 2013 and should go into an elliptical orbit around Mars 1 year later.

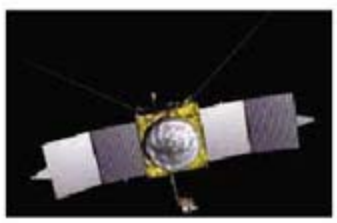

–RACHEL ZELKOWITZ

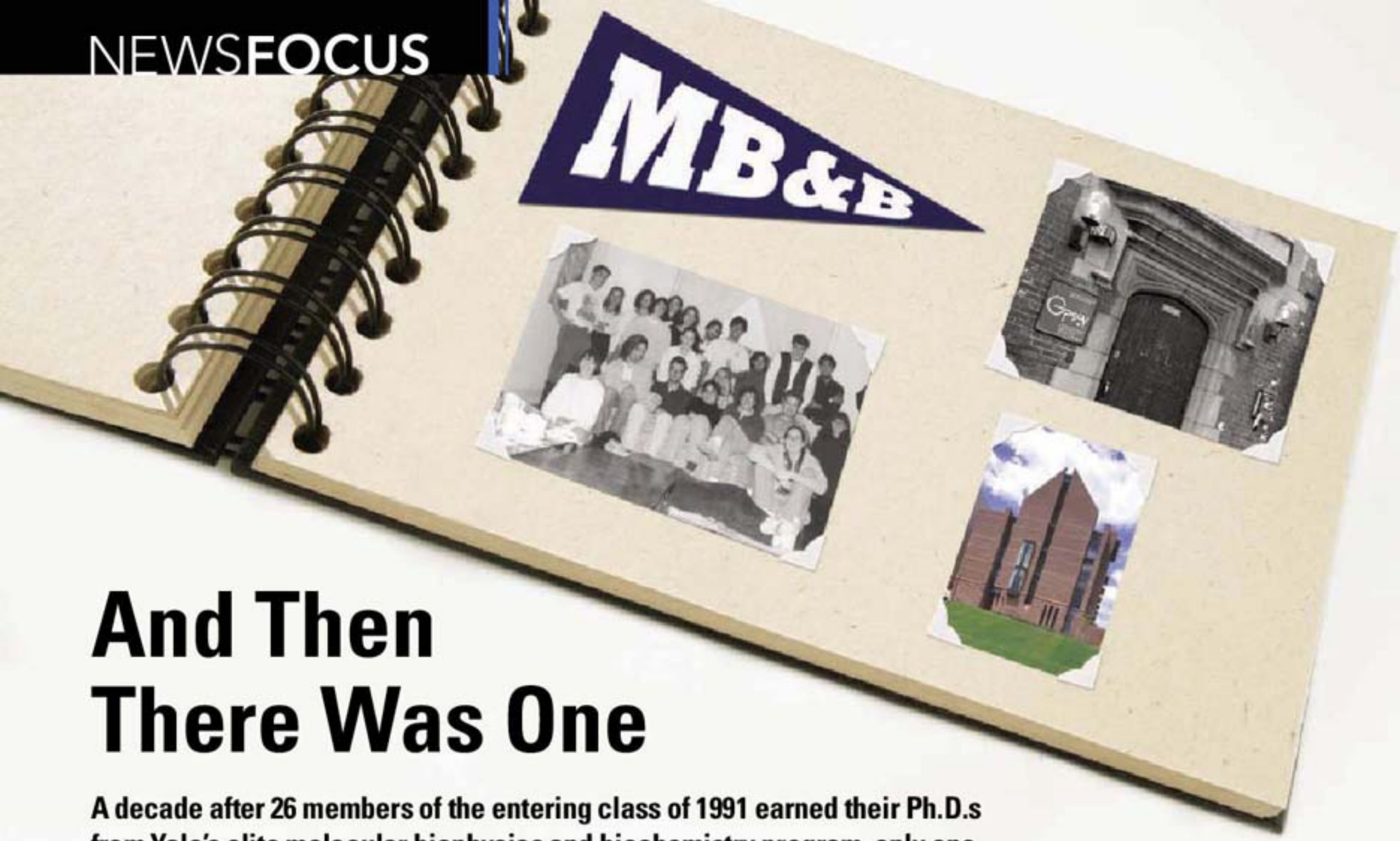

And Then There Was One

A decade after 26 members of the entering class of 1991 earned their Ph.D.s from Yale's elite molecular biophysics and biochemistry program, only one holds a tenured faculty position. But is an exodus from academia a bad thing?

Tricia Serio had been a big fish in the small, student-oriented biology department at Lehigh University in southeastern Pennsylvania. But could the daughter of a close-knit, working-class family in New Jersey, the first sibling to go away to college, make it as a graduate student at a research-intensive, Ivy League university?

Serio wasn't the only one feeling insecure as she arrived at the summer orientation weekend put on by the molecular biophysics and biochemistry (MB&B) program at Yale University. The size of the incoming class of 1991—with 30 students, it was more than twice the norm—had spawned a false rumor that the dean had accidentally mailed acceptance letters to dozens of students on the waiting list. The orientation was intended to ease those doubts among first-year Ph.D. students. So after spending the day listening to MB&B faculty members talk about their research, Serio headed to the GPSCY (Graduate and Professional Student Center at Yale) bar on the New Haven campus to unwind and compare notes with her classmates.

That's when the GPSCY cast its spell on her. Amid the low ceiling, concrete walls, cheap furniture, and spilt beer in this basement grad student hangout, Serio's fears began to dissipate. Seeing how easily the "adults"—professors and older graduate students—mingled with people like herself at the bottom of the food chain, Serio decided that she might belong after all. I could be comfortable here, she thought.

Online
sciencemag.org
Podcast interview with the author of this article.

She was right, and not just about graduate school. In her last year in the program, Serio married Jeffrey Laney, a third-year MB&B student she had met at the mixer. Then she did a postdoc with Susan Lindquist at the University of Chicago in Illinois and was hired by Brown University in 2002 (along with Laney, who comes up for tenure in 2009–10). Named a Pew Scholar in 2003, she received her first R01 grant from the National Institutes of Health (NIH) in 2006. And this spring, at the age of 38, she was awarded tenure.

Back at the GPSCY (which has since been upgraded and now bears the name Gryphon's Pub), Dan Zimmer wasn't having any trouble blending into his new surroundings. Maybe it was his undergraduate degree from the Massachusetts Institute of Technology (MIT) in Cambridge and the 2 years he had spent doing summer research. In any event, Zimmer remembers feeling pretty confident about his ability to handle the coursework, pick a good lab, nail his thesis, and embark on an academic career.

Zimmer was midway through the MB&B program before he began to question whether that path was right for him. It wasn't until his postdoc at the University of California, Berkeley, that he realized Serio and other "academically bound" colleagues had a passion for independent research that he just didn't share. "I don't think I ever developed that trait," he says. "I didn't have a specific area of science that I loved and wanted to pursue."

Sensing that the collaborative nature of industrial research would be a better match,

CREDITS (TOP TO BOTTOM): CORBIS; MICHAEL MARSLAND/YALE; COURTESY OF KATHY SEGGERSON GLEASON; MICHAEL MARSLAND/YALE; JOHN ABROMOWSKI

Work and play. Both the Bass Center for Molecular and Structural Biology on Yale's Science Hill and the GPSCY bar were landmarks for MB&B students.

Zimmer left Berkeley in 2001 and became the 50th employee of a fledgling biotech company in Cambridge. In April, the same month in which Serio got the news that cemented her academic status, Zimmer's employer changed its name from Microbia to Ironwood to reflect its expanded mission to discover, develop, and market its own drugs. After a series of promotions, Zimmer is now in charge of the company's drug-discovery program.

Coming from the University of Hawaii, where she had grown up as a fourth-generation Filipino-American, Tammy Spain was thrilled at the chance to earn a doctoral degree from Yale. Meeting over drinks at the GPSCY, she and Serio quickly became friends and first-year roommates, and both chose to study under virologist George Miller. Spain also became friends with Zimmer, and the two dated before they went their separate ways.

- Associate director, Florida Center of Excellence for Biomolecular Identification and Targeted Therapeutics
- University of South Florida, Tampa
- Age: 41 • Yale adviser: George Miller

But unlike her two classmates, who have put down strong roots in academia and industry, respectively, Spain is still searching for her true path in science. After doing two postdocs and working in industry and for the public sector, Spain was hired this spring by the University of South Florida, Tampa, to manage a new center designed to help faculty members from many disciplines find commercial applications for their work in detecting pathogens, diagnosing diseases, and targeted therapeutics. "I'm drawn to new things," says Spain, who says the job lets her combine her knowledge of microbiology with her real-world experience. "And I like to be where the action is."

Choosing a career

On its Web site, the MB&B program declares that its mission is "to prepare students for careers as independent investigators in molecular and structural biology." In academia, that typically means the ability to sustain a lab with peer-reviewed funding from NIH. The mission rests on the premise that the U.S. research enterprise, acknowledged as the finest in the world, affords anyone with sufficient talent and determination the chance to become a successful scientist.

But that premise, a core tenet for academic biomedical researchers, has been sorely tested in recent years. They've watched the NIH budget, their most important source of funding, remain essentially flat for the past 5 years after doubling over the previous 6 years. That dismal funding picture has shrunk their already slim chances of obtaining the resources to become independent investigators. One unfortunate outcome, say community leaders, is that promising young scientists are being pushed out of academic research.

- Principal investigator, discovery
- Ironwood, Cambridge, Massachusetts
- Age: 39 • Yale adviser: Don Crothers

But is that true? *Science* decided to examine that argument by looking at the career paths of one group of young biomedical scientists who would seem to have an inside track on such jobs: the MB&B class to which Serio, Zimmer, and Spain belong. Twenty-six of the 30 students who entered the elite program in September 1991 earned their Ph.D. degrees in 1997 or 1998 and have spent the next decade spreading their wings. What are they—13 men and 13 women—doing now? And what role did NIH's funding roller coaster play in their decisions?

The answers come in 26 different flavors, and some of them might surprise you. Serio is the only graduate from the 1991 entering class who holds a tenured position. Five others are doing science in an academic setting, and a seventh is a university research administrator. But of those, only Matthew Goldberg, who in 2005 joined the University of Texas (UT) Southwestern Medical Center in Dallas as an assistant professor of neurology, currently has a tenure-track position. "When we started grad school, we all planned to go into academia and run our own labs," recalls Kathy Seggerson Gleason, now an adjunct biology faculty member at a small, 4-year college outside Denver, Colorado, who says she's currently "on hiatus" after adopting a child last year from China.

- CEO, A-CUBE Inc.
- Burlingame, California
- Age: 44 • Yale adviser: Axel Brunger

The small number in academic science doesn't mean the rest of the graduates have turned their backs on the profession. Roughly two-thirds of the graduates are employed in the life sciences and are "using" their degrees. Of those, 11 are working in the biotechnology industry—four doing research, and seven holding a variety of administrative positions. There's also a patent lawyer who works with biotech companies. Three graduates have gone into the information technology sector. *Science* could not confirm the job status of three other graduates. Four class members left within the first year of the program, one after an internal investigation into allegations of scientific misconduct.

"I would have guessed that the percentage in tenure-track positions would be higher, maybe 20% to 25% [rather than 7%]," says Mark Solomon, an MB&B professor and director of graduate studies at Yale. "But we're not just aiming for replacement faculty. That's not the reality anymore. There are a lot of good opportunities out there."

How many of the graduates would be in academic positions if the funding picture were brighter? That's impossible to say with any certainty. But most MB&Bers said they had other reasons for steering clear of academia. Some cited a strong interest in industry, and others mentioned family or personal reasons. Several say their training experiences soured them on following in their advisers' footsteps.

For some MB&Bers, academia was never really an option. "Even as an undergraduate in college, I never bought into the concept of being a professor," says

CREDITS (TOP TO BOTTOM): PAUL ZIMMER; DALY SANTANA; MAKOTO SAKAMOTO

Deborah Kinch, associate director for regulatory affairs at Biogen Idec in Cambridge. "Being a grad student is the last bastion of indentured servitude, and being a faculty member is pretty much the same thing, at least until you get tenure. Earning the same low salary and fighting for every grant—that was the last thing I wanted to do."

Despite those reservations, Kinch and her classmates uniformly praise the training that they received. "Those were formative years for me, and I learned to think independently," says Jennifer Holmes, now a patent attorney at Ropes & Gray LLP in Boston, who has been friends with Kinch since their undergraduate days at Mount Holyoke College in South Hadley, Massachusetts, and who worked alongside her in Solomon's cell cycle lab. "A Ph.D. is highly valued in this field. It's definitely opened doors for me."

The road to New Haven

Although they come from different backgrounds, the members of the 1991 MB&B class share a love for science that goes back to childhood. Tori Williams Reid, one of three students on an NIH-funded MARC (Minority Access to Research Careers) fellowship, recalls getting first a microscope and then a chemistry set from her mother. "She had no familiarity with science, but she must have perceived something in me," says Reid, who joined Accenture, the global consulting giant, shortly after graduation and moved around the country on a series of corporate assignments. In July, Reid left the company to start a home-care business for seniors.

For most MB&Bers, pursuing a career in science meant striking off on one's own. "If I hadn't gotten into the University of Illinois, I'd probably be making tractors," says Brian DeDecker, a research assistant professor at the University of Colorado, Boulder. DeDecker grew up in a small Midwestern town and was the first in his family to go to college. One exception is Jing Xu, who helps life science companies develop their business plans as an independent consultant based in San Diego, California. Studying science was the equivalent of going into the family business, she says. "Both my parents are chemists, and I grew up [in Xiamen, China] with the expectation that I would go into science."

Once the record-sized class descended on Yale in the fall of 1991, they began to worry that some of them weren't supposed to be there. To help convince herself that she belonged, Julia Pinsonneault says she took the first-year coursework very seriously. "I was obsessed with my grades," confesses Pinsonneault, who last month ended what she calls "the world's longest postdoc"—an 11-year ordeal—by becoming a research scientist in the pharmacology department at Ohio State University in Columbus. Chad Brautigam, a research scientist in the structural biology laboratory at UT Southwestern, says he went a bit in the opposite direction. "By the second semester, I was burnt out. I had worked really hard as an undergraduate, and I was so tired of taking tests that I let things go a little."

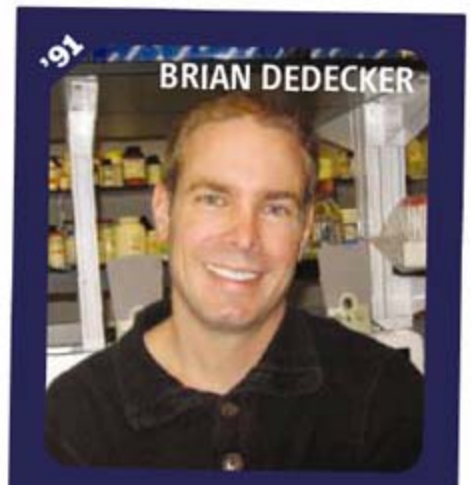

Goldberg, who had taken a year off to work in a nuclear magnetic resonance (NMR) lab at Harvard University, was chagrined to find that his undergraduate physics degree from the University of Michigan, Ann Arbor, had left him unprepared to grasp the secrets of living cells. "All of a sudden I had to learn biochemistry and cellular biology and genetics," he notes. He and a few other MB&Bers even took an undergraduate biochem course to catch up.

To help each other out, the class met regularly for informal study sessions in which they pooled their knowledge. "The biophysics was a challenge for me," recalls William Russ, now an assistant professor in the pharmacology department at UT Southwestern, who was a biochemistry major at Cornell University. "Fortunately, I had some friends from physics who struggled with memorizing the molecular biology but who loved the equations." In contrast, most MB&Bers say their professors weren't much help. "It came so easy to them, they didn't know how to explain it to somebody who didn't already understand," says Spain.

In addition to taking a full load of courses, first-class MB&B students were required to do three 10-week lab rotations covering both molecular biophysics and biochemistry. The rotations gave students a chance to dip their toes into both wet and dry science and helped prepare them for qualifying exams in both areas. The large size of the 1991 class made the normal jockeying for spots even more intense.

In October, the class went on a departmental retreat at Woods Hole Marine Biological Laboratory. Cowed by the subject matter, Russ was planning a "token" rotation in biophysics when his eventual adviser, Donald Engleman, a structural biologist, pulled him aside and gave him a piece of career advice that he's never forgotten. " 'You have a question, and you learn what you need to learn to answer it,' he told me," Russ recalls. "Everything I've done since the MB&B program is an extension of that conversation."

CREDITS (TOP TO BOTTOM): WILLIAM KINCH; DAVID SILVIAN; AIDAN DEDECKER; MARC V. REID

What Peter Kosa, now director of business development at XOMA, a northern California biotech company, learned in his first year was that he needed to take a year off. "I fell in love with structural biology after seeing these tremendous 3D pictures of molecules interacting with each other," he says about his decision to join the lab of Paul Sigler, a senior scientist with an impressive track record who had recently joined the Yale faculty. But Kosa had also fallen in love with a former classmate at Swarthmore College, where he had majored in biochemistry. After getting married, the couple decided they wanted to spend a year together "living somewhere we haven't lived before."

Kosa knew that he was bucking the odds. But after obtaining Sigler's backing and approval from the department, he spent a year working in an HIV lab at the University of Utah. True to his word, he returned in 1993 and 5 years later completed his Ph.D.

Settling into a lab

Although most students say they were able to get into the lab of their choice, those relationships weren't necessarily lasting ones or even helpful to their careers. "I wanted to work on solid-state NMR, which was still fairly new, and I picked a young faculty member," says DeDecker. "But the project, which was really more of a technique, didn't go anywhere." DeDecker blames himself for the misstep. "I'm not very politically savvy. I just wanted to find something that was cool and that interested me." Learning from that experience, he then joined Sigler's lab.

Macarena Parra, a payload scientist for life science missions at NASA Ames Research Center in northern California, says she got off to a rocky start under David Gonda, a young scientist just setting up his yeast lab, and never fully recovered. Not only was the project a stretch for a graduate student, she says in retrospect, but she missed the collegial, interdisciplinary research atmosphere she had enjoyed as an undergraduate at Rensselaer Polytechnic

THE YALE 1991 MB&B CLASS: WHERE ARE THEY NOW?

	NAME	STATUS	POSITION	LOCATION
ACADEMIA	Chad Brautigam	Research	Assistant professor, Department of Biochemistry	University of Texas Southwestern Medical Center, Dallas
	Brian DeDecker	Research	Assistant research professor, MCD biology department	University of Colorado, Boulder
	Kathy Seggerson Gleason	Teaching	Adjunct instructor	Regis University, Denver, Colorado
	Matthew Goldberg	Tenure-track	Assistant professor of neurology	University of Texas Southwestern Medical Center, Dallas
	Julia Pinsonneault	Research	Research scientist, Department of Pharmacology	Ohio State University, Columbus
	William Russ	Research	Assistant professor, Department of Pharmacology	University of Texas Southwestern Medical Center, Dallas
	Tricia Serio	Tenured	Associate professor, Department of MCBB	Brown University, Providence, Rhode Island
	Tammy Spain	Administration	Associate director, Florida Center of Excellence for Biomolecular Identification and Targeted Therapeutics	University of South Florida, Tampa
BIO INDUSTRY	Albert Crescenzo	Consultant	Symyx Technologies	Iselin, New Jersey
	Deborah Kinch	Supervisory	Associate director, regulatory affairs, Biogen Idec	Cambridge, Massachusetts
	Peter Kosa	Supervisory	Director of business development, XOMA	Berkeley, California
	Athena Nagi	Research	Principal scientist, analytical sciences, Amgen	Longmont, Colorado
	Nobuyuki Ota	Supervisory	Chief Executive Officer, A-CUBE Inc.	Burlingame, California
	Macarena Parra	Research	Research scientist, NASA Ames Research Center	Moffett Field, California
	Laura Silvian	Research	Crystallography group leader, Biogen Idec	Cambridge, Massachusetts
	G. Koji Sonoda	Supervisory	Senior manager, library, Amgen	Thousand Oaks, California
	Joseph Toth	Research	Senior scientist, Adnexus Therapeutics	Waltham, Massachusetts
	Jing Xu	Consultant	Nacalai USA and BioMinerva Group	San Diego, California
	Dan Zimmer	Supervisory	Principal investigator, discovery, Ironwood	Cambridge, Massachusetts
OTHER	Jennifer Holmes	Patent law	Associate, Ropes & Gray, LLP	Boston, Massachusetts
	Peter Klosterman	IT industry	Software engineer, Flash Foto	Oakland, California
	Tori Williams Reid	Entrepreneur	Right at Home (home-care for seniors)	Hillsborough, North Carolina
	Michael Reifler	IT industry	Facility systems integrator, Whole Foods Market	Mid-Atlantic Region

STATUS NOT KNOWN			
	L. Rochelle Bazemore Adviser: Nancy Ruddle	David Ledman Adviser: Robert Fox	Catherine Smith Adviser: Lynne Regan

graduate student. "But then she realized I wasn't a postdoc, and she said, 'I don't see any reason to continue talking with you.' That's when I realized there is a prescribed path that people were supposed to follow, for no good reason." Regan, her former adviser, says that Nagi's decision not to do a postdoc "was very unusual, because the assumption is that anyone who wants a science-related job will do one. But it worked out for her."

To Kinch, the idea of moving lockstep into an academic postdoc "started to look like a trap." But avoiding that trap also required a bit of luck. "Biogen had just begun a postdoc program, and it was being handled by the temp agency that I was working for," she recalls. "They had just posted it, and I went for an interview and got hired that day." A year later, she was hired as a full-time employee.

Kosa remembers how his initial excitement about being a graduate student faded as he soldiered through his doctoral program. "At the beginning, they are paying you to go to school, and you think, 'Wow, what could be better?' But by the end, it just seems like a low-paying job."

Kosa's days as an academic scientist were numbered once, as a postdoc at Harvard, he got a taste of the burgeoning biotech industry in and around Cambridge. "I wanted to understand the nonscientific side of the biotech industry, and my work was too basic to be applied," he says. So he left Harvard and enrolled in an MBA program at the MIT Sloan School of Management, turning a student project into a biotech start-up that performed liver toxicity testing with a technology billed as a "liver on a chip." Upon graduation, he counseled venture capitalists looking to invest in the biotech industry, and in 2006, he joined Bayer HealthCare before moving last month to XOMA.

The idea of going to law school first occurred to Holmes midway through her graduate training after a patent lawyer described her work at one of the alternative-career seminars. But it would be several years until Holmes acted on that impulse, and only after she had tested the waters by working as a patent agent for a law firm.

"I had wanted to be a scientist for as long as I can remember," she says. "So it was scary when I started to second-guess myself." Working and going to school full-time, Holmes received her law degree in 2004 and joined the patent division of Ropes & Gray. "I didn't hate my project," she says about her work on kinase substrates in Solomon's lab. "It was more of a realization that most of science is about making small contributions. Not everybody can cure cancer or even get the cover of *Science* or *Nature*."

Committed to a career in academia, DeDecker has struggled to move up the academic ladder. But NIH's budget has been the least of his obstacles. "The way to get a job is to have a famous person say [about you] that 'this is the best person I've seen in the last 40 years.' Unfortunately, I haven't been very good luck for senior scientists."

At Yale, he studied crystallography under Sigler, who in January 2000 died after suffering a heart attack while walking to work. DeDecker says a decision to "learn something new" after his Ph.D. and to do it at the University of Cambridge in the U.K. has also hurt him professionally. "I'm really glad I did it," he says about his 2-year postdoc in protein engineering. "But going abroad is a bit of a career killer. I had to start over again when I came back to the States."

For his second postdoc, DeDecker joined crystallographer Don Wiley at Harvard's new Institute of Chemistry and Cell Biology, which planned to do large-scale screening of small molecules. "It was a grand plan, and it looked like a good thing," he says. But DeDecker admits that he had a hard time "finding my place." And tragically, in November 2001, Wiley died after falling off a bridge over the Mississippi River while attending a scientific conference in Memphis, Tennessee.

Learning from their mistakes

Several members of the MB&B class were faced with some tough choices as they sought to carve out their scientific niche. In 2001, Spain moved to south Florida with her physician husband—they have since divorced—so that he could establish his practice. "In coming down here, I pretty much knew that I was giving up an academic research position," she says.

She left the door ajar, however, by taking a second postdoc. "I was developing preliminary data that I hoped to use to write up an R01 application," she explains. "But the person I was working under had run into funding problems, and the lab was limping along with only one NIH grant. So he decided to incorporate my work in his next application. I don't really fault him. What else could he do?"

That experience pushed her into the arms of industry. "If I'm going to work my butt off, I want to be in control," she recalls thinking. She posted her resume online, where it was picked up by a recruiter for a south Florida company that was setting up a molecular biology unit to develop military sensors that would detect biological contaminants in the environment. The resulting negotiations were a refreshing change from academia, she says. "I asked for double my salary [$66,000], and they gave it to me," she says.

Kinch was already ensconced at Biogen when professional disaster struck. A member of the scientific team that had sought government approval for the anti-inflammatory drug Tysabri, Kinch arrived at work one morning in February 2005 to discover that the com-

CREDITS (TOP TO BOTTOM): FAYFOTO/BOSTON; JESSICA KOSA; SEAN MAYS

pany had suddenly pulled it from the market after three patients taking it to treat multiple sclerosis developed a rare neurological condition. "It was very demoralizing. But it's part of the business, and you roll with the punches." Tysabri was subsequently remarketed with restrictions on its use, and in 2006, Kinch decided she wanted to learn more about the regulatory side of the business. "We pretend that we're the FDA [U.S. Food and Drug Administration] reviewers, and we try to spot holes in the data," she says about her current position. "It's a lot of fun."

For Nobuyuki Ota, the death of a colleague thrust him into the role of CEO of A-CUBE Inc., a small Burlingame, California–based start-up company that is using computer models to design novel monoclonal antibodies. Trained as a bioinformaticist under Axel Brunger at Yale, Ota had met the company's founder, Hisaaki Kawakatsu, while working on ligand recognition as a postdoc in David Agard's biophysics and biochemistry lab at the University of California, San Francisco. Their conversation had stimulated Ota's interest in "modifying the biology and health of an organism," in other words, finding clinical applications for what he had been doing at a molecular level. Returning to Japan to tend to his ailing parents, Ota began looking for venture capital to launch the company. Soon after, Kawakatsu was diagnosed with cancer. When he died a year later, in 2006, Ota took the reins.

Before starting A-CUBE, Ota says he turned down two tenure-track university offers because they were in bioinformatics, "and I'm more interested now in antibody medicine." He also prefers what he regards as the greater transparency of commercial research. "In academia, some of the papers are not reliable and the findings are not reproducible," he says. "In industry, if you don't make a very good antibody, there are tests that can prove it doesn't work. So you have to be honest."

Parra says she tries to be honest with herself in assessing her career options. Part of a team from government, industry, and academia that last year successfully launched GeneSat-1, a miniaturized biological package tucked aboard another payload, she's learned to cope with both the pressure and the tenuous nature of her position. "There's always the fear of budget cuts," she says, noting that at one point she and her colleagues would receive layoff notices every other Friday, only to have them rescinded on Monday.

Right now, she likes what she's doing—PharmaSat, her current project, is due to go up later this year—enough to stick with it and see what happens. "I've mellowed. I've decided to stay and wait for the pink slip." Losing her job would be hard, but there would at least be a small silver lining, she says: It would give her more time to work on a two-passenger biplane that she and her boyfriend are building.

Doing whatever it takes

Goldberg, who studies Parkinson's disease and has developed a strain of knockout mice that helps him explore its molecular pathways, has always been a realist in assessing what it will take to carve out a career in academic research. That approach has meant both deliberate zigzags and some serendipitous turns along the way.

After working on protein aggregation in Arthur Horwich's NMR lab at Yale, he chose to do a postdoc with Jie Shen, then a new assistant professor of neurology at Harvard Medical School in Boston. "I wanted to do something more applied," he explains. "Neurodegeneration was the logical next step to put my thesis to work. And with the growth in the aging population and the increase in neurodegenerative diseases, I figured I should enter a field that would be in demand."

One week before he joined Shen's lab, however, she called with some surprising news: "She said a mutation of the gene I had been studying is the first that has been linked to Parkinson's." Goldberg, a protein biochemist, suddenly needed to know a lot about mice genetics. And as a postdoc, he was in a perfect position to do so. "I learned the techniques, and then I trained everybody else."

That clear-eyed recognition of what's needed to get the job done is part of the reason fellow MB&Bers said that they were not surprised to learn that Goldberg and Serio are the only members of the 1991 class to hold tenured or tenure-track positions. "Tricia was always a very driven, type-A personality," recalls DeDecker. "She's a very good scientist, but she also knows the business of science, what it takes to get into the right lab, in a hot field, and get the best out of the situation. I also give Matt lots of credit for branching out and changing fields."

DeDecker is hoping that a tenure-track position will open up within his department. Russ says that he's thinking of looking this fall for a tenure-track position that would begin as early as the 2009–10 academic year. Neither has abandoned their original dreams of running their own labs. But both men have no illusions about what it will take to succeed. "I'm putting in an NIH grant, although realistically, my chances are awful," says DeDecker. "If I calculated the odds, I'd have to stop. But you just have to have some sort of faith in your ability." Goldberg is even more convinced that the payoff will come. "The most important thing is to keep applying," he says.

Serio, the only one from the class of 1991 who's hit that particular jackpot, epitomizes that nose-to-the-grindstone attitude. In an e-mail to *Science* the day after learning she had been recommended for tenure, she admitted sheepishly that the news was a bit anticlimactic. "I kept thinking that I would sleep well if this happened. But I was up working until one [a.m.] last night. Some habits die hard, I guess."

–JEFFREY MERVIS

CREDITS: (TOP TO BOTTOM): COURTESY OF JULIA PINSONNEAULT; RACHELLE GAUDET; MIKE GLEASON

AGRICULTURAL RESEARCH

Australia's New Era for GM Crops

The new leaders of Western Australia have promised to rescind a moratorium on transgenic crops that has put a damper on R&D

CANBERRA—Australia's 2-century-long effort to adapt wheat to its arid heartland has made it a research leader on this staple grain. Hoping to draw from that expertise, Thomas Lumpkin, director general of the International Maize and Wheat Improvement Center in El Batán, Mexico, exhorted scientists in Australia to develop genetically modified (GM) wheat resistant to pests and tolerant to salty soil at a Crawford conference here earlier this month. GM varieties, he said, could boost global wheat yields, which had grown by up to 2.5% a year in the 1990s but have risen only 1% a year in the past decade.

Australian scientists may soon be able to take up that gauntlet. Four years ago, the governing Labor Party in Western Australia (WA), the country's breadbasket, banned growing GM crops in the state. But after elections last week, the Liberal and National parties formed a coalition that will oust Labor—and the Liberals have promised to rescind the GM moratorium. "It's an exciting time for agricultural R&D," says Mike Jones, director of the WA State Agricultural Biotechnology Centre in Perth.

The surprising election outcome is the latest boost for transgenic crops in Australia. Five years ago, the Office of the Gene Technology Regulator and Food Standards Australia and New Zealand approved GM canola as safe for the environment and for consumption. In 2004, four canola-growing states, arguing that a GM-free label would deliver premium export prices, banned GM canola. Two states—New South Wales and Victoria—lifted their bans earlier this year.

But WA's anti-GM stance has taken a heavy toll. "The political climate has driven out agricultural biotech investment in the state. Venture capital has dried up, the major companies are walking away, and so are the scientists," says Ian Edwards, former CEO of Grain Biotech Australia in Bull Creek, WA. Edwards founded the company in 1998 to address WA's most pressing problem: salt. Much of the state's wheat is grown on saline land that drags down wheat yields by as much as 20%. Grain Biotech Australia developed GM wheat with a salt-resistance gene cloned from the *Arabidopsis* plant. An early-stage field trial 3 years ago of the salt-tolerant wheat had promising results, Edwards says. But WA's moratorium on commercialization of GM crops deterred investors and salt-resistant wheat is languishing on a shelf, he adds.

Shifting into high gear. Australian researchers have a growing number of GM varieties in field trials.

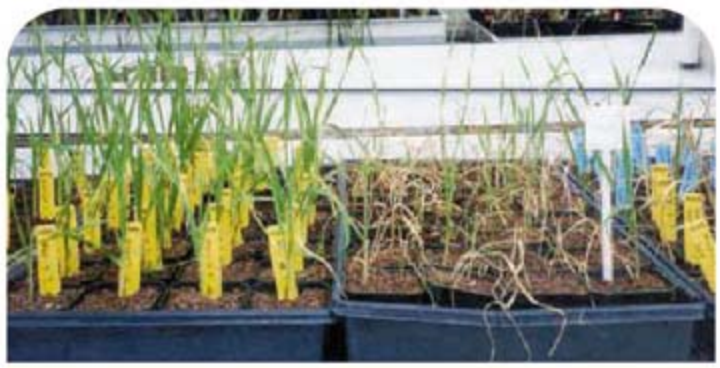

CREDIT: MOLECULAR PLANT BREEDING CRC

GM DOWN UNDER: FIELD TRIALS OF SELECTED VARIETIES IN AUSTRALIA

VARIETY	STATUS OF FIELD TRIALS
High-fructan perennial rye grass	Beginning soon
Low-lignin tall fescue	Beginning soon
Insect-resistant cotton	In progress
Drought-tolerant wheat	In progress
Boron-tolerant barley	In progress
Fiber-enriched barley	In progress
Fungus-resistant bananas	Beginning soon
Vitamin A and iron-fortified bananas	Beginning soon
Waterlogging-tolerant cotton	In progress
Low GI wheat	In progress

WA's outgoing government had argued that the GM-free label is a boon, but an analysis last May by the Australian Bureau of Agricultural and Resource Economics showed that the reverse is true. The federal agency estimated that WA would forfeit AUS$180 million in revenue over the next 10 years if it continues to outlaw herbicide-resistant GM canola, which produces higher yields at lower costs. The bureau predicts that if Australia as a whole forgoes new GM wheat and canola varieties, that could lop $918 million a year off its GNP in a fiercely competitive world market by 2018.

Although South Australia also has a moratorium on growing GM crops, research and development is flourishing there. The trace element boron, at elevated soil levels, stunts plant growth. Last year, a team led by Peter Langridge, CEO of the Australian Centre for Plant Functional Genomics in Glen Osmond, identified a gene conferring boron tolerance in barley (*Science*, 30 November 2007, p. 1446). A barley variety with that gene is now in field trials. The center is also testing GM barley that produces more β glucan, a component of dietary fiber linked to lower rates of colorectal cancer and heart disease. "We're 5 to 10 years off from having a commercial crop," says Langridge. "Our hope is that the moratorium will be lifted by then."

Victoria's move to lift its moratorium has certainly buoyed researchers' spirits in the state, which is home to Australia's dairy industry. Scientists there are tweaking pasture clover and ryegrass to reduce the amount of methane cows release during digestion; nearly one-eighth of Australia's greenhouse gas emissions are from cows. The Molecular Plant Breeding Cooperative Research Centre, based in Bundoora, with outposts across Australia, has several GM varieties in field trials in Victoria. One is ryegrass engineered to produce less lignin and more fructan, which leads to less fermentation in the cow's stomach and hence less methane. In Victoria's private sector, Hexima Limited, a biotech firm based in Melbourne, formed an alliance last month with DuPont's Pioneer Hi-Bred International to commercialize fungus-resistance technologies for corn and soybeans.

The state with the sunniest outlook, perhaps, is Queensland, which has never had a GM ban. "The government has been very aggressive in the development of biotechnology," says James Dale of Queensland University of Technology in Brisbane. Here the main objective is to protect Australia's AUS$300 million banana industry. Bananas are under threat from Fusarium wilt and a second fungal disease, black sigatoka. Last October, tropical race 4, a virulent new strain of Fusarium wilt that has decimated plantations across Asia, slipped into Australia's Northern Territory. Dale's group is about to start trials of fungus-resistant bananas.

The embrace of GM in other parts of Australia—and abroad—makes some WA scientists envious. "When I see hundreds of thousands of small farmers in [India] sowing GM crops, it's very disheartening to come back to WA," says Jones. That is about to change: The Australian state that may need GM technology the most should now have a chance to benefit.

–ELIZABETH FINKEL

Elizabeth Finkel is a writer in Melbourne, Australia.

LETTERS

edited by Jennifer Sills

Tailoring AIDS Prevention

I AGREE WITH M. POTTS *ET AL.* ("REASSESSING HIV PREVENTION," Policy Forum, 9 May, p. 749) that HIV prevention efforts should be continually reappraised. Potts *et al.* call attention to the well-recognized limitations of prevention strategies based solely on condom promotion, HIV testing, and sexually transmitted infection (STI) treatment; however, in their eagerness to promote different strategies, namely, addressing concurrent partnerships and male circumcision, they risk replacing one overly narrow prescription with another equally narrow one.

HIV prevention responses need to be tailored to their contexts, and it is unfortunate that Potts *et al.* have chosen to illustrate their argument about generalized HIV epidemics by using a graphic of UNAIDS estimates for global resource needs, which aggregate all low- and middle-income countries, most of which (75%) are experiencing low and concentrated epidemics. It is not surprising that a good proportion of the HIV expenditure is focused on activities addressing the high-risk populations that are the predominant feature of these epidemics.

For the subset of countries experiencing generalized or hyper-endemic scenarios, UNAIDS estimates of resource needs are very different (see figure) (*1*). There is a strong emphasis on youth (calling for $362 million, or 11% of resources); community mobilization and communication ($339 million, 11% of resources); and workplace interventions ($437 million, 13% of resources), which primarily focus on delaying sexual debut, decreasing multiple partnerships (both concurrent and serial), and promoting condom use in casual sex. In addition, resources are needed to bring about the most rapid feasible increase of male circumcision in young adults (estimated to be 2.5 million circumcisions by the year 2010 in the 12 most highly affected countries). Finally, the importance of HIV testing in generalized epidemics cannot be discounted now that around half of all HIV infections occur between discordant couples.

PAUL R. DE LAY

Department of Evidence, Monitoring and Policy, Joint United Nations Programme on HIV/AIDS (UNAIDS), Geneva, Switzerland. E-mail: delayp@unaids.org

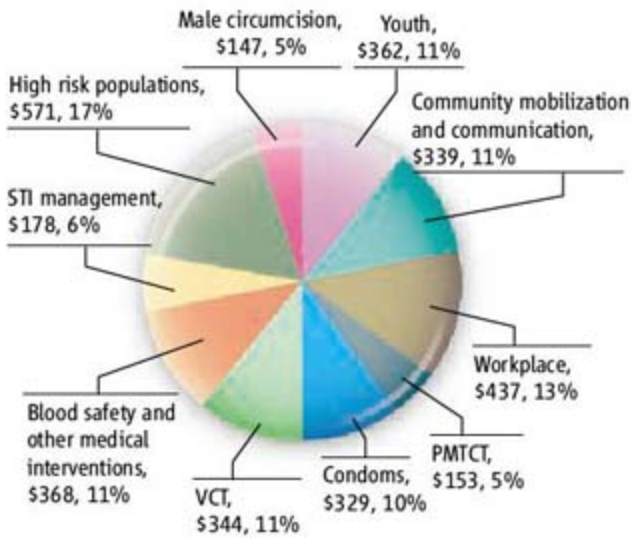

HIV prevention. This UNAIDS pie chart illustrates the financial resources required to achieve universal access to HIV prevention, treatment, care, and support by 2010, including countries with hyper-endemic and generalized epidemics. Together, resources total U.S. $3.2 billion. Figures shown are millions of U.S. dollars and percentage of total prevention.

Reference

1. The figure and additional information are available as Supporting Online Material (www.sciencemag.org/cgi/content/full/321/5896/1631a/DC1).

HIV Testing for Whole Populations

THE POLICY FORUM "REASSESSING HIV PREVENTION" (M. POTTS *ET AL.*, 9 MAY, P. 749) SUMMARIZES current approaches to control of HIV infections. Although these strategies have shown some reduction in prevalence of HIV infections, they are not fully effective. Clearly, new approaches should be considered.

One approach, first proposed by Montaner *et al.* (*1*), would be to test entire populations for HIV infection using polymerase chain reaction (PCR) and then to treat all positives with antiretroviral therapy (HAART). This may be effective, given that patients with the low viral loads achievable by HAART treatment are generally not infectious by sexual routes (*2*–*4*) or by maternal transmission to newborns (*5*, *6*).

This approach would be expensive. We estimate that application to all 17 sub-Saharan countries with HIV prevalence of >5% would cost an average of about $20 billion per year, assuming that screening of populations would take place every 5 years. This is a very high figure, but it is affordable by the major donor nations and would likely have substantial health benefits.

The approach would face other challenges as well. Extensive training of laboratory and field personnel would be required. Fear of the stigma involved in HIV positivity would have to be addressed by widespread publicity stressing the advantages of HAART for those infected, and for those not yet infected, in the populations screened. This has been effective in Brazil, where 170,000 infected people are already being treated with HAART. This has resulted in stable HIV prevalence (0.6%) since the initiation of widespread screening and treatment in 2000 (*7*).

Such a bold plan would require controlled studies to assure its efficacy, but the benefits would likely outweigh the costs.

ALFRED M. PRINCE

Hepatitis Research Foundation, 349 Stone Hill Road, Pound Ridge, NY 10576, USA.

References

1. J. S. G. Montaner *et al.*, *Lancet* **368**, 531 (2006).
2. T. C. Quinn *et al.*, *N. Engl. J. Med.* **342**, 921 (2000).
3. J. Castilla *et al.*, *J. Acquir. Immune Defic. Syndr.* **40**, 96 (2005).
4. M. S. Cohen *et al.*, *J. Clin. Invest.* **118**, 1244 (2008).
5. K. M. De Cock *et al.*, *JAMA* **283**, 1175 (2000).
6. J. McIntire, *Curr. Opin. Infect. Dis.* **19**, 33 (2006).
7. S. Okie, *N. Engl. J. Med.* **354**, 1077 (2006).

Response

AT THE TIME OF PUBLICATION, WE UNDERstood that only the global funding estimates were available. Now that a separate breakdown for "hyper-endemic and generalized" epidemics has also been made available, we note that the requested funding for these would comprise only a little over 20% of the global total, even though such epidemics account for over two-thirds of all HIV infections worldwide (*1*). Also, although 5% of this funding would be dedicated to circumcision programs, the large majority of resources would continue to be allocated to other interventions, for which the evidence of prevention impact in generalized epidemics is much weaker. Although we hope that some of "youth, community mobilization, communication, and workplace interventions" would focus on decreasing multiple partnerships, past experience suggests that most of the emphasis may be on strategies such as condom promotion, delay/abstinence approaches for youth, and HIV testing (*2*–*4*). Even in this graphic specifically for generalized epidemics, it appears that total funding for circumcision and partner reduction would probably continue to be dwarfed by support for more standard prevention approaches.

Perhaps it is time for major international organizations to reassess whether strategies such as STI treatment and HIV testing and counseling are still "proven approaches" for HIV prevention (*5*). Seven of eight randomized trials of STI treatment had no impact on HIV incidence in Africa (*6*), and a recent workplace-based trial examining the impact of HIV testing and counseling (*7*) found that people randomized to the intensive counseling arm had considerably (although not significantly) higher HIV infection rates and, as in another recent study also from Africa (*8*), the sexual behavior of people testing HIV-negative was evidently riskier than in those not tested.

We have not seen sufficient evidence that HIV testing reduces HIV transmission in serodiscordant couples, nor have we seen evidence that "around half of all HIV infections occur between discordant couples." Recent CDC data from Uganda suggest that most married people who recently acquired HIV were infected by an extramarital partner or by their spouse who had recently acquired HIV from an extramarital partner (*9*). Many of the latter were probably in the brief "acute infection" period, when HIV infectivity is much higher yet undetectable by a standard HIV test (*10*). It is crucial to address the multiple and concurrent partnerships that mainly drive these generalized HIV epidemics (*2*, *3*, *11*).

Regarding Prince's bold proposal to test large populations in Africa for HIV infection and treat all who test positive, it is true that others have made similar proposals, and some observational data from Taiwan, British Columbia, and Brazil may suggest an association between the expansion of AIDS treatment and decreased HIV transmission (*12*). Unfortunately, good ideas do not translate into effective public health strategies unless they are feasible. For example, even with considerable public policy support, the adequate identification and treatment of HIV-infected pregnant mothers has still not been attainable in most of sub-Saharan Africa (*1*). In many places the attrition rate of those starting HIV treatment has been distressingly high (*13*), and potential development of resistance to these medications—and consequent resurgence of viral load and thus infectiousness—will remain a concern.

Furthermore, the proposal to test populations every 5 years would miss almost everyone during the period of acute (early) infection, when, as mentioned, a substantial portion of transmission takes place (*10*). Finally, the Brazilian parallel appears unconvincing because HIV prevalence was much lower than in Africa and the medical infrastructure was much stronger; prevalence has also remained stable, during the same period, in almost every other Latin American country, even though most were not providing access to HIV treatment (*1*). Although we agree that novel initiatives are needed, they must first be tested in rigorous, small-scale studies before being considered, at an unprecedented annual cost (over double the current total funding for HIV-AIDS globally), across a continent.

Population-level disease control efforts must be evidence-based, culturally acceptable, and feasible (as male circumcision and partner reduction are). We reaffirm our call for a reassessment and reprioritization of strategies, involving shifting more attention and resources to those approaches most likely to have a population-level impact on reducing HIV transmission and saving human lives, particularly in the hardest-hit regions of Africa. As the head of the Gates Foundation's Global Health Program recently argued, it is time to pursue a truly evidence-based approach, instead of continuing to rely largely on "consensus views" about what works for prevention (*14*).

DANIEL HALPERIN,[1] MALCOLM POTTS,[2] DOUG KIRBY,[3] JEFF KLAUSNER,[4] RICHARD WAMAI,[1] ANN SWIDLER,[5] ELLIOT MARSEILLE,[6] JULIA WALSH,[2] NORMAN HEARST[7]

[1]Harvard University School of Public Health, Boston, MA 02115, USA. [2]School of Public Health, University of California at Berkeley, Berkeley, CA 94720, USA. [3]ETR Associates, Scotts Valley, CA 95066, USA. [4]San Francisco Department of Public Health, San Francisco, CA 94103, USA. [5]Department of Sociology, University of California at Berkeley, Berkeley, CA 94720, USA. [6]Health Strategies International, Walnut Creek, CA 94596, USA. [7]Department of Family and Community Medicine, University of California at San Francisco, San Francisco, CA 94143, USA.

References

1. UNAIDS, the Joint United Nations Programme on HIV/AIDS, *AIDS Epidemic Update* (UNAIDS Publ.UNAIDS/07.27E/JC1322E, UNAIDS, Geneva, 2007); www.unaids.org/en/KnowledgeCentre/HIVData/EpiUpdate/EpiUpdArchive/2007/default.asp.
2. J. D. Shelton, *Lancet* **370**, 1809 (2007).
3. H. Epstein, *The Invisible Cure: Africa, the West and the Fight Against AIDS* (Farrar Straus & Giroux, New York, 2007).
4. D. Wilson, D. T. Halperin, *Lancet* **372**, 423 (2008).
5. Global HIV Prevention Working Group, *Bringing HIV Prevention to Scale: An Urgent Global Priority,* June 2007; www.globalhivprevention.org/pdfs/PWG-HIV_prevention_report_FINAL.pdf.

6. R. H. Gray, M. J. Wawer, *Lancet* **371**, 2064 (2008).
7. E. L. Corbett *et al.*, *AIDS* **21**, 483 (2007).
8. L. Sherr *et al.*, *AIDS* **21**, 851 (2007).
9. R. Bunnell *et al.*, paper presented (#980) at 15th Annual Conference on Retroviruses and Opportunistic Infections, Boston, MA, 3 to 6 February 2008.
10. J. D. Shelton, *Lancet* **372**, 273 (2008).
11. T. Mah, D. T. Halperin, *AIDS Behav.*, 10.1007/s10461-008-9433-x (2008).
12. J. S. G. Montaner *et al.*, *Lancet* **368**, 531 (2006).
13. S. Rosen, M. P. Fox, C. J. Gill, *PLoS Med.* **4**, e298, 10.1371/journal.pmed.0040298 (2007).
14. T. Yamada, *N. Engl. J. Med.* **358**, 1324 (2008).

Effects of Expanded Mosquito Range

THE AGGRESSIVE SPREAD OF *AEDES ALBOPICTUS* as it has leapfrogged across geographic boundaries was well documented by M. Enserink in his News Focus story, "A mosquito goes global" (16 May, p. 864). The impact of *Ae. albopictus* on vector-borne disease transmission dynamics remains unresolved; however, this debate was only portrayed in terms of direct effects. Indirect effects must be considered as well. Larval competition between *Ae. albopictus* and other mosquito species that co-occur in its newly expanded range is well documented (*1*). Laboratory-based competitive experiments revealed that *Ochlerotatus triseriatus* mosquitoes (*2*)—the primary vector for La Crosse virus (LACV) in the United States—develop disseminated LACV infections more often when emerging from containers shared with *Ae. albopictus* (*3*). Alto and colleagues (*4*, *5*) have similarly shown that the indirect effects of larval competition can enhance mosquito susceptibility to dengue and Sindbis viruses. The need for an ecological perspective including both direct and indirect effects when discussing diseases whose transmission includes elements of native species, introduced species, humans, and the transport of goods across the planet is increasingly important in this era of globalization (*6*).

SARAH N. BEVINS

Department of Microbiology, Immunology, and Pathology, Colorado State University, Fort Collins, CO 80523, USA. E-mail: bevins@lamar.colostate.edu

References
1. S. A. Juliano, L. P. Lounibos, *Ecol. Lett.* **8**, 558 (2005).
2. J. F. Reinert, *J. Am. Mosquito Contr.* **16**, 3 (2000).
3. S. N. Bevins, *Biol. Invasions*, in press (available at www.springerlink.com/content).
4. B. W. Alto, L. P. Lounibos, S. Higgs, S. A. Juliano, *Ecology* **86**, 3279 (2005).
5. B. W. Alto, L. P. Lounibos, C. N. Mores, M. H. Reiskind, *Proc. R. Soc. B* **275**, 463 (2008).
6. K. E. Jones *et al.*, *Nature* **451**, 990 (2008).

TECHNICAL COMMENT ABSTRACTS

COMMENT ON "Age and Evolution of the Grand Canyon Revealed by U-Pb Dating of Water Table–Type Speleothems"

Joel Pederson, Richard Young, Ivo Lucchitta, L. Sue Beard, George Billingsley

Polyak *et al.* (Reports, 7 March 2008, p. 1377) reported speleothem data leading to their inference that the western Grand Canyon incised much earlier than previously thought. This contradicts several lines of published geological knowledge in the region, hinges upon unjustified hydrogeological assumptions, and is based on two anomalous data points for which we offer alternative explanations.

Full text at www.sciencemag.org/cgi/content/full/321/5896/1634b

COMMENT ON "Age and Evolution of the Grand Canyon Revealed by U-Pb Dating of Water Table–Type Speleothems"

Philip A. Pearthree, Jon E. Spencer, James E. Faulds, P. Kyle House

Polyak *et al.* (Reports, 7 March 2008, p. 1377) reported that development of the western Grand Canyon began about 17 million years ago. However, their conclusion is based on an inappropriate conflation of Plio-Quaternary incision rates and longer-term rates derived from sites outside the Grand Canyon. Water-table declines at these sites were more likely related to local base-level changes and Miocene regional extensional tectonics.

Full text at www.sciencemag.org/cgi/content/full/321/5896/1634c

RESPONSE TO COMMENTS ON "Age and Evolution of the Grand Canyon Revealed by U-Pb Dating of Water Table–Type Speleothems"

Victor Polyak, Carol Hill, Yemane Asmerom

Pederson *et al.* and Pearthree *et al.* offer critical comments on our study of the age and evolution of the Grand Canyon. Both sets of authors question our use of incision rates from two sample sites located outside the canyon and present alternative interpretations of our data. As we explain, even without the sites in question, our data support a "precursor" western Grand Canyon older than 6 million years.

Full text at www.sciencemag.org/cgi/content/full/321/5896/1634d

Letters to the Editor

Letters (~300 words) discuss material published in *Science* in the previous 3 months or issues of general interest. They can be submitted through the Web (www.submit2science.org) or by regular mail (1200 New York Ave., NW, Washington, DC 20005, USA). Letters are not acknowledged upon receipt, nor are authors generally consulted before publication. Whether published in full or in part, letters are subject to editing for clarity and space.

HISTORY OF SCIENCE

The Life of a Magus and Martyr

Michael Dirda

Giordano Bruno
Philosopher/Heretic
by Ingrid D. Rowland
Farrar, Straus and Giroux, New York, 2008. 345 pp. $27. ISBN 9780809095247.

After eight years in prison and numerous cross-examinations, Giordano Bruno (1548–1600) was trundled onto an ass and transported to a Roman marketplace, where he was burned at the stake for heresy. The Holy Office—the Italian version of the Spanish Inquisition—announced that the recalcitrant Bruno steadfastly refused to accept that during the Mass the elevated host was transformed into Christ's body, argued that hell didn't exist and that no one is damned to eternal punishment, asserted that praying to saints was a waste of time, and maintained that nothing that the Church believes can be proved. Because of such views, Bruno was duly handed over to the secular authorities for execution—and ever since has been revered as a martyr to freedom of thought and expression. But in the past 40 or so years, this former Franciscan priest has also stood at the center of ongoing arguments about the nature of science during the Renaissance.

As Ingrid D. Rowland writes in her new biography, Bruno "more boldly than anyone in his age, including Kepler and Galileo … declared that the universe was made of atoms and that it was infinite in size"—and infinitely old, too. He also argued for the multiplicity of worlds and that the stars were suns, with planets circling them. Going far beyond Copernicus's heliocentrism, he judged that the motions of our solar system were small potatoes compared to the larger rhythms of the universe as a whole. The cosmos pulsed with life and incessant mutability; everything was constantly transformed, constantly renewed.

Today this all sounds eminently reasonable and quite modern. But is it? In her classic 1964 book on Bruno (*1*), Frances A. Yates argued, with impressive scholarship, that this Renaissance thinker was essentially a magus—a believer in the occult, especially of the ancient Egyptian magic represented by the esoteric writings of Hermes Trismegistus (eventually proved to be forgeries). She held that 16th-century alchemists, magicians, and natural philosophers, such as Cornelius Agrippa and John Dee, were engaged in the same task as any modern scientist: Trying to make sense of how nature worked and then, at least in some instances, trying to make practical use of that knowledge.

While Yates's books on the Renaissance occult continue to make for exceptionally lively reading—they are packed with information about Egyptian magic, Renaissance Platonism, Jewish Cabala, and Gnostic beliefs in the divinity of man—she does tend to see secret occult influences almost everywhere, even in the design of the Globe Theater. Certainly, Rowland's *Giordano Bruno: Philosopher/Heretic* deliberately downplays the more hermetic elements in Bruno's career and is far more sober-minded than the enthusiastic Yates.

Still, Rowland (a professor in the University of Notre Dame's School of Architecture, in Rome) can't avoid the fact that Bruno never seems to have done any kind of hands-on experimentation or research. As she says, "Bruno's versatility—part poet, part artist, part natural philosopher, part moralist, part theologian—makes him hard to fit into contemporary ideas of science." Yet, "[t]he fact that Bruno was more interested in models of the universe than in the gathering of precise observational data does not make him less 'scientific' than colleagues like [Tycho] Brahe—science as we know it did not yet exist, and besides, in its present-day form it still depends as vitally on thought problems as on the gathering of data. His ability to treat models of the universe as just that—models—was an ability that modern scientists still recognize as an essential part of their own discipline."

Bruno's various "thought experiments" took many forms: a comic play, an epic poem about the infinite size of the universe ("On the Immense and the Numberless"), explorations of mathematical magic, reinterpretations of the meaning of the constellations (the wonderfully titled "The Expulsion of the Triumphant Beast"), sequences of poems about love and philosophy ("The Heroic Frenzies"), reflections on atomic particles ("On the Triple Minimum"), philosophical dialogues like "The Ash Wednesday Supper," and even guides to the use of symbols and talismans to gain control over people's actions ("On Bonds in General"). Rowland does no more than mention this last work, but so rich is Bruno's thought that Ioan P. Couliano has presented convincing evidence (*2*) that in this treatise Bruno adumbrated modern techniques of advertising, subliminal messaging, and brainwashing.

During his lifetime, though, the philosopher may have been best known for his prodigious memory. In his youth, he mastered, then greatly refined, the classical techniques of mnemonics, wherein one associates places in a familiar building with the facts one wants to recall. (For his own "theater of memory," Bruno seems to have eventually settled on intricate complexes of interlocking circles, possibly representing aspects of the zodiac.) Such memory skills weren't just useful in the age before computers. Bruno, according to Rowland, argued that "[t]he real point of the artificial memory … was to order sense perceptions, imagination, and, ultimately, understanding to reflect the basic harmony of the world itself."

Of course, harmony was actually not much in evidence during the tempestuous 16th century. Like so many scholars before him, Bruno wandered around most of Europe, stopping in Naples, Geneva, Paris, London, Oxford (where he was mocked for his accent), Germany, Prague, and Venice, constantly seeking cities

Where the pyre burned. Ettore Ferrari's statue (1889) in the Campo de' Fiori, Rome.

CREDIT: MATS RIGGLÖV/JUPITER IMAGES

The reviewer, the author of *Classics for Pleasure* and several other collections of essays, is a longtime columnist for the *Washington Post Book World*. E-mail: mdirda@gmail.com

free of religious and political strife and patrons who might support a philosopher and teacher. Unfortunately, Bruno's wasn't the most attractive of personalities, for while he was regarded as a brilliant conversationalist (according to the poet Fulke Greville), he could also be prickly and mean, as well as both misogynistic and licentious.

Rowland tells Bruno's life story clearly, in concise chapters, but only touches on his ideas and various works: She is clearly happiest in describing Naples during the Renaissance or in presenting a detailed account of Bruno's imprisonment and trial. Annoyingly, she refers repeatedly to "the Nolan philosophy"—Bruno was born in Nola—but nowhere does she make clear exactly what this is, a serious matter given that the Nolan and his philosophy even now seem to represent different things to different people. Despite these cavils, *Giordano Bruno: Philosopher/Heretic* is a good place to start learning about a fascinating man and a still-controversial thinker.

References

1. F. A. Yates, *Giordano Bruno and the Hermetic Tradition* (Univ. Chicago Press, Chicago, 1964).
2. I. P. Couliano, *Eros and Magic in the Renaissance*, M. Cook, Transl. (Univ. Chicago Press, Chicago, 1987).

10.1126/science.1162479

PHYSICS

Master of the Universe

Peter Coles

On the bookshelves of just about every practicing cosmologist (or at least those of a certain age, like me) you will find a copy of Steven Weinberg's *Gravitation and Cosmology* (*1*). What made this 1972 book such a classic was not just its combination of clarity and mathematical rigor but also its service as a kind of manifesto for a newly emerging scientific discipline. Not until the completion of Einstein's general theory of relativity in 1916 was it possible to embark on the most ambitious project in the history of physical science: the construction of a self-contained theory of the origin and evolution of the cosmos and all its contents.

Because Einstein's theory was about both space and time, cosmology would be not just geography but history too. Gradually the pieces began to fall into place. Observations made by Edwin Hubble in the 1920s helped establish the idea that we live in an expanding universe; theoretical work by Alexander Friedman and Georges Lemaître had shown that such an expansion could be described by the equations of Einstein's theory. Studies of the synthesis of helium from hydrogen by George Gamow and others suggested that the universe must have been much hotter in the past than it is now. The cosmic microwave background, discovered by accident in 1965 by Arno Penzias and Robert Wilson, was quickly identified as electromagnetic radiation left over from some form of primordial fireball. These developments together established the Big Bang theory as a promising framework for understanding the universe. By the 1970s, although many important pieces of the puzzle were still missing, cosmology was nevertheless on the threshold of great things.

Cosmology

by Steven Weinberg

Oxford University Press, Oxford, 2008.
611 pp. $90, £45.
ISBN 9780198526827.

During the intervening 36 years, Weinberg (a professor in the physics and astronomy departments at the University of Texas, Austin) has pursued a physics career of the utmost distinction, winning the Nobel Prize in 1979 along with a host of other awards for his contributions to the theory of elementary particles. He completed a mammoth, three-volume treatise on quantum field theory (*2*) and has made brilliant contributions to science popularization, including the most famous book about the Big Bang theory (*3*). With *Cosmology*, he returns to the titular topic. The result is not only fascinating in itself but also as a token of the massive changes that have taken place in the field over the past three decades.

As cosmology has matured it has also expanded, so it now incorporates several branches of physics and astronomy that previously stood apart from it. For example, particle physicists have been drawn to cosmology because the early stages of the Big Bang supply the ultrahigh energies needed to probe the microscopic structure of matter. For them the universe is a laboratory that can be used to probe the fundamental laws of nature. Astronomers tend to have a different perspective, one in which the largest visible structures—galaxies and galaxy clusters—are interesting in their own right and the excitement is in learning about how they are put together, how they came into being, and how they are evolving.

Until recently cosmology was also a rather abstract and theoretical discipline, but huge improvements in instrumental technology now sustain a vigorous interplay between observation and theory. Detailed measurements of the pattern of fluctuations in the cosmic microwave background and deep maps obtained from surveys of the distribution of galaxies have been exhaustively modeled using state-of-the-art computer simulations. Over the past decade, this process has led to the construction of a "concordance" model that successfully accounts—at least in a broad-brush sense—for all the observed properties of our universe.

These dramatic changes are reflected in the contents of this new monograph. For a start, the "Gravitation" part of the earlier title has gone completely. Inside, the treatment of Einstein's theory is condensed into about 20 pages and relegated to an appendix. Weinberg explains his reason for doing this in the Preface: general relativity has not changed much, so it is not worth repeating what he has already written. Instead, he devotes much of *Cosmology* to new developments generated by particle cosmologists—including several elements of the concordance scenario that had not even been thought of in 1972, such as nonbaryonic dark matter, vacuum energy, and cosmic inflation. Weinberg distills these topics into a concentrated but wonderfully lucid account of concordance cosmology that displays an appreciation of the importance of empirical evidence that is unfortunately rare in the field of particle cosmology. He subsequently focuses on the origin of fluctuations in the primordial universe that were (probably) generated by inflation, were responsible for the patterns we see in the microwave background, and seeded the formation of galaxies. Instead of merely reviewing the available literature on this topic, Weinberg has systematically re-derived all the key results and linked them together with text that communicates the deepest level of physical understanding.

The material is technically challenging, but in Weinberg's sure hands the synthesis becomes remarkably accessible for those able to cope with the mathematics. The result is a tour de force that even established cosmologists will learn from. Any scientist interested in cosmology should read it, although absolute beginners should probably try something a little gentler first.

References

1. S. Weinberg, *Gravitation and Cosmology: Principles and Applications of the General Theory of Relativity* (Wiley, New York, 1972).
2. S. Weinberg, *The Quantum Theory of Fields* (Cambridge Univ. Press, Cambridge, 1995–2000).
3. S. Weinberg, *The First Three Minutes: A Modern View of the Origin of the Universe* (Basic, New York, 1977).

10.1126/science.1163155

The reviewer is in the School of Physics and Astronomy, Cardiff University, Cardiff CF24 3AA, UK. E-mail: peter.coles@astro.cf.ac.uk

ENVIRONMENTAL ECONOMICS

Development and Conservation Goals in World Bank Projects

Biodiversity protection does not undermine poverty alleviation goals in development projects, especially under sustainable finance and market mechanisms.

Peter Kareiva,[1,2]* Amy Chang,[3] Michelle Marvier[2]

Poverty alleviation and economic development are often thought to be incompatible with environmental protection and biodiversity conservation. Previous reviews of integrated conservation and development projects (ICDPs) have found frequent failures, leading many conservationists to conclude that such joint efforts are unwise (*1*, *2*). Countering this pessimism is the argument that conservation can enhance economic development because undegraded nature supplies valuable ecosystem services (*3*–*7*). We found that World Bank projects with biodiversity goals were as successful in all development objectives, including poverty reduction and private sector development, as those that focused solely on development. Success was elusive for all types of projects: <20% of projects were rated as highly satisfactory, regardless of whether they were concerned with only development or a combination of development and biodiversity goals. The one predictor of highly satisfactory outcomes for projects involving biodiversity was the use of market mechanisms or sustainable finance approaches.

Since 1947, the World Bank has granted loans to fund over 11,000 projects, with the primary goals being economic development and poverty alleviation, but often with secondary goals that entail environment or biodiversity protection. Aid for biodiversity has grown following the 1992 Earth Summit in Rio de Janeiro (*5*).

As part of its project cycle, the World Bank produces Implementation Completion Reports (ICRs) in which completed projects are rated for overall performance and sustainability (*8*) (fig. S1). Because of their consistent format and large number, World Bank ICRs provide an untapped resource for investigating the compatibility of economic development and environmental or conservation goals. Although ICRs have weaknesses, the World Bank's comprehensive and standardized evaluation system is unrivaled, and the reports are not simply affirmations of success. Depending on the objective being scored, 15 to 40% of the projects examined here were rated as unsatisfactory or highly unsatisfactory.

To ask whether the inclusion of environmental goals hinders the success of World Bank development projects, we identified projects with ICRs completed during July 1998 to August 2006 when their format remained constant. We compared outcome scores from randomly selected projects that included both environmental and development goals to projects that lacked environmental goals ($n = 97$). The development-only projects were also randomly selected, but constrained so that pairs of environmental and nonenvironmental projects were matched by nation. Matching by nation ensured that any differences detected could not be attributed to geographic biases. In terms of overall performance, development-only projects scored no better than the development plus environment projects (see chart, left). If anything, development-only projects tended to more frequently earn an unsatisfactory ranking.

Projects categorized as having environmental goals included efforts aimed at irrigation and improved water quality, and thus might not be widely considered as conservation. To sharpen the analyses, we next focused on World Bank projects that explicitly included biodiversity goals. There are many fewer of these projects to sample from. In fact, we selected every available biodiversity project approved between 1993 and 2007 and with an ICR completed between July 1998 and August 2006 ($n = 61$). Then we randomly sampled development projects without biodiversity or broader environmental goals, again matched by nations to the extent possible ($n = 51$) and otherwise by region ($n = 10$). Comparing biodiversity and development projects to development projects, we found no evidence of a tradeoff associated with the addition of a biodiversity emphasis (see chart, page 1639, top).

ICRs also provide evaluations of more specific objectives such as environment, poverty reduction, gender equity, private sector development, and public sector management (table S1). Considering these objectives one at a time, development-only and combined development and biodiversity projects differed in only one category: environmental objectives. Only 2% of biodiversity projects had negligible environmental outcomes compared with 22% of nonbiodiversity projects. In no specific objective did biodiversity projects underperform compared with nonbiodiversity projects, including financial, poverty alleviation, or gender objectives. Thus, the data indicate no cost in terms of reduced performance if biodiversity is included as a project goal, but a significant reduction in environmental outcomes if biodiversity is not an explicit project

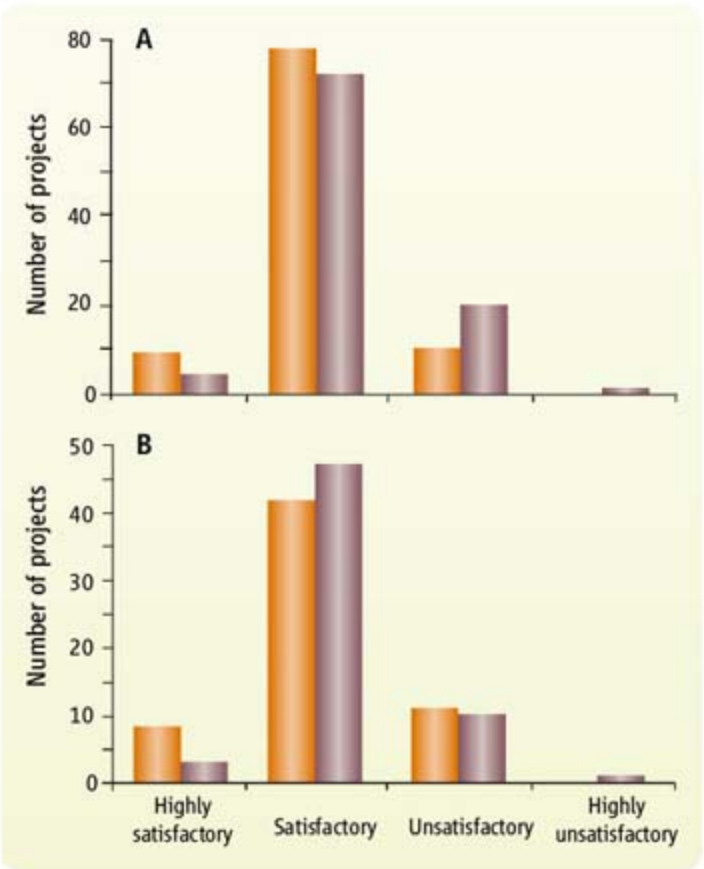

ICR outcome ratings for (A) environment (orange) versus nonenvironment projects and **(B)** biodiversity (orange) versus nonbiodiversity projects (purple). Ratings for environment projects were slightly higher than those for nonenvironment projects ($P = 0.063$, Fisher's exact test). Ratings for biodiversity and nonbiodiversity projects did not differ significantly ($P = 0.318$, Fisher's exact test).

[1]The Nature Conservancy, Seattle, WA 98105, USA. [2]Environmental Studies Institute, Santa Clara University, Santa Clara, CA 95053, USA. [3]The Nature Conservancy, Santa Clara, CA 95053, USA.

*Author for correspondence. E-mail: pkareiva@tnc.org

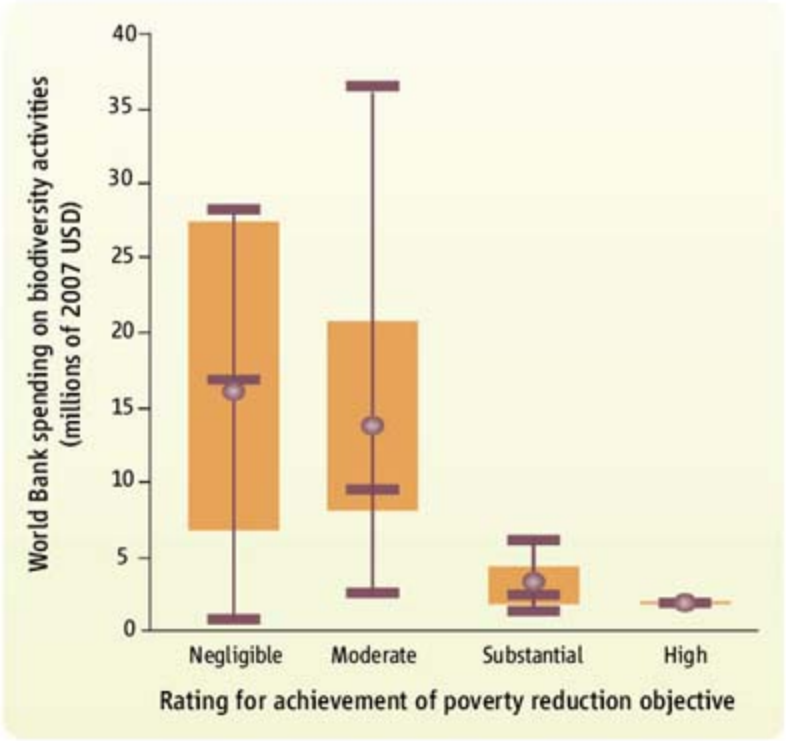

World Bank spending for biodiversity, broken down by ratings for achievement of poverty reduction objective. Data are from 30 biodiversity projects that included an explicit poverty reduction objective and for which World Bank spending on biodiversity was available (*9*). Boxes delineate 25th to 75th percentiles. Top, middle, and bottom purple bars represent the maximum, 50th percentile, and minimum values, respectively. Filled circles represent means. Sample sizes are $n = 6$, 20, 3, and 1 for negligible, moderate, substantial, and high achievement of poverty reduction objectives. USD, U.S. dollars.

focus. Moreover, total project costs (inflation-adjusted to 2007 values) for biodiversity projects were on average less than half those for nonbiodiversity projects (t test on log-transformed values, $P < 0.001$).

Although biodiversity projects did not perform more poorly than development-only projects, a substantial fraction (17.5%) were viewed as generally unsatisfactory and only 15% were assessed as having a substantial or better impact on poverty reduction. To probe biodiversity projects more deeply, we asked whether the amount spent by the World Bank on biodiversity activities affected achievement of poverty reduction objectives. Within biodiversity projects, the more money that was spent on biodiversity activities, the less likely was project success with respect to poverty reduction (ordinal regression: estimate = -8.58×10^{-8}, SEM = 4.38×10^{-8}, $P = 0.05$; see chart, below). More money spent on biodiversity may imply that social goals were relatively neglected.

Beyond funding, project design might influence outcome. Although it is difficult to quantify project design, a 2006 World Bank report (*9*) recorded the presence or absence of ten activities for each biodiversity project: (i) institution building, policies, and strategic planning; (ii) inventory, research, and monitoring; (iii) enhancing public awareness and education; (iv) protected areas; (v) enhancing production landscapes; (vi) sustainable financing and market mechanisms; (vii) nature tourism; (viii) tending to the needs of indigenous peoples; (ix) promoting biodiversity in agricultural settings; and (x) controlling invasive species. Activity profiles existed for 57 of the sampled biodiversity projects. We used ordinal regression to explore whether the presence of any of these activities was a predictor of overall success. Only sustainable financing and market mechanisms was associated with a highly satisfactory outcome [estimate, –1.848 ± 0.826 (SEM), $P = 0.025$] or a high likelihood of sustainability (estimate, –2.097 ± 0.810, $P = 0.01$; see chart, below).

Our examination of World Bank projects does not support assumptions about any negative impact of environmental or biodiversity objectives on the achievement of development objectives. This does not mean that conservation and development win-wins are easy to obtain. But it does mean that one should not assume a priori that melding conservation objectives onto development objectives is a bad idea. In addition, the only predictor of overall biodiversity project success was the presence of market mechanisms and sustainable finance. This finding supports arguments that the key to success in conservation is the development of market mechanisms and new sources of finance for conservation (*10*–*13*).

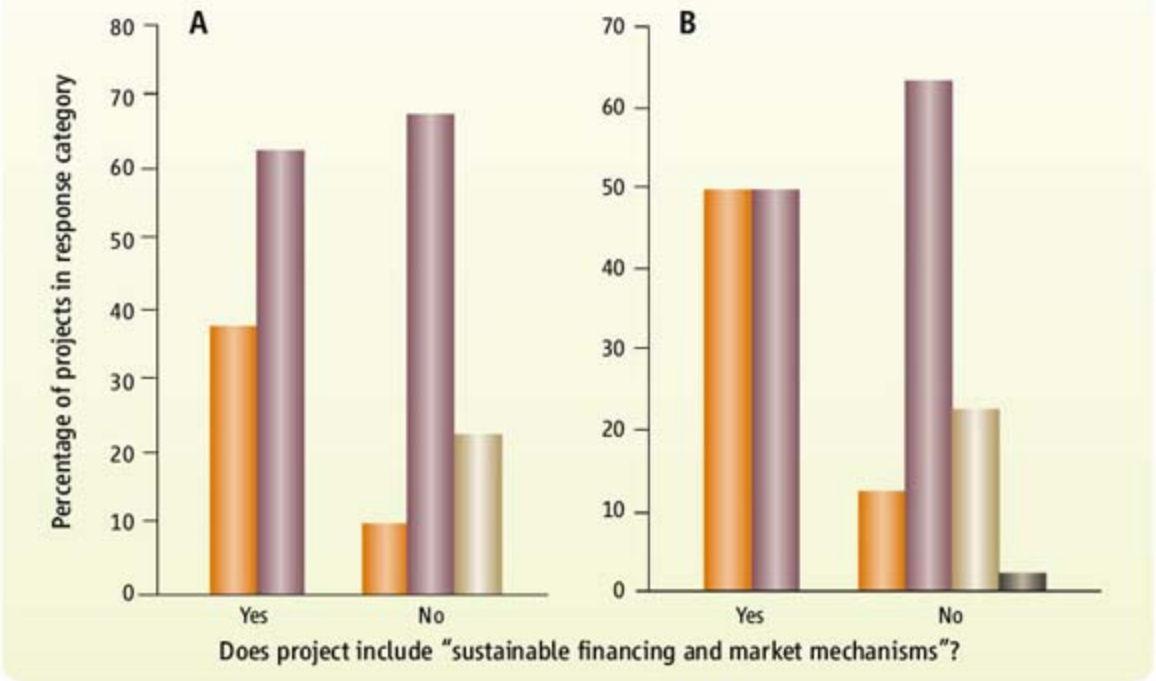

The effect of sustainable financing and market mechanisms on overall success and sustainability of biodiversity projects. (**A**) Project outcome is rated as highly satisfactory (orange), satisfactory (purple), or unsatisfactory (tan). (**B**) Project sustainability is rated as highly likely (orange), likely (purple), unlikely (tan), or highly unlikely (dark gray). Eight projects included sustainable financing and market mechanisms, and 49 projects did not.

References

1. A. Agrawal, K. Redford, "Poverty, development, and biodiversity conservation: Shooting in the dark?" (WCS Working Paper No. 26, Wildlife Conservation Society, New York, 2006).
2. J. G. Robinson, K. H. Redford, in *Getting Biodiversity Projects to Work: Towards More Effective Conservation and Development*, T. O. McShane, M. P. Wells, Eds. (Columbia Univ. Press, New York, 2004), pp. 10–34.
3. D. Kaimowitz, D. Sheil, *Biotropica* **39**, 567 (2007).
4. Millennium Ecosystem Assessment, *Ecosystems and Human Well-Being: Synthesis* (Island Press, Washington, DC, 2005), p. 137.
5. H. Tallis, P. Kareiva, M. Marvier, A. Chang, *Proc. Natl. Acad. Sci. U.S.A.* **105**, 9457 (2008).
6. A. Balmford *et al.*, *Science* **297**, 950 (2002).
7. R. K. Turner *et al.*, *Ecol. Econ.* **46**, 493 (2003).
8. World Bank, www.worldbank.org, accessed September 2007.
9. K. MacKinnon, K. Luz, C. Sobrevila, E. Wright, *The World Bank and Biodiversity 1988–2005: Mountains to Coral Reefs* (World Bank, Washington, DC, 2006).
10. J. D. Sachs, W. V. Reid, *Science* **312**, 1002 (2006).
11. I. Koziell, I. R. Swingland, *Philos. Trans. R. Soc. London Ser. A* **360**, 1807 (2002).
12. S. R. Carpenter *et al.*, *Science* **314**, 257 (2006).
13. S. Pagiola, A. Arcenas, G. Platais, *World Dev.* **33**, 237 (2005).

Supporting Online Material
www.sciencemag.org/cgi/full/321/5896/1638/DC1

10.1126/science.1162756

COMPUTER SCIENCE

Weaving a Web of Trust

Analysis of online social networks may provide a metric for establishing trust in user-generated content.

Jennifer Golbeck

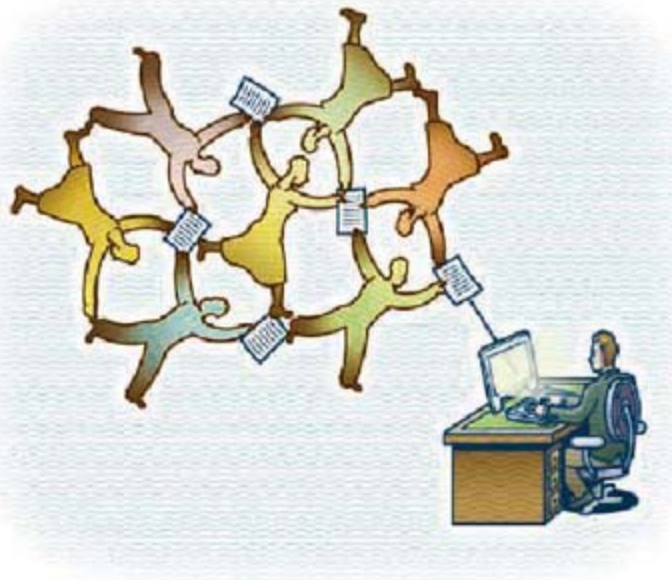

Got it...with a little help from my "trusted" friends.

Increasingly, people are studying social and collaborative Web technologies for use in science (*1*, *2*). However, issues such as privacy, confidentiality, and trust arise around the use of these technologies. Science is crucially based on knowing provenance—who produced what, how and where—and on the Web, trusting scientific information is becoming more difficult for both scientists and the general public. User-generated content, even from professionals, can be opinionated (both informed and uninformed), inaccurate, and deceiving. With an overwhelming amount of information of questionable origin and reliability, finding trusted information created by trusted people is the new challenge. The use of social trust relationships for this task is both practical and necessary as the Web evolves.

The term "trust" has traditionally been used in a security context, referring to authentication, identity, and authorization. Advances in these areas have been critical for the Web to evolve as it has. However, with the increase in user-generated content, a new type of trust is needed. Social trust relationships capture similarity in perspective. Sociological definitions of trust generally have two major components: a belief and a willingness to take some action based on that belief (*3*, *4*). Although this type of trust is often unsuitable for critical security applications, it has other uses that are leading it to become more important. In the context of the Web, trust translates to belief that an information producer will create useful information, plus a willingness to commit some time to reading and processing it. Thus, if users can identify the information producers they trust online, then they can spend their time more effectively by working with information from them.

Research has shown that trust is a good metric for identifying useful content; trust reflects similarity in opinions both overall (*5*) and in nuanced ways that are especially important. Further experiments have shown that filtering information based on trust is particularly effective when the user's opinion differs from that of the average population (*6*). Essentially, when users most need information based on their viewpoint, using social trust can provide it.

The most important challenge to using social trust in this way is estimating how much one user will trust another. With hundreds of millions of users on the Web, it is extremely unlikely that any two will know one another. There are hundreds of online social networks with more than a billion accounts among them. This wealth of publicly available social relationships offers one mechanism for estimating trust between users. A number of algorithms exist for computing trust from social networks (*7*–*10*) that rely on the network structure or similarity measures between users. However, these algorithms have only just begun to explore the space of understanding the dynamics of trust and trying to compute it. Techniques from machine learning and probabilistic reasoning could be used to create better algorithms for trust inference. The complex systems approaches to understanding network structure (*11*) and dynamics and discovering community structure (*12*) also hold promise.

Once established, the benefits of trust come from using it in applications. For the scientific community, trust can add context to content, using it to rate, sort, and filter information. The benefits of trust have been shown through several more general applications. Recommender systems, which suggest items to users on the basis of user profiles, are popular and have been successful for topics as diverse as movies (*6*) and ski routes (*7*). E-mail, where the trust that the recipient has in the sender is used to rank messages (*13*), is another application. Peer-to-peer systems have also used trust from social networks to improve routing by relying on peers controlled by trusted people (*14*).

These applications have been evaluated and shown to improve the way people access user-generated content. However, there is much work to be done in this area. The most critical is identifying sources of trusted information. Although we have algorithms that work well on social networks where users rate the trustworthiness of their peers, this sensitive information is never publicly shared, making it difficult for third-party applications to make use of that trust. More mechanisms are needed that can infer trust accurately from less sensitive sources. Further development is also necessary to understand the circumstances where trust offers the most benefit. In current research, trust-based applications never perform worse than simpler counterparts, but they do not always perform appreciably better. We have some initial insights into when trust works best, but a more systematic understanding will improve when and how we use it.

Social trust relationships may transform the way scientists, and the general public, use the Web. Over the past 5 years, research has shown the practicality of computing social trust and the benefits of using it. As the amount of user-generated content increases, the need for this social approach to information filtering also grows. The success of trust-based methods depends on additional research to identify where they offer the most benefit, as well as an understanding that social trust is needed on the Web as much as it is in the real world.

College of Information Studies, University of Maryland, College Park, MD 20742, USA. E-mail: jgolbeck@umd.edu

References

1. C. A. Goble, D. C. De Roure, in *WORKS '07: Proceedings of the 2nd Workshop on Workflows in Support of Large-Scale Science* (Association for Computing Machinery, New York, 2007), pp. 1–2.
2. N. Gray, T. Linde, *Semantic Knowledge Underpinning Astronomy (SKUA): Case for Support to Joint Information Systems Committee e-Infrastructure Programme*, June 2007, http://myskua.org.
3. M. Deutsch, *The Resolution of Conflict* (Yale Univ. Press, New Haven, CT, 1973).

4. P. Sztompka, *Trust: A Sociological Theory* (Cambridge Univ. Press, Cambridge, 1999).
5. C.-N. Ziegler, J. Golbeck, *Decision Support Serv.* **43**, 460 (2006).
6. J. Golbeck, in *Proceedings of the Fourth International Conference on Trust Management*, K. Stølen *et al.*, Eds. (Springer-Verlag, Berlin, 2006), pp. 93–104.
7. P. Avesani, P. Massa, R. Tiella, in *Proceedings of the 2005 Association for Computing Machinery Symposium on Applied Computing* (Association for Computing Machinery, New York, 2005), pp. 1589–1593.
8. U. Kuter, J. Golbeck, in *Proceedings of the National Conference on Artificial Intelligence (AAAI)* (2007), www.aaai.org/Library/AAAI/2007/aaai07-218.php.
9. R. Levien, A. Aiken, in *7th USENIX Security Symposium* (USENIX Association, Berkeley, CA, 1998), pp. 229–242.
10. C.-N. Ziegler, G. Lausen, in *Proceedings of the IEEE International Conference on e-Technology, e-Commerce, and e-Service* (IEEE Computer Society Press, Taipei, 2004).
11. M. Mitchell, *Artif. Intell.* **170**, 1194 (2006).
12. M. Girvan, M. E. Newman, *Proc. Natl. Acad. Sci. U.S.A.* **99**, 7821 (2002).
13. J. Golbeck, J. Hendler, in *Proceedings of the First Conference on Email and Anti-Spam* (IEEE Computer Society Press, 2004), www.ceas.cc/papers-2004/177.pdf.
14. S. Marti, thesis, Stanford University (2005).

10.1126/science.1163357

DEVELOPMENTAL BIOLOGY

Apoptosis Turbocharges Epithelial Morphogenesis

Mechanical forces that contribute to tissue movement during animal morphogenesis may include those generated by cell death during development.

Lance A. Davidson

Programmed cell death, or apoptosis, occurs throughout animal development. In the fruit fly *Drosophlia melanogaster*, apoptosis occurs in distinctly restricted patterns as tissues and organs form (*1*). First thought to play a role in eliminating malformed cells during embryogenesis, flies with mutations in apoptosis genes showed lethal phenotypes (*2*). Although the role of apoptosis during early stages of morphogenesis appeared critical, the reasons were not clear. On page 1683, in this issue, Toyama *et al.* (*3*) reveal that programmed cell death contributes to the mechanical forces that drive cell movements and cell shape changes during epithelial morphogenesis in the *Drosophila* embryo to construct the free-living larva.

The early embryo establishes the larval body plan, protecting internal organs and muscles within a tough epidermis. Once gastrulation has positioned mesoderm and endoderm, a process called dorsal closure completes the body plan by sealing yolk and the amnioserosa, the last of extraembryonic tissues, within the epidermis (see the figure). At the start of dorsal closure, the amnioserosa and dorsal epidermis are adjacent to each other, forming a cohesive epithelial sheet of cells tightly connected by junctions along their outer apical surface.

Multiple forces drive dorsal closure as the dorsal epidermis spreads and amnioserosal cells constrict. These opposing changes in surface areas ensure closure. Through a detailed biomechanical analysis that combines high-resolution imaging and cell and genetic manipulation, Toyama *et al.* find that apoptosis contributes between half and a third of the forces needed to seal the dorsal epithelium over the embryo. Their study is the most recent example of quantitative analyses of morphogenesis in *Drosophila*, addressing questions on the physical mechanics of dorsal closure (*4*), elongation of the germ band (comprising multiple germ layers on the ventral side of the embryo that curves around the embryo) (*5*, *6*), cell shape changes in the ommatidia during compound eye development (*7*), as well as the origin of epithelial architecture (*8*) and maintenance during wing differentiation (*9*).

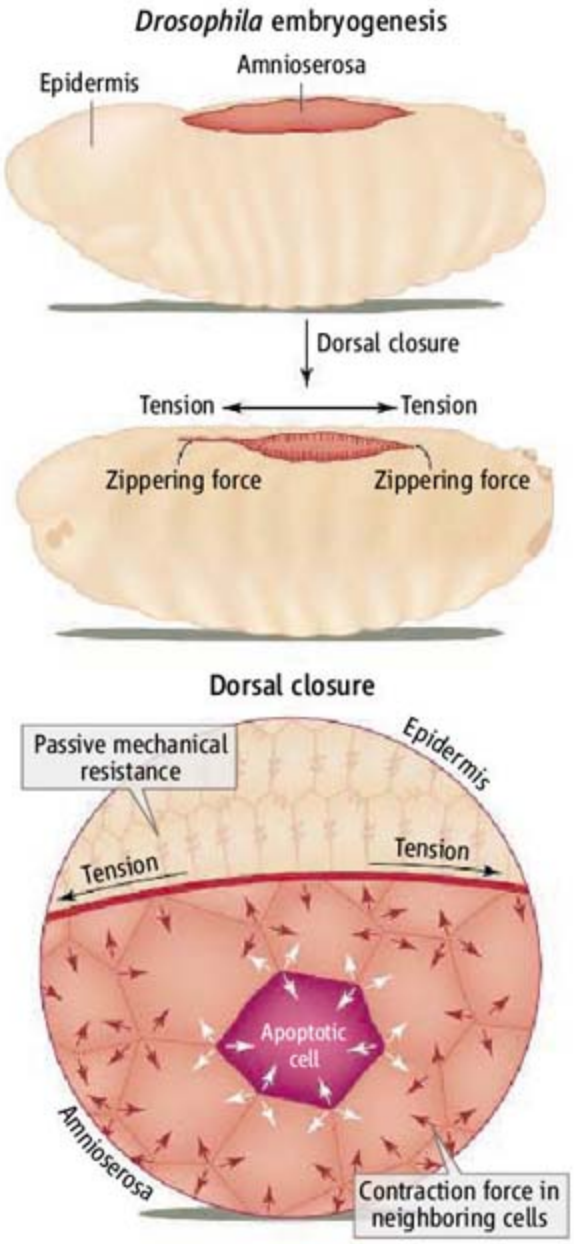

The sum of forces. A schematic of dorsal closure in the *Drosophila* embryo. Multiple forces contribute to, and resist, closure.

Epithelial morphogenesis is the sum of a variety of cellular and mechanical processes, but how do they integrate with each other? For the actions of cells on one side of the embryo to contribute to movements on the other, forces generated at one side must be transmitted through physical connections between cells to move tissues on the other side. Forces may originate from a single source or from multiple locations, but the tissue movements are in response to the sum of vector forces from these multiple locations. The challenge is to distinguish between forces that are due to nonautonomous macroscopic phenomena like germ-band retraction, or autonomous processes, such as contraction of the apical regions of cells within the amnioserosa, or the removal of apoptotic cells from particular locations, as they contract their exposed surface and move into the embryo. Resolving this "vector sum" into constituent forces will help to determine how specific cellular and molecular processes contribute to dorsal closure.

Unlike complex three-dimensional cases of epithelial morphogenesis that involve bending or rolling an epithelial sheet of cells into a tube, the two-dimensional mechanics within the plane of a sheet of epithelial cells makes dorsal closure more tractable and appealing to theoreticians and physicists. In previous work (*4*), the group behind the current study revealed the relative forces driving dorsal closure and their tissue origins. Using laser microdissection, they cut slits in the

Department of Bioengineering, University of Pittsburgh, Pittsburgh, PA 15260, USA. E-mail: lad43+@pitt.edu

CREDIT: P. HUEY/SCIENCE

epithelial sheet in numerous locations during dorsal closure and followed the subsequent rate of closure with time-lapse confocal microscopy. Surprisingly, the authors observed that no single site of dissection prevented closure. This is probably because the forces that drive closure are distributed among several tissues. In the present work, Toyama *et al.* add the power of genetics to alternatively block programmed cell death or stimulate high levels of cell death specifically in the amnioserosa, and find that dorsal closure is delayed or precocious, respectively.

To quantify the contribution of apoptosis to the vector sum, Toyama *et al.* present a descriptive physics of dorsal closure. The authors surmised that forces are transmitted within and between the amnioserosa and dorsal epidermis through cell-cell junctions along the outer surface of epithelial sheet. Ablating a single cell-cell junction (with a laser) releases the tension locally, and neighboring cells recoil to a new mechanical equilibrium. By following the velocity of newly freed cell-cell junctions, the authors deduced higher tension within the epithelium in embryos with high rates of apoptosis and low tension when cell deaths are blocked.

The occurrence of apoptosis during dorsal closure was discovered nearly 15 years ago (*1*), but its role has not been understood. The simplest explanation was that cell death contributes to dorsal closure by removing surface area from the amnioserosa. However, apoptosis removes only around 10% of the amnioserosa (the rest is resorbed after the epidermis has sealed over it). Alternatively, apoptosis might trigger contraction in other cells that would increase tension within the epithelium and promote cell movement. But strong evidence for this hypothesis is still lacking.

Toyama *et al.* suggest that additional contractive forces may be generated by the neighbors of the dying cell, as they actively excise the dying cell from the amnioserosa. Activation of apical contraction in neighboring cells plays a major role in the excision of cells undergoing apoptosis (*10*) and in the removal of laser-ablated cells (*11*) from epithelial sheets. The spreading of contraction-activation could greatly increase force generation to include neighbors of each apoptotic cell. But why must the contraction-activation signal stop there? Just as forces equilibrate quickly in the epithelium, it seems equally likely that contraction-activation of cell apical surfaces may spread through the entire amnioserosa triggered by even sparse and infrequent dying cells. Such a trigger may resolve another paradox—that the magnitude and spatiotemporal pattern of apoptosis in the amnioserosa vary greatly from embryo to embryo, suggesting that simple removal of dying cells may not be a particularly robust mechanism for ensuring dorsal closure. By serving as a trigger, apoptosis could amplify the contractile efforts to include larger numbers of cells in the amnioserosa.

The coincidence of cell death and epithelial morphogenesis is striking and prompts a rethinking of the role of programmed cell death during morphogenesis. It has been 10 years since the basic intracellular pathways that lead to apoptosis during development were elaborated (*12*), yet the triggers and downstream effectors of apoptotic signals are just beginning to be understood (*13*). Clearly, apoptosis initiates dynamic remodeling of the cytoskeleton (*14*). Whether forces generated during apoptosis contribute to vertebrate morphogenesis remains to be seen, but its ubiquity (*15*) suggests widespread implications and the need for further studies.

References

1. J. M. Abrams, K. White, L. I. Fessler, H. Steller, *Development* **117**, 29 (1993).
2. K. White *et al.*, *Science* **264**, 677 (1994).
3. Y. Toyama, X. G. Peralta, A. R. Wells, D. P. Kiehart, G. S. Edwards, *Science* **321**, 1683 (2008).
4. M. S. Hutson *et al.*, *Science* **300**, 145 (2003).
5. C. Bertet, L. Sulak, T. Lecuit, *Nature* **429**, 667 (2004).
6. J. T. Blankenship, S. T. Backovic, J. S. Sanny, O. Weitz, J. A. Zallen, *Dev. Cell* **11**, 459 (2006).
7. J. Kafer, T. Hayashi, A. F. Maree, R. W. Carthew, F. Graner, *Proc. Natl. Acad. Sci. U.S.A.* **104**, 18549 (2007).
8. M. C. Gibson, A. B. Patel, R. Nagpal, N. Perrimon, *Nature* **442**, 1038 (2006).
9. R. Farhadifar, J. C. Roper, B. Aigouy, S. Eaton, F. Julicher, *Curr. Biol.* **17**, 2095 (2007).
10. J. Rosenblatt, M. C. Raff, L. P. Cramer, *Curr. Biol.* **11**, 1847 (2001).
11. M. Tamada, T. D. Perez, W. J. Nelson, M. P. Sheetz, *J. Cell Biol.* **176**, 27 (2007).
12. M. D. Jacobson, M. Weil, M. C. Raff, *Cell* **88**, 347 (1997).
13. H. Steller, *Cell Death Differ.* **15**, 1132 (2008).
14. O. Ndozangue-Touriguine, J. Hamelin, J. Breard, *Biochem. Pharmacol.* **76**, 11 (2008).
15. A. Glucksmann, *Biol. Rev.* **26**, 59 (1951).

10.1126/science.1164583

CLIMATE CHANGE

Illuminating the Modern Dance of Climate and CO_2

Peter Cox[1] and Chris Jones[2]

Records of Earth's past climate imply higher atmospheric carbon dioxide concentrations in the future.

Climate and atmospheric carbon dioxide (CO_2) concentrations have been coupled through much of Earth's history: CO_2 influences climate through the greenhouse effect, but climate also influences CO_2 through its impact on the stores of carbon on the land and in the oceans. This two-way coupling between climate and CO_2 will have a large influence on how the climate changes over the course of the 21st century. Currently, the amount of CO_2 emitted as a result of human activities is about double the amount required to explain the rate of increase of atmospheric CO_2 (*1*). The remainder is absorbed by land and ocean carbon sinks, which have thus been acting to slow climate change. Will they continue to do so? Data on the Earth's past can illuminate this modern dance of climate and CO_2.

First-generation coupled climate-carbon cycle models (C-CC models) suggest that the ocean and especially land sinks will become progressively less efficient at absorbing CO_2 under global warming (*2*). All such models in the Intergovernmental Panel on Climate Change (IPCC) 4th Assessment Report project higher atmospheric CO_2 by 2100 once the impacts of climate change on the carbon cycle are accounted for (*1*). All models produce increasing carbon sinks as a result of increasing atmospheric CO_2 concentration, which is partially offset by reducing sinks as a result of climate change. The impacts of climate change on the carbon cycle thus lead to a higher fraction of human CO_2 emissions remaining in the atmosphere, and therefore an acceleration of global warming. However, the amount of extra CO_2 simulated by the models varies by an order of magnitude, from the relatively inconsequential [~30 parts per million by volume (ppmv)] (*3*) to the alarming (~250 ppmv) (*4*). It is critically important to reduce this range of uncertainty in climate-carbon cycle feedbacks, because it leads to large uncertainties in the emissions cuts required to stabilize climate at different CO_2 concentrations (*5*).

[1]School of Engineering, Computing and Mathematics, University of Exeter, Exeter EX4 4QF, UK. [2]Met Office Hadley Centre, Exeter EX1 3PB, UK. E-mail: p.m.cox@exeter.ac.uk, chris.d.jones@metoffice.gov.uk

Why can we not use the 20th-century climate record to determine which C-CC models are likely to be most accurate? Temperature and CO_2 have both increased almost continuously through the 20th century, making it difficult to separate the positive impacts of CO_2 on carbon sinks from the negative impacts of global warming on these sinks. The existing C-CC models can roughly reproduce the 20th-century increase in CO_2 despite having great variations in the relative impacts of CO_2 and climate change on carbon sinks. Models in which both effects are large can reproduce the observational record, but so can models in which both effects are small (see the figure, left panel). However, these different possibilities result in a wide range in the projected CO_2 concentration by 2100 under a given human CO_2 emissions scenario (*2*). We clearly need other observational constraints to tie down the climate-carbon feedback.

Interannual variability in the atmospheric CO_2 concentration is a ubiquitous signal in the observational record that could help us distinguish between different models. The growth rate of atmospheric CO_2 varies from year to year as a result of climatic anomalies associated with the El Niño–Southern Oscillation (*6*) and volcanic eruptions (*7*), and this can be seen in some C-CC general circulation models (GCMs). We find that models with a larger sensitivity of CO_2 growth rate to interannual climate variations also show a stronger climate-carbon feedback. As a result, the observed interannual variability provides an additional observational constraint on the sensitivity of carbon stores to climate (see the horizontal lines in the figure, left panel). However, the relatively small number of C-CC GCMs means that the gradient of this relation is not well constrained, so the overall uncertainty in the extra CO_2 to be expected for each unit of warming is still very large, ranging from 3 to 31 ppmv/K (see description of methods).

How can paleoclimatic data help? The key challenge is to find a period in the past when CO_2 has varied mainly as a result of a natural climate variation with a time scale relevant to 21st-century climate change. The most marked example of coupled variations between climate and CO_2 concerns the glacial-interglacial cycles, but these cycles occur on time scales of 1000 to 100,000 years, and thus involve processes that may not be relevant to century-scale climate change (*8*). By contrast, the Little Ice Age (LIA) perturbation in climate (*9*) and CO_2 (*10*) is much smaller, but has the advantage of having occurred over a time scale of a few centuries.

The perturbations of climate and CO_2 during the LIA period from 1500 to 1750 are strongly correlated, with climate leading CO_2 by ~50 years (*11*). These records indicate a tight relation between CO_2 and climate, with a gradient of 40 ppmv/K. However, given the discrepancies between different temperature reconstructions, and the uncertainties associated with interpreting Northern Hemisphere climate proxies in terms of global mean temperature, we estimate a gradient of 20 to 60 ppmv of CO_2 per kelvin of global warming (see the figure, middle panel).

This is a conservative estimate based on the assumption that human CO_2 emissions from land-use change (*12*) were not significant in the LIA, which seems consistent with the strong lead-lag relationship between climate and CO_2 during this period. Even so, the estimate is at the high end of the 20th-century simulations with the IPCC C-CC models, encompassing only the model with the largest feedback over this period. When considered alongside contemporary constraints, the LIA data thus enable a much tighter constraint on the climate and CO_2 dependences of the carbon cycle (see the figure, right panel).

The LIA data imply that atmospheric CO_2 will increase more quickly with global warming than most models suggest. One implication is that the 20th-century CO_2 rise due to anthropogenic emissions may have been amplified by 20 to 30 ppmv through the impacts of global warming on natural carbon sinks. Furthermore, the existence of a strong climate effect on the carbon cycle indicates that larger emissions cuts are required to stabilize CO_2 concentrations at a given level. The LIA is just one example of a natural climatic anomaly in the past that can provide insights into the strength of the coupling between the Earth's climate and carbon cycle. Paleoclimatic data cannot tell us how to meet the challenge of managing 21st-century climate change, but they can help us to better understand the nature of this challenge.

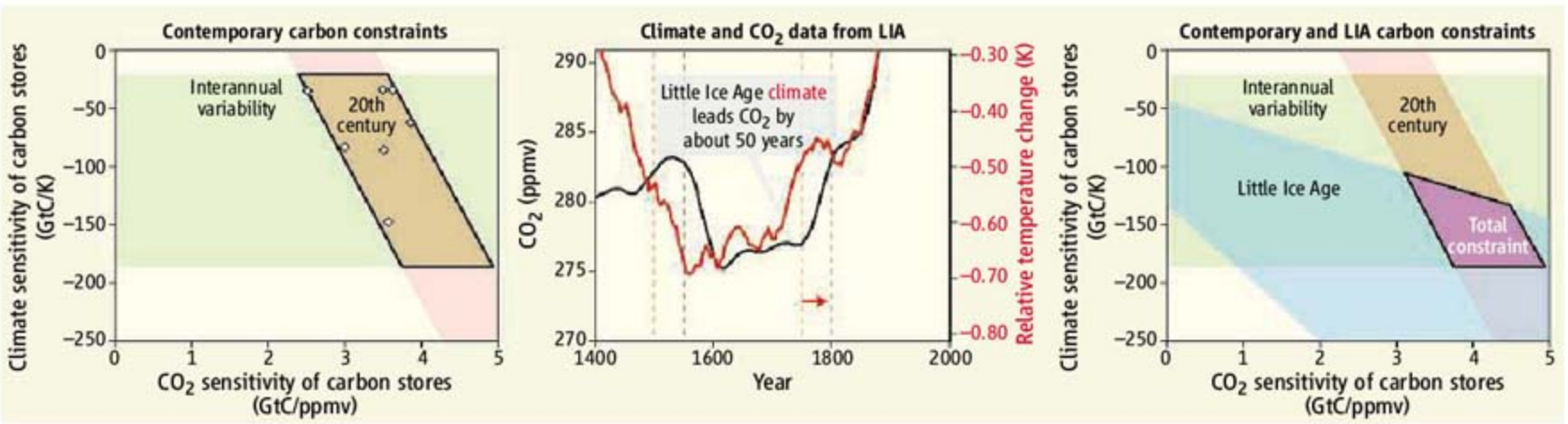

Impact of Little Ice Age (LIA) data on estimates of climate-carbon feedback. **(Left)** Constraints on the climate and CO_2 sensitivities of the carbon cycle based on 20th-century trends (pink) and interannual variability (green). The diagonal band at the top right corner represents the combinations of climate and CO_2 effects on the carbon cycle that are consistent with the 20th-century record. This band has a finite width because of substantial uncertainties in the net land-use emissions of CO_2. As a result, it encompasses the 20th-century simulations of all seven current C-CC GCMs, even though these models predict a wide range of climate-carbon feedbacks for the 21st century. We exclude from this plot the four Earth System Models of Intermediate Complexity (EMIC) reported in (*2*), because these models lack interannual variability. **(Middle)** Variation of climate (red) and CO_2 (black) through the LIA (1500 to 1750) (*9*, *10*). **(Right)** Total constraint on the climate and CO_2 sensitivities of the carbon cycle (purple rhombus) once the LIA constraint is added to the contemporary constraints. Inclusion of the LIA data substantially reduces the overall uncertainty in the carbon cycle responses to both climate and CO_2.

References and Notes

1. K. L. Denman *et al.*, in *Climate Change 2007: The Physical Science Basis. Contribution of Working Group I to the Fourth Assessment Report of the Intergovernmental Panel on Climate Change*, S. Solomon *et al.*, Eds. (Cambridge Univ. Press, Cambridge, UK, 2007), chap. 7.
2. P. Friedlingstein *et al.*, *J. Climate* **19**, 3337 (2006).
3. I. Y. Fung, S. C. Doney, K. Lindsay, J. John. *Proc. Natl. Acad. Sci. U.S.A.* **102**, 11201 (2005).
4. P. M. Cox, R. A. Betts, C. D. Jones, S. A. Spall, I. J.

Totterdell, *Nature* **408**, 184 (2000).
5. C. D. Jones, P. M. Cox, C. Huntingford, *Tellus B* **58**, 603 (2006).
6. C. D. Jones, M. Collins, P. M. Cox, S. A. Spall. *J. Climate* **14**, 4113 (2001).
7. C. D. Jones, P. M. Cox, *Global Biogeochem. Cycles* **15**, 453 (2001).
8. D. Archer, D. Kheshgi, E. Maier-Reimer. *Geophys. Res. Lett.* **24**, 405 (1997).
9. A. Moberg, D. M. Sonechkin, K. Holmgren, N. M. Datsenko, W. Karlen, *Nature* **433**, 613 (2005).
10. D. M. Etheridge *et al.*, *J. Geophys. Res.* **101**, 4115 (1996).
11. M. Scheffer, V. Brovkin, P. M. Cox, *Geophys. Res. Lett.* **33**, L10702, 10.1029/2005GL025044 (2006).
12. W. F. Ruddiman, *Clim. Change* **61**, 261 (2003).
13. This paper is based on a presentation given at the Leverhulme Climate Symposium 2008: "Earth's Climate: Past, Present and Future." We thank the Coupled Climate-Carbon Cycle Model Intercomparison Project (C⁴MIP) for providing model outputs for this analysis.

The contribution of C.J. was supported by the Defra and MoD Integrated Climate Programme (Contract number: GA01101, CBC/2B/0417_Annex C5).

Supporting Online Material
www.sciencemag.org/cgi/content/full/321/5896/1642/DC1
Methods
Figs. S1 to S4
References

10.1126/science.1158907

MICROBIOLOGY

Desperately Seeking New Antibiotics

New approaches for discovering the next generation of antibiotics are needed to combat the rise in bacteria that are resistant to current drugs.

David J. Payne

The need for new antibiotics is undisputed (*1*). Recent studies estimate that more people die from the methicillin–resistant *Staphylococcus aureus* (MRSA) bacterium than from HIV in the United States (*2*), and the Centers for Disease Control and Prevention estimates that more than 90,000 people die from hospital-acquired bacterial infections in the United States each year. Numerous reports have illustrated the "perfect storm" of rising bacterial resistance to antibiotics and an industry pipeline ill-equipped to address the need for new antibacterial drugs (*3*, *4*) (see the figure). Consequently, the reports by Haydon *et al.* on page 1673 in this issue (*5*) and by Rasko *et al.* (*6*) are important because they validate and illustrate the therapeutic potential of two new antibacterial drug targets. In addition, the paper by Hiratsuka *et al.* on page 1670 in this issue (*7*) identifies a biosynthetic pathway that may provide new antibacterial strategies for certain species of bacteria.

Haydon *et al.* report the discovery of a class of drugs that targets the bacterial protein FtsZ. FtsZ is related to the human cytoskeletal protein β-tubulin and is essential in bacterial cell division in most Gram-positive and Gram-negative pathogens, where it polymerizes to form a ring at the mid cell that enables septum formation. The authors show by crystallographic analysis that their lead molecule (PC190723) binds to the region of FtsZ that is analogous to the site that the anticancer drug Taxol binds to in β-tubulin (Taxol interferes with microtubule dynamics and blocks cell division). Moreover, they show that PC190723 possesses in vitro potency against MRSA, and is effective in a mouse model of *S. aureus* infection. Importantly, through mutational and bacterial physiology experiments, Haydon *et al.* show that the antibacterial effect of PC190723 is via inhibition of FtsZ. The discovery of these inhibitors of FtsZ illustrates the potential of this protein as a novel and exploitable antibacterial drug target.

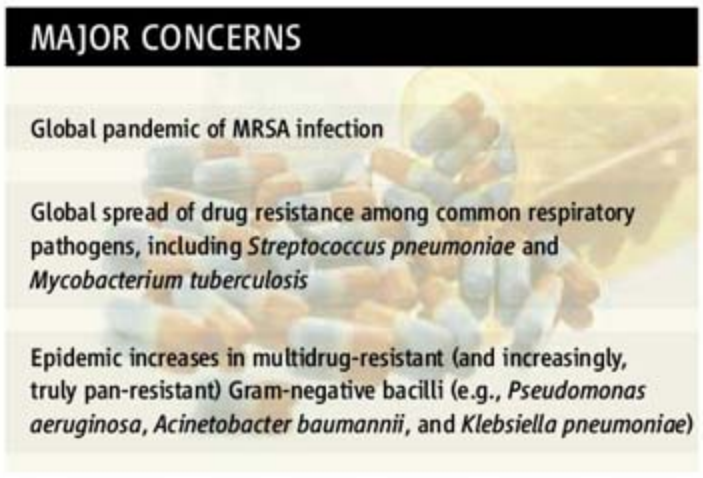

Bad bugs need drugs. Three major areas of concern that need new antibiotics [as defined by the Infectious Diseases Society of America (*4*)].

Whereas inhibition of FtsZ prevents bacterial growth, Rasko *et al.* describe an alternative drug approach that cripples the bacteria's ability to maintain an infection. The authors discovered a compound (LED209) that inhibits the bacterial enzyme QseC. This target is a histidine kinase that autophosphorylates upon sensing either host signaling molecules (the hormones norepinephrine and epinephrine) or bacterial molecules (called autoinducers) associated with quorum-sensing (cell-to-cell communication among bacteria). This phosphorylation event leads to the expression of key virulence genes, and *Escherichia coli* with a mutant form of QseC is unable to trigger expression of these virulence genes and shows decreased growth in an animal infection model. QseC homologs are found in most clinically important Gram-negative pathogens. Rasko *et al.* elegantly demonstrate that LED209 inhibits QseC-dependent expression of virulence genes triggered by either the autoinducer AI-3 or by epinephrine. In animal models of infection, LED209 was not effective in protecting against *E. coli* infection, but oral dosing of LED209 3 hours before and after infection with *Salmonella typhimurium* protected mice from infection. In addition, fewer bacteria were recovered from the spleens and livers of animals treated with LED209 compared with controls. Therefore, this work demonstrates the potential of an "antivirulence" strategy for tackling bacterial infections. None of the currently available antibiotics employ such a mechanism of action.

Hiratsuka *et al.* illustrate the power of bacterial genomics to identify potential new targets for anti-infective strategies. Most microorganisms use a biosynthesis pathway encoded by the *men* genes to produce menaquinone, a molecule needed for bacterial anaerobic respiration. However, the authors deduced that some bacteria such as *Streptomyces coelicolor*, *Helicobacter pylori*, and *Campylobacter jejuni* lack these genes, yet still synthesize menaquinone. To identify this new route of synthesis, the authors compared the genomes of microorganisms that use the known *men* pathway with bacteria that lack the *men* genes. This eventually led to four candidate genes, each of which were previously annotated as encoding "hypothetical proteins." Each of these genes was disrupted, and the resulting mutants all required menaquinone for growth. The authors then used biochemical and analytical approaches to identify the various intermediate molecules at each step in the new menaquinone

Antibacterial Disease Performance Unit, Infectious Diseases Center of Excellence, GlaxoSmithKline, Collegeville, PA 19426, USA. E-mail: david.j.payne@gsk.com

PHOTO CREDIT: JUPITER IMAGES

biosynthesis pathway (which they named the futalosine pathway, after the first intermediate molecule). The lack of this pathway in humans and its presence in bacteria such as *Chlamydia* (which causes urethritis and respiratory tract infections), *H. pylori* (which can cause stomach ulcers), *C. jejuni* (which causes gastroenteritis often associated with food poisoning), and *Spirochaetes* (which cause syphilis and lyme disease) could make it an attractive antibacterial drug target for these specific pathogens.

The development pipeline for systemic antibiotics consists almost entirely of new versions of decades-old classes of antibiotics, such as β-lactams, quinolones, macrolides, and glycopeptides. New classes of antibacterial drugs directed against new bacterial targets are urgently needed. Unfortunately, there are insufficient novel antibiotics in development to address this challenge, partly because of decreased investment in this sector and also because of the substantial difficulty of finding small-molecule drug leads. Despite a wealth of new bacterial targets, high-throughput screening for inhibitory compounds in this therapeutic area has been less successful than in any other (*8*), a likely cause being the unique chemical diversity needed to inhibit bacterial enzymes. Consequently, the work by Haydon *et al.* and Rasko *et al.* is important because they have identified inhibitors of their targets with the potential for pharmaceutical development. However, turning these "leads" into drugs remains a challenge. For example, antibacterials typically need to be administered at higher doses than most other drugs, emphasizing the need for compounds that can achieve high exposures in humans but that are also extremely safe at these high doses

For the last 10 to 15 years, antibacterial research and development has focused on the validated approach of designing small molecules that inhibit bacterial growth. However, perhaps now is the time to consider alternative strategies. For example, targeting virulence factors as described by Rasko *et al.* may create more effective drugs with a lower propensity to select for resistance. However, the amount of attenuation achieved by such antivirulence drugs and the consequences of potentially not eradicating the bacteria from the infection need careful consideration. Such drugs may need to be combined with antibacterial agents to achieve their full potential. Other promising approaches include developing inhibitors of bacterial drug resistance mechanisms or bacterial drug efflux pumps for combination with specific antibacterials that could rejuvenate entire classes of antibiotics against multidrug-resistant pathogens. In addition, rather than the traditional approach of seeking antibiotics that cover a broad set of pathogens, exploiting targets that are specific for only certain pathogens, such as those described by Hiratsuka *et al.*, may be a more productive strategy. This would also have the advantage of creating antibiotics that will enable highly targeted therapy and remove the considerable drug discovery challenge of having to identify a single molecule that penetrates, and is equipotent against, a range of potentially diverse species of bacteria (*8*). However, this approach will succeed only be with the availability of diagnostics that can very rapidly and accurately identify the specific infecting pathogen, and it may be some time before such tools are available for a range of common pathogens. Consequently, the need for new antibiotics merits investment across a spectrum of traditional and higher-risk approaches to optimize the chances of creating promising new antibiotics.

References

1. G. Taubes, *Science* **321**, 356 (2008).
2. R. M. Klevens, M. A. Morrison, S. K. Fridkin, *JAMA* **17**, 1763 (2007).
3. The Royal Society, "Innovative mechanisms for tackling antibiotic resistance"; http://royalsociety.org/displaypagedoc.asp?id=30717 (2008).
4. B. Spellberg *et al.*, *Clin. Infect. Dis.* **46**, 155 (2008).
5. D. J. Haydon *et al.*, *Science* **321**, 1673 (2008).
6. D. A. Rasko *et al.*, *Science* **321**, 1078 (2008).
7. T. Hiratsuka *et al.*, *Science* **321**, 1670 (2008).
8. D. J. Payne, M. N. Gwynn, D. J. Holmes, D. L. Pompliano, *Nat. Rev. Drug Discov.* **6**, 29 (2007).

10.1126/science.1164586

CHEMISTRY

Fluorous Tags Unstick Messy Chemical Biology Problems

Separation and identification of biological molecules from complex mixtures can be made easier with fluorinated labeling groups and separation media.

Dennis P. Curran

Department of Chemistry, University of Pittsburgh, Pittsburgh, PA 15208, USA. E-mail: curran@pitt.edu

Everyone knows that nothing sticks to Teflon-coated products, such as cookware, raincoats, and ski waxes (and, figuratively, even to some politicians). The prevalence of "nonstick" products coated with Teflon [poly(tetrafluoroethylene)] shows that with some engineering effort, Teflon can adhere to metals, textiles, and plastics. At the molecular level, the perfluoroalkyl groups [–$(CF_2)_n$–] that comprise Teflon tend to repel organic and inorganic molecules but have attractive interactions with other perfluoroalkyl (R_F) groups and along with fluorinated solvents can form separate fluorous phases. Organic chemists exploit perfluoroalkyl groups in small-molecule synthesis and separation by applying them as tags for separations with fluorous silica gel and solvents. Recent innovations suggest that a wide range of potential applications of fluorous tags could be realized in chemical biology as well, not only in separations and derivatization but also in identification because of the distinctive signatures of these tags in mass spectrometry.

Separation tags can enable rapid partitioning of a relatively complex mixture (such as cell isolates or products of cell-based protein synthesis) into tagged and untagged fractions. For example, a streptavidin affinity column will fasten molecules with a biotin tag and let the untagged molecules pass. Separation tags that are commonly used with biomolecules include polymer beads or surfaces, as well as other molecular tags such as polyhistidine.

Given the success of these commonly used separation tags, why are fluorous tags of interest? First, separation tags typically also have to accommodate—better yet, facilitate—biomolecule synthesis and analysis methods. Fluorous tags provide separation handles that are relatively inert and do not compromise synthetic reactions or analysis operations.

Second, tag systems such as streptavidin-biotin rely on very strong fastening interactions (covalent bonds or powerful ionic or molecular recognition forces) that may be difficult to unfasten during product recovery. Fluorous tags behave more like molecular "Post-it notes." For example, when synthetic chemists use fluorous solid-phase extraction

(FSPE) for separations (*1*), only the fluorous-tagged molecules stick to the gel column in the first elution (typically in a wet organic solvent). The tagged molecules are then easily washed off and captured with a fluorophilic solvent. In a very early chemical biology application, a group at Dupont reacted the free amines of proteins with fluorous isocyanates ($R_FN{=}C{=}O$) and showed that the resulting fluorous-tagged proteins could be absorbed onto both solid and liquid fluorous phases (*2*).

Fluorous separation techniques have an added bonus if the subsequent identification steps involve mass spectrometry (MS). In fluorous proteomics (see the figure, top panel), a complex peptide (or protein) sample is subjected to a selective reaction with a fluorous reagent that targets a specific chemical functional group, such as thiols of cysteines (*3*). The resulting complex sample of labeled and unlabeled peptides is then dramatically enriched in the labeled peptides by FSPE. Subsequent MS analysis to identify the fluorous-tagged peptides and, hence, their precursor proteins is actually easier than with untagged proteins. The fluorous tags are not prone to fragmentation, so the spectra are less complicated. Furthermore, molecules bearing fluorous tags are easily ionized and have mass peaks that are readily identified. The fluorous reagents and separation materials are also inexpensive compared to those used in established proteomics techniques.

Fluorous methods are also proving useful in the synthesis and microarray analysis of polysaccharides and sugar derivatives, which are much more challenging than proteins (see the figure, middle panel). Monosaccharides bearing a fluorous tag at the anomeric center (the carbon atom that determines the stereochemistry of the glycoside linkage) have been converted to disaccharides by using the techniques of fluorous synthesis (*4*). Here, standard methods of solution-phase carbohydrate synthesis are used, but the fluorous tags enable separation of the target products from by-products much more rapidly than in other approaches.

Separation tags are often removed at the end of such syntheses, much like removing packaging materials from a shipment. Microarray methods usually involve a "repackaging" of the molecules so that they can be attached by covalent bonds onto the slide. Another bonus of the fluorous approach is that there is no repackaging; the fluorous-tagged carbohydrates can be directly spotted onto fluorous slides to make microarrays for screening.

Like fluorous silica gel, the slides have a fluorous bonded phase, and the affinity of the tags for the bonded phase allows the slides to be washed with detergent solutions during analysis without removing the spots or compromising their morphologies. The spotted slides are exposed to fluorescently labeled lectins (selective carbohydrate-binding proteins) for analysis. The nonstick nature of the fluorous slides minimizes nonspecific adsorption of lectins other than to the carbohydrate target. The fluorous-fluorous interaction suffices to hold tagged molecules onto the slide, but like Post-it notes, the fluorous spots can easily be peeled off after analysis. This technique has already yielded information on binding of heptoses to lectins (*5*) and identified new small molecule inhibitors of histone deacetylase (*6*).

The recently introduced technique of nanostructure-initiator mass spectrometry (NIMS) is showing promise as an alternative to current MS analysis methods (*7*) for large biomolecules that are not readily volatilized. In the original incarnation of NIMS, perfluorosiloxanes were used as initiators for laser vaporization of analytes into the gas phase. The fluorous features of these initiators have also been captured and used in an enzymatic assay (see figure, bottom panel). In proof-of-principle experiments, a fluorous-labeled disaccharide was immobilized in the fluorous nanopores of a NIMS chip. The chip was exposed to enzymes that either add or remove a saccharide ring. Subsequent MS analysis directly detected the fluorous-tagged elongated or truncated products. The sensitivity of this so-called Nimzyme assay for the presence of enzymes in solution was much better than traditional colorimetric assays and was comparable with fluorescence methods (500-fg level).

The Nimzyme analysis has already been used to characterize the enzymatic activity of crude cell lysates from thermophilic bacteria. Here, the ability to wash away the huge background of the cell lysate while retaining the fluorous-tagged enzyme products for MS analysis is central to the success of the assay. That, combined with the inherent attractive features of NIMS, recommends the assay for high-throughput bioprospecting applications.

These early innovations herald the expansion of fluorous methods into chemical biology. If they catch hold, then perhaps we can say that something sticks to Teflon after all.

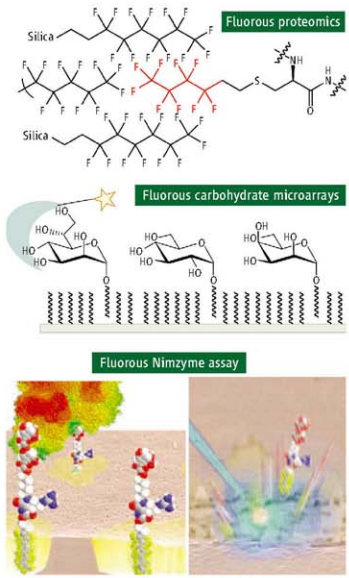

Just sticky enough. (**Top**) Fluorous proteomics. A polypeptide bearing a fluorous tag on a cysteine is held onto a fluorous silica gel column during a first elution while nontagged molecules pass through. (**Middle**) Carbohydrate microarrays. An assortment of fluorous-tagged carbohydrates are arrayed into spots on a slide having a fluorous bonded phase. A fluorescently labeled lectin (blue region with star) binds to the carbohydrates but washes readily off the fluorous slide. (**Bottom**) Nimzyme assay (*7*). A glycosidase enzyme in a crude lysate operates on a substrate held to a surface by a fluorous siloxane. The lysate is washed away. The siloxane now functions as an initiator to help quantify the activity by MS analysis. [Copyright (2008) National Academy of Sciences USA]

References

1. W. Zhang *et al.*, *Tetrahedron* **62**, 11837 (2006).
2. R. K. Kobos *et al.*, *Tibtech* **7**, 101 (1989).
3. S. M. Brittain *et al.*, *Nat. Biotechnol.* **23**, 463 (2005).
4. K. S. Ko *et al.*, *J. Am. Chem. Soc.* **127**, 13162 (2005).
5. F. A. Jaipuri *et al.*, *Angew. Chem. Int. Ed.* **47**, 1707 (2008).
6. A. J. Vegas *et al.*, *Angew. Chem. Int. Ed.* **46**, 7960 (2007).
7. T. R. Northen *et al.*, *Proc. Nat. Acad. Sci. U.S.A.* **105**, 3678 (2008).

10.1126/science.1158721

CREDIT (BOTTOM PANEL): TRENT NORTHEN

Ancient Permafrost and a Future, Warmer Arctic

Duane G. Froese,[1]* John A. Westgate,[2] Alberto V. Reyes,[1] Randolph J. Enkin,[3] Shari J. Preece[2]

Areas of permafrost are subdivided into continuous (>90% frozen ground), discontinuous (>50%), and sporadic (<50%) permafrost zones (Fig. 1A). Permafrost outside the continuous permafrost zone is particularly vulnerable to future climate change because it is near the melting point and because the depth of frozen ground is typically thin (a few to tens of meters). Permafrost in northwest North America warmed in the late 20th century (*1*), and numerical models predict widespread and severe permafrost degradation under 21st-century climate-warming scenarios (*2*), with potential for concomitant release of stored carbon (*3*). However, our limited knowledge of the response of permafrost to past warming makes it difficult to evaluate the future response (*4*).

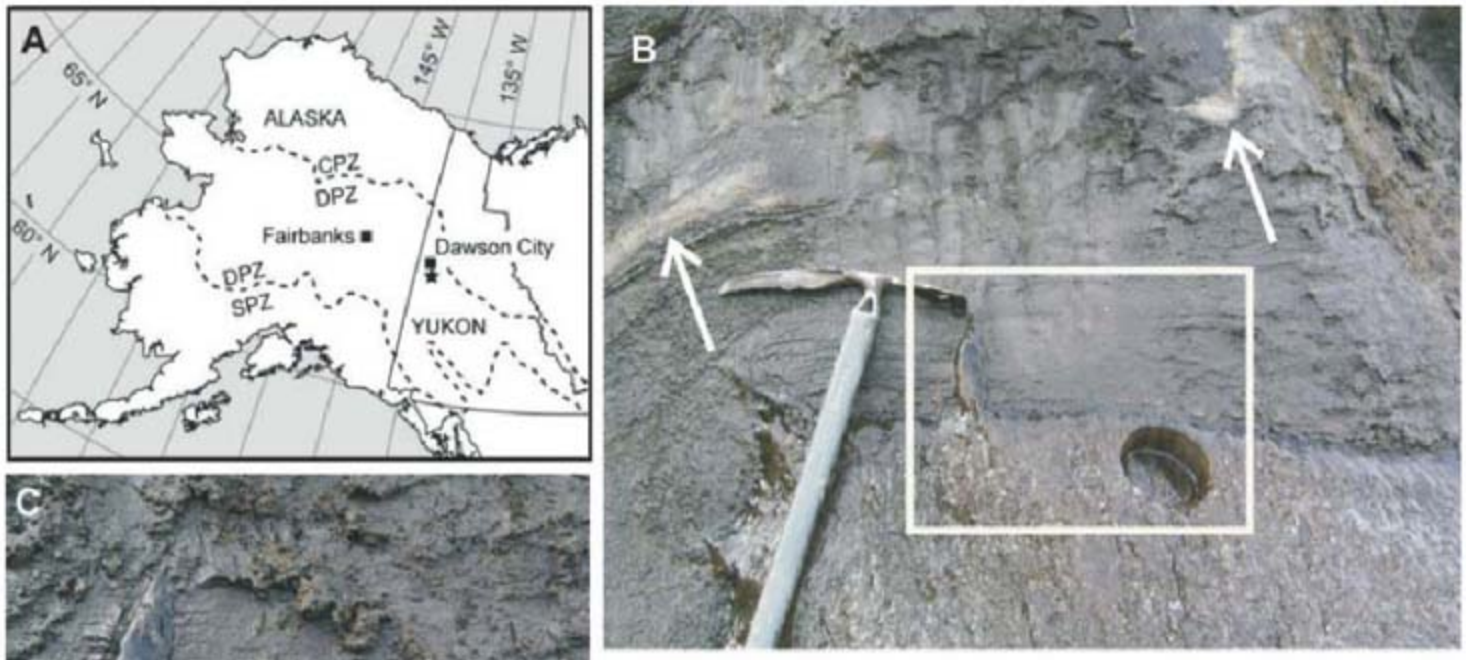

Fig. 1. (**A**) Permafrost zones of northwestern North America (continuous, discontinuous, and sporadic are CPZ, DPZ, and SPZ, respectively) and study site location (*). (**B**) Top of relict ice wedge with beds of Gold Run tephra (740,000 ± 60,000 yr B.P.) marked by arrows. (**C**) Close-up [box in (B)] of relict secondary wedge on ice wedge surface (scale bar = 10 cm).

We investigated relict ground ice within the discontinuous permafrost zone of central Yukon Territory, Canada. Permafrost in this area is warm (>–2°C), up to a few tens of meters thick, and strongly controlled by local site conditions; permafrost is generally sparse or absent on south-facing slopes and in areas lacking insulating vegetation cover. At the Dominion Creek site, large vertically foliated ice bodies (ice wedges) are present within a few meters of the surface (*5*). The ice composing the wedge is distinctive because of the presence of vertical foliations with parallel air bubbles. These ice wedges formed at the former surface through thermal contraction cracking and infilling by surface water and freezing and would necessarily have had an overlying active layer (seasonally thawed horizon) when the ice wedge formed. Seasonal melting of the paleoactive layer truncated the top of the ice body, producing a flat upper surface, with some secondary wedge growth present at the ice wedge surface, indicating that the paleoactive layer is present (Fig. 1, B and C).

A volcanic ash called the Gold Run tephra was recovered from within the paleoactive layer and tion of the tephra. Two independent age estimates for the tephra were made on glass by using the isothermal plateau and the diameter-corrected fission-track methods. These estimates provide a weighted-mean age of 740,000 ± 60,000 years before the present (yr B.P.) (table S1) and are consistent with faunal ages associated with this bed and the normal magnetic polarity of the surrounding sediments (*5*).

The relict ice wedge overlain by the Gold Run tephra represents the oldest ice known in North America and is evidence that permafrost has been a long-term component of the North American cryosphere. Importantly, this finding demonstrates that permafrost has survived within the discontinuous permafrost zone since at least the early-Middle Pleistocene. This age range includes several glacial-interglacial cycles, including marine isotope stages 5e and 11, both considered to be longer and warmer than the present interglaciation (*6*). The presence of relict Middle Pleistocene permafrost suggests that the controls on permafrost thickness and distribution, such as surface cover (which insulates permafrost), deeper ground ice (which cools shallow permafrost), and excess ice (which retards thaw due to latent heat effects), are still not adequately considered in numerical models of permafrost degradation (*7*). This study highlights the resilience of permafrost to past warmer climate and suggests that permafrost and associated carbon reservoirs that are more than a few meters below the surface may be more stable than previously thought.

References and Notes

1. T. E. Osterkamp, *Global Planet. Change* **49**, 187 (2005).
2. D. M. Lawrence, A. G. Slater, *Geophys. Res. Lett.* **32**, L24401 (2005).
3. S. A. Zimov, E. A. G. Schurr, F. S. Chapin III, *Science* **312**, 1612 (2006).
4. J. Overpeck *et al.*, *Eos* **86**, 312 (2005).
5. Details available as supporting online material on *Science* Online.
6. J. Jouzel *et al.*, *Science* **317**, 793 (2007); published online 3 July 2007 (10.1126/science.1141038).
7. C. R. Burn, F. E. Nelson, *Geophys. Res. Lett.* **33**, L21503 (2006).
8. Funding provided by Natural Sciences and Engineering Research Council of Canada grants to D.G.F. and J.A.W. and by an Alberta Ingenuity New Faculty Award to D.G.F.

Supporting Online Material

www.sciencemag.org/cgi/content/full/321/5896/1648/DC1
SOM Text
Table S1
References

10 March 2008; accepted 16 June 2008
10.1126/science.1157525

[1]Department of Earth and Atmospheric Sciences, University of Alberta, Edmonton, AB T5M 0M3, Canada. [2]Department of Geology, University of Toronto, Toronto, ON M5S 3B1, Canada. [3]Geological Survey of Canada–Pacific, Sidney, BC V8L 4B2, Canada.

*To whom correspondence should be addressed. E-mail: duane.froese@ualberta.ca

Transient Electronic Structure and Melting of a Charge Density Wave in $TbTe_3$

F. Schmitt,[1] P. S. Kirchmann,[2] U. Bovensiepen,[2]* R. G. Moore,[1,3] L. Rettig,[2] M. Krenz,[2] J.-H. Chu,[1] N. Ru,[1] L. Perfetti,[2] D. H. Lu,[3] M. Wolf,[2,4] I. R. Fisher,[1,5] Z.-X. Shen[1,3,5]*

Obtaining insight into microscopic cooperative effects is a fascinating topic in condensed matter research because, through self-coordination and collectivity, they can lead to instabilities with macroscopic impacts like phase transitions. We used femtosecond time- and angle-resolved photoelectron spectroscopy (trARPES) to optically pump and probe $TbTe_3$, an excellent model system with which to study these effects. We drove a transient charge density wave melting, excited collective vibrations in $TbTe_3$, and observed them through their time-, frequency-, and momentum-dependent influence on the electronic structure. We were able to identify the role of the observed collective vibration in the transition and to document the transition in real time. The information that we demonstrate as being accessible with trARPES will greatly enhance the understanding of all materials exhibiting collective phenomena.

In quantum matter, the emergence of order and collective modes associated with order are key areas to gain knowledge on electronic correlations and collective behavior. Charge density wave (CDW) materials are among the well-established examples that have had a major impact on our understanding of quantum many-body problems (*1*). Recent efforts on RTe_3 (where R = rare earth element) have identified it to be a model system to study Fermi surface (FS) nesting-driven CDW formation (*2*–*8*). The study of the electronic structure and FS of RTe_3 by means of angle-resolved photoemission spectroscopy (ARPES) has played a major role in developing our current knowledge (*2*, *3*, *5*).

However, conventional ARPES can only provide very limited information on the collective excitations that are important to understand the nature of the many-body state. Important many-body collective modes, such as the CDW amplitude mode (*9*), can only be detected, for example, by Raman spectroscopy (*10*), which cannot be directly linked to the CDW gap modulation (the defining signature of the mode) (*1*). Time- and angle-resolved photoemission spectroscopy (trARPES) offers the capability to simultaneously capture the single-particle (frequency domain) and collective (time domain) information, thus making it possible to directly probe the link between the collective modes and single-particle states that form the charge density wave.

We report on femtosecond time- and angle-resolved photoemission of $TbTe_3$, where we identify the amplitude mode of the CDW state through an inspection of time- and $\vec{k}$-dependent modulations of the single-particle spectral function $A(\omega,\vec{k},t)$ in the CDW state (here ω is the electron energy, $\vec{k}$ is the electron momentum, and t is the time between excitation and probing). For sufficiently high excitation densities, melting of the charge-ordered state is observed by closing of the CDW band gap through transient recovery of the ungapped electronic dispersion that otherwise can only be observed above the CDW transition temperature.

The details of the ARPES and trARPES experiments, as well as a short introduction to the CDW physics in $TbTe_3$, are presented in (*11*). First, we used ARPES to characterize the charge dynamics of the CDW system $TbTe_3$ in thermal equilibrium. $TbTe_3$ is a member of the RTe_3 family of compounds that exhibit a FS nesting-driven CDW formation (*4*, *7*, *8*). The diamond-shaped normal-state FS of RTe_3 can be described well by a tight binding (TB) model (*2*, *3*, *5*, *11*, *12*) (Fig. 1A). When the transition temperature T_c for $TbTe_3$ is 335 K (*8*), the CDW gap at 300 K is almost closed (Fig. 1A). At a T_c of 100 K, the gap extends further around the FS (Fig. 1A′). We analyzed the Brillouin zone (BZ) near the diamond tips through the region in which the CDW gap appears (indicated by red arcs in Fig. 1, A and A′) as a function of energy $E - E_F$ (where E is the electron energy and E_F is the Fermi energy). The intensity maps in Fig. 1, B and B′, show a p-like (*11*) Te band at ~0.5-eV binding energy that disperses weakly and a p-like (*11*) Te conduction band (CB) that disperses through E_F above T_c and exhibits the CDW gap well below (Fig. 1, C and C′).

We leveraged the marked progress in pump-probe spectroscopy at ultrafast time scales for trARPES (*13*–*20*). We pumped the CDW system optically with an infrared (1.5-eV) laser pulse of 50-fs width and subsequently probed it

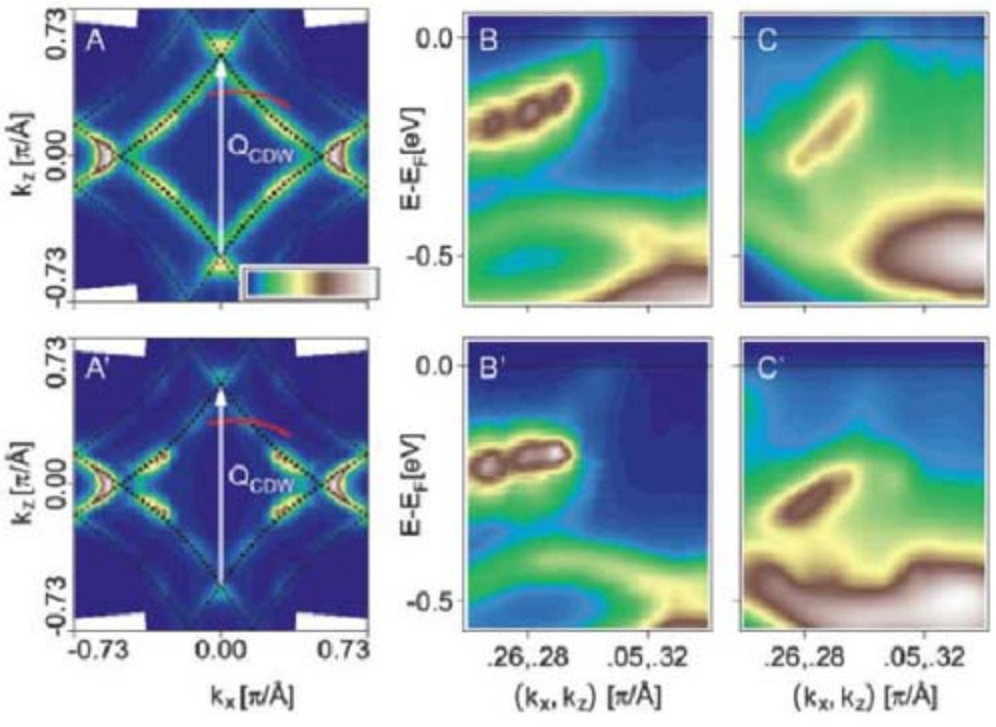

Fig. 1. Measurements taken at 300 K (upper panels) and 100 K (lower panels). Throughout the figures, the photoelectron intensity is encoded in a false-color scale [inset in (A)]. (**A** and **A′**) FS maps from ARPES of $TbTe_3$ at 300 K (A) and 100 K (A′). TB model (black dotted lines) and CDW nesting vector Q_{CDW} (white arrow) are indicated. The position of the cuts shown in (B) and (B′) and (C) and (C′) is marked in (A) and (A′) (red curve). (**B** and **B′**) Cuts extracted by interpolation from the data taken by conventional ARPES at a photon energy of 23 eV. (**C** and **C′**) Respective cuts done using the trARPES system at a probe photon energy of 6 eV. See (*11*) for experimental details.

[1]Department of Applied Physics, Via Pueblo Mall, Stanford University, Stanford, CA 94305, USA. [2]Fachbereich Physik, Freie Universität Berlin, Arnimallee 14, 14195 Berlin, Germany. [3]Stanford Synchrotron Radiation Laboratory, 2575 Sand Hill Road, Menlo Park, CA 94025, USA. [4]Fritz-Haber-Institut, Department of Physical Chemistry, Faradayweg 4-6, 14195 Berlin, Germany. [5]Geballe Laboratory for Advanced Materials, 476 Lomita Mall, Stanford University, Stanford, CA 94305, USA.

*To whom correspondence should be addressed. E-mail: uwe.bovensiepen@physik.fu-berlin.de (U.B.); zxshen@stanford.edu (Z.-X.S.)

after a variable delay by photoemitting electrons with an ultraviolet (6-eV) laser pulse of 90-fs width, resulting in a total experimental time resolution of 0.1 ps (*11*). Thus, the time-dependent evolution of the electron occupation (*13*–*15*) and the transient single-particle spectral function (*16*, *17*) was probed, and with that, the fingerprint of collective excitations (*21*) and transitions (*22*, *23*) were also probed. Figure 1, C and C′, shows the same cuts across the BZ as the ones seen in Fig. 1, B and B′, but the former were taken with our trARPES setup using 6-eV femtosecond laser pulses (but without optical excitation). The good agreement ensures that we probe the same BZ position in conventional ARPES as well as with trARPES in what follows.

The electron spectral intensity is shown (Fig. 2, A and B) at the FS well below T_{CDW} (where T_{CDW} is the CDW phase-transition temperature) as a function of pump-probe delay for two excitation densities F, representing incident pump fluence. Starting with $F = 0.3$ mJ/cm^2, Fig. 2C depicts spectra before, at, and after the optical excitation. Optical excitation populates states above E_F by hot electrons and has minor influence on the occupied states at 0 fs.

The continuous population of states above E_F occurs through electron-electron scattering within the experimental time resolution because, under the excitation conditions used, inelastic electron-electron scattering is known to be the dominant relaxation process within the first few 100 fs (*13*–*15*, *24*). This efficient scattering ensures that effects of coherent polarization are negligible and that we observe a transient electronic population. Within 400 fs, the electron distribution has thermalized, and the broadening of the Fermi-Dirac distribution indicates a significantly enhanced electron temperature T_{el}. In addition, the CB state shows a considerable shift of its spectral weight toward E_F after pumping, maximized at 400 fs (Fig. 2A). During this time, the excess energy resides in the electronic system. As T_{el} is enhanced with respect to the lattice temperature, we attribute these effects to the hot electron distribution (*16*, *17*). Electrons and lattice then equilibrate through electron-phonon scattering within ~1 ps. Beyond that time, the analysis of the transient binding energy and center of mass reveals an oscillatory behavior (Fig. 2E). Oscillatory changes of the CB state are well resolved to persist for several picoseconds, and we determined a frequency $\Omega_{CB} \approx 2.3$ THz. For the Te band, the changes are much weaker, and a Fourier transformation (*11*) yields a periodic contribution at $\Omega_{Te} \approx 3.6$ THz. Thus, the CB is clearly more susceptible to the excitation.

Photo-doping (electron-hole pair excitations generated by optical pumping) causes the electronic part of the CDW to decrease almost instantaneously. This starts a movement of the ionic part of the CDW because of the instantaneous change in electronic screening. Because the pump pulse duration is shorter than the oscillation period, a phase relation with respect to time zero is established (*25*). When the CDW amplitude is above its equilibrium value, the ions will be driven back by a steep rise in the lattice strain energy. When the CDW amplitude is below equilibrium, the steep loss of the energy gained from electron-phonon interaction will drive them back. The ions thus start to oscillate (*1*). This amplitude mode would then be excitable and directly observable with our technique. Based on the data presented so far and those to follow, we attribute the 2.3-THz oscillation to the amplitude mode. Our data directly reveal that the amplitude mode oscillation drives the CB and thus the CDW gap modulation.

We increased F to 2 mJ/cm^2 to show further evidence that is consistent with this assignment. Respective data are shown in Fig. 2B. Clearly, the impact of oscillations on the electronic states has increased. The spectral function of the CB state depends on the oscillation phase, as seen from spectra at 160 and 300 fs given in Fig. 2D. However, these spectra do not suggest a simple shift and broadening of the line, but rather a more complex transient state with this strong perturbation of the CDW state. Variations of the CB line are analyzed by center-of-mass determination, accounting for the transfer of spectral weight and avoiding assumptions of particular spectral profiles. The time evolution appears to be separated into two regimes: (i) Two pronounced initial oscillations display a different periodicity of 280 and 380 fs, respectively. (ii) After 1 ps, weak oscillations are found at 3.6 THz (Fig. 2F, black line).

Within the first ps, no phase correlation between the impact of modes on the CB and Te bands is encountered (Fig. 2F). After 1 ps, maxima in the CB oscillations tend to fall onto minima in the Te transient. The Te band oscillations are now well resolved, and we find that $\Omega_{Te} = 3.6$ THz (Fig. 2F). Recent Raman spectroscopy on RTe_3 shows that the Ω_{Te} mode cannot be assigned to one of the four Raman-active A_{1g} modes predicted for the undistorted lattice and that it probably results from the CDW (*26*). This oscillation is robustly present in all of our measurements, regardless of BZ position, temperature, or pump power. However, Lavagnini *et al.* (*26*) show the oscillation to decrease and eventually vanish with increasing temperature or pressure above T_{CDW} (*26*).

To strengthen the evidence leading to our previous assignment, we include fluence variations at

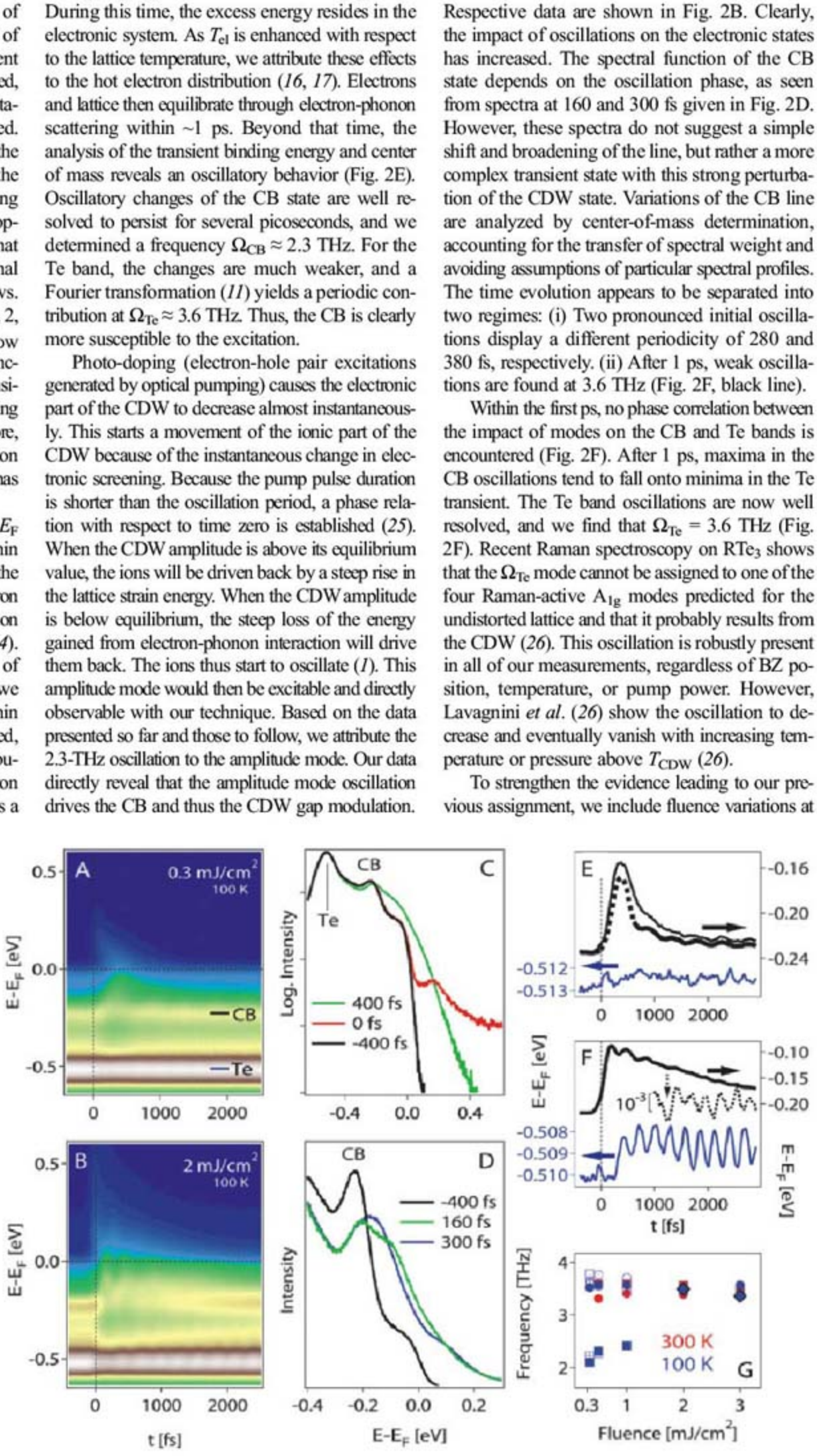

Fig. 2. (**A** and **B**) Photoelectron intensity as a function of energy and delay taken at k_F and 100 K. (A), (C), and (E) were measured at weak fluences (0.3 mJ/cm^2); (B), (D), and (F) were measured at strong fluences (2 mJ/cm^2). (**C** and **D**) Spectra from (A) and (B) at selected delays on a logarithmic (linear) intensity scale. (**E** and **F**) Time-dependent binding energy of the Te band (blue lines) and the CB (black lines) for weak and strong fluences, respectively. Analysis was done by fitting Lorentzians to the Te [blue lines in (E) and (F)] and CB [bold black line in (E)] states. Far from equilibrium at small delays and high fluences, the center of mass was determined for the CB [thin black line in (E), bold black line in (F)] [see (*11*) for method details]. The dotted black section in (E) indicates the region in which Lorentz fitting is not applicable (*11*), whereas the dotted black curve in (F) is a magnification of the center of mass (thick black curve). (**G**) The determined frequencies of the collective modes are summarized for 300 and 100 K as a function of incident pump fluence. Circles, Te band; squares, CB; solid symbols, energy variation; symbols with a center dot, amplitude; symbols with a center cross, linewidth variation. Diamonds indicate the frequency of the first moment from (F).

100 and 300 K. Figure 2G summarizes these results and displays the observed frequencies for both modes as a function of fluence. At 300 K, only the Te mode (3.6 THz) is observed, whereas at 100 K, two modes are identified for $F \leq 1$ mJ/cm^2. As for 300 K, thermodynamic fluctuations are expected to hamper the excitation of the amplitude mode, which again suggests that the 2.3-THz mode is the CDW amplitude mode. We also note that this frequency regime is typical of the CDW systems (*27*). Recent Raman (*26*) and time-dependent reflectivity (*28*) studies also come to the conclusion that the 2.3-THz mode is connected to the formation of the CDW.

The trARPES experiment provides an explicit link between the amplitude mode and CDW gap modulation via a momentum-dependent analysis: In a nesting-driven CDW, the electrons are most susceptible to scattering by the CDW phonon wave vector Q_{CDW} at the FS as the Lindhardt response function increases rapidly upon approaching k_F (here, k_F is the electron momentum at the Fermi energy) (*1*). We therefore expect that a modulation in the CDW amplitude and thus a modulation in CDW order parameter (i.e., the gap magnitude) influences the electronic band structure the most at or near k_F. Following this simple argument, this k-dependence should be present independent of perturbation strength. Figure 3A defines the BZ position where the data of Fig. 3, B to D, have been recorded. Figure 3, B to D, establishes a pronounced momentum-dependent excitation of the electronic structure. While away from the FS (below E_F), the CB energy does not vary; the largest change indeed occurs on the FS.

Our finding also has implications well beyond the specific materials we study. Conventional ARPES offers superior energy and angle resolution and is able to detect the effect of collective modes in the form of dispersion kinks or spectral dips (*29*). The interpretation of their assignment and the impact on the low-lying electronic structure, however, requires sophisticated theoretical and often model-dependent calculations. Current technology limits the accessible BZ region, energy, and angle resolution of trARPES. Nevertheless, trARPES is able to directly probe the transient interplay between collective modes and single-particle states in theory-independent ways and thus complements conventional ARPES.

We now turn to a momentum-specific analysis of the electronic excitation and the response of the lattice to reveal the process of the ultrafast melting of the CDW state. Figure 3, E to I, shows the momentum-dependent data for selected delays; the full data set is available as a supplemental movie online. At 0 fs, the CDW gap is preserved, and the dispersion of the CB represents a localized state as prior to pumping. However, in the vicinity of k_F (red dot in Fig. 3, E to I), an intensity increase at $E - E_F = 0.15$ eV coinciding with an unoccupied state as observed in Fig. 2C is encountered and represents instantaneous photo-doping of the system. At 100 fs (i.e., delayed with respect to the excitation), the gap is closed and the dispersion of the band resembles the quasi-free electron dispersion known from spectra taken at 300 K (Fig. 1). We term this excitation regime "strongly perturbative," as the excitation results in an ultrafast melting of the charge-ordered state. Notably, the conduction electrons recover their wavelike nature, as they are still strongly k-dependent, despite the intense excitation and resulting intense scattering.

Thus, we have identified a delay in the ultrafast CDW melting with respect to the photo-doping. This is related to the mechanism of CDW formation. Because of coupling between lattice vibrations (phonons) to the electrons, electronic energy is gained if a phonon with a wave vector Q, which nests two regions of the FS, freezes in the crystal, leading to a charge density modulation. Upon cooling, this energy gain becomes larger than the energy loss from the lattice deformation, and the system undergoes a phase transition into the CDW state. Because formation of the CDW requires freezing of a phonon (i.e., nuclear motion), the inverse process of melting cannot proceed faster than the respective motion. Considering that photo-doping modifies the screened ion potential such that it sustains a delocalized state, the ion cores still have to propagate to the potential minima in the presence of screening carriers, which explains the observed delay in the CDW melting. This result provides a direct and vivid demonstration of the electron-phonon interaction being the origin of the CDW formation.

This result also raises the question of whether the transition is complete after 100 fs. We return to the strong perturbation case with $F = 2$ mJ/cm^2 (Fig. 2 B, D, and F), where we have indicated earlier that the physics can be divided into two regimes according to the time delays. Between 1 and 3 ps, when the melting of the CDW is complete and the amplitude mode no longer exists, only the 3.6-THz Te phonon oscillation is observed. This is most clearly seen in the black dotted curve in Fig. 2F, which has the same frequency. Below 1 ps, the situation is complex. Whereas the gap is closed at 100 fs, a transient "equilibrium" outside the CDW state has not been established yet. The ions cannot stop once excited and will continue to oscillate as previously discussed. Thus, we expect the system to oscillate between a localized CDW state and a delocalized molten CDW state en route to the transient equilibrium beyond 1 ps. The mode associated with this oscillation is related to the amplitude mode but is not quite the same.

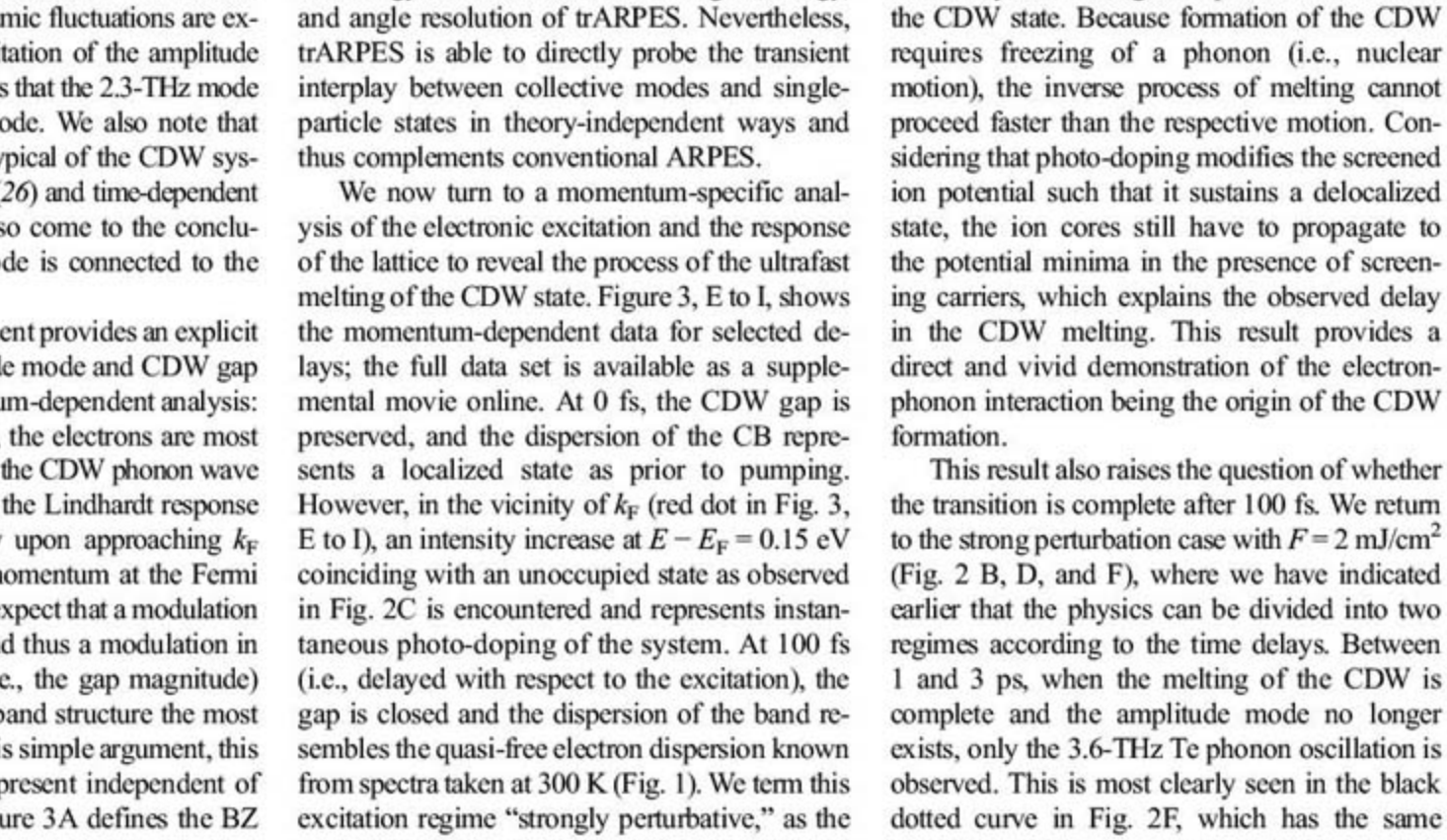

Fig. 3. (**A**) Detail of the FS plot in Fig. 1A′ with indicated positions (white circles) of time-resolved data shown in (**B**) to (**D**) for fixed k as a function of time delay. Indicated cut position (red line) of photoelectron intensity is shown as a function of energy, and position [(**E**) to (**I**)] for a momentum scan is shown as a function of time delays. All data were collected at 100 K and $F = 2$ mJ/cm^2. k_F is marked in (E) to (I) (red dot). Error bars indicate the distance to the neighboring sample points, which is a good estimate for the error of k_F.

References and Notes

1. G. Grüner, *Density Waves in Solids*, vol. 89 of *Frontiers in Physics* (Addison-Wesley, Reading, MA, 1994).
2. V. Brouet *et al.*, *Phys. Rev. Lett.* **93**, 126405 (2004).
3. V. Brouet *et al.*, *Phys. Rev. B* **77**, 235104 (2008).
4. E. DiMasi, M. C. Aronson, J. F. Mansfield, B. Foran, S. Lee, *Phys. Rev. B* **52**, 14516 (1995).
5. G.-H. Gweon *et al.*, *Phys. Rev. Lett.* **81**, 886 (1998).
6. A. Fang, N. Ru, I. R. Fisher, A. Kapitulnik, *Phys. Rev. Lett.* **99**, 046401 (2007).
7. C. Malliakas, S. Billinge, H. Kim, M. Kanatzidis, *J. Am. Chem. Soc.* **127**, 6510 (2005).
8. N. Ru *et al.*, *Phys. Rev. B* **77**, 035114 (2008).
9. P. B. Littlewood, C. M. Varma, *Phys. Rev. B* **26**, 4883 (1982).
10. R. Sooryakumar, M. V. Klein, *Phys. Rev. B* **23**, 3213 (1981).
11. Materials and methods are available as supporting material on *Science* Online.
12. J. Laverock *et al.*, *Phys. Rev. B* **71**, 085114 (2005).
13. W. S. Fann, R. Storz, H. W. K. Tom, J. Bokor, *Phys. Rev. B* **46**, 13592 (1992).
14. M. Lisowski *et al.*, *Appl. Phys. A* **78**, 165 (2004).
15. U. Bovensiepen, *J. Phys. Condens. Matter* **19**, 083201 (2007).
16. L. Perfetti *et al.*, *Phys. Rev. Lett.* **97**, 067402 (2006).
17. P. A. Loukakos *et al.*, *Phys. Rev. Lett.* **98**, 097401 (2007).
18. D. M. Fritz *et al.*, *Science* **315**, 633 (2007).
19. P. Baum, D.-S. Yang, A. H. Zewail, *Science* **318**, 788 (2007).
20. C. v. Korff Schmising *et al.*, *Phys. Rev. Lett.* **98**, 257601 (2007).
21. J. Demsar, K. Biljaković, D. Mihailovic, *Phys. Rev. Lett.* **83**, 800 (1999).
22. A. Cavalleri, T. Dekorsy, H. H. W. Chong, J. C. Kieffer, R. W. Schoenlein, *Phys. Rev. B* **70**, 161102 (2004).
23. M. Chollet *et al.*, *Science* **307**, 86 (2005).
24. B. Rethfeld, A. Kaiser, M. Vicanek, G. Simon, *Phys. Rev. B* **65**, 214303 (2002).
25. T. Dekorsy, G. C. Cho, H. Kurz, *Coherent Phonons in Condensed Media*, vol. 76 of *Springer Topics in Applied Physics* (Springer, Berlin, 2000).
26. M. Lavagnini *et al.*, preprint available at http://arxiv.org/abs/0806.1455v1 (2008).
27. G. Travaglini, L. Mörke, P. Wachter, *Solid State Commun.* **45**, 289 (1983).
28. R. V. Yusupov *et al.*, preprint available at http://arxiv.org/abs/0807.1022v1 (2008).
29. A. Damascelli, Z. Hussain, Z.-X. Shen, *Rev. Mod. Phys.* **75**, 473 (2003).

30. We thank L. DeGiorgi *et al.* and D. Mihailovic *et al.* for fruitful discussions. We acknowledge funding from the Max-Planck-Gesellschaft through the International Max Planck Research School and by the Deutsche Forschungsgemeinschaft through BO 1823/2, Sfb 450, and the Heisenberg program. This work is supported by the U.S. Department of Energy Office of Basic Energy Science, Division of Materials Science and Engineering.

Supporting Online Material

www.sciencemag.org/cgi/content/full/1160778/DC1
Materials and Methods
SOM Text
Figs. S1 to S5
References
Movie S1

21 May 2008; accepted 1 August 2008
Published online 14 August 2008;
10.1126/science.1160778
Include this information when citing this paper.

Coupled Superconducting and Magnetic Order in $CeCoIn_5$

M. Kenzelmann,[1,2] Th. Strässle,[3] C. Niedermayer,[3] M. Sigrist,[4] B. Padmanabhan,[3] M. Zolliker,[1] A. D. Bianchi,[5] R. Movshovich,[6] E. D. Bauer,[6] J. L. Sarrao,[6] J. D. Thompson[6]

Strong magnetic fluctuations can provide a coupling mechanism for electrons that leads to unconventional superconductivity. Magnetic order and superconductivity have been found to coexist in a number of magnetically mediated superconductors, but these order parameters generally compete. We report that close to the upper critical field, $CeCoIn_5$ adopts a multicomponent ground state that simultaneously carries cooperating magnetic and superconducting orders. Suppressing superconductivity in a first-order transition at the upper critical field leads to the simultaneous collapse of the magnetic order, showing that superconductivity is necessary for the magnetic order. A symmetry analysis of the coupling between the magnetic order and the superconducting gap function suggests a form of superconductivity that is associated with a nonvanishing momentum.

$CeCoIn_5$ is a clean ambient-pressure d-wave superconductor (*1*) and crystallizes in a tetragonal structure (Fig. 1). Because of its proximity to a magnetic quantum critical point, it features strong antiferromagnetic correlations that result in an enhancement of the effective electronic mass and heavy-fermion behavior (*2*). However, $CeCoIn_5$ undergoes a transition to superconductivity before magnetic order can be established (*2*, *3*). The superconducting gap function has probably a d_{x2-y2} symmetry (*4*–*7*), and it is generally believed that superconductivity in $CeCoIn_5$ is mediated by magnetic fluctuations. The Fermi surface is strongly two-dimensional (*8*, *9*), and superconductivity in an applied field is Pauli-limited (*10*), that is, it is destroyed by a coupling of external magnetic fields to the spins of the Cooper pairs and not by orbital depairing. $CeCoIn_5$ features an unusual field-temperature (*H-T*) phase diagram (*11*, *12*): below $T_0 = 0.31$ $T_c = 1.1$ K (T_c, critical temperature), the transition from the normal to the superconducting state is first-order (*10*, *11*). Further, there is evidence for a second superconducting phase, the "**Q** phase," which exists only when $T <$ 0.3 K and with high fields close to the upper critical field (*11*, *13*, *14*). It has been suggested (*11*, *15*) that this high-field phase may represent a superconducting phase that was proposed by Fulde, Ferrell, Larkin, and Ovchinnikov (FFLO) and that carries a finite momentum as a result of the Zeeman splitting of the electron bands (*16*, *17*).

A rich interplay between magnetic order and superconductivity is characteristic of heavy-fermion superconductors, with either magnetic order preceding the onset of superconductivity or superconductivity occurring in the vicinity of a quantum critical point (*18*, *19*). Superconductivity in $CeCoIn_5$ is special in that it occurs close to a magnetic quantum critical point, but so far there has been no direct evidence of long-range magnetic order anywhere in the *H-T* phase diagram (*2*). However, there is microscopic evidence from nuclear magnetic resonance (NMR) measurements for field-induced magnetism for high fields ($\sim H = 11$ T) in the tetragonal plane and for temperatures below which the $H_{c2}(T)$ phase boundary becomes first-order (H_{c2}, upper critical field) (*20*). The NMR results were interpreted as evidence that the **Q** phase is a phase in which superconductivity and magnetic order coexist, but the character of the superconducting state could not be ascertained.

We used high-field neutron diffraction to directly search for magnetic Bragg peaks within the **Q** phase. The measurements were done at low temperatures and the field was applied along the crystallographic [1 –1 0] direction in the tetragonal basal plane. For this field direction, the upper critical field in the zero-temperature limit is $H_{c2}(0) =$ 11.4 T. The neutron diffraction data for wave-vectors along the (h, h, 0.5) reciprocal direction is shown in Fig. 2. Here, h represents the wave-vector transfer along either the [100] or the [010] direction in reciprocal lattice units (r.l.u.). When $10.5\ \mathrm{T} < H < 11.4$ T, neutron scattering provides clear evidence of Bragg peaks that arise from a magnetic structure that is modulated with the ordering wave-vector $\mathbf{Q} = (q, q, 0.5)$ (*21*) and that are present at neither higher nor lower fields outside of the **Q** phase (hence its name). Here, q represents the wave-vector for which the magnetic Bragg peak has most intensity and indicates the modulation of the magnetic structure along the a and b axes. The width of the peaks is resolution-limited, so the magnetic order extends over a length scale $\xi > 60$ nm. This is much larger than the diameter of vortex cores, which is of the order of the coherence length $\xi_0 \sim 10$ nm (*5*), and so magnetic order is not limited to the vortex cores.

The field and temperature dependence of the peak intensity of the $\mathbf{Q} = (q, q, 0.5)$ magnetic Bragg peak obtained from a fit to a Gaussian line shape is shown in Fig. 2. The magnetic order at $T = 60$ mK has a gradual onset with increasing field and collapses at the superconducting phase boundary H_{c2} in a first-order transition (Fig. 3A). The intensity of the magnetic Bragg peak can also be suppressed by increasing the temperature (Fig.

[1]Laboratory for Developments and Methods, Paul Scherrer Institute, CH-5232 Villigen, Switzerland. [2]Laboratory for Solid State Physics, Eidgenössische Technische Hochschule (ETH) Zurich, CH-8093 Zurich, Switzerland. [3]Laboratory for Neutron Scattering, ETH Zurich, and Paul Scherrer Institute, CH-5232 Villigen, Switzerland. [4]Institut für Theoretische Physik, ETH Zurich, CH-8093 Zurich, Switzerland. [5]Département de Physique and Regroupement Québécois sur les Matériaux de Pointe, Université de Montréal, Montréal, Quebec H3C 3J7, Canada. [6]Condensed Matter and Thermal Physics, Los Alamos National Laboratory, Los Alamos, NM 87545, USA.

3B); the signal disappears at the same temperature at which specific heat measurements show evidence of a second-order phase transition (*11*). The neutron data suggest a transition that is second-order in temperature but first-order in field. The incommensuration q of the Bragg peak position is not field-dependent, as can be seen in the inset of Fig. 3A. The *H-T* phase diagram (Fig. 1) shows that magnetic order exists only in the superconducting **Q** phase and not in the normal phase, which demonstrates that superconductivity is essential for magnetic order. Our results provide evidence that the ground state in this field and temperature range in the vicinity of $H_{c2}(0)$ has a multicomponent order parameter that directly couples superconductivity and magnetism. This type of order is at least partly due to strong antiferromagnetic fluctuations, arising from the proximity to a magnetic quantum critical point in $CeCoIn_5$.

Our experiment shows that the magnetic structure is a transverse amplitude-modulated incommensurate spin-density wave whose magnetic moments are orientated along the tetragonal c axis, modulated with the incommensurate wave-vector $(q, q, 0.5)$ perpendicular to the magnetic field. Neighboring Ce^{3+} magnetic moments that are separated by a unit cell lattice translation along the c axis are antiparallel (Fig. 1). The amplitude of the magnetic moment (m) at $T = 60$ mK and $H = 11$ T of $m = 0.15(5)$ Bohr magnetons (μ_B) is considerably smaller than expected for the Ce^{3+} free ion, possibly due to the Kondo effect. The direction of the ordered magnetic moment is consistent with magnetic susceptibility measurements (*1*) that identify the c axis as the easy axis, and it is also consistent with zero-field inelastic neutron measurements in which strong antiferromagnetic fluctuations have been observed that are polarized along the c axis (*22*).

The magnetic structure that satisfies NMR data (*20*) was described by an ordering wave-vector $\mathbf{Q} = (q, 0.5, 0.5)$ with unspecified q and the ordered magnetic moment along the applied field that was along the [100] direction. Our neutron measurements of field along the [1–10] direction reveal a magnetic order for which both the ordering wave-vector $\mathbf{Q} = (q, q, 0.5)$ and the ordered moments are perpendicular to the applied magnetic field, in contrast to the NMR data. This difference suggests that the direction of the incommensurate modulation **Q** depends on the field direction, and that the order wave vector can be tuned with a rotation of the magnetic field in the basal plane. Finally, the absence of magnetic Bragg peaks at $H = 11$ T when $T > 0.3$ K confirms the interpretation of the NMR measurements (*20*) that the fluctuations for $0.3\text{ K} < T < T_0$ are short-ranged and possibly only present inside the vortex cores.

The observation that magnetism exists only in the presence of superconductivity is in stark contrast to other materials in which long-range magnetic order and superconductivity merely coexist for a small magnetic field or pressure range because of their different origins (*18*, *19*). Because no magnetic order is observed in $CeCoIn_5$ above the upper critical field H_{c2}, the relation between magnetic order and superconductivity is fundamentally different and cannot be seen as a competition. Instead, it appears that $CeCoIn_5$ in fields greater than H_{c2} gives rise to strong antiferromagnetic fluctuations that condense into magnetic order with decreasing magnetic field only through the opening of an electronic gap and restructuring of the Fermi surface at the superconducting phase boundary. This means that the second-order magnetic quantum phase transition is inaccessible because, in its proximity, there is no energy scale associated with the antiferromagnetic fluctuations, and the superconducting energy gap becomes the dominant energy scale and determines the magnetic ground-state properties.

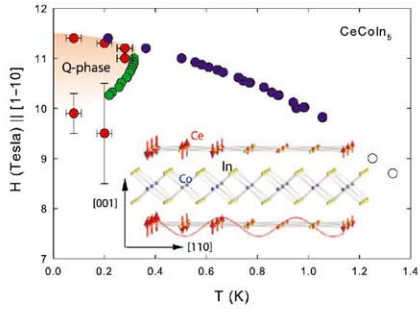

Fig. 1. *H-T* phase diagram of $CeCoIn_5$ with the magnetically ordered phase indicated by the red shaded area. The blue and open circles indicate a first- and second-order transition measured by specific heat (*11*), respectively, separating the superconducting from the normal phase. The green circles indicate a second-order phase transition inside the superconducting phase (*11*), and the red circles indicate the onset of magnetic order as measured in our experiment, showing that the magnetic order only exists in the **Q** phase. **(Inset)** Magnetic structure of $CeCoIn_5$ at $T = 60$ mK and $H = 11$ T. The red arrows show the direction of the static magnetic moments located on Ce^{3+}, and the yellow and blue circles indicate the position of the In and Co ions. The depicted structure does not include a possible uniform magnetization along the magnetic field direction. The solid red line indicates the amplitude of the Ce^{3+} magnetic moment along the c axis, projected on the (h, h, l) plane.

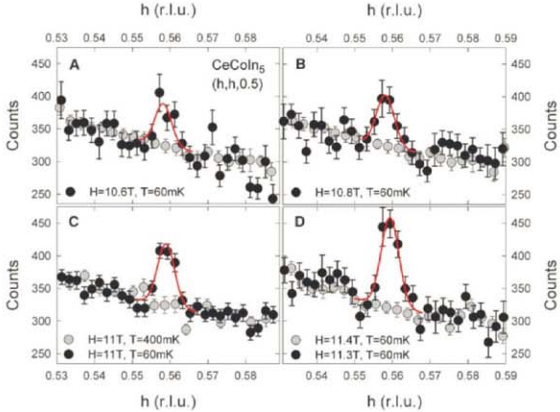

Fig. 2. The solid circles represent the neutron-scattering intensity at $T = 60$ mK for wave vectors $(h, h, 0.5)$ as a function of h for different fields as observed in the center channel of the position-sensitive detector (psd), showing the presence of a magnetic neutron diffraction peak at $(1 - q, 1 - q, 0.5)$ with $q = 0.44$ for **(A)** $H = 10.6$ T, **(B)** $H = 10.8$ T, **(C)** $H = 11$ T, and **(D)** $H = 11.3$ T. The gray circles in (A) and (B) represent the best estimate of the background, whereas they represent the neutron scattering intensity in (C) at $H = 11$ T and $T = 400$ mK and in (D) at $H = 11.4$ T and $T = 60$ mK. The solid red lines are fits of a Gaussian function to the magnetic scattering.

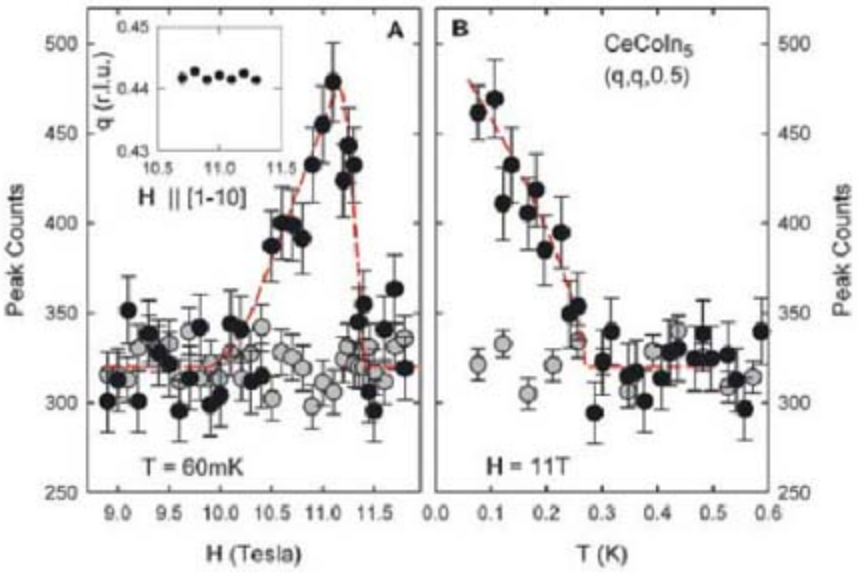

Fig. 3. Neutron-scattering intensity at (*q*, *q*, 0.5), (**A**) as a function of field at $T = 60$ mK and (**B**) as a function of temperature at $H = 11$ T. The gray circles represent the background scattering taken from the two nearest to the center channels of the psd. The dashed red line in (A) is a guide to the eye, whereas the dashed line in (B) describes the background and the onset of the magnetic order in a second-order phase transition with $\beta = 0.365$ fixed to the critical exponent of the three-dimensional Heisenberg universality class. The inset shows that the *q* is field-independent.

The intimate link between superconductivity and magnetic order in $CeCoIn_5$ suggests the presence of a specific coupling between these order parameters (*23*). The multicomponent magneto-superconducting phase can be reached via two second-order phase transitions through a suitable path in the *H-T* phase diagram, which justifies the construction of a phenomenological Landau coupling theory. If one assumes that the superconducting gap at zero field Δ_d has d_{x2-y2} symmetry, the possible coupling terms for magnetic fields in the basal plane that preserve time-reversal symmetry and conserves momentum can be written as $V_1 = \Delta^*_d M_q (H_x\Delta^{(5)}_{y,-q} + H_y\Delta^{(5)}_{x,-q}) + c.c.$, $V_2 = \Delta^*_d M_q (H_xD_x - H_yD_y)\Delta^{(2)}_{-q} + c.c.$, and $V_3 = \Delta^*_d M_q (H_xD_y - H_yD_x)\Delta^{(3)}_{-q} + c.c.$ Here, $(\Delta^{(5)}_{x,-q}, \Delta^{(5)}_{y,-q})$ belongs to the two-component even-parity Γ^+_5 state, $\Delta^{(2)}_{-q}$ and $\Delta^{(3)}_{-q}$ are the Γ^-_2 and Γ^-_3 odd-parity states (*24*), *c.c.* stands for the complex conjugate of the preceding term, and M_q is the magnetic-order parameter. These additional superconducting order parameters include a finite momentum $-q$. (D_x, D_y) is the gauge invariant gradient. Introducing the magnetic field allows one to couple M_q in linear order to preserve time-reversal symmetry. These combinations allow for a second-order phase transition within the superconducting phase and a first-order transition to the nonmagnetic normal state. For the coupling term V_2, no magnetic structure is induced for fields $\mathbf{H} \parallel [100]$. Given the weak dependence of the **Q** phase on the magnetic field orientation in the basal plane, our measurements suggest the presence of a V_1 or V_3 coupling term, inducing the finite-momentum even-parity Γ^+_5 state or the odd-parity Γ^-_3 state.

This Landau theory shows that incommensurate magnetic order induces a superconducting gap function that carries a finite momentum—the first experimental evidence of a superconducting condensate that carries a momentum. However, we show that this state may not arise purely from Pauli paramagnetic effects and the formation of a new pairing state between exchange-split parts of the Fermi surface, a state commonly known as the FFLO state (*16*, *17*). In the FFLO state, the pairing state carries a momentum of the Cooper pair that depends on the magnetic field via $|q| = 2\mu_B H/\hbar v_F$, where v_F is the Fermi velocity. However, the inset of Fig. 3A shows that $|q|$ is field-independent in $CeCoIn_5$, at odds with this prediction, which indicates that an additional superconducting pairing channel with finite momentum is induced in conjunction with the cooperative appearance of magnetic order.

A superconducting order that carries momentum illustrates the wealth of quantum phases that can exist in solid matter. The important microscopic role of magnetic fluctuations in the formation of Cooper pairs in $CeCoIn_5$ is self-evident because superconductivity emerges at $H_{c2}(0)$ simultaneously with ordered magnetism.

References and Notes

1. C. Petrovic *et al.*, *J. Phys. Condens. Matter* **13**, L337 (2001).
2. A. D. Bianchi, R. Movshovich, I. Vekhter, P. G. Pagliuso, J. L. Sarrao, *Phys. Rev. Lett.* **91**, 257001 (2003).
3. J. Paglione *et al.*, *Phys. Rev. Lett.* **91**, 246405 (2003).
4. K. Izawa *et al.*, *Phys. Rev. Lett.* **87**, 057002 (2001).
5. N. J. Curro *et al.*, *Phys. Rev. B* **64**, 180514 (2001).
6. R. Movshovich *et al.*, *Phys. Rev. Lett.* **86**, 5152 (2001).
7. A. Vorontsov, I. Vekhter, *Phys. Rev. Lett.* **96**, 237001 (2006).
8. D. Hall *et al.*, *Phys. Rev. B* **64**, 212508 (2001).
9. R. Settai *et al.*, *J. Phys. Condens. Matter* **13**, L627 (2001).
10. A. D. Bianchi *et al.*, *Phys. Rev. Lett.* **89**, 137002 (2002).
11. A. D. Bianchi, R. Movshovich, C. Capan, P. G. Pagliuso, J. L. Sarrao, *Phys. Rev. Lett.* **91**, 187004 (2003).
12. A. D. Bianchi *et al.*, *Science* **319**, 177 (2008).
13. K. Kakuyanagi *et al.*, *Phys. Rev.* **94**, 047602 (2005).
14. T. Watanabe *et al.*, *Phys. Rev. B* **70**, 020506 (2004).
15. H. A. Radovan *et al.*, *Nature* **425**, 51 (2003).
16. P. Fulde, R. A. Ferrell, *Phys. Rev.* **135**, A550 (1964).
17. A. I. Larkin, Y. N. Ovchinnikov, *Sov. Phys. JETP* **20**, 762 (1965).
18. P. Monthoux, D. Pines, G. G. Lonzarich, *Nature* **450**, 1177 (2007).
19. J. Flouquet *et al.*, *C. R. Phys.* **7**, 22 (2006).
20. B. L. Young *et al.*, *Phys. Rev. Lett.* **98**, 036402 (2007).
21. Materials and methods are available as supporting material on *Science* Online.
22. C. Stock, C. Broholm, J. Hudis, H. J. Kang, C. Petrovic, *Phys. Rev. Lett.* **100**, 087001 (2008).
23. A. Aperis, G. Varelogiannis, P. B. Littlewood, B. D. Simons, *J. Phys. Cond. Mat.*, in press; preprint available at http://arxiv.org/PS_cache/arxiv/pdf/0804/0804.2460v1.pdf.
24. M. Sigrist, K. Ueda, *Rev. Mod. Phys.* **63**, 239 (1991).

25. Work at ETH was supported by the Swiss National Science Foundation under contract PP002-102831. This work is based on experiments performed at the Swiss spallation neutron source SINQ, Paul Scherrer Institute, Villigen, Switzerland, and was supported by the Swiss National Center of Competence in Research program Materials with Novel Electronic Properties. Work at Los Alamos was performed under the auspices of the U.S. Department of Energy and supported in part by the Los Alamos Laboratory Directed Research and Development program. A.D.B. received support from the Natural Sciences and Engineering Research Council of Canada (Canada), Fonds Québécois de la Recherche sur la Nature et les Technologies (Québec), and the Canada Research Chair Foundation.

Supporting Online Material

www.sciencemag.org/cgi/content/full/1161818/DC1
Materials and Methods
References

16 June 2008; accepted 7 August 2008
Published online 21 August 2008;
10.1126/science.1161818
Include this information when citing this paper.

Shape Changes of Supported Rh Nanoparticles During Oxidation and Reduction Cycles

P. Nolte,[1] A. Stierle,[1]* N. Y. Jin-Phillipp,[1] N. Kasper,[1] T. U. Schulli,[2] H. Dosch[1]

The microscopic insight into how and why catalytically active nanoparticles change their shape during oxidation and reduction reactions is a pivotal challenge in the fundamental understanding of heterogeneous catalysis. We report an oxygen-induced shape transformation of rhodium nanoparticles on magnesium oxide (001) substrates that is lifted upon carbon monoxide exposure at 600 kelvin. A Wulff analysis of high-resolution in situ x-ray diffraction, combined with transmission electron microscopy, shows that this phenomenon is driven by the formation of a oxygen–rhodium–oxygen surface oxide at the rhodium nanofacets. This experimental access into the behavior of such nanoparticles during a catalytic cycle is useful for the development of improved heterogeneous catalysts.

Many industrial chemicals and fuels are synthesized with the use of heterogeneous, solid-phase catalysts that often contain metals in the form of nanoparticles (NPs). The direct study of these catalysts is challenging, and model catalysts such as single crys-

tals and vicinal surfaces have been extensively investigated and have provided important insights (*1*–*3*). The emerging challenge for fundamental research is to provide a detailed microscopic understanding of the different physical and chemical processes that take place at NPs during catalytic reactions. Although there is a consensus that NPs should exhibit enhanced catalytic activity because (i) they posses an increased number of undercoordinated atoms and (ii) different low-index facets coexist [which should facilitate mass transport and thereby lift kinetic barriers known from single crystal surfaces (*4*)], it is still an open question as to whether the metallic or the oxidized state of the particle is the catalytically more active phase [Langmuir-Hinshelwood versus Mars–van Krevelen mechanism (*5*, *6*)]. During catalytic cycling experiments, NPs undergo reversible size changes that are associated with cyclic shape changes, material redispersion, and sintering (*7*, *8*).

Among the many catalytically active metals, the 4d transition metals [Ru, Rh, Pd, and Ag (*1*)] are finding increased use in organic reactions, the synthesis of biologically active compounds under sufficiently mild conditions, and the treatment of contaminated water. Rh is a well-known catalyst for hydrocarbon and CO oxidation, as well as for NO_x reduction in three-way car catalysts (*9*). Recent experimental and theoretical studies of 4d transition metal single-crystal surfaces carried out near atmospheric pressures suggest that their catalytic activities are related to an ultrathin metal oxide film on the surface (*5*, *10*–*12*). In the case of Rh, a hexagonal O–Rh–O trilayer structure forms basically independently of the surface orientation whenever the oxygen chemical potential is near that of the bulk oxide (*11*, *13*, *14*). To date, it is not clear if such surface oxides do also form on the different facets of NPs and, if so, whether they are relevant in industrial catalysis.

In the past, transmission electron microscopy (TEM) has shown that metal NPs undergo shape changes as a function of the gas composition (*15*–*17*). Scanning tunneling microscopy experiments on the top facet of flat NPs have illustrated oxygen-induced superstructures at the edges of different facets (*18*), and recently, the shape of unsupported Pd and Rh NPs was investigated by density functional theory as a function of the oxygen chemical potential using the Wulff construction (*19*). The results of these experiments prove that surface oxides stabilize the low-index (100), (110), and (111) facets at chemical potentials near that for bulk oxide formation, which results in an overall rounding of the NPs.

To upgrade our microscopic understanding of the catalytic activity of NPs, the interplay between the shape and size change of the NPs and the oxidation/reduction process must be established. Here, we report an in situ high-resolution x-ray diffraction (XRD) study of epitaxial Rh NPs on MgO(001) during oxidizing and reduction reactions, which uncovers a reversible facet rearrangement of the NP in direct relation to the formation of oxygen-induced superstructures. From a quantitative analysis of the extended reciprocal-space maps that have been recorded from the Rh nanofacets at elevated temperatures and under varying gas atmospheres, we can access the average NP shape and size with atomic resolution and obtain robust atomic insights into the structure of the surface oxide forming on the facets.

The XRD experiments were performed at beamline BM32 of the European Synchrotron Radiation Facility and at the Max Planck beamline of the Angström Quelle Karlsruhe. The photon energies were 11.04 and 10.5 keV, respectively. The in situ x-ray analysis was complemented by high-resolution TEM (HRTEM) performed on a JEOL 1250 atomic-resolution microscope that is operated at 1250 kV (*20*).

In the first experimental setup, we deposited the Rh NPs in situ at a substrate temperature of 670 K in the BM32 ultrahigh vacuum (UHV) surface XRD chamber, after cleaning the MgO substrates by sputtering and annealing under oxygen atmosphere (*20*). After the growth and an initial oxidation/reduction cycle, the sample was annealed at 970 K to achieve the equilibrium shape of the NPs. Wide-angle diffraction reciprocal-space mapping and grazing-incidence small-angle scattering (GISAXS) were performed simultaneously (*20*). In the second experimental setup, Rh was deposited on MgO in a laboratory UHV chamber, annealed at 870 K, and the sample was subsequently transferred into a portable UHV XRD chamber, which was shipped to the synchrotron radiation facility while maintaining UHV conditions. The epitaxial relation between the Rh NPs and the MgO substrate was determined from reciprocal-space scans in high-symmetry directions. We find that the Rh NPs grow in a cube-on-cube epitaxy on MgO(001), with an in-plane angular distribution of 1.7°. After the annealing, the average lattice constant of the particles is equal to the bulk value for Rh (a_{fcc} = 0.380 nm, where fcc is face-centered cubic), resulting in a misfit of 9% to the MgO substrate. The particles exhibit a typical size distribution of ~30%.

Figure 1A is a schematic view of the NP model together with the four shape parameters N_P, N_T, N_B, and N_E, which can be interrogated by XRD (*21*). N_P describes the particle diameter given by $a_{fcc}/\sqrt{2}\cdot N_P$; N_T and N_B describe the number of atomic layers involved in the top and bottom part of the particle, respectively. The parameter N_E gives the number of layers removed from the particle corners to form the side [100] type facets. The extended reciprocal-space maps contain detailed information about the shape and size of nanoscale objects (*22*). This is illustrated in Fig. 1B, which shows an experimental wide-range reciprocal-space map of the (110) plane taken at 600 K. The (111) Bragg reflection in the center of the map is interconnected with the neighboring Bragg reflections by broad intensity ridges along the [001], [–1,1,1], and [1,–1,1] directions that emanate perpendicularly from the associated facets. The observation and quantitative analysis of these so called "crystal truncation rods" (*23*) in four symmetry-equivalent directions gives direct evidence for the truncated pyramidal shape of the nano-objects under investigation.

To obtain detailed information on the size and shape of the NPs, high-resolution reciprocal-space maps have been recorded from $(H,K) = (-0.5,0.5)$ to $(0.5,-0.5)$ and from $L = 0.6$ to 0.84, as indicated by the white box in Fig. 1B (here, H, K, and L represent the Miller indices of the bulk reciprocal lattice). In Fig. 2A (top) a high-resolution map of

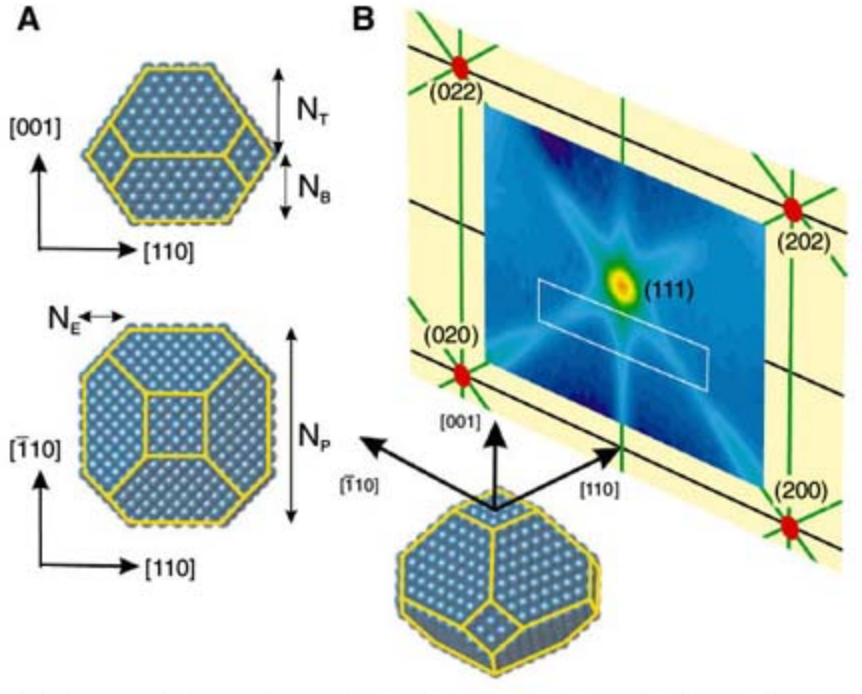

Fig. 1. (**A**) Schematic representation of the particle shape for fcc-based NPs. The lateral particle size is characterized by $a_{fcc}/\sqrt{2}\cdot N_P$, its height by $a_{fcc}/2\cdot(N_T + N_B)$, and the missing edge atoms by N_E. For a Wulff shaped particle (without substrate), $N_T = N_B$ and $N_E = N_P - N_T$ (*25*). (**B**) (110) plane reciprocal-space map of clean Rh NPs on MgO(001) with an average lateral size of 8 nm. Fcc bulk coordinates are used throughout the text, if not otherwise indicated. The white box indicates the area for high-resolution scans used for the quantitative analysis. The reciprocal-space area close above the Bragg peaks cannot be used, because it contains, on the (111) type rods, signal from internal twinning of the particles at ($^4/_3$,$^2/_3$,$^4/_3$), ($^2/_3$,$^4/_3$,$^4/_3$), and equivalent positions (Fig. 4).

[1]Max-Planck-Institut für Metallforschung, Heisenbergstrasse 3, D-70569 Stuttgart, Germany. [2]Institut Nanosciences et Cryogénie/Service de Physique des Matériaux et des Microstructures, Commissariat à l'Energie Atomique, Grenoble, 38054 Grenoble Cedex 09, France.

*To whom correspondence should be addressed. E-mail: stierle@mf.mpg.de

the clean particles is plotted, as observed at 600 K under UHV conditions. The data can be understood in a straightforward way within a kinematical diffraction theory that discloses NPs with truncated octahedral shape (*20*). Figure 2A (middle) shows the best intensity fits associated with the average particle shape presented in Fig. 2A (bottom).

A straightforward understanding of the shape of a NP is provided by the Wulff construction, which is based on the rule $\frac{\gamma_i}{h_i}$ = constant (here, γ_i is the surface energy of facet plane i with distance h_i from the center of the unsupported particle) (*24*). From the fit to the data, we obtain the following parameter values: $N_P = 31 \pm 1$, $N_T = 20 \pm 1$, $N_B = 5 \pm 1$, and $N_E = 3 \pm 1$, corresponding to an average NP diameter of 8.3 nm and an average NP height of 4.8 nm. For the ratios of the surface energies, we deduce $\frac{\gamma_{100}}{\gamma_{111}} = \frac{h_{100}}{h_{111}} = \sqrt{3} \cdot \frac{N_T}{N_P} = 1.12 \pm 0.09$ for the top facets, which agrees well with the theoretical value of $(\gamma_{100}/\gamma_{111})^* = 1.16$ (*19*), but $\frac{\gamma_{100}}{\gamma_{111}} = \sqrt{3}\frac{N_P - N_E}{N_P} = 1.56 \pm 0.06$ for the side facets (the asterisk indicates theoretical values). This marked deviation from the expected value of $(\gamma_{100}/\gamma_{111})^*$ means that the side facets are noticeably smaller than predicted by the Wulff argument. We suggest that this observation is related to strain and/or NP edge effects (line tensions) neglected in the Wulff approach. The Rh NP adhesion energy $E_{ad} = \gamma_{100} \cdot \frac{N_T - N_B}{N_T} = 108 \pm 10$ meV/Å^2 (*25*) is less than the theoretical value $E_{ad}^* = 130$ meV/Å^2 associated with one extended monolayer of Rh on MgO(001), which is in-line with the trend that the adsorption energy decreases as a function of the Rh coverage (*26*).

In the next step, the Rh NPs were exposed to 3×10^{-5} mbar O_2 at 600 K [i.e., above the oxygen chemical potential for Rh_2O_3 bulk oxide formation (*27*)], and we simultaneously recorded the XRD pattern (Fig. 2, B and C). We observed a distinct change in the XRD signal (see difference map in Fig. 2B) that essentially consists of an intensity enhancement along the (001) rod and an intensity loss along the (111) rods, which can also be observed in the large area difference map in fig. S2B (*28*). The best fit to this x-ray intensity change (Fig. 2B) results in an average NP shape as characterized by $N_P = 31 \pm 1$, $N_T = 16 \pm 1$, $N_B = 5 \pm 1$, and $N_E = 7 \pm 1$ (Fig. 2C), with an unchanged average NP diameter of 8.3 nm and a reduced average height of 4 nm. These reconfigured Rh NPs now have a nanosized oxide skin composed of an ultrathin hexagonal surface oxide layer, as we explain below.

An unexpected result of this analysis is that the area of both the (100) side facets and the (001) top facet increases upon oxidation (*29*). This result implies that only intraparticle mass transport takes place during oxidation, which removes Rh atoms from the (100) side and top facets with an average amount that corresponds to the number of atoms incorporated into the surface oxide layers on all facets. However, the strong increase of the (110) facet area, which is predicted by theory (*19*) for the conditions applied, was not observed. Furthermore, no additional facets are formed in between the top (001) and (111) facets (they would readily be observable via additional diffraction intensities).

To get a microscopic insight into the forces that drive this NP shape transformation, we interrogated the atomistic structure of the oxidized (001) and (111) facets by quantitative surface XRD. Figure 3A shows a line scan along the (1,–1,0) direction ($L = 0.3$) associated with clean NPs and NPs exposed to 2×10^{-5} mbar oxygen at 500 K, which witnesses the formation of an oxygen-induced (3x1) superstructure at the top (001) nanofacet that progressively disappears upon further oxidation. The intensity of these superstructure reflections cannot be explained by a simple oxygen chemisorption structure; it is rather in line with a shifted-row structure that creates threefold adsorption sites for oxygen (Fig. 3B). The two-dimensional character of this structure can be inferred from the rodlike diffraction pattern (fig. S4). A similar structure appears during the oxidation of $Pt_{25}Rh_{75}$(100) single crystals (*30*) as a precursor for the surface oxide formation on Rh(100) (*13*).

When the sample temperature was only slightly increased to 550 K, a fast transformation takes place on the (001) top facets from the (3×1) adsorption structure to the hexagonal surface oxide that forms a c(2×8) coincidence structure with the underlying Rh lattice (Fig. 3, C and E) (*13*). At the same time, on the (111) side facets a hexagonal surface oxide is formed with a p(9×9) coincidence structure. The c(2×8) coincidence structure on the (001) facets and the p(9×9) structure on the (111) facets give rise to additional peaks that can be readily identified (Fig. 3C).

In the presence of the surface oxide on both the (111) and (100) facets, the theoretical value of the surface free energy ratio is lowered to $(\gamma_{100}/\gamma_{111})^* = 0.9$ (*19*). This value needs to be compared with our experimental data $(\gamma_{100}/\gamma_{111}) = \sqrt{3} \cdot \frac{N_T}{N_P} = 0.89 \pm 0.09$ and $(\gamma_{100}/\gamma_{111}) = \sqrt{3}\frac{N_P - N_E}{N_P} = 1.34 \pm 0.07$ for the top and side (100) facets, respectively. Thus, the observed increase of the total (100) type facet surface area is in good agreement with the Wulff prediction and can be directly related to the slightly higher stability of the surface oxide on the (100) facets, as compared with the (111) facets. Although bulk oxide formation is thermodynamically favored under the conditions applied (*27*), the surface oxide at

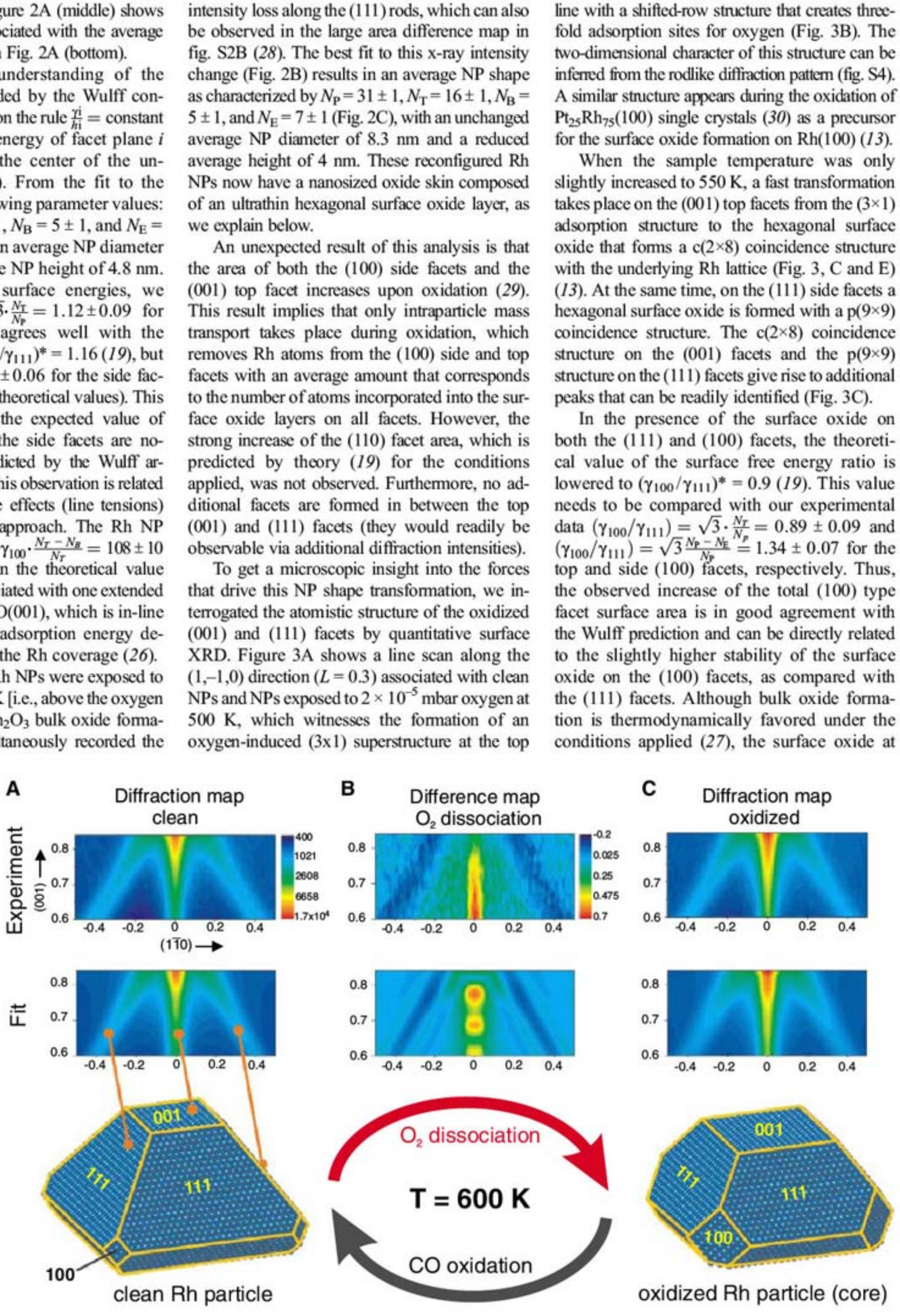

Fig. 2. (**A**) (Top) (110) diffraction map of clean Rh particles at 600 K. (Middle) Fitted diffraction map corresponding to the average particle shape given below. (**B**) (Top) oxygen-induced signal change in the (110) plane. (Middle) Simulated signal change for particles with increased (100) side facet area. (**C**) (Top) Experimental (110) diffraction map at 600 K and 2×10^{-5} mbar O_2 pressure. (Middle) Fitted diffraction map for particles under oxygen exposure. (Bottom) Best-fit core particle shape after oxidation.

the Rh nanofacets is metastable and prevents bulk oxide growth.

A further key observation is that the oxygen-induced shape change of the Rh NPs is fully reversible when the surface oxide is removed by CO exposure (at 1×10^{-5} mbar). The observed x-ray intensity line scans (Fig. 3, C and E) obtained after reduction are identical to the clean particle scans, which is evidence for decomposition of the facet oxide layers. Simultaneously, the oxygen-induced intensity change of the scattering from the (111) and (001) facets (Fig. 2B) is reversible, as can be inferred from the line scans in fig. S3, demonstrating the reformation of the clean particle facets.

Complementary information on the shape of the Rh NPs has been obtained by GISAXS (*31*), which has been carried out parallel to the above surface XRD experiment and by cross-section HRTEM (*20*). The observed marginal changes of the GISAXS patterns and associated line scans for two different azimuths confirm that the average particle size does not change during the oxidation and reduction process (fig. S5). The cross-section TEM image (Fig. 4) taken of a Rh NP on MgO(001) along the (110) direction uncovers a NP shape that corresponds very well with the x-ray results (dashed line in Fig. 4A). We also observed structures with a different periodicity on the particle facets that can be identified as oxide over layers. In some cases (for instance, on the right facet of the particle in Fig. 4A), a one-monolayer-thick oxide layer can be observed with atomic resolution. The zoomed-in view of the white box in Fig. 4A reveals a surface layer on the (111) facet with a different periodicity, a finding that is strongly supported by the simulated TEM image contrast for the O–Rh–O surface oxide trilayer (box in Fig. 4B). The observation that the surface oxide is present, even after exposure of the sample to ambient conditions and the rather destructive TEM specimen preparation, gives us the first evidence for the presence of noticeable kinetic barriers toward bulk oxide formation once the surface oxide is formed.

Our high-resolution in situ oxidation experiments demonstrate that the surface oxide O–Rh–O trilayer stabilizes Rh NPs with low-index facets. We assume that this reversible shape transformation also occurs for smaller particles [as long as they have (111) and/or (100) facets] and that the observed surface oxide formation at the facets of the NPs also takes place in oxidation catalysis involving Rh NPs under technologically relevant conditions.

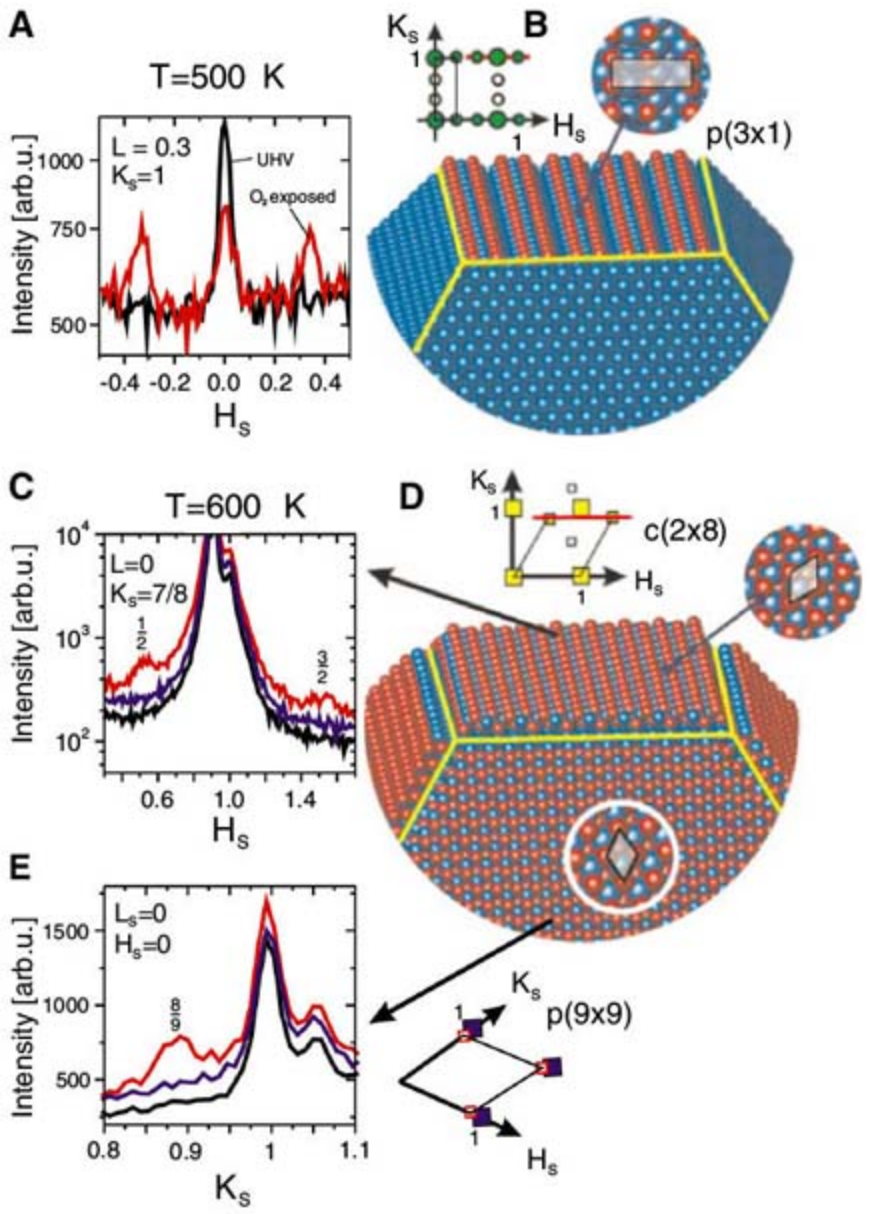

Fig. 3. (**A**) Line scans along the H_S direction in (100) surface coordinates (*13*). Black line, clean particles; red line, under oxygen exposure. (**B**) Reciprocal- and real-space lattice of the (3×1) shifted-row superstructure on the (001) particle top facet. The scans in (A) were performed at $K_S = 1$; see red line. The peaks at $H_S = -1/3$ and $1/3$ are characteristic for the (3×1) superstructure. (**C**) H_S scan in (100) surface coordinates ($K_S = 7/8$) along the red line in the top reciprocal lattice in (D). Satellite peaks at $H_S = 1/2$ and $H_S = 3/2$ give evidence for the c(2×8) coincidence structure of the hexagonal surface oxide (*13*) (hexagonal real- and reciprocal-space unit cells are indicated). (**D**) Structural model of a Rh NP on MgO, covered on all facets by a O–Rh–O trilayer surface oxide. (**E**) K scan along the (01) direction in surface coordinates (*11*) of the (111) side facet pictured in (D). The reflection at $K_S = 8/9$ stems from the surface oxide. (C and E) Black lines, clean surface; red lines, under oxygen exposure; blue lines, after CO reduction.

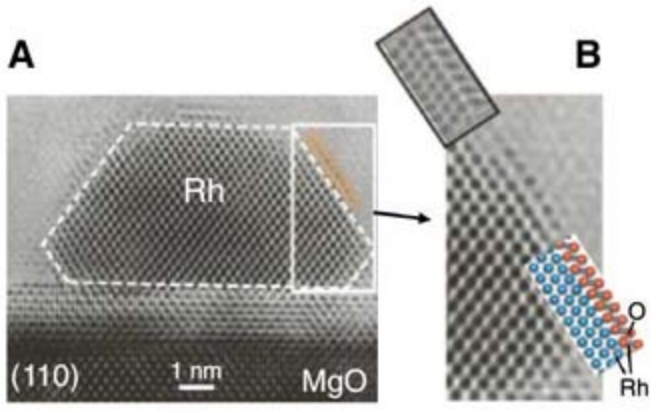

Fig. 4. (**A**) HRTEM micrograph of a Rh particle on MgO(001) in (110) view. On the left side, close to the substrate, a small twin is present with (111) twinning plane. From the XRD data, we can infer that ~5% of the particles are twinned. The dashed line represents the particle shape derived from the XRD data for the oxidized particles. The white box denotes the zoomed-in area of the surface oxide on (111) facets plotted in (B). (**B**) Atomically resolved structure of the O–Rh–O trilayer surface oxide on the (111) facets. In the box, a TEM image simulation is plotted as obtained from the structural model in the second inset. The dark spots correspond to Rh atom rows.

References and Notes

1. G. Ertl, H. Knözinger, F. Schüth, J. Weitkamp, *Handbook of Heterogeneous Catalysis* (Wiley-VCH, Weinheim, Germany, 2008).
2. M. D. Ackermann *et al.*, *Phys. Rev. Lett.* **95**, 255505 (2005).
3. J. G. Wang *et al.*, *Phys. Rev. Lett.* **95**, 256102 (2005).
4. E. Lundgren *et al.*, *Phys. Rev. Lett.* **92**, 046101 (2004).
5. B. L. M. Hendriksen, S. C. Bobaru, J. W. M. Frenken, *Surf. Sci.* **552**, 229 (2004).
6. C. H. F. Peden *et al.*, *J. Phys. Chem.* **92**, 1563 (1988).
7. M. A. Newton, C. Belver-Coldeira, A. Martinez-Arias, M. Fernandez-Garcia, *Angew. Chem. Int. Ed.* **46**, 8629 (2007).
8. M. Bäumer *et al.*, *Phys. Chem. Chem. Phys.* **9**, 3541 (2007).
9. H. S. Gandhi, G. W. Graham, R. W. McCabe, *J. Catal.* **216**, 433 (2003).
10. H. Over *et al.*, *Science* **287**, 1474 (2000).
11. J. Gustafson *et al.*, *Phys. Rev. Lett.* **92**, 126102 (2004).
12. J. Rogal, K. Reuter, M. Scheffler, *Phys. Rev. Lett.* **98**, 046101 (2007).
13. J. Gustafson *et al.*, *Phys. Rev. B* **71**, 115442 (2005).
14. C. Dri *et al.*, *J. Chem. Phys.* **125**, 094701 (2006).
15. P. L. Hansen *et al.*, *Science* **295**, 2053 (2002).
16. G. Rupprechter, K. Hayek, H. Hofmeister, *J. Catal.* **173**, 409 (1998).
17. C. R. Henry, *Surf. Sci. Rep.* **31**, 231 (1998).
18. K. Hojrup Hansen, Z. Sljivancanin, E. Lægsgaard, F. Besenbacher, I. Stensgaard, *Surf. Sci.* **505**, 25 (2002).
19. F. Mittendorfer, N. Seriani, O. Dubay, G. Kresse, *Phys. Rev. B* **76**, 233413 (2007).
20. See the supporting online material for details.
21. N. Kasper *et al.*, *Surf. Sci.* **600**, 2860 (2006).
22. U. Pietsch, V. Holy, T. Baumbach, *High-Resolution X-Ray Scattering* (Springer, New York, 2004).
23. I. K. Robinson, D. J. Tweet, *Rep. Prog. Phys.* **55**, 599 (1992).
24. G. Wulff, *Z. Kristallogr.* **34**, 445 (1901).
25. W. L. Winterbottom, *Acta Metall.* **15**, 303 (1967).
26. S. Nokbin, J. Limtrakul, K. Hermansson, *Surf. Sci.* **566–568**, 977 (2004).
27. This corresponds to a chemical oxygen potential (*19*) $\mu = -1.04$ eV. $\mu(Rh_2O_3)$ is -1.23 eV.
28. Noticeable oxygen-induced lattice distortions lead to intensity asymmetries between the low-Q and high-Q side of the associated Bragg point (where Q is the x-ray momentum transfer). Inspection of fig. S2B shows that this is not observed.

29. For slightly larger particles (diameter D = 9 nm), the formation of (100) side facet rods, in addition to (110) side facet rods, is observed upon oxidation. The latter is not observed for particles with D = 8 nm; for both see fig. S2.
30. M. Sporn *et al.*, *Surf. Sci.* **416**, 384 (1998).
31. G. Renaud *et al.*, *Science* **300**, 1416 (2003).

32. We thank G. Richter and M. Pudleiner for the preparation of Rh/MgO reference samples, N. Jeutter for help with the x-ray experiments, and the European Union for financial support under contract no. NMP3-CT-2003-505670 (NANO2).

Supporting Online Material

www.sciencemag.org/cgi/content/full/321/5896/1654/DC1

Materials and Methods
SOM Text
Figs. S1 to S5
References

22 May 2008; accepted 12 August 2008
10.1126/science.1160845

Polymer Pen Lithography

Fengwei Huo,[1,2]* Zijian Zheng,[1,2]* Gengfeng Zheng,[1,2] Louise R. Giam,[2,3] Hua Zhang,[1,2]† Chad A. Mirkin[1,2,3]‡

We report a low-cost, high-throughput scanning probe lithography method that uses a soft elastomeric tip array, rather than tips mounted on individual cantilevers, to deliver inks to a surface in a "direct write" manner. Polymer pen lithography merges the feature size control of dip-pen nanolithography with the large-area capability of contact printing. Because ink delivery is time and force dependent, features on the nanometer, micrometer, and macroscopic length scales can be formed with the same tip array. Arrays with as many as about 11 million pyramid-shaped pens can be brought into contact with substrates and readily leveled optically to ensure uniform pattern development.

Lithography is used in many areas of modern science and technology, including the production of integrated circuits, information storage devices, video screens, microelectromechanical systems (MEMS), miniaturized sensors, microfluidic devices, biochips, photonic bandgap structures, and diffractive optical elements (*1*–*6*). Generally, lithography can be divided into two categories on the basis of patterning strategy: parallel replication and serial writing. Parallel replication methods such as photolithography (*7*), contact printing (*8*–*11*), and nanoimprint lithography (*12*) are useful for high-throughput, large-area patterning. However, most of these methods can only duplicate patterns, which are predefined by serial writing approaches and thus cannot be used to arbitrarily generate different patterns (i.e., one photomask leads to one set of feature sizes for a given wavelength). In contrast, serial writing methods—including electron-beam lithography (EBL), ion beam lithography, and many scanning probe microscopy (SPM)–based methods (*13*–*16*)—can create patterns with high resolution and registration but are limited in throughput (*17*, *18*). Indeed, only recently have researchers determined ways to use two-dimensional cantilever arrays for dip-pen nanolithography (DPN) to produce patterned structures made of molecule-based materials over areas as large as square centimeters (*19*, *20*).

DPN uses an "ink"-coated atomic force microscope (AFM) tip to deliver soft or hard materials (e.g., molecular inks, nanoparticles, or sol gels) to a surface with high registration and sub-50-nm resolution in a "constructive" manner (*3*, *16*, *21*–*23*). When combined with high-density cantilever arrays, DPN is a versatile and powerful tool for constructing molecule-based patterns over relatively large areas with moderate throughput (*1*). The limitations of DPN are (i) the inability to easily and rapidly work across the micro- and nanometer-length scales in a single experiment (typically, either sharp tips are optimized to generate nanoscale features or blunt tips are used to generate microscale features) (*24*) and (ii) the need for fragile and costly two-dimensional cantilever arrays to achieve large-area patterning. Indeed, no simple strategy exists that allows one to rapidly pattern molecule-based features with sizes ranging from the nanometer to millimeter scale in a parallel, high-throughput, and direct-write manner. We report the development of polymer pen lithography (PPL), a low-cost, cantilever-free lithographic approach that, thus far, allows a digitized pattern to be printed at spot sizes ranging from 90 nm to hundreds of μm simply by changing the force and time over which the ink is delivered.

In contrast with DPN and other SPM-based lithographies, which typically use hard silicon–based cantilevers, PPL uses elastomeric tips without cantilevers [typically polydimethylsiloxane (PDMS)] (*25*, *26*) to deliver ink. A typical polymer pen array (Fig. 1) contains thousands of pyramid-shaped tips that are made with a master prepared by conventional photolithography and subsequent wet chemical etching (fig. S1) (*27*). The pyramids are connected by a thin PDMS backing layer (50 to 100 μm thick) that is adhered to a glass support before curing. The glass support and thin backing layer significantly improve the uniformity of the polymer pen array over large areas, to date up to an entire 3-inch (76.2-mm) wafer surface (Fig. 1B and fig. S2) (*27*). When the sharp tips of the polymer pens are brought in contact with a substrate, ink is delivered at the points of contact (Fig. 1A). An important feature for ensuring uniform ink delivery over large areas is that the amount of light reflected from the tips increases greatly when the tips make contact with the substrate (movie S1) (*27*). Thus, the transparent elastomer polymer pen array allows us to determine visually when all of the pens are in contact with an underlying substrate. The otherwise daunting task of leveling the array can be tackled in an experimentally straightforward manner.

We performed our PPL experiments with an Nscriptor system (NanoInk, Skokie, IL) equipped with a 90-μm closed loop scanner and commercial lithography software (DPNWrite, DPN System-2, NanoInk, Skokie, IL). Depending on intended use, the pitch of a pen array is deliberately set between 20 μm and 1 mm,

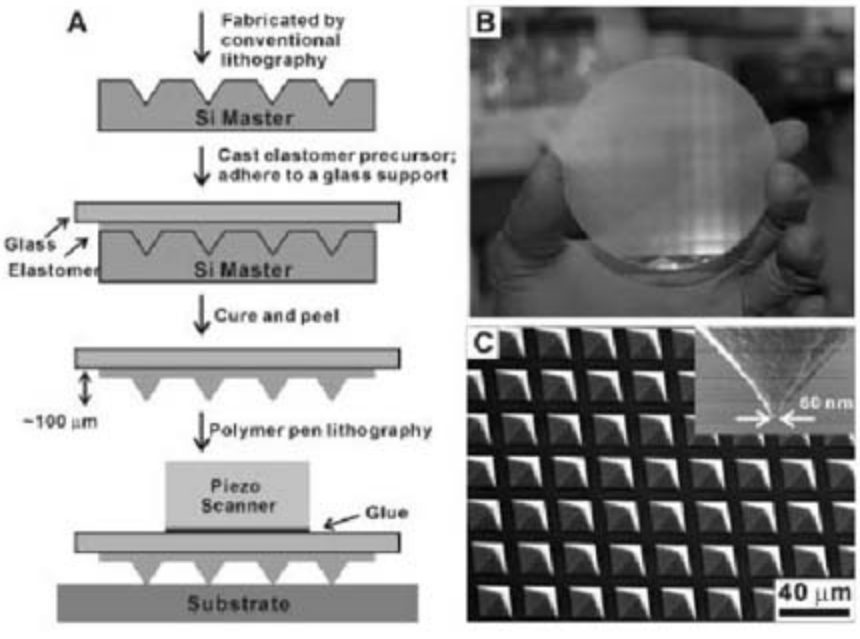

Fig. 1. (**A**) A schematic illustration of the polymer pen lithography setup. (**B**) A photograph of an 11-million-pen array. (**C**) Scanning electron microscope image of the polymer pen array. The average tip radius of curvature is 70 ± 10 nm (inset).

[1]Department of Chemistry, Northwestern University, 2145 Sheridan Road, Evanston, IL 60208–3113, USA. [2]International Institute for Nanotechnology, Northwestern University, 2145 Sheridan Road, Evanston, IL 60208–3113, USA. [3]Department of Materials Science and Engineering, Northwestern University, 2145 Sheridan Road, Evanston, IL 60208–3113, USA.

*These authors contributed equally to this work.
†Current address: School of Materials Science and Engineering, Nanyang Technological University, 50 Nanyang Avenue, Singapore 639798, Singapore.
‡To whom correspondence should be addressed. E-mail: chadnano@northwestern.edu

corresponding to pen densities of 250,000/cm^2 and 100/cm^2, respectively. Larger pitch arrays are required to make large features (micrometer or millimeter scale) but also can be used to make nanometer-scale features. All of the pens are remarkably uniform in size and shape, with an average tip radius of 70 ± 10 nm (Fig. 1C). In principle, this value could be reduced substantially with higher-quality masters and stiffer elastomers. Finally, for many of the experiments we reported, we demonstrate capabilities with an array that contains either 15,000 or 28,000 pyramid-shaped pens, but we have made and demonstrated patterning capabilities with arrays with as many as ~11,000,000 pens (fig. S3) (*27*).

In a typical experiment, a polymer pen array (1 cm^2 in size) was inked by immersing it in a saturated solution of 16-mercaptohexadecanoic acid (MHA) in ethanol for 5 min followed by rinsing with ethanol. The inked pen array was used for generating 1-μm diameter MHA dot patterns on a thermally evaporated polycrystalline gold substrate (25 nm Au with a 5 nm Ti adhesion layer coated on Si) by bringing it in contact with the gold surface for 0.1 s. This process was repeated 35 times to generate a 6 by 6 array of MHA dots (less than 10% deviation in feature diameter). The exposed gold on this MHA patterned substrate was subsequently etched (20 mM thiourea, 30 mM iron nitrate, 20 mM hydrochloric acid, and 2 mM octanol in water) to yield raised structures that are approximately 25 nm in height and easily imaged by optical microscopy (Fig. 2A).

A defining characteristic of PPL, in contrast with DPN and most contact printing strategies, which are typically viewed as force-independent (*21*), is that it exhibits both time- and force-dependent ink transport. As with DPN, features made by PPL exhibit a size that is linearly dependent on the square root of the tip-substrate contact time (fig. S4) (*27*–*29*). This property of PPL, which is a result of the diffusive characteristics of the ink and the small size of the delivery tips, allowed us to pattern submicrometer features with high precision and reproducibility (variation of feature size is less than 10% under the same experimental conditions).

The force dependence of PPL derives from the "soft" nature of the elastomer pyramid array. Indeed, the microscopic pyramidal tips can be made to deform with successively increasing amounts of applied force, which can be controlled by simply extending the piezo in the vertical direction (*z*-piezo). Although such deformation has been regarded as a major drawback in contact printing (it can result in "roof" collapse and limit feature size resolution), with PPL, the controlled deformation can be used as an adjustable variable, allowing control of the tip-substrate contact area and the resulting feature size. Within the force range allowed by *z*-piezo extension, one can observe a near linear relation between piezo extension and feature size at a fixed contact time of 1 s (Fig. 2B).

At the point of initial contact and a relative extension of 0.5 μm, the sizes of the MHA dots do not significantly differ and are both ~500 nm, indicating that the bulk of the polymer pen array compresses before the pyramid-shaped tips significantly deform. This observation is consistent with the known force-strain curves associated with PDMS (*25*). This type of buffering is fortuitous and essential for leveling because it provides extra tolerance in bringing all of the tips in contact with the surface without tip deformation and significantly changing the intended feature size. When the *z*-piezo extends 1 μm or more, the tips exhibit significant and controllable deformation (Fig. 2B).

Because of the force dependency of PPL, we do not have to rely on the time-consuming, meniscus-mediated ink diffusion process to generate large features. Indeed, we can generate either nanometer- or micrometer-sized features in only one printing cycle by simply adjusting the degree of tip deformation. As proof of concept, 6 by 6 gold square arrays, where each square in a row was written with one printing cycle at different tip-substrate forces but a constant 1-s tip-substrate contact time, were fabricated by PPL and subsequent wet chemical etching (Fig. 2C). The largest and smallest gold squares are 4 μm and 600 nm on edge, respectively. This experiment does not define the feature size range attainable in a PPL experiment but rather is a demonstration of the multiple scales accessible by PPL at a fixed tip-substrate contact time (1 s in this case).

Unlike conventional contact printing, PPL allows for the combinatorial patterning of molecule-based and solid-state features with dynamic control over feature size, spacing, and shape. As in conventional lithography of images, the polymer tips are used to form a dot pattern of the intended pattern or structure. As proof of concept, we used a polymer pen array with 100 pyramidal tips spaced 1 mm apart to generate 100 duplicates of an integrated gold circuit. The width of each electrode in the center of the circuit is 500 nm, whereas the width of each electrode lead going to these nanometer-scale electrodes is 10 μm, and the size of the external bonding pad is 100 by 100 μm^2 (Fig. 2D). Because the Nscriptor provides only a 90 by 90 μm^2 scanner, the circuits were divided into 35 80 by 80 μm^2 subpatterns that were then stitched together by manually moving the stage motor after each subpattern was generated. This limitation could be addressed by programming the movement of the stage motor relative to the positions of the multiple subpatterns. To accommodate both resolution and throughput concerns, we used different relative *z*-piezo extensions at different positions of the circuit, where 0 (initial contact), 2, and 6 μm were used for the central electrodes, electrode leads, and bonding pads, respectively. As

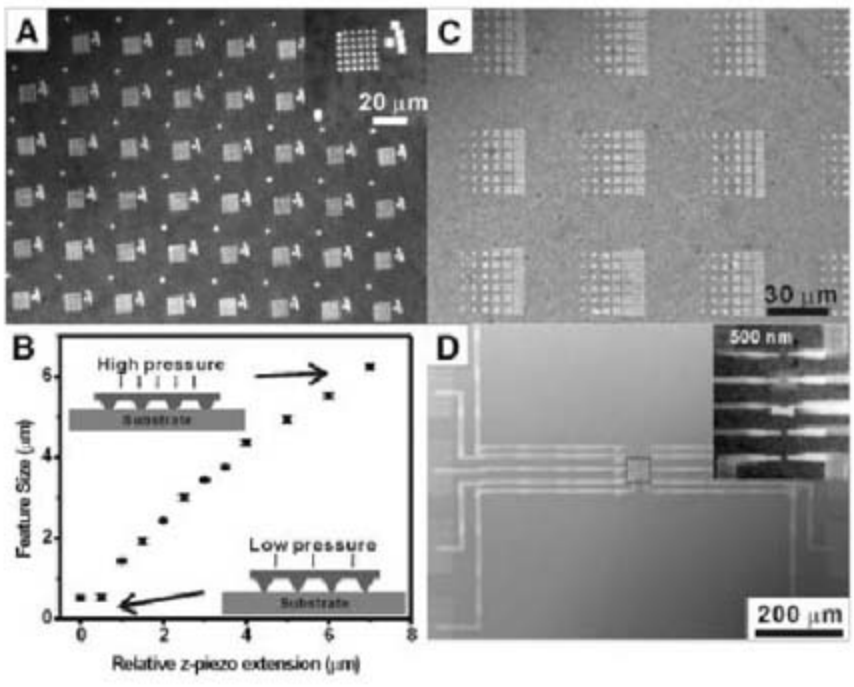

Fig. 2. (**A**) Optical image of a 480-μm by 360-μm section of a one million gold dot array (6 by 6 within each block) on a silicon substrate (using a pen array with 28,000 pyramid-shaped tips). (**B**) MHA dot size as a function of relative *z*-piezo extension. The results were obtained using a polymer pen array with 15,000 pyramid-shaped tips at 25°C with a relative humidity of 40%. (**C**) Optical image of arrays of gold squares generated at different *z*-piezo extensions (using a pen array with 28,000 pyramid-shaped tips). (**D**) An optical microscope image of a multidimensional gold circuit fabricated by PPL. The inset shows a magnified SEM image of the circuit center.

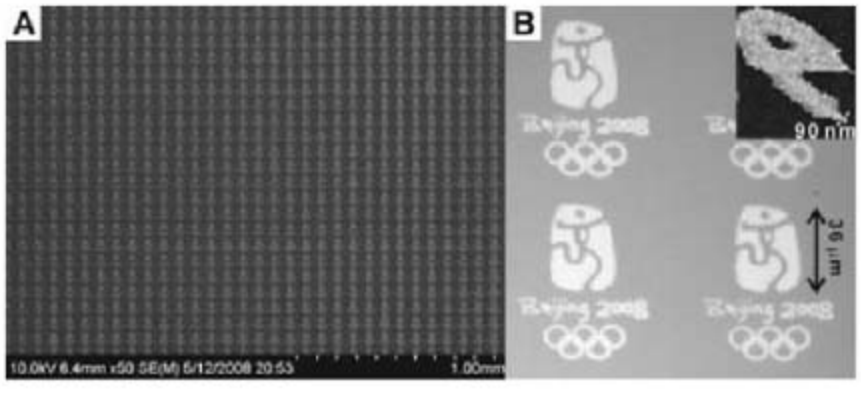

Fig. 3. (**A**) SEM image of a representative region of ~15,000 miniaturized duplicates of the 2008 Beijing Olympic logo. (**B**) A zoom-in optical image of a representative replica. The inset shows a magnified SEM image of the letter "e."

a result, writing a 100 by 100 μm^2 area requires only 400 printing cycles (less than 0.5 s for each cycle), and the total time required to generate 100 duplicates of the circuit is ~2 hours. Re-inking of the pen array is not necessary because the PDMS behaves as a reservoir for the ink throughout the experiment (*28*, *29*). This relatively high-throughput production of multiscale patterns would be difficult, if not impossible, to do by EBL or DPN.

The force dependence and maskless nature of PPL allow many structural variants to be created without the hurdle of designing a new master by a throughput-impeded serial process. In addition, PPL can be used with sub-100-nm resolution with the registration capabilities of a closed-loop scanner. For example, PPL was used to generate 15,000 replicas of the 2008 Beijing Olympic logo on gold with MHA as the ink and subsequent wet chemical etching (Fig. 3A). Each logo was generated using the multiscale capabilities of PPL from a 70 by 60 μm^2 bitmap. The letters and numbers "Beijing 2008" were generated from ~20,000 90-nm dots (initial contact), whereas the picture and Olympic rings were made from ~4,000 600-nm dots at higher array-substrate contact forces (relative piezo extension = 1 μm). These structures were created by holding the pen array at each spot for 0.05 s and traveling between spots at a speed of 60 μm/s. A representative portion of the ~15,000 replicas (yield > 99%) generated across the 1-cm^2 substrate shows their uniformity (Fig. 3B). The total time required to fabricate all of these structures was less than 40 min.

The time- and force-dependent ink transport properties of the polymer pen pyramid arrays provide a tunability to PPL that may allow other patterning capabilities to be developed. Because PPL is a direct-write technique, it is also ideal for fabricating arrays of structures made of soft matter, such as proteins (fig. S5) (*27*), making it potentially useful in the life sciences as well.

References and Notes

1. C. A. Mirkin, *ACS Nano* **1**, 79 (2007).
2. K. Salaita, Y. H. Wang, C. A. Mirkin, *Nat. Nanotechnol.* **2**, 145 (2007).
3. D. S. Ginger, H. Zhang, C. A. Mirkin, *Angew. Chem. Int. Ed.* **43**, 30 (2004).
4. Y. Xia, G. M. Whitesides, *Angew. Chem. Int. Ed.* **37**, 550 (1998).
5. Y. Xia, G. M. Whitesides, *Annu. Rev. Mater. Sci.* **28**, 153 (1998).
6. M. Qi *et al.*, *Nature* **429**, 538 (2004).
7. T. Ito, S. Okazaki, *Nature* **406**, 1027 (2000).
8. Y. L. Loo, R. L. Willett, K. W. Baldwin, J. A. Rogers, *J. Am. Chem. Soc.* **124**, 7654 (2002).
9. Z. Zheng, O. Azzaroni, F. Zhou, W. T. S. Huck, *J. Am. Chem. Soc.* **128**, 7730 (2006).
10. A. Kumar, G. M. Whitesides, *Appl. Phys. Lett.* **63**, 2002 (1993).
11. M. N. Yousaf, B. T. Houseman, M. Mrksich, *Proc. Natl. Acad. Sci. U.S.A.* **98**, 5992 (2001).
12. S. Y. Chou, P. R. Krauss, P. J. Renstrom, *Science* **272**, 85 (1996).
13. S. Xu, S. Miller, P. E. Laibinis, G. Y. Liu, *Langmuir* **15**, 7244 (1999).
14. M. Geissler, Y. Xia, *Adv. Mater.* **16**, 1249 (2004).
15. B. D. Gates *et al.*, *Chem. Rev.* **105**, 1171 (2005).
16. R. D. Piner, J. Zhu, F. Xu, S. Hong, C. A. Mirkin, *Science* **283**, 661 (1999).
17. S. Kramer, R. R. Fuierer, C. B. Gorman, *Chem. Rev.* **103**, 4367 (2003).
18. R. Maoz, S. R. Cohen, J. Sagiv, *Adv. Mater.* **11**, 55 (1999).
19. S. Lenhert, P. Sun, Y. Wang, H. Fuchs, C. A. Mirkin, *Small* **3**, 71 (2007).
20. K. Salaita *et al.*, *Angew. Chem. Int. Ed.* **45**, 7220 (2006).
21. S. Hong, C. A. Mirkin, *Science* **288**, 1808 (2000).
22. L. M. Demers *et al.*, *Science* **296**, 1836 (2002).
23. K.-B. Lee, S.-J. Park, C. A. Mirkin, J. C. Smith, M. Mrksich, *Science* **295**, 1702 (2002).
24. For instance, DPN fabrication of a 10-μm by 10-μm MHA feature on a gold substrate with a conventional Si_3N_4 cantilever (radius of curvature = 20 to 60 nm) takes ~30 min.
25. H. Schmid, B. Michel, *Macromolecules* **33**, 3042 (2000).
26. T. W. Odom, J. C. Love, D. B. Wolfe, K. E. Paul, G. M. Whitesides, *Langmuir* **18**, 5314 (2002).
27. Materials and methods are available as supporting material on *Science* Online.
28. H. Zhang, R. Elghanian, N. A. Amro, S. Disawal, R. Eby, *Nano Lett.* **4**, 1649 (2004).
29. X. Wang *et al.*, *Langmuir* **19**, 8951 (2003).

30. C.A.M. acknowledges the U.S. Air Force Office of Scientific Research (AFOSR), the Defense Advanced Research Projects Agency (DARPA), and NSF (Nanoscale Science and Engineering Center program) for support of this research. C.A.M. is grateful for a NIH Director's Pioneer Award and a National Security Science and Engineering Faculty Fellowship from the U.S. Department of Defense. L.R.G. acknowledges the NSF for a Graduate Research Fellowship.

Supporting Online Material

www.sciencemag.org/cgi/content/full/1162193/DC1
SOM Text
Figs. S1 to S5
References
Movie S1

23 June 2008; accepted 1 August 2008
Published online 14 August 2008;
10.1126/science.1162193
Include this information when citing this paper.

4D Electron Diffraction Reveals Correlated Unidirectional Behavior in Zinc Oxide Nanowires

Ding-Shyue Yang, Changshi Lao, Ahmed H. Zewail*

The confined electronic structure of nanoscale materials has increasingly been shown to induce behavior quite distinct from that of bulk analogs. Direct atomic-scale visualization of nanowires of zinc oxide was achieved through their unique pancake-type diffraction by using four-dimensional (4D) ultrafast electron crystallography. After electronic excitation of this wide-gap photonic material, the wires were found to exhibit colossal expansions, two orders of magnitude higher than that expected at thermal equilibrium; the expansion is highly anisotropic, a quasi–one-dimensional behavior, and is facilitated by the induced antibonding character. By reducing the density of nanowires, the expansions reach even larger values and occur at shorter times, suggesting a decrease of the structural constraint in transient atomic motions. This unanticipated ultrafast carrier-driven expansion highlights the optoelectronic consequences of nanoscale morphologies.

Major changes in the physical, chemical, or optical properties of a substance can occur as a result of shrinking dimension and changing morphology down to the nanometer scale, primarily because of quantum confinement and surface effects. Quantum dots and nanotubes are examples of such structures, which have the potential for a variety of applications [for reviews, see (*1*–*7*)]. Among the materials that show promising features for optoelectronics, such as blue-green laser diodes and photonic devices, the wide-gap semiconductor zinc oxide (ZnO) has been one of the most-investigated nanowire materials (*8*, *9*). At the nanoscale, design of such structures requires fundamental understanding of electronic and nuclear degrees of freedom in the unique nanowire architecture because they control the effective carrier mobility and properties along the wires. With optical methods [for a review, see (*10*)], the transient response can be probed, but, because of the wavelengths involved, the atomic-scale structural changes are not determined; electrons of the appropriate wavelength provide the means for the visualization of both.

We report visualization of the structure and dynamics of vertically aligned ZnO nanowires with use of time-resolved electron crystallography. The nanowire array was synthesized via a bottom-up process of physical vapor deposition (*11*). A single-crystal sapphire of $(11\bar{2}0)$ surface with a 100-nm GaN layer (grown by metal-organic chemical vapor deposition) was used as the collection substrate. Reaction parameters such as the chamber pressure and temperature and the gas flow rate were varied to obtain the nanowires, which were supported by an ~2-μm layer of ZnO on the substrate, as a vertically aligned array. As shown in Fig. 1, A and B, the wires have an average diameter of ~150 nm, a length of ~2 μm, and an average spacing of ~300 nm. We also studied nanowires prepared by an entirely different method [hydrothermal synthesis (*12*)], and for this case the density of wires is notably lower, as seen in Fig. 1C. Both specimens were characterized by scanning electron microscopy (SEM) (Fig. 1, A and C); transmission electron microscopy and x-ray diffraction measurements

have also been used to characterize the products of the two aforementioned methods (*11*, *12*).

Electron packets at near-grazing angles (θ_{in} = 2.7°) were invoked in our ultrafast electron crystallography apparatus (fig. S1) (*13*, *14*). A heating pulse preceded in time the electron packet and was used to excite the carriers of the wires. Frames of the far-field diffraction were recorded at different delay times and with a tilted geometry (for velocity mismatch compensation), which enabled the reported spatiotemporal resolution (*15*–*18*); see supporting online material (SOM) for details. From the observed intensities, positions, and widths of the Bragg diffractions, we obtained the change of atomic positions with time, the structural factor, and the transient inhomogeneity in the wires. By varying the fluence, the influence of carrier density on structural dynamics was examined and, in this case, the wires were directly excited. The maximum optical fluence applied was 22.5 mJ cm^{-2} (*19*). Lastly, by using two arrays of nanowires, the effect of their packing density on the substrate was elucidated.

The static structure of the ZnO nanowires without the optical excitation was determined by recording the diffraction patterns at different incidence angles (rocking curves); patterns of two zone axes are given in Fig. 2, A and B. With the electron beam propagating along the [110] direction, the patterns consist of both the Bragg spots and the first-order-Laue-zone (FOLZ) diffractions (*20*), and all have horizontally elongated ("pancake") shapes, as seen in Fig. 2A. With a 30° rotation of the specimen, the electron beam becomes directed along the [100] axis, and we only observe the Bragg spots at a larger incidence angle; this is because the FOLZ diffractions are out of the camera region (Fig. 2B). The spacings between the diffraction spots (from the center of the pancakes) translate to the lattice constants of $a = b = 3.25(0)$ Å and $c = 5.20(8)$ Å, entirely consistent with the values for a wurtzite structure of ZnO crystals obtained by x-ray diffraction and calculations (*10*, *21*).

The pancake horizontal shape of the Bragg spots (Fig. 2, A and B insets) is distinct from the spots seen in bulk crystal diffraction and mirrors the hexagonal nanostructured wire. Because of the wires' nanoscale geometry and the attractive inner potential, V_I, inside the material, the diffracted electron beam is refracted and gives rise to a horizontal spread. Quantitatively, this geometry effect can be described by considering the analog of Snell's law in optics (*22*), giving

$$\sin\theta_{vac} = (1 + eV_I/E_k)^{1/2}\sin\theta_I \quad (1)$$

where θ_{vac} and θ_I are, respectively, the angles in the vacuum and inside the wires, with respect

Physical Biology Center for Ultrafast Science and Technology, Arthur Amos Noyes Laboratory of Chemical Physics, California Institute of Technology, Pasadena, CA 91125, USA.

*To whom correspondence should be addressed. E-mail: Zewail@caltech.edu

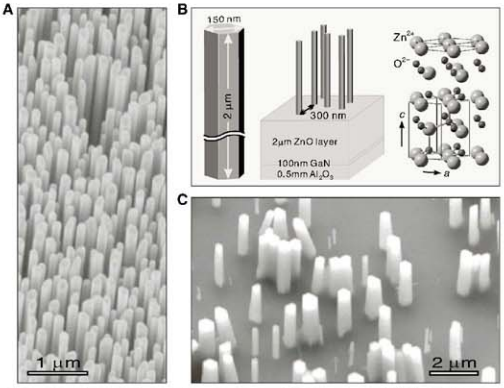

Fig. 1. Scanning electron micrographs and structure of ZnO nanowires. (**A**) The SEM image of the array fabricated through physical vapor deposition. The high-density wires are vertically aligned. Gold nanoparticles may be present dispersively as a result of the catalyst-assisted synthesis (*11*). (**B**) The structure (from the known inorganic crystal structure database) together with a schematic showing the average diameter and length of a single wire, the average spacing between wires, and the layer composition below the ZnO array sample. (**C**) The SEM image of the array fabricated through hydrothermal synthesis. The vertically aligned wires are thicker, on the average, and form an array with a much lower density. No gold nanoparticles are present in the nanowires because a metallic catalyst is not required for this wet-chemistry synthesis method (*12*).

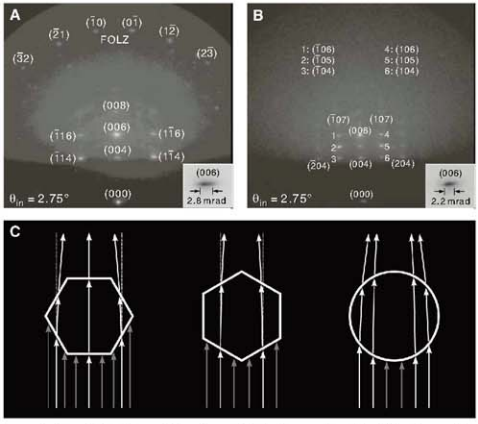

Fig. 2. Pancake-type diffraction and the shape effect of nanowires. The diffraction patterns were obtained at an incidence angle of θ_{in} = 2.75°, with the electron beam propagating along the [110] direction (**A**) and the [100] direction (**B**). From the well-indexed Bragg spots and FOLZ diffractions, the wurtzite ZnO structure is determined; the undiffracted (unblocked) electrons form the (000) spot. The insets show the enlarged horizontal width of the (006) Bragg spot. (**C**) Refraction of the probing electrons at the vacuum-material interface and the overall beam deflection caused by the different orientations and geometries of a nanowire (top view).

to the surface normal, and E_k is the kinetic energy of the incident electron, which in our case is 30 keV. In general, when the surface layers are perfectly parallel and $eV_I << E_k$, as in typical ultrafast electron crystallography experiments (*14*, *16*–*18*), this effect is negligible, but for the nanowires the situation is different (Fig. 2C), and the refraction can be invoked to obtain the geometry of the wires (*23*).

For a hexagonal wire, with the two orientations of 30° rotation difference (Fig. 2C, left and middle), there are two angles of deflection, $\sqrt{3}V_I/E_k$ and $V_I/\sqrt{3}E_k$. Thus, the intensity profile of the pancake is the sum of the contributions from the center and the two sides of the hexagon. For a cylindrical wire (Fig. 2C, right), the intensity profile is determined by the deflections, $\tan\theta_{vac}(V_I/E_k)$, with a width that resembles the case shown on the left of Fig. 2C. The difference between the two geometries is easy to discern: if circular, the rotation of the nanostructure would give no variation in the horizontal spot width, which is inconsistent with the experimental observation. For ZnO, V_I is 15.9 V (*24*). With the camera being 16.8 cm away from the nanowires, additional diffraction intensities near ±0.92 mrad (Fig. 2C, left) and ±0.31 mrad (Fig. 2C, middle) result in the horizontal spread from the spot center. Accordingly, this shape effect properly accounts for the observations made for the two zone axes (Fig. 2, A and B). Moreover, from the fact that the probing direction in Fig. 2A is [110] we determine the facets of nanowires to be of {110}, which is again consistent with the preferential growth (*11*). It should be noted that the vertical spot width did not increase, a consequence of the unique elongated geometry.

Structural dynamics of the wires were obtained from the diffraction frames at different delay times after the optical excitation. The intensity decrease and the vertical spot movement for each Bragg spot were evident in the diffraction. Whereas all of the diffraction spots move downward at early times and recover the original positions at longer times, the unblocked (undiffracted) direct beam did not change, thus eliminating the possibility of surface charging or surface potential change at all fluences used (fig. S2A). Quantitative analysis was carried out by fitting the vertical and horizontal intensity profiles of Bragg spots with a pseudo-Voigt function, yielding temporal evolution profiles not only of the spot intensities and positions but also of the widths (*14*); see SOM and fig. S2B. The results are presented in Figs. 3 and 4. Typical behavior is shown for the (006) Bragg spot: Whereas the intensity and vertical width are very similar in behavior and nearly recover (Fig. 3A) in only 200 ps, the rise of expansion along the *c* axis is delayed in time by ~15 ps and decays on a much longer time scale, reaching completion in about 1 ns.

The fluence dependence of the expansion, intensity, and width indicates the role of the (electron-hole) carriers. When the maximum *c*-axis expansion is plotted as a function of fluence in a log-log plot, the dependence follows a linear relationship with a slope value of 2.5 (Fig. 3B, inset). The energy of the exciting photon is less than half of the energy gap of ZnO (3.37 eV) (*10*, *21*) and also less than half of the energy gap of wurtzite GaN (3.44 eV) (*11*). Thus, the carriers are generated in the ZnO nanowires by energetically allowed three-photon excitation (3PA) and/or by enhanced two-photon absorption (2PA), both of which are due to the geometry of the nanostructure. When the experiments were repeated on a single-crystal ZnO sample (0.5 mm thick) at the highest fluence, we failed to observe diffraction changes, suggesting a significant change in the band gap/carrier density in the wires (*25*). Energetically, the excitation by 2PA generates carriers of somewhat lower energy than the band gap in the Γ region, where the momentum is zero; by 3PA, the above-gap excitation becomes possible (*21*) in the Γ–M(K) regions with momentum along ⟨110⟩ (⟨100⟩).

The change of the expansion, intensity, and width at different fluences rises after the zero of time and reaches the maximum value nearly at the same time, also consistent with the fact that the wires were directly excited and not heated through a substrate with energy transport through the wire. For the intensity and width $\tau_{1/2}$ = 17 ps and for the expansion $\tau_{1/2}$ = 32 ps, where $\tau_{1/2}$ is the time at half-maximum, and the error is ±2 ps (SOM). The in-plane component of the nanowire, the horizontal lattice expansion derived from the change in the horizontal spacing between $(\bar{1}14)$ and $(1\bar{1}4)$ spots, is much smaller and only noticeable at the highest fluence, with a significantly faster recovery time (Fig. 4A). The intensity change of $(\bar{1}14)$ and $(1\bar{1}4)$ spots share a similar temporal evolution with that of the (006) spot but are shifted to earlier time by ~5 ps (Fig. 4B). Lastly, as noted in Fig. 4C, the *c*-axis expansion is higher in amplitude for the low-density array and rises faster than the rate observed for the high-density array.

From the results presented for structure, dynamics, and fluence and density dependences, the following picture emerges. The wires display correlated, nonequilibrium behavior in that the behavior is anisotropically driven by the potential of the carriers generated by the excitation, that is, by the electronic change in bonding. Thermal expansion of the material [with the coefficient $\alpha_c = 2.49 \times 10^{-6}\ K^{-1}$ (*21*)] would give $\Delta c/c \sim 2 \times 10^{-4}$ ($\Delta T \sim 80$ K), which is two orders of magnitude smaller than the observed values. At the highest fluence used, the observed expansion of 1 to 2% would correspond to a temperature rise

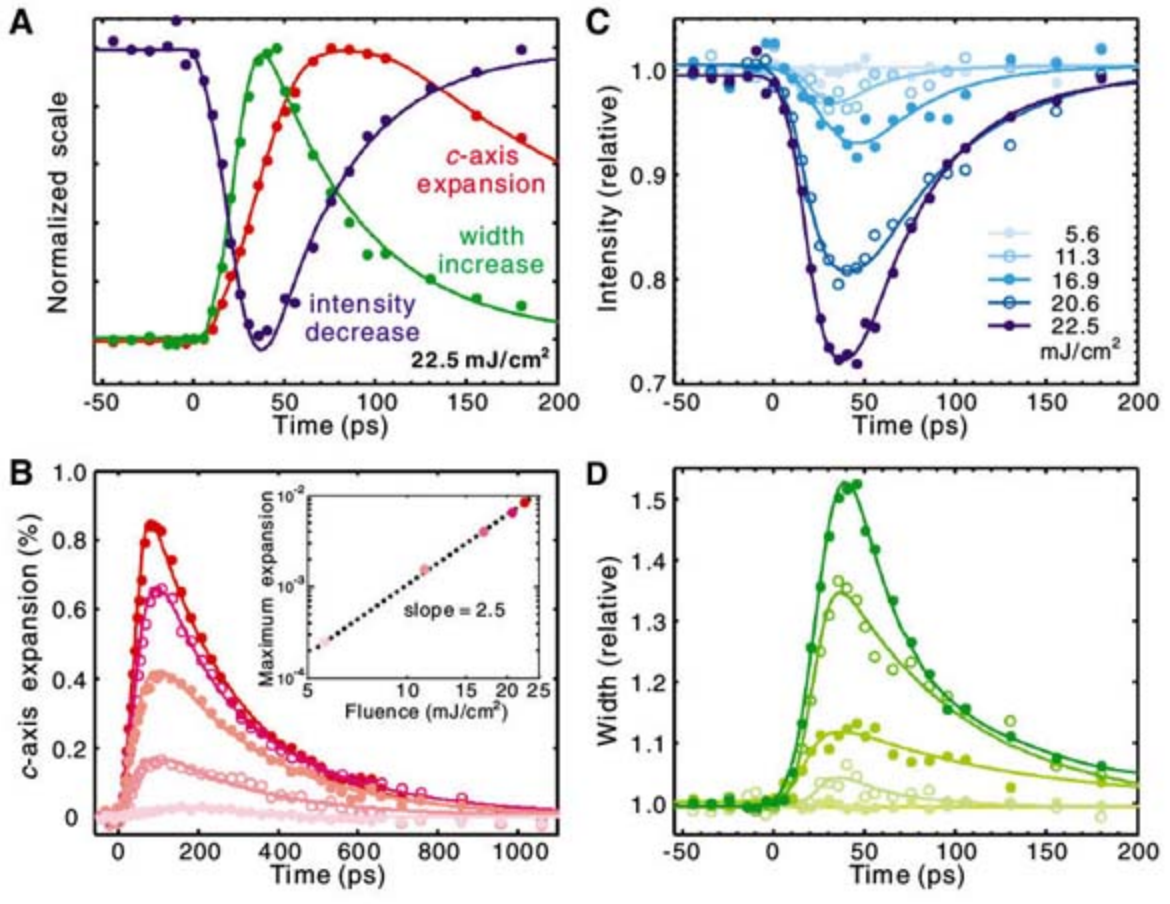

Fig. 3. Structural dynamics. Changes of the *c*-axis expansion, diffraction intensity, and vertical width of the (006) Bragg spot with time and at different excitation fluences. All solid lines are fits to the data (see text and SOM). (**A**) The intensity decrease (blue dots) and width increase (green dots) behave similarly and precede the buildup of structural expansion (red dots). In ~200 ps the former two diffraction features almost recover the original values, whereas the decay of expansion appears on a longer time (ns) scale. (**B**) A significantly larger *c*-axis expansion was obtained at higher excitation fluences. The fitted slope in the log-log plot (inset) indicates that the maximum expansion is proportional to the fluence to the power of 2.5. At all fluences, however, the expanded nanowires nearly return to their original structure in ~1 ns. (**C** and **D**) A more significant intensity decrease and a larger vertical width increase were observed after a stronger excitation. At the lowest fluence used, however, no appreciable diffraction changes were observed.

of 4000 to 8000 K, far beyond the decomposition temperature of 1975 K (*21*). In other words, the dynamics are not controlled by a thermal-like, incoherent expansion resulting from bonding anharmonicity but instead by the buildup of amplitudes because of the collective motions of atoms in the wire.

In a one-dimensional model, which considers the influence of a force induced by the excitation field, we can calculate the diffraction resulting from wavelike atomic motions in the wires. The speed of sound along the *c* axis in ZnO is 6200 m s^{-1}, and over the length of the wire (2 μm) we would expect a round-trip wave recurrence of 650 ps if the force field is impulsive [see figure 2b in (*26*)], contrary to what was observed. Instead, we observed a buildup of the expansion and gradual recovery on a longer time scale (Fig. 3B), a behavior that is obtainable when a sustaining excitation force field is operative [see figure 4a in (*26*)]. This sustaining force is the result of carriers' persistence and the potential they generate over the excitation length, in this case of micrometer scale (*14*).

The anisotropic expansion reflects an induced antibonding character along the wire direction. Because the initial carrier generation is near Γ (by 2PA) and in the in-plane Γ–M(K) region (by 3PA), carrier-carrier scattering becomes necessary in order to reach the Γ–A region along the wire *z* direction (the Zn–O bonding). As a result, the maximum vertical expansion lags in time the change of both the intensity and width. Besides the temporal behavior discussed, several observations support this conclusion. First, the restructuring for the expansion occurs on a much longer time scale than those of the intensity and width, and it is similar to the decay time of photoluminescence (radiative recombination) of ~1 to 2 ns (*27*). Second, the horizontal expansion is absent at lower fluences and at our highest fluence changes on a much shorter time scale (Fig. 4A). Lastly, as the excitation fluence increases, the density of carriers increases, leading to the observed larger longitudinal expansion (*28*).

When these different sets of experiments were repeated on the low-density nanowire array (Fig. 4, C and D), we observed similar behavior to that of the high-density array but with the largest expansion reaching as much as 2% and occurring at earlier times. These observations suggest that, in the low-density materials, the nanowires are more free to collectively expand, reaching a nonequilibrium effective "temperature" of 8000 K through the electronic potential change of carriers that weaken the Zn–O bonding. Modeling of the electronic-nuclear coupling may quantify this behavior. Although the average separation between wires is 300 nm in the high-density array, the inhomogeneity in distribution (clustering) becomes essential to the extent of the expansion.

Visualization of atomic motions during structural change reveals the direct role of electron-nuclear correlations that ultimately control the behavior of macroscopic phenomena, such as the optoelectronic effect in zinc oxide. The unexpected material behavior reported here for confined nanostructures is unobservable when the studies are made in the equilibrium state. Only when observed with atomic-scale spatial and femtosecond temporal resolutions can we acquire fundamental understanding of structural perturbations and relaxations for different optical and chemical dopings and hence the optimization of function at the nanoscale.

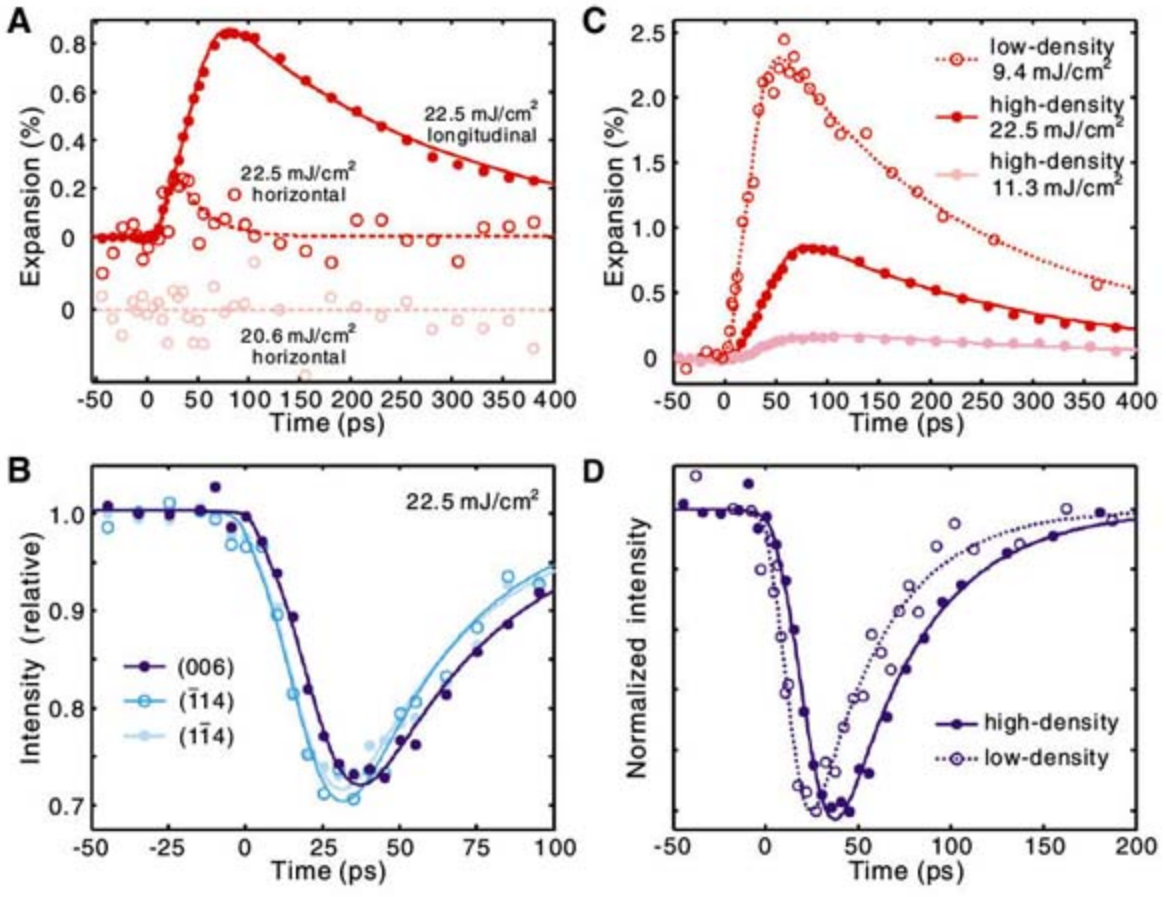

Fig. 4. Anisotropic expansions and density effect. Comparison between the longitudinal and horizontal structural dynamics and between the longitudinal dynamics obtained for the high- and low-density arrays. (**A**) Horizontal expansion of a wire (open circles) obtained from the horizontal spacing between $(\bar{1}14)$ and $(1\bar{1}4)$ Bragg spots; it is much smaller when compared to the longitudinal expansion (dots) and is only seen at our highest fluence. It also exhibits a faster decay. (**B**) The intensities of $(\bar{1}14)$ and $(1\bar{1}4)$ spots decrease at earlier time than that of the (006); however, their temporal behaviors are alike. (**C** and **D**) Longitudinal expansion and diffraction intensity of the low-density array (open circles) share similar overall temporal evolution with those from the high-density array (dots) but rise on a faster time scale. Even at a smaller excitation fluence, the *c*-axis expansion of the wires in the low-density array is significantly larger than that obtained at higher fluences for the high-density array (C).

References and Notes

1. M. L. Steigerwald, L. E. Brus, *Acc. Chem. Res.* **23**, 183 (1990).
2. S. Iijima, *Nature* **354**, 56 (1991).
3. G. M. Whitesides, J. P. Mathias, C. T. Seto, *Science* **254**, 1312 (1991).
4. Y. Cui, Q. Wei, H. Park, C. M. Lieber, *Science* **293**, 1289 (2001).
5. A. P. Alivisatos, *Science* **271**, 933 (1996).
6. C. B. Murray, C. R. Kagan, M. G. Bawendi, *Annu. Rev. Mater. Sci.* **30**, 545 (2000).
7. Y. Xia *et al.*, *Adv. Mater.* **15**, 353 (2003).
8. Z. L. Wang, *J. Phys. Condens. Matter* **16**, R829 (2004).
9. Z. L. Wang, *Mater. Today* **10**, 20 (2007).
10. Ü. Özgür *et al.*, *J. Appl. Phys.* **98**, 041301 (2005).
11. X. Wang *et al.*, *J. Am. Chem. Soc.* **127**, 7920 (2005).
12. L. E. Greene *et al.*, *Nano Lett.* **5**, 1231 (2005).
13. A. H. Zewail, *Annu. Rev. Phys. Chem.* **57**, 65 (2006), and references therein.
14. D.-S. Yang, N. Gedik, A. H. Zewail, *J. Phys. Chem. C* **111**, 4889 (2007).
15. P. Baum, A. H. Zewail, *Proc. Natl. Acad. Sci. U.S.A.* **103**, 16105 (2006).
16. N. Gedik, D.-S. Yang, G. Logvenov, I. Bozovic, A. H. Zewail, *Science* **316**, 425 (2007).
17. P. Baum, D.-S. Yang, A. H. Zewail, *Science* **318**, 788 (2007).
18. F. Carbone, P. Baum, P. Rudolf, A. H. Zewail, *Phys. Rev. Lett.* **100**, 035501 (2008).
19. A near-infrared pulse of 800 nm (1.55 eV) with a full width at half-maximum (FWHM) of 120 fs was used for the excitation of ZnO nanowires; see SOM for the geometry of excitation and probing on the specimen. The initial rise of signals was checked by using time delays of 2 ps (SOM). The polarization was parallel to the cross section of wires, and, in order to ensure uniform excitation of the target region, the electron-probed area on the sample was kept relatively small (~1 mm).
20. Z. L. Wang, *Reflection Electron Microscopy and Spectroscopy for Surface Science* (Cambridge Univ. Press, Cambridge, 1996).
21. S. Adachi, Ed., *Handbook on Physical Properties of Semiconductors* (Kluwer Academic, Boston, 2004).
22. A. Ichimiya, P. I. Cohen, *Reflection High Energy Electron Diffraction* (Cambridge Univ. Press, Cambridge, 2004), pp. 20–23.
23. We emphasize that the direct electron beam has a horizontal FWHM of ~1.8 mrad on the camera screen, which is smaller than the observed spreads of 2.8 and 2.2 mrad for the two orientations. Given the relatively large diameter of the nanowires (~150 nm), the Scherrer-type broadening [$D\Delta s \sim 1$, where D is the particle size and Δs is the scattering spread on the screen (*29*)] is only <0.05 mrad. Most importantly, the vertical width of Bragg spots is much narrower than the horizontal one for the same electron beam used (Fig. 2).
24. E. Müller *et al.*, in *Microscopy of Semiconducting Materials* (Springer, New York, 2006), pp. 303–306.
25. For ZnO crystals, the 2PA is negligible; the 3PA is weak, with a coefficient of ~0.01 cm^3 GW^{-2} and saturation

intensity of tens of GW cm^{-2} at 800 nm (*30*, *31*). The vertically aligned ZnO wires exhibit significant enhancement of optical nonlinearities: The 2PA coefficient (α_2) is greater than 10^3 cm GW^{-1} (*32*, *33*), and the wires show strong 3PA at high excitation intensities (*34*). The increased multiphoton absorption has been attributed to the local-field enhancement because of the surface states and the interaction between the aligned wire facets (*32*). With the 2PA coefficient of $\alpha_2 \sim 4 \times 10^3$ cm GW^{-1}, the effective penetration depth at our $I = 75$ GW cm^{-2} is ~33 nm. However, because of saturation this length can reach micrometers.

26. J. Tang, D.-S. Yang, A. H. Zewail, *J. Phys. Chem. C* **111**, 8957 (2007).
27. M. H. Huang *et al.*, *Science* **292**, 1897 (2001).
28. We note that the promptness of the intensity and width change (*14*) comes from the direct cascade of optical (and acoustic) phonon generation, which in this case amounts to ~20 for 3PA. Because the initial excitation induces in-plane movements of atoms, the intensity of $(\bar{1}14)$ and $(1\bar{1}4)$ spots should decrease before that of the (006), as observed experimentally.
29. B. E. Warren, *X-Ray Diffraction* (Dover, New York, 1990).
30. J. He, Y. Qu, H. Li, J. Mi, W. Ji, *Opt. Express* **13**, 9235 (2005).
31. B. Gu, J. He, W. Ji, H.-T. Wang, *J. Appl. Phys.* **103**, 073105 (2008).
32. H. W. Lee *et al.*, *Chem. Phys. Lett.* **447**, 86 (2007).
33. S. Xiao *et al.*, *Chin. Phys. B* **17**, 1291 (2008).
34. C. F. Zhang, Z. W. Dong, G. J. You, S. X. Qian, H. Deng, *Opt. Lett.* **31**, 3345 (2006).

35. This work was supported by the NSF and the Air Force Office of Scientific Research in the Gordon and Betty Moore Center at Caltech. We wish to thank Z. L. Wang for providing the samples, which were made by P. Fei and S. Xu, and K. Xu for the help with the SEM measurement in J. R. Heath's laboratory at Caltech.

Supporting Online Material

www.sciencemag.org/cgi/content/full/321/5896/1660/DC1
Materials and Methods
Figs. S1 to S3
References

19 June 2008; accepted 13 August 2008
10.1126/science.1162049

Chondrulelike Objects in Short-Period Comet 81P/Wild 2

Tomoki Nakamura,[1]* Takaaki Noguchi,[2] Akira Tsuchiyama,[3] Takayuki Ushikubo,[4] Noriko T. Kita,[4] John W. Valley,[4] Michael E. Zolensky,[5] Yuki Kakazu,[1] Kanako Sakamoto,[1] Etsuko Mashio,[3] Kentaro Uesugi,[6] Tsukasa Nakano[7]

The Stardust spacecraft returned cometary samples that contain crystalline material, but the origin of the material is not yet well understood. We found four crystalline particles from comet 81P/Wild 2 that were apparently formed by flash-melting at a high temperature and are texturally, mineralogically, and compositionally similar to chondrules. Chondrules are submillimeter particles that dominate chondrites and are believed to have formed in the inner solar nebula. The comet particles show oxygen isotope compositions similar to chondrules in carbonaceous chondrites that compose the middle-to-outer asteroid belt. The presence of the chondrulelike objects in the comet suggests that chondrules have been transported out to the cold outer solar nebula and spread widely over the early solar system.

Many small particles were recovered from the Jupiter-family short-period comet 81P/Wild 2 by the Stardust mission (*1*). The particles are thought to represent dust that was present in the outer regions of the early solar system where Kuiper belt objects, the predecessor of short-period comets, presumably formed. The comet Wild 2, now orbiting between Mars and Jupiter, had a wider orbit reaching the Kuiper belt [30 to 50 astronomical units (AU) from the Sun] before 1974 (*2*). Asteroids are principally located much closer (3 to 5 AU) to the Sun and are presumed to be the parent bodies of the primitive class of meteorites, chondrites. These are mostly [up to 80% (*3*, *4*)] made up of chondrules, which were formed in the solar nebula around 4.565 billion years ago (*5*) by multiple episodes of total or partial melting of preexisting solid particles typically smaller than 1 mm in diameter. Here, we

[1]Department of Earth and Planetary Science, Faculty of Science, Kyushu University, Hakozaki, Fukuoka 812-8581, Japan. [2]College of Science, Ibaraki University, 2-1-1 Bunkyo, Mito 310-8512, Japan. [3]Department of Earth and Space Science, Graduate School of Science, Osaka University, Toyonaka 560-0043, Japan. [4]Department of Geology and Geophysics, University of Wisconsin-Madison, Madison, WI 53706–1692, USA. [5]Astromaterials Research and Exploration Science, NASA Johnson Space Center, Houston, TX 77058, USA. [6]Japan Synchrotron Radiation Research Institute, SPring-8, Sayo, Hyogo 679-5198, Japan. [7]Geological Survey of Japan, Advanced Industrial Science and Technology, Tsukuba 305-8567, Japan.
*To whom correspondence should be addressed. E-mail: tomoki@geo.kyushu-u.ac.jp

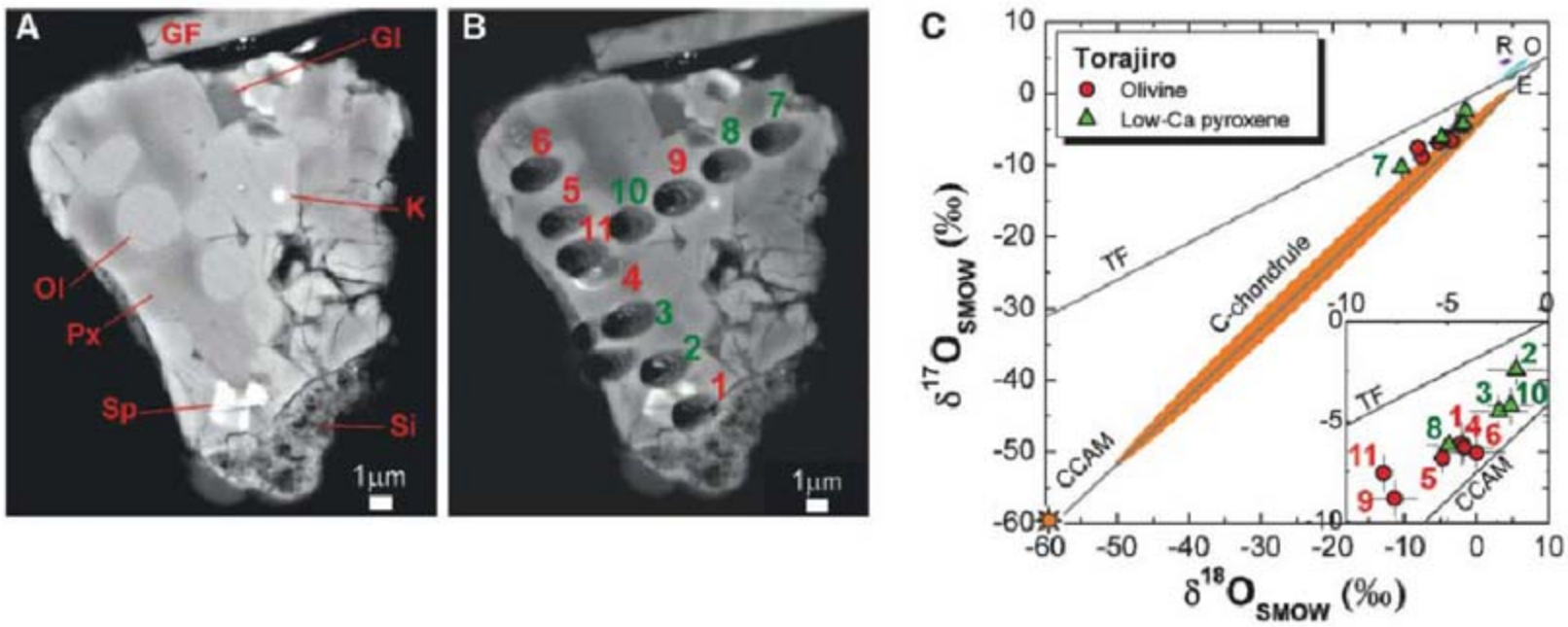

Fig. 1. Mineralogical, textural, and isotopic features of Torajiro. (**A**) Backscattered electron (BSE) image of a cross section showing a porphyritic texture. Vesiculate melted aerogel is present with a sharp contact with Torajiro, indicating that Torajiro itself was not melted during the hypervelocity impact into aerogel. Gl, glass; K, kamacite; Ol, olivine; Px, low-Ca pyroxene; Sp, Cr-spinel; Si, silica aerogel; and GF, glass fiber holding the particle. (**B**) BSE image showing spots analyzed with ion microprobe for oxygen isotope ratios. We made two sets of line analysis at 3-μm intervals by using a small Cs^+ beam 2 μm in diameter. (**C**) Oxygen isotope ratios of olivine and low-Ca pyroxene. The data point numbers correspond to those in (B). Compositional fields of chondrules in various chondrites, including enstatite (E) (*17*), ordinary (O) (*15*), and rumuruti (R) (*16*); carbonaceous (C) (*19*, *20*) chondrites are also shown for comparison. The Sun symbol indicates the oxygen composition of the Sun (*31*). TF, terrestrial fractionation line; CCAM, carbonaceous chondrite anhydrous mixing line. Error bars represent ±2 SD.

report that the Stardust samples include chondrule-like objects. Fifty particles from comet Wild 2 were first analyzed by synchrotron radiation x-ray diffraction and microtomography to identify crystalline particles that retain original characteristics of cometary dust (*6*). Four particles, named Torajiro, Gozen-sama, Gen-chan, and Lilly, were chosen for detailed analysis (*7*).

Torajiro (C2054,0,35,6) is a terminal particle extracted from a small branch of track 35 (*7*). Electron microscopy (EM) of the polished surface shows a porphyritic texture (Fig. 1A) that consists mainly of olivine [$Fo_{79\text{-}80}$ (see table S1 for chemical composition)], low-Ca pyroxene [$En_{86}Wo_3$ ~ $En_{79}Wo_5$ (table S1)], small kamacite blebs, and mesostasis glass enriched in SiO_2 and Al_2O_3 (table S1). On one side, olivine grains are poikilitically enclosed within pyroxene. Subhedral Cr-rich spinels are in contact with olivine. Ion-microprobe analysis (11 points as shown in Fig. 1B) indicates that Torajiro is heterogeneous in oxygen isotopic ratios (Fig. 1C). Olivine grains have a $\delta^{18}O$ relative to standard mean ocean water ($\delta^{18}O_{SMOW}$) of –8 to –4 per mil (‰). Low-Ca pyroxene, with slightly high Al_2O_3 and CaO contents (spot 7 in table S1), has a $\delta^{18}O$ of –10‰, whereas other pyroxenes (table S1) have a higher $\delta^{18}O$ of –5 to –2‰.

Gozen-sama (C2081,1,108,1) is the largest terminal particle (40 μm in diameter) in track 108 (*7*). Tomographic analysis shows that this particle contains many small round FeNi metal inclusions (Fig. 2A). EM of the polished surface indicates that it has a poikilitic texture (Fig. 2B); two rounded olivines (Ol-A and Ol-B) are enclosed within low-Ca pyroxene. Both grains are uniformly Fo_{95} (table S1). Low-Ca pyroxene is $En_{95}Wo_1$ (table S1) and monoclinic (*7*).

The oxygen isotope ratios of the crystals in Gozen-sama (10 points shown in Fig. 2C) are heterogeneous (Fig. 2D). Ol-A has the lowest $\delta^{18}O$ and varies from –50 to 2‰, whereas Ol-B has a higher $\delta^{18}O$, from 2 to 5‰. The low-Ca pyroxene has a composition intermediate between the two olivines. Analyses with a smaller primary beam (36 points shown in Fig. 2D and fig. S6) revealed that Ol-A contains a 3-μm-by-5-μm core area highly enriched in ^{16}O ($\delta^{18}O < -10‰$) (Fig. 2D and table S2), whereas the $\delta^{18}O$ of the rim is close to that of the surrounding low-Ca clinopyroxene.

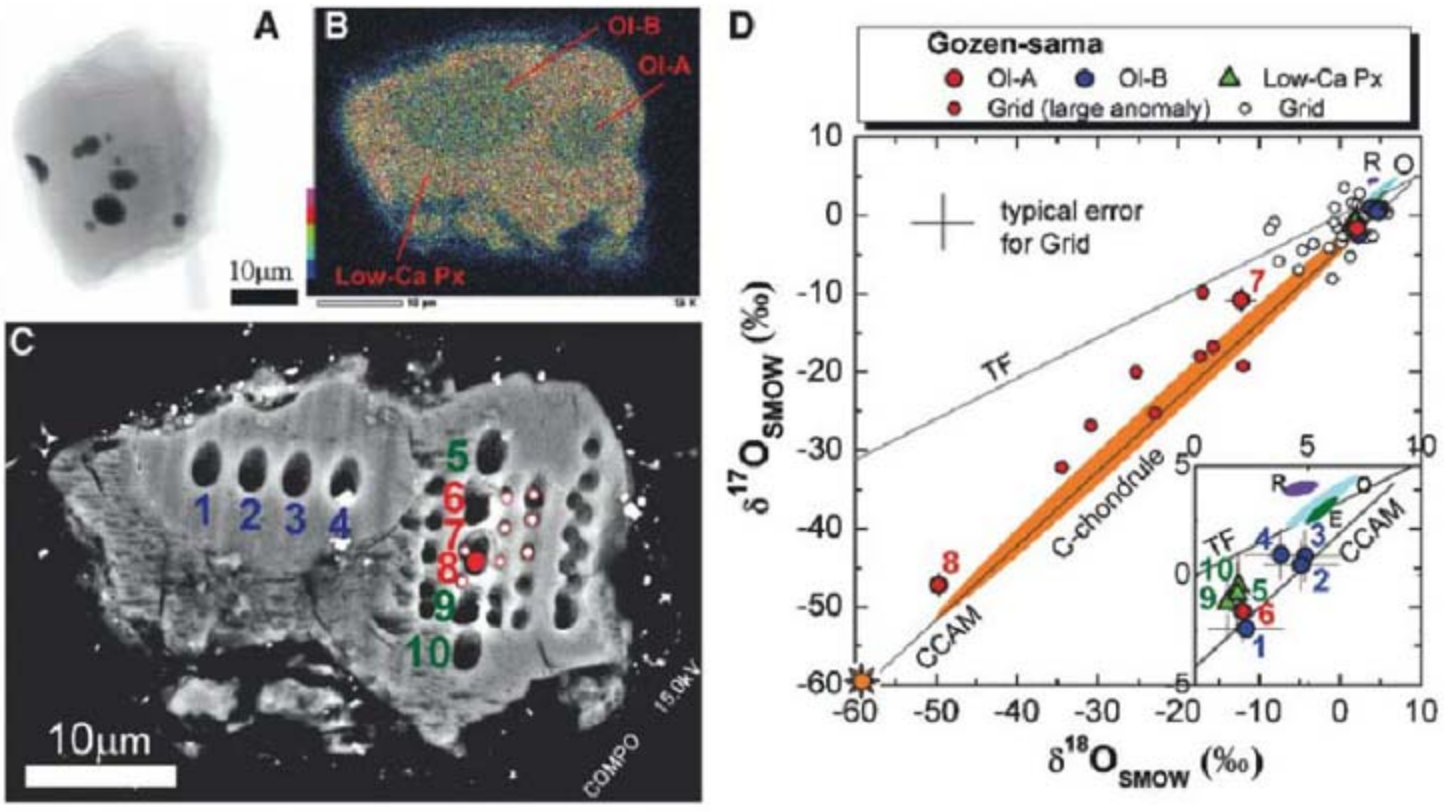

Fig. 2. A large terminal particle, Gozen-sama, 40 μm in diameter. **(A)** Transmitted x-ray image showing that the particle contains many rounded dark inclusions of FeNi metal. The presence of a crescent-shaped inclusion on the far-left-hand side of the particle suggests ablation of the surface layers during capture. **(B)** Silicon x-ray map of a cross section showing a typical poikilitic fabric, in which two olivine phenocrysts (Ol-A and Ol-B) are contained within a low-Ca pyroxene oikocryst (low-Ca Px). (B) is rotated 90° counterclockwise relative to (A). **(C)** BSE image of the cross section in the same frame as (B), showing 10 2-μm diameter spots (numbered, average precision is ±1.3‰, 2 SD) and 36 smaller less precise 1-μm small spots (average precision is ±4.1‰, 2 SD) by ion microprobe. The 2-μm spot with a solid red dot shows the most negative oxygen anomaly, and 1-μm spots with outlined red marks show a surrounding large anomaly. **(D)** Oxygen isotope ratios obtained from 2-μm spots (numbered large marks) and 1-μm spots (small marks). The small red marks are data from the outlined red marks in (C). The star symbol indicates the oxygen isotopic composition of the Sun (*31*). Error bars represent ±2 SD.

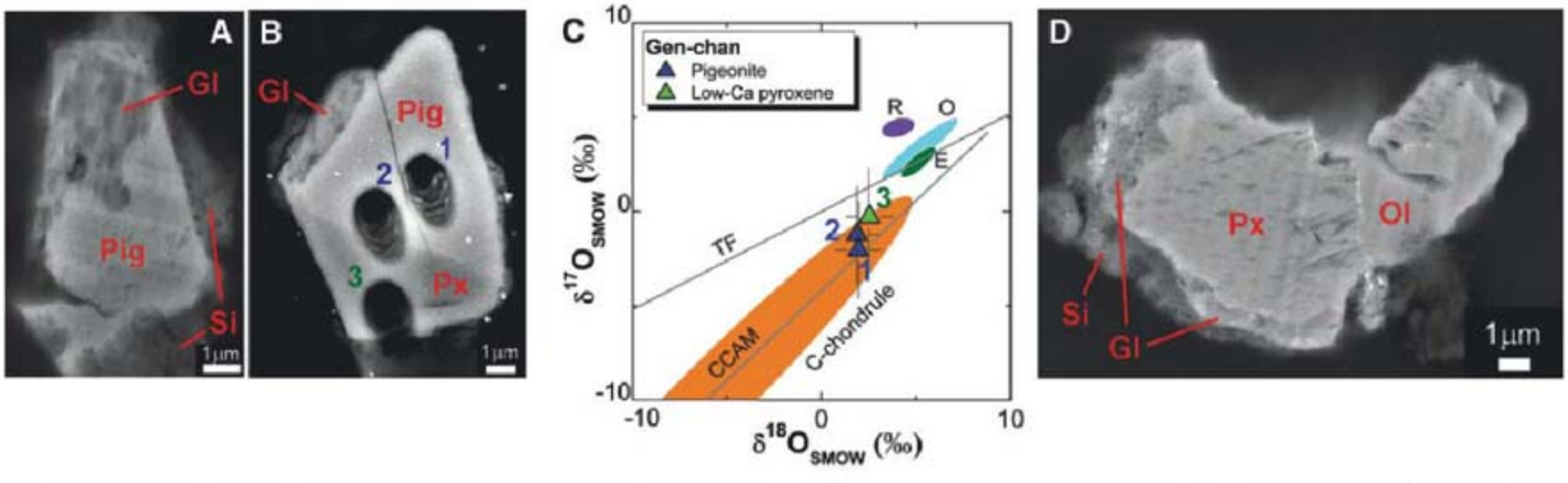

Fig. 3. **(A)** BSE image of a cross section of Gen-chan. **(B)** BSE image of another cross section of Gen-chan, wherein three spots analyzed for oxygen composition are shown. **(C)** Oxygen isotope ratios of pyroxenes in Gen-chan. The numbers correspond to those in (B). **(D)** BSE image of a cross section of Lilly. The thin white line between olivine and pyroxene is chromite. Gl, glass; Ol, olivine; Px, low-Ca pyroxene; Pig, pigeonite; Si, silica aerogel. Error bars represent ±2 SD.

Gen-chan (C2081,1,108,7) is a terminal particle of track 108. Observation of the polished surface shows Mn-rich pigeonite [$En_{84}Wo_{11}$ (table S1)], low-Ca pyroxene [$En_{97}Wo_2$ (table S1)], and SiO_2- and Al_2O_3-rich glass (Fig. 3, A and B, and table S1). The corroded shape of the pigeonite suggests resorption during partial melting or crystallization as hopper crystals. Oxygen isotope ratios in the pyroxenes are almost nearly constant (Fig. 3C).

Lilly (C2054,0,35,4) was located on the wall of track 35, close to Torajiro. It contains a large low-Ca pyroxene [$En_{89}Wo_4$ (table S1)] in contact with Mn-rich olivine [Fo_{91} and 2.0 weight percent (wt %) MnO (table S1)] and SiO_2- and Al_2O_3-rich glass or possibly albitic plagioclase (Fig. 3D). Submicroscopic chromite grains smaller than 100 nm in size are entrained at the boundary between pyroxene and olivine. We did not perform ion-microprobe analysis on this particle because it was difficult to polish.

Most chondrules in meteorites are characterized by (i) igneous porphyritic or poikilitic textures suggestive of partial melting at high temperatures; (ii) presence of glass formed during rapid cooling, which is directly in contact to silicates; and (iii) dominant occurrence of Mg-rich olivine and low-Ca pyroxene with minor amounts of rounded Fe-metal inclusions (*3*, *4*), suggestive of crystallization under reducing conditions in space. These characteristics are observed in the four particles from Comet Wild 2. Therefore, these particles are chondrulelike objects formed by short-duration partial melting. The high abundance of low-Ca pyroxene sets them apart from other high-temperature objects, such as calcium aluminum–rich inclusions (CAIs) (*3*) and amoeboid olivine aggregates (*8*).

Before capture, the particles had been larger than the present size because they were ablated and disaggregated during deceleration in the aerogel (*9*). The entrance-hole sizes of impact tracks 35 and 108 [1.0 mm by 1.5 mm and 0.35 mm by 0.55 mm, respectively (fig. S3)] give an upper limit for the size of the initial incoming particles. It is uncertain whether any two particles from the same track (Gozen-sama and Gen-chan from track 108 and Torajiro and Lilly from track 35) were parts of a single chondrule before their capture, but the idea cannot be ruled out because Gozen-sama and Gen-chan contain low-Ca pyroxene with a similar Fe/Mg ratio (table S1). Compared with average meteorite porphyritic chondrules (*3*, *4*), the crystal size of olivine in Torajiro and Gozen-sama [mostly 2 to 10 μm (Figs. 1A and 2B)] is much smaller. But some chondrites, such as the ALH-85085 CH chondrite, have similarly fine-grained chondrules (*10*).

In Torajiro and Gozen-sama, olivine and pyroxene have heterogeneous oxygen composition along the slope 1 line (Figs. 1C and 2D). Therefore, they should have formed through partial melting of precursor materials with various oxygen compositions. This is clearly seen in Gozen-sama, in which Ol-A and Ol-B show an extremely different $\delta^{18}O$, whereas pyroxene shows a homogeneous $\delta^{18}O$ intermediate between the two olivines (Fig. 2D), indicating that olivine grains are partial-melting residue and that pyroxene crystallized from the melt. During heating, the Fe/Mg ratios of Ol-A and Ol-B almost equilibrated (table S1), but the oxygen isotope heterogeneity was preserved because oxygen diffusion in olivine (*11*) is much slower than Fe-Mg exchange in olivine (*12*). The extreme heterogeneity of oxygen isotope ratios in Gozen-sama may indicate spatial and temporal differences in the nebular-gas composition from which precursor olivine grains formed (*13*). After heating, Gozen-sama cooled rapidly; otherwise, the low-Ca pyroxene would not be monoclinic (*14*).

Major element abundances of olivine, pyroxene, and mesostasis glass in the four cometary particles (table S1) are within the range of compositions defined by a majority of meteorite chondrules (*3*, *4*). However, the range of oxygen isotope ratios of these particles spans the entire range observed for chondrules in carbonaceous chondrites (Figs. 1C, 2D, and 3C). None of the data plots on or above the terrestrial mass fractionation line, which clearly resolves these particles from ordinary (*15*) and rumuruti (*16*) chondrite ($\Delta^{17}O$ = >0‰) and enstatite (*17*) chondrite ($\Delta^{17}O$ = 0‰) objects. Therefore, the chondrulelike objects in Wild 2 are most similar to type-I and -II olivine-pyroxene chondrules in carbonaceous chondrites. Spectroscopic studies infer that carbonaceous chondrites came from asteroids located mainly at the mid- to outer asteroid belt, whereas ordinary and enstatite chondrites are from the inner asteroid belt (*18*). Therefore, the Wild 2 chondrulelike objects have a strong relation with chondrules in the outer asteroid belt.

One notable difference from known carbonaceous chondrite chondrules is the extremely ^{16}O-rich sample, Gozen-sama (table S1). Most meteorite chondrules show a more limited range ($\delta^{18}O$ > –15‰) (*19*) with few exceptions (down to –51‰ in $\delta^{18}O$) (*20*). Furthermore, MnO concentrations in some olivines [0.8 wt % in Torajiro and 2.0 wt % in Lilly (table S1)] and pyroxenes [0.6 wt % in Torajiro and 5.1 wt % in Gen-chan (table S1)] in Wild 2 chondrulelike objects are higher than those in meteorite chondrules [lower than 0.5 wt % in most cases (*3*)]. Although the origin of MnO enrichment is not clear (*21*), it is commonly observed in Wild 2 olivine and pyroxene (*22*).

Our study demonstrates that chondrulelike objects were present at Kuiper belt–formation regions. These objects may be present in the other studied Wild 2 particles based on the presence of roedderite, a characteristic mineral of alkali-rich chondrules (*23*), and Si-O-Al–rich glass in contact to pyroxene (*24*). The presence of both chondrulelike objects and CAIs (*25*) in Wild 2 suggests that high-temperature components of short-period comets and asteroids are similar.

The gas density in the protoplanetary disk decreased with distance from the Sun (*26*). In situ production of chondrules in the Kuiper belt region by shock-wave propagation would require a gas density much higher than that envisaged by standard solar nebular models (*27*). Otherwise, the temperature of preexisting solid dust precursors would not reach the melting point (*27*). Therefore, formation of chondrules directly in the Kuiper belt is unlikely.

Similarities in oxygen isotope ratios between cometary chondrulelike objects and asteroidal chondrules suggest that chondrules formed in the inner solar nebula and were transported to the outer nebula by an X-wind (*28*) or outward flow in the midplane (*29*). The CAI particle called Inti (*1*) contains (Ti, V)N (*30*), the highest temperature condensate from a gas with solar composition, which also requires the material transportation across the solar nebula. The most ^{16}O-rich composition of Wild 2 chondrulelike objects is –49.7 ± 0.9‰ in $\delta^{18}O$ (table S1) and that of the Wild 2 CAI (*25*) is –41.6 ± 1.3‰ in $\delta^{18}O$, suggesting that both sampled a common oxygen reservoir during formation, probably from an inner solar nebula with the same oxygen composition as the Sun (*31*).

References and Notes

1. D. Brownlee *et al.*, *Science* **314**, 1711 (2006).
2. M. Królikowska, S. Szutowicz, *Astron. Astrophys.* **448**, 401 (2006).
3. A. J. Brearley, R. H. Jones, in *Planetary Materials*, J. J. Papike, Ed. (Mineralogical Society of America, Chantilly, VA, 1998), chap. 3, pp. 1–398.
4. J. N. Grossman, A. E. Rubin, H. Nagahara, E. A. King, in *Meteorites and the Early Solar System*, J. F. Kerridge, M. S. Matthews, Eds. (Univ. Arizona Press, Tucson, AZ, 1988), pp. 619–659.
5. Y. Amelin, A. N. Krot, I. D. Hutcheon, A. A. Ulyanov, *Science* **297**, 1678 (2002).
6. T. Nakamura *et al.*, *Meteorit. Planet. Sci.* **43**, 247 (2008).
7. Materials and methods are available as supporting material on *Science* Online.
8. L. J. Chizmadia, A. Rubin, J. T. Wasson, *Meteorit. Planet. Sci.* **37**, 1781 (2002).
9. G. J. Flynn *et al.*, *Science* **314**, 1731 (2006).
10. J. N. Grossman, A. E. Rubin, G. J. MacPherson, *Earth Planet. Sci. Lett.* **91**, 33 (1988).
11. O. Gérard, O. Jaoul, *J. Geophys. Res.* **94**, 4119 (1989).
12. R. Dohmen, T. Chakraborty, *Phys. Chem. Miner.* **34**, 409 (2007).
13. J. Aléon, A. El Goresy, E. Zinner, *Earth Planet. Sci. Lett.* **263**, 114 (2007).
14. J. R. Smyth, *Am. Mineral.* **59**, 345 (1974).
15. R. N. Clayton, T. K. Mayeda, J. N. Goswami, E. J. Olsen, *Geochim. Cosmochim. Acta* **55**, 2317 (1991).
16. M. K. Weisberg *et al.*, *Geochim. Cosmochim. Acta* **55**, 2657 (1991).
17. R. N. Clayton, T. K. Mayeda, *Proc. Lunar Planet. Sci. Conf.* **XVI**, 142 (1985).
18. M. J. Gaffey, J. F. Bell, D. P. Cruikshank, in *Asteroid II*, R. P. Binzel, T. Gehrels, M. S. Matthews, Eds. (Univ. Arizona Press, Tucson, AZ, 1989), pp. 98–127.
19. R. N. Clayton, *Annu. Rev. Earth Planet. Sci.* **21**, 115 (1993).
20. R. H. Jones *et al.*, *Geochim. Cosmochim. Acta* **68**, 3423 (2004).
21. W. Klöck, K. L. Thomas, D. S. Mckay, H. Palme, *Nature* **339**, 126 (1989).
22. M. E. Zolensky *et al.*, *Science* **314**, 1735 (2006).
23. D. J. Joswiak *et al.*, *38th Lunar Planet. Sci. Conf.* abstract 2142; www.lpi.usra.edu/meetings/lpsc2007/pdf/2142.pdf (2007).
24. K. Tomeoka, N. Tomioka, I. Ohnishi, *Meteorit. Planet. Sci.* **43**, 273 (2008).
25. K. D. McKeegan *et al.*, *Science* **314**, 1724 (2006).
26. C. Hayashi, K. Nakazawa, Y. Nakagawa, in *Protostars and Planets II*, D. C. Black, M. S. Matthews, Eds. (Univ. Arizona Press, Tucson, AZ, 1985), pp. 1100–1153.

27. A. Iida, T. Nakamoto, H. Susa, *Icarus* **153**, 430 (2001).
28. F. H. Shu, H. Shang, A. E. Glassgold, T. Lee, *Science* **277**, 1475 (1997).
29. F. J. Ciesla, *Science* **318**, 613 (2007).
30. D. E. Brownlee *et al.*, *39th Lunar Planet. Sci. Conf.* abstract 1978; www.lpi.usra.edu/meetings/lpsc2008/pdf/1978.pdf (2008).
31. K. D. McKeegan *et al.*, *39th Lunar Planet. Sci. Conf.* abstract 2020; www.lpi.usra.edu/meetings/lpsc2008/pdf/2020.pdf (2008).

32. We thank K. Nakamura-Messenger, T. Iwazumi, Y. Wakabayashi, A. Koyama, T. Mori, Y. Suzuki, A. Takeuchi, Y. Terada, H. Nagahara, and H. Yoshida for technical support; M. Sekiya, H. Miura, and M. Uesugi for discussion; and KEK and SPring-8 for experiments. This work was supported by the Japan Society for the Promotion of Science, the NASA Stardust Sample Analysis, and Cosmochemistry Programs. The Wisconsin Secondary Ion Mass Spectrometer Laboratory is partly supported by NSF.

Supporting Online Material
www.sciencemag.org/cgi/content/full/321/5896/1664/DC1
Materials and Methods
SOM Text
Figs. S1 to S6
Tables S1 and S2
References

27 May 2008; accepted 19 August 2008
10.1126/science.1160995

Political Attitudes Vary with Physiological Traits

Douglas R. Oxley,[1*] Kevin B. Smith,[1*] John R. Alford,[2] Matthew V. Hibbing,[3] Jennifer L. Miller,[1] Mario Scalora,[4] Peter K. Hatemi,[5] John R. Hibbing[1]†

Although political views have been thought to arise largely from individuals' experiences, recent research suggests that they may have a biological basis. We present evidence that variations in political attitudes correlate with physiological traits. In a group of 46 adult participants with strong political beliefs, individuals with measurably lower physical sensitivities to sudden noises and threatening visual images were more likely to support foreign aid, liberal immigration policies, pacifism, and gun control, whereas individuals displaying measurably higher physiological reactions to those same stimuli were more likely to favor defense spending, capital punishment, patriotism, and the Iraq War. Thus, the degree to which individuals are physiologically responsive to threat appears to indicate the degree to which they advocate policies that protect the existing social structure from both external (outgroup) and internal (norm-violator) threats.

The nature and source of political attitudes have been the subject of much study (*1*–*3*). Traditionally, such attitudes were believed to be built from sensible, unencumbered reactions to environmental events (*4*), but more recent research emphasizes the built-in, almost "automated" quality of many political responses (*5*), which has been suggested to be based in brain activation variations in limbic regions (*6*–*8*). The research task is now to determine why some people seem primed to adopt certain political attitudes, whereas others appear primed to adopt quite different attitudes. For example, although images and reminders of the terrorist attacks of 9-11 produce an aggregate shift in political views (*9*, *10*), the reasons for individual variability in the degree of attitudinal shifts are unknown.

One possibility is that people vary in general physiology and that certain of these variations encourage the adoption of particular political attitudes. Broad, physiologically relevant traits such as feelings of disgust and fear of disease have been suggested to be related to political attitudes (*11*, *12*), and political beliefs can be predicted by observing brain activation patterns in response to unanticipated events, such as one letter of the alphabet appearing on a computer screen when the respondent expected a different letter (*13*). A connection between self-reports of felt threat and political attitudes has also been identified in previous research (*14*–*19*).

The physiology of response to a perceived threat is an attractive topic of investigation because an appropriate response to environmental threat is necessary for long-term survival and because perceived threat produces a variety of reasonably well-mapped, physically instantiated responses (*20*). If the threat is abrupt, a defensive cascade of linked, rapid extensor-flexor movement occurs throughout the body within 30 to 50 ms (*21*), presumably to reduce vital-organ vulnerability (e.g., eye blink and retraction of the head). Less immediately, perceived threat causes signals from the sensory cortex to be relayed to the thalamus and ultimately to the brain stem, resulting in heightened noradrenergic activity in the locus ceruleus (*22*). Acetylcholine, acting primarily through the amygdala but also through the hypothalamic-pituitary-adrenal axis (*23*), stimulates release of epinephrine, which in turn leads to activation of the sympathetic division of the autonomic nervous system. Though these basic response patterns apply in all people, individual sensitivity to perceived threat varies widely (*24*).

To test the hypothesis that variations in physical sensitivity to threat are associated with political beliefs, in May 2007, we conducted a random telephone sample of the population of Lincoln, Nebraska. Participants were screened [see supporting online material (SOM)] to identify those with strong political attitudes (regardless of the content of those attitudes), and qualifying individuals were invited to a lab in the city. During the first visit, the 46 participants completed a survey instrument (see SOM) ascertaining their political beliefs, personality traits, and demographic characteristics. During the second session, about 2 months after the first, participants were attached to physiological equipment, making it possible to measure skin conductance and orbicularis oculi startle blink electromyogram (EMG) response (*25*).

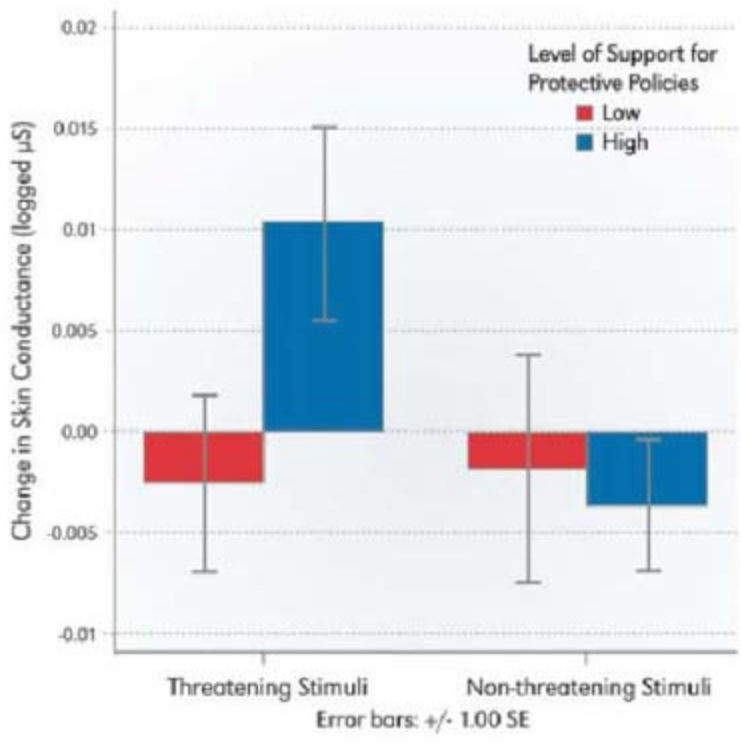

Fig. 1. Changes in skin conductance (in microsiemens) resulting from the viewing of threatening and nonthreatening images for high supporters and low supporters of socially protective policies. Difference of means tests: threatening stimuli $t = 1.98$, $P = 0.05$; nonthreatening stimuli $t = 0.284$, $P = 0.77$, two-tailed tests. All skin conductance data have been logged. Support for policies is measured by self-reported positions on 18 issues relevant to group life (see text), with "high support" including those participants above the median of support and "low support" including those participants below the median.

[1]Department of Political Science, University of Nebraska-Lincoln, Lincoln, NE 68588, USA. [2]Department of Political Science, Rice University, Houston, TX 77251, USA. [3]Department of Political Science, University of Illinois, Urbana-Champaign, Urbana, IL 61801, USA. [4]Department of Psychology, University of Nebraska-Lincoln, Lincoln, NE 68588, USA. [5]Virginia Institute for Psychiatric and Behavioral Genetics, Richmond, VA 23298, USA.

*These authors contributed equally to this work.
†To whom correspondence should be addressed. E-mail: jhibbing@unl.edu

Skin conductance "has been closely linked with the psychological concepts of emotion, arousal, and attention" and "provides relatively direct and undiluted representation of sympathetic activity" (*26*). Arousal causes increased moisture in the outer layers of the skin that in turn enhances conductivity, making it possible to assess sympathetic activation by recording changes in the level of skin conductance. Each participant was shown three separate threatening images (a very large spider on the face of a frightened person, a dazed individual with a bloody face, and an open wound with maggots in it) interspersed among a sequence of 33 images. After logging the data to normalize the distribution, we computed the change in the mean level of skin conductance (SCL) from the previous interstimulus interval (10 s) to the stimulus of interest (20 s). This calculation isolates the change in skin conductance induced by the stimulus and reduces the effects of baseline variations across participants (*27*). We computed the mean change in SCL induced by the three threatening stimuli and determined whether this mean difference was related to variations in preference for socially protective policies (described below). Similar procedures were conducted for three nonthreatening stimuli shown during the series (a bunny, a bowl of fruit, and a happy child).

The other physiological measure was orbicularis oculi startle blink response, an involuntary response to a startling noise. Harder blinks (higher blink amplitudes) are indicative of a heightened "fear state" (*28*). The threatening stimulus was a loud, standardized level of white noise heard by participants (through headphones) at seven unexpected moments while they were looking at a computer screen containing nothing but a focus point. As is common practice (*28*), we first took the logarithm of the data and then computed participants' average blink amplitude. Because surprising subjects with a sudden, jarring noise is likely to affect all physiological indicators, we conducted the startle portion of the study after completing separate tests on skin conductance. The order of the images and the timing of the auditory startle were randomized once, and then that program was presented to all participants.

The survey instrument contained a battery of items asking respondents whether they agreed with, disagreed with, or were uncertain toward 28 individual political concepts—the well-known Wilson-Patterson format (*29*). We identified particular positions on 18 of these policy issues as those most likely to be held by individuals particularly concerned with protecting the interests of the participants' group, defined as the United States in mid-2007, from threats. These positions are support for military spending, warrantless searches, the death penalty, the Patriot Act, obedience, patriotism, the Iraq War, school prayer, and Biblical truth; and opposition to pacifism, immigration, gun control, foreign aid, compromise, premarital sex, gay marriage, abortion rights, and pornography. We do not label these collections of policy positions as either "liberal" or "conservative" because we measure only one aspect of ideologies and exclude other aspects such as positions on economic issues. We take no stance on whether these positions actually promote the stability and cohesion of the social unit; we only assert that, given the common frames of the modern American policy, those most concerned about social protection will tend to be attracted to the particular policy positions listed.

We computed a summary measure of each participant's stances on the 18 political issues such that those positions suggesting a concern for protecting the social unit were given higher scores. To test the skin conductance portion of our analysis, we divided participants into two groups according to their level of concern for protecting the social unit: those above the median and those below. Participants whose policy positions suggest more concern for protecting the social unit were distinguished by an increase in skin conductance when threatening stimuli were presented (Fig. 1). Those whose positions suggest less concern for protecting the social unit, by contrast, were mostly unaffected by those same stimuli and the difference in these two groups was statistically significant ($P = 0.05$). When participants were shown nonthreatening stimuli, there was no statistically significant difference ($P = 0.77$) in skin conductance changes between the two groups (Fig. 1).

Uncontrolled, bivariate results have the potential to mislead. We therefore regressed each participant's summary level of support for socially protective political policies on changes in skin conductance as well as on four sociodemographic variables commonly used as predictors of political attitudes: gender, age, income, and education (race and ethnicity were not controlled because all but one participant was self-identified as white and non-Hispanic). With the effects of these sociodemographic variables controlled, the effect of increases in skin conductance when viewing threatening stimuli was positive and significant ($P < 0.01$), with a large standardized regression coefficient (0.377) (Table 1). When nonthreatening images were viewed, however, changes in skin conductance appeared to be unrelated to political attitudes pertaining to protecting the social order. In this multiple regression model, the standardized regression coefficient for skin conductance change was statistically insignificant ($P = 0.96$), small, and slightly negative (−0.007) (Table 2).

A further test of this pattern is possible when, for each participant, mean skin conductance change occasioned by the viewing of the nonthreatening stimuli is subtracted from mean skin

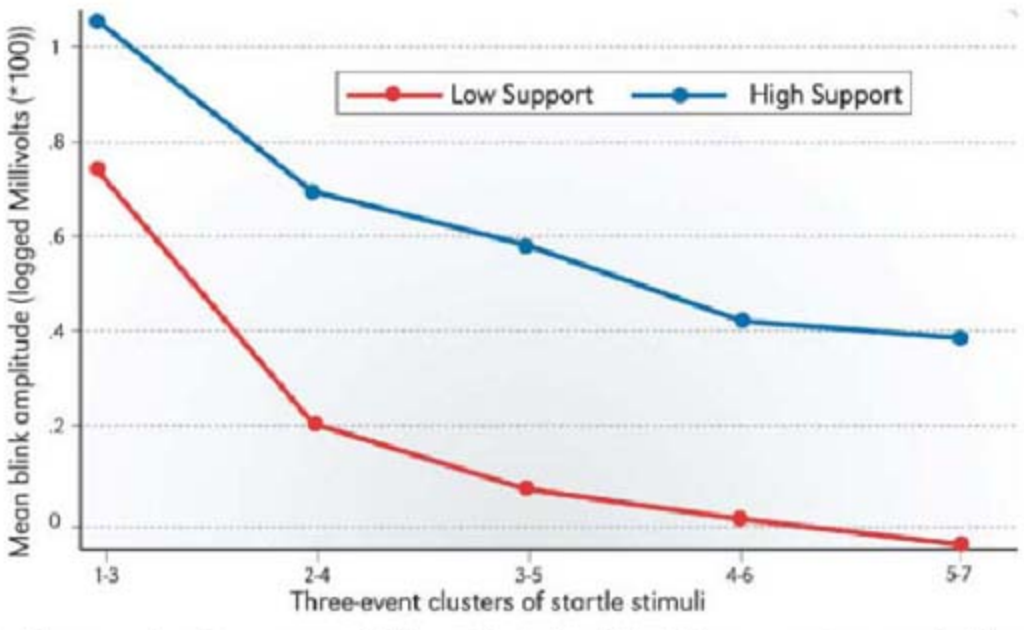

Fig. 2. Three-event moving average of blink amplitude (in millivolts) in response to seven startling noises administered at unexpected times during the absence of visual stimuli for high supporters and low supporters of socially protective politics. Lines represent mean response for the two groups for each cluster of three responses and are designed to show habituation. All blink amplitude data have been converted to logarithm values so readings less than 0 are possible. Support for policies is as described in Fig. 1.

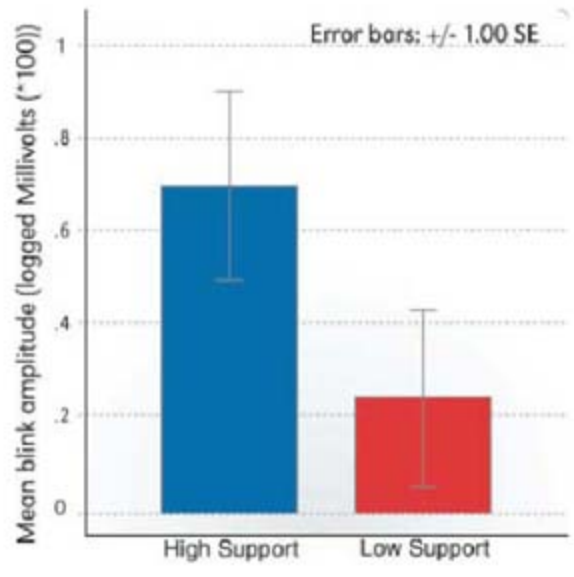

Fig. 3. Mean blink amplitude in response to all seven startling noises for high supporters and low supporters of socially protective politics. Bars are mean blink amplitudes (in millivolts). Difference of means tests for overall means: $t = 1.64$, $P = 0.10$. Support for policies is as described in Fig. 1.

conductance change when viewing the threatening stimuli. When this variable was entered into the multiple regression with age, income, education, and gender, it was in the expected direction (greater relative reaction to threatening stimuli correlates with more support for socially protective policies), sizable (standardized regression coefficient = 0.28), and statistically significant ($P = 0.04$). Full results of this analysis are presented in the SOM.

Table 1. Explaining support for socially protective policies with physiological reactions to threatening images. Results of ordinary least squares (OLS) regression with support for socially protective policies (possible range from 0 to 18), with higher numbers indicating attitudes more supportive of policies thought to protect the social unit regressed on five explanatory variables: gender (0 = male; 1 = female), age (in years), education (six categories ranging from "did not finish high school" to "college degree plus"), income (six categories ranging from an annual salary of less than $20,000 to an annual salary of more than $100,000), and changes in skin conductance level (SCL) occasioned by the viewing of threatening images. Descriptive statistics on the variables and further discussion of the regression techniques are available in the SOM. *$P < 0.05$, two-tailed t test.

Variable	Unstandardized coefficient (SE)	Standardized coefficient
SCL	92.2* (29.03)	0.377
Income	−0.395 (0.471)	−0.10
Education	−1.63* (0.465)	−0.42
Age	0.19 (0.10)	0.235
Gender	−2.34 (1.3)	−0.20
Constant	−353* (193)	
N	46	
Adj. R-square	0.37	

Table 2. Explaining support for socially protective policies with physiological reactions to nonthreatening images. Results of regression (OLS) with support for socially protective policies regressed on five explanatory variables. Variables are the same as those described for Table 1 except that skin conductance (SCL) is the change in skin conductance occasioned by the viewing of nonthreatening images. Descriptive statistics and further discussion of the regression techniques are available in the SOM. *$P < 0.05$, two-tailed t test.

Variable	Unstandardized coefficient (SE)	Standardized coefficient
SCL	−1.8 (35.08)	−0.007
Income	−0.438 (0.533)	−0.115
Education	−1.57* (0.53)	−0.408
Age	0.165 (0.11)	0.204
Gender	−2.23 (1.52)	−0.196
Constant	−304* (217)	
N	46	
Adj. R-square	0.21	

Table 3. Explaining support for socially protective policies with blink amplitude in response to startling noises. Results of regression (OLS) with support for socially protective policies regressed on five explanatory variables. Variables are the same as those described for Table 1 except that mean amplitude is the mean blink amplitude for each participant following seven startle events (see Fig. 1). Descriptive statistics and further discussion of the regression techniques are available in the SOM, as is further discussion of the startle technique and measurement procedures. *$P < 0.05$, two-tailed t test.

Variable	Unstandardized coefficient (SE)	Standardized coefficient
Mean amplitude	1.67* (0.75)	0.286
Income	−0.320 (0.500)	−0.08
Education	−1.76* (0.498)	−0.458
Age	−0.187 (0.10)	0.232
Gender	−2.71 (1.45)	−0.239
Constant	−348 (204)	
N	46	
Adj. R-square	0.30	

Startle blink EMG responses habituate (*28*) (Fig. 2), but the tendency for high blink amplitudes to correlate with respondents supportive of protective policies was consistent across the exercise and was also apparent for the overall means (Fig. 3). Although the difference was not significant in the bivariate analysis, when the sociodemographic controls were added to better specify the model, the coefficient for blink amplitude was again in the predicted (positive) direction, sizable (standardized regression coefficient = 0.286), and statistically significant ($P = 0.03$) (Table 3).

Our data reveal a correlation between physiological responses to threat and political attitudes but do not permit firm conclusions concerning the specific causal processes at work. Particular physiological responses to threat could cause the adoption of certain political attitudes, or the holding of particular political attitudes could cause people to respond in a certain physiological way to environmental threats, but neither of these seems probable. More likely is that physiological responses to generic threats and political attitudes on policies related to protecting the social order may both derive from a common source. Parents could both socialize their children to hold certain political attitudes and condition them to respond in a certain way to threatening stimuli, but conditioning involuntary reflex responses takes immediate and sustained reinforcement and punishment, and it is unlikely that this conditioning varies systematically across political beliefs.

Alternatively, political attitudes and varying physiological responses to threat may both derive from neural activity patterns, perhaps those surrounding the amygdala. There is a connection between localized activation of the amygdala and aversive startle response (*30*). Amygdala activity is also crucial in shaping responses to socially threatening images (*31*, *32*) and may be connected to political predispositions. Indeed, given that political and social attitudes are heritable (*33*–*36*) and that amygdala activity also has been traced to genetics (*37*–*40*), genetic variation relevant to amygdala activity could affect both physiological responses to threat and political attitudes bearing on threats to the social order.

Our findings suggest that political attitudes vary with physiological traits linked to divergent manners of experiencing and processing environmental threats. Consequently, our research provides one possible explanation for both the lack of malleability in the beliefs of individuals with strong political convictions and for the associated ubiquity of political conflict.

References and Notes

1. A. Campbell, P. E. Converse, W. E. Miller, D. E. Stokes, *The American Voter* (John Wiley, New York, 1960).
2. P. E. Converse, in *Ideology and Discontent*, D.E. Apter, Ed. (Free Press, New York, 1964).
3. J. R. Zaller, *The Nature and Origins of Mass Opinion* (Cambridge Univ. Press, New York, 1992).
4. B. I. Page, R. Y. Shapiro, *The Rational Public* (Univ. of Chicago Press, Chicago, 1992).
5. M. Lodge, C. Taber, *Pol. Psychol.* **26**, 455 (2005).

6. G. E. Marcus, W. R. Neuman, M. Mackuen, *Affective Intelligence and Political Judgment* (Univ. of Chicago Press, Chicago, 2000).
7. R. McDermott, *Perspect. Polit.* **2**, 691 (2004).
8. D. Westen, *The Political Brain* (Public Affairs, New York, 2007).
9. M. J. Landau *et al.*, *Pers. Soc. Psychol. Bull.* **30**, 1136 (2004).
10. S. Fahmy, S. Cho, W. Wanta, Y. Song, *Vis. Commun. Q.* **13**, 3 (2006).
11. J. Faulkner, M. Schaller, J. H. Park, L. A. Duncan, *Group Process. Intergroup Relat.* **7**, 333 (2004).
12. C. D. Navarrete, D. M. T. Fessler, *Evol. Hum. Behav.* **27**, 270 (2006).
13. D. M. Amodio, J. T. Jost, S. L. Master, C. M. Lee, *Nat. Neurosci.* **10**, 1246 (2007).
14. J. T. Jost, J. Glaser, A. W. Kruglanski, F. J. Sulloway, *Psychol. Bull.* **129**, 339 (2003).
15. J. T. Jost, *Am. Psychol.* **61**, 651 (2006).
16. L. Huddy, S. Feldman, C. Taber, G. Lahav, *Am. J. Pol. Sci.* **49**, 593 (2005).
17. S. Feldman, *Pol. Psychol.* **24**, 593 (2003).
18. K. Stenner, *The Authoritarian Dynamic* (Cambridge Univ. Press, New York, 2005).
19. F. Pratto, J. Sidanius, L. M. Stallworth, B. F. Malle, *J. Pers. Soc. Psychol.* **67**, 741 (1994).
20. W. B. Cannon, *Bodily Changes in Pain, Hunger, Fear, and Rage* (Appleton, New York, 1915).
21. M. M. Bradley, P. J. Lang, in *Handbook of Psychophysiology*, J. T. Cacioppo, L. G. Tassinary, G. G. Berntson, Eds. (Cambridge Univ. Press, New York, 2007).
22. M. E. Thase, R. H. Howland, in *Handbook of Depression*, E. E. Beckham and W. R. Leber, Eds. (Guilford, New York, 1995).
23. E. Lemche *et al.*, *Hum. Brain Mapp.* **27**, 623 (2006).
24. G. H. Grosser, H. Wechser, M. Greenblatt, *The Threat of Impending Disaster* (MIT Press, Cambridge, MA, 1971).
25. Materials and methods are described in the SOM.
26. M. E. Dawson, A. M. Shell, D. L. Filion, in *Handbook of Psychophysiology*, J. T. Cacioppo, L. G. Tassinary, G. G. Berntson, Eds. (Cambridge Univ. Press, New York, 2007).
27. A. Miller, J. Long, in *Developmental Psychophysiology*, L. A. Schmidt, S. J. Segalowitz, Eds. (Cambridge Univ. Press, New York, 2007).
28. P. J. Lang, M. M. Bradley, B. N. Cuthbert, *Psychol. Rev.* **97**, 377 (1990).
29. G. D. Wilson, J. R. Patterson, *Br. J. Soc. Clin. Psychol.* **7**, 264 (1968).
30. S. Anders, M. Lotze, M. Erb, W. Grodd, *Hum. Brain Mapp.* **23**, 200 (2004).
31. C. L. Larson *et al.*, *Biol. Psychiatry* **60**, 410 (2006).
32. D. A. Fitzgerald, M. Angstad, L. M. Jelsone, P. J. Nathan, K. L. Phan, *Neuroimage* **30**, 1441 (2006).
33. N. G. Martin *et al.*, *Proc. Natl. Acad. Sci. U.S.A.* **83**, 4364 (1986).
34. L. Eaves *et al.*, *Twin Res.* **2**, 62 (1999).
35. J. R. Alford, C. L. Funk, J. R. Hibbing, *Am. Polit. Sci. Rev.* **99**, 153 (2005).
36. J. H. Fowler, L. A. Baker, C. T. Dawes, *Am. Polit. Sci. Rev.* **102**, 233 (2008).
37. Z. F. Mainen, *Nat. Neurosci.* **10**, 1511 (2007).
38. H. Bracha, D. Yoshioka, N. Masakawa, D. Stockman, *J. Affect. Disord.* **88**, 119 (2005).
39. C. A. Ponder *et al.*, T. C. Gilliam, A. A. Palmer, *Genes Brain Behav.* **6**, 736 (2007).
40. A. R. Hariri *et al.*, *Science* **297**, 400 (2002).

41. We thank E. Whitaker, C. Jacobs, B. Sexton, K. A. Espy, J. Brehm, D. Bulling, and the James Long Company for their invaluable assistance. Financial support was provided by the NSF (SES-0721378 and SES-0721707), the ManTech Corporation, and the University of Nebraska–Lincoln's Strategic Research Cluster Grant program.

Supporting Online Material

www.sciencemag.org/cgi/content/full/321/5896/1667/DC1
Materials and Methods
SOM Text
Fig. S1
Tables S1 to S6
Appendix 1

11 March 2008; accepted 18 August 2008
10.1126/science.1157627

An Alternative Menaquinone Biosynthetic Pathway Operating in Microorganisms

Tomoshige Hiratsuka,[1] Kazuo Furihata,[2] Jun Ishikawa,[3] Haruyuki Yamashita,[4] Nobuya Itoh,[1] Haruo Seto,[5] Tohru Dairi[1]*

In microorganisms, menaquinone is an obligatory component of the electron-transfer pathway. It is derived from chorismate by seven enzymes in *Escherichia coli*. However, a bioinformatic analysis of whole genome sequences has suggested that some microorganisms, including pathogenic species such as *Helicobacter pylori* and *Campylobacter jejuni*, do not have orthologs of the *men* genes, even though they synthesize menaquinone. We deduced the outline of this alternative pathway in a nonpathogenic strain of *Streptomyces* by bioinformatic screening, gene knockouts, shotgun cloning with isolated mutants, and in vitro studies with recombinant enzymes. As humans and commensal intestinal bacteria, including lactobacilli, lack this pathway, it represents an attractive target for the development of chemotherapeutics.

In prokaryotes, ubiquinone and menaquinone (MK) are lipid-soluble molecules that shuttle electrons between the membrane-bound protein complexes in the electron-transport chain (*1*, *2*). For example, the facultative anaerobe *Escherichia coli* uses ubiquinone (CoQ-8) under aerobic conditions but uses MK 8 when it is grown anaerobically. By contrast, many Gram-positive aerobes such as *Bacillus subtilis* contain only MKs. MK biosynthesis is therefore essential for the survival of these strains. In mammalian cells, ubiquinone plays a role in the electron-transport chain in the inner mitochondrial membrane, and MK functions as an essential vitamin for the biological activation of a family of proteins involved in blood coagulation (*3*), bone metabolism (*4*), and cell-cycle regulation (*5*). The biosynthesis of MK had been mainly studied in *E. coli*. In this organism, chorismate, which is derived from the shikimate pathway, is converted into MK by seven enzymes (MenA to MenG, Fig. 1). Although humans lack this pathway, essential amounts of MK are normally supplied in the diet.

There is no trace of *menF*, *menD*, *menC*, *menE*, and *menB* gene orthologs in the genome of *Streptomyces coelicolor* A3(2) (*6*–*8*), even though it produces MKs. Similarly, some pathogens that synthesize MK, including *Helicobacter pylori* and *Campylobacter jejuni*, have also been reported to lack *men* gene homologs (*9*–*12*). We performed a tracer experiment with *S. coelicolor* A3(2) and [U-$^{13}C_6$]glucose to test whether an alternative pathway to MK operated in the strain. We found that the labeling patterns of MK differed from those of the classical pathway and that 1,4-naphthoquinone-6-carboxylic acid (Fig. 1) (or its reduced form, 1,4-dihydroxy-6-naphthoate) was an intermediate, which suggests that MK is indeed biosynthesized by an alternative route in this species (*13*). We have identified the genes, enzymes, and biosynthetic intermediates responsible for this alternative pathway, which we have named the futalosine pathway.

We started our investigations by screening genome databases, as well as mutants that require MK for growth. We found that some microorganisms in the epsilon categories of Proteobacteria, Actinobacteria, and the *Deinococcus-Thermus* bacteria groups lacked *men* gene orthologs despite the fact that most of these strains are known to synthesize MKs. From among these, we selected four microorganisms for further analysis: *H. pylori*, *C. jejuni*, *Thermus thermophilus* (*14*) and *S. coelicolor*. We also made comparisons with microorganisms in which the known MK biosynthetic pathway operates, including *E. coli* (*15*), *Bacillus subtilis* (*16*), *Corynebacterium glutamicum* (*17*), and *Mycobacterium tuberculosis* (*18*). To find candidate genes, we first estimated orthologous genes as reciprocal best-hit pairs using the BLAST (Basic Local Alignment Search Tool) program (*19*) with a cutoff *e* value < 10^{-10} and then searched for candidate genes present in the *men* negative group but absent in the *men* positive group. We eventually identified ~50 candidate genes in *S. coelicolor* A3(2). Putative transcriptional regulators and membrane proteins such as adenosine triphosphate–binding cassette transporters that are known to transport a

[1]Biotechnology Research Center, Toyama Prefectural University, Toyama 939-0398, Japan. [2]Division of Agriculture and Agricultural Life Science, The University of Tokyo, Bunkyo-ku, Tokyo 113-8657 Japan. [3]Department of Bioactive Molecules, National Institute of Infectious Diseases, Shinjuku-ku, Tokyo 162-8640, Japan. [4]Advanced Materials Research and Development Laboratory, ADEKA Corporation, Arakawa-ku, Tokyo 116-8553, Japan. [5]Faculty of Applied Bioscience, Tokyo University of Agriculture, Setagaya-ku, Tokyo 156-8502, Japan.

*To whom correspondence should be addressed. E-mail: dairi@pu-toyama.ac.jp

wide variety of metabolic compounds were excluded, leaving four candidates: SCO4326, SCO4327, SCO4506, and SCO4550. The products of these genes had been annotated as hypothetical proteins.

In a series of disruption experiments in *S. coelicolor* A3(2), each candidate gene was replaced with a thiostrepton-resistance gene by double-crossover homologous recombination (*20*). We knocked out all of the candidate genes with agar plates containing MK 4 (having a C20 prenyl side chain), which was commercially available and was substituted for the MK 8 (having a C40 prenyl side chain) usually found in *Streptomyces* strains. Disruption of each of the mutants was confirmed by polymerase chain reaction (PCR) analysis (Fig. 2 and fig. S1). The mutants disrupted at SCO4326, SCO4327, SCO4506, and SCO4550 required MK 4 for their growth. The MKs purified from the mutants were confirmed as MK 4 by high-performance liquid chromatography (HPLC) (Fig. 3 and fig. S2). We also confirmed that the phenotypes of the mutants did not reflect polar effects, a phenomenon in which a disruption of the gene located upstream affected the expression of the downstream gene when these genes constituted an operon (*21*).

To identify the complete set of genes in the alternative pathway, we used N-methyl-N-nitro-N-nitrosoguanidine mutagenesis to obtain mutants that required MK 4 for their growth. Twenty-six mutants were obtained, of which 14 were complemented by plasmids carrying genes we had identified from bioinformatic screening. Shotgun cloning experiments were performed with the other 12 mutants as hosts. Eventually, we succeeded in complementing the mutants by a plasmid carrying the SCO1494, SCO1495, and SCO1496 genes, which encode 3-dehydroquinate synthase, shikimate kinase I, and chorismate synthase, respectively. The mutants were then grown on medium containing shikimate, chorismate, or *o*-succinylbenzoate (an intermediate in the classical pathway) instead of MK 4, but growth was seen only on chorismate (Fig. 4), suggesting that they lacked functional chorismate synthase or shikimate kinase. Because the reaction catalyzed by chorismate synthase is irreversible (*22*), it appeared that the alternative pathway branches at chorismate.

Cocultivation revealed that each of the four mutants could grow together with the others, even in the absence of MK 4, suggesting that mutagenesis had blocked different points in the MK biosynthetic pathway and that intermediates had accumulated in the culture broth that allowed

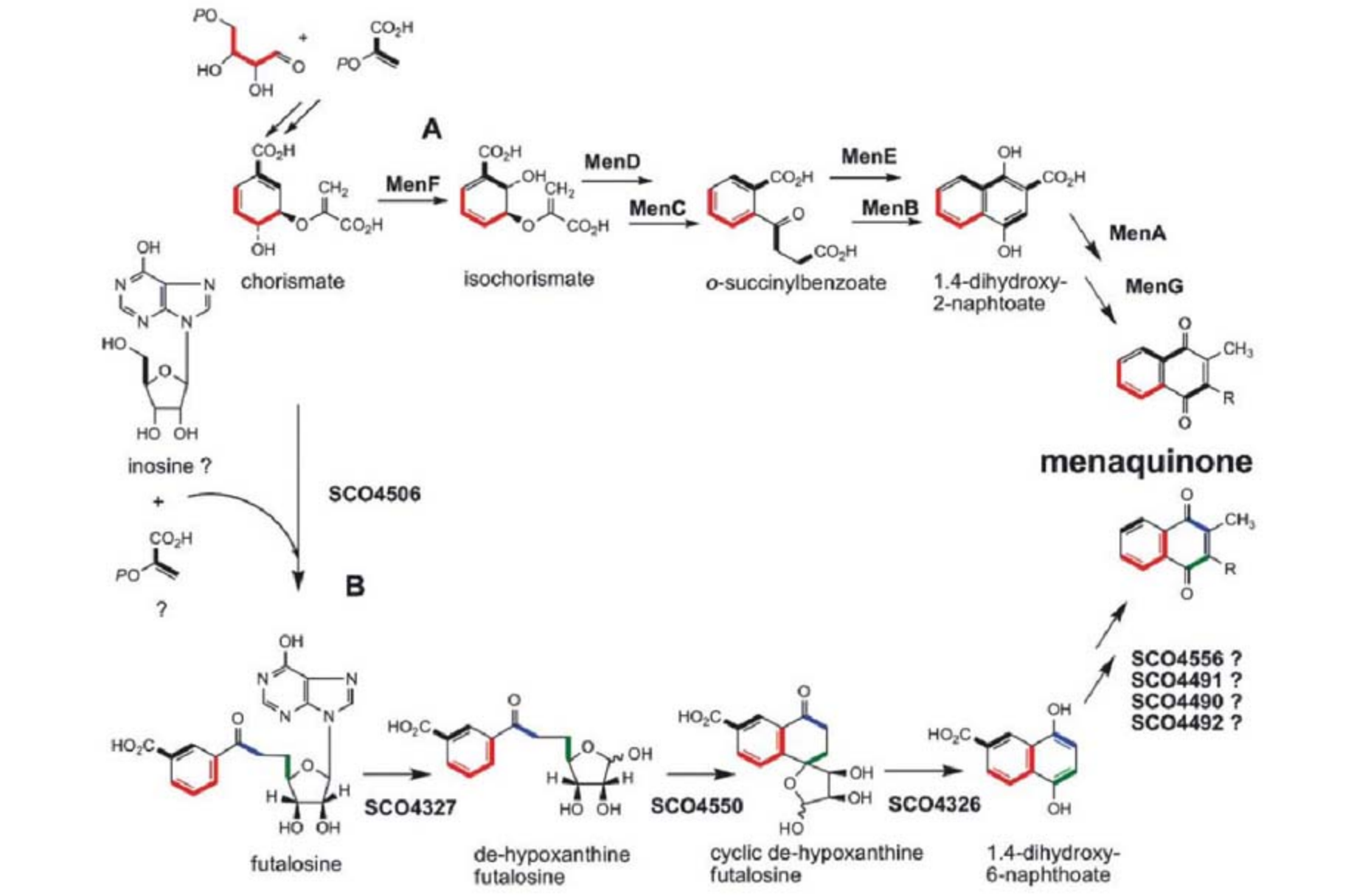

Fig. 1. MK biosynthetic pathways. (**A**) Classical pathway. Chorismate, which is derived from the shikimate pathway, is initially converted into isochorismate by MenF, isochorismate synthase, and then into 2-succinyl-6-hydroxy-2,4-cyclohexadiene-1-carboxylate by MenD, which is a thiamine-dependent enzyme. This compound is dehydrated by MenC to give an aromatic compound, *o*-succinylbenzoate, followed by the attachment of coenzyme A to yield *o*-succinylbenzoyl-CoA by MenE. *o*-Succinylbenzoyl-CoA is then converted into 1,4-dihydroxy-2-naphthoate by MenB. In the last two steps of the pathway, MK is synthesized by MenA and MenG, which catalyze prenylation and *S*-adenosylmethionine-dependent methylation, respectively. Red and black bold lines show carbons originated from erythrose-4-phosphate and phosphoenolpyruvate, respectively. (**B**) Alternative pathway. Green and blue bold lines indicate two carbon units derived from C-5 and C-6 of glucose via different metabolic pathways. Based on the annotation of the open reading frames of *S. coelicolor* A3(2), we presumed that SCO4491 (prenylation), SCO4556 (methylation), SCO4490 (decarboxylation), and SCO4492 (decarboxylation) would be involved in the late step of the MK biosynthetic pathway, although we did not have any direct evidence.

the mutants to compensate. We then cultivated each mutant in the presence of MK 4, the broth was centrifuged, and the supernatant was concentrated in vacuo. After MK 4 was removed by ethyl acetate extraction, the concentrated aqueous layer was added to an agar plate, and growth of the other mutants on this medium was examined (fig. S3). Our results indicated that the blocked points in the MK biosynthesis of the mutants occurred in the following order: SCO4506, SCO4327, SCO4550, and SCO4326.

To purify the intermediates, we first used the SCO4506 and SCO4327 mutants as an intermediate converter and a secretor, respectively. The intermediate was extracted as above, and nuclear magnetic resonance (NMR) and mass spectrometry (MS) (figs. S4 and S5) confirmed the compound as futalosine (Fig. 1). This compound has previously been isolated from the culture broth of a *Streptomyces* strain (*23*). Because the SCO4327 protein has weak similarities to some nucleosidases, we expected it to release hypoxanthine from futalosine. We prepared a SCO4327 recombinant for an in vitro assay; however, no products were formed. It was unclear why the recombinant lacked enzymatic activity, but we assumed that it might be unstable. Hence, we prepared an ortholog of SCO4327 in the extreme thermophile *T. thermophilus* HB8 (TTHA0556 recombinant) (fig. S6), expecting it to be highly thermostable. When the recombinant TTHA0556 was incubated with futalosine, two reaction products were generated. One (fig. S7, peak B) was confirmed as hypoxanthine by HPLC mass spectral analysis (LC-MS). The other (fig. S7, peak C) was purified by reverse-phase preparative HPLC, and its structure was determined by infrared (IR) spectral, MS, and NMR analyses (figs. S8 to S11) as dehypoxanthine (dehypoxanthinyl) futalosine (DHFL) (Fig. 1). This was confirmed as an intermediate in the alternative pathway by a bioassay using the

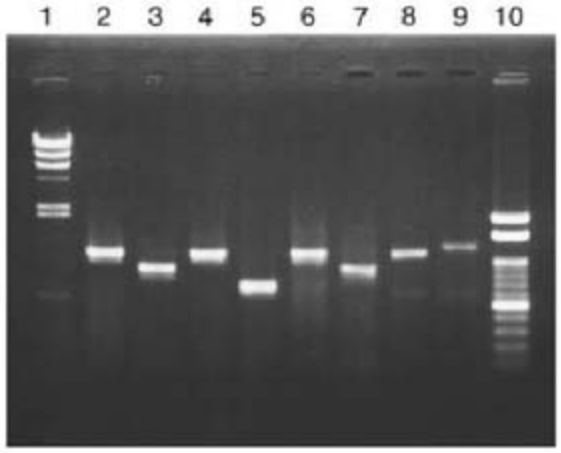

Fig. 2. PCR analyses of genomic DNAs of the SCO4506-disrupted, SCO4326-disrupted, SCO46327-disrupted, and SCO4550-disrupted strains. Genomic DNAs were prepared from the wild-type strain and the disruptants and used for templates for PCR analyses. The amplified fragments were analyzed by agarose gel electrophoresis as follows: molecular marker (lanes 1 and 10); wild-type (lanes 3, 5, 7, and 9); SCO4326-disruptant (lane 2); SCO4327-disruptant (lane 4); SCO4306-disruptant (lane 6); and SCO4550-disruptant (lane 8). The sizes of amplified fragments are schematically shown in fig. S1.

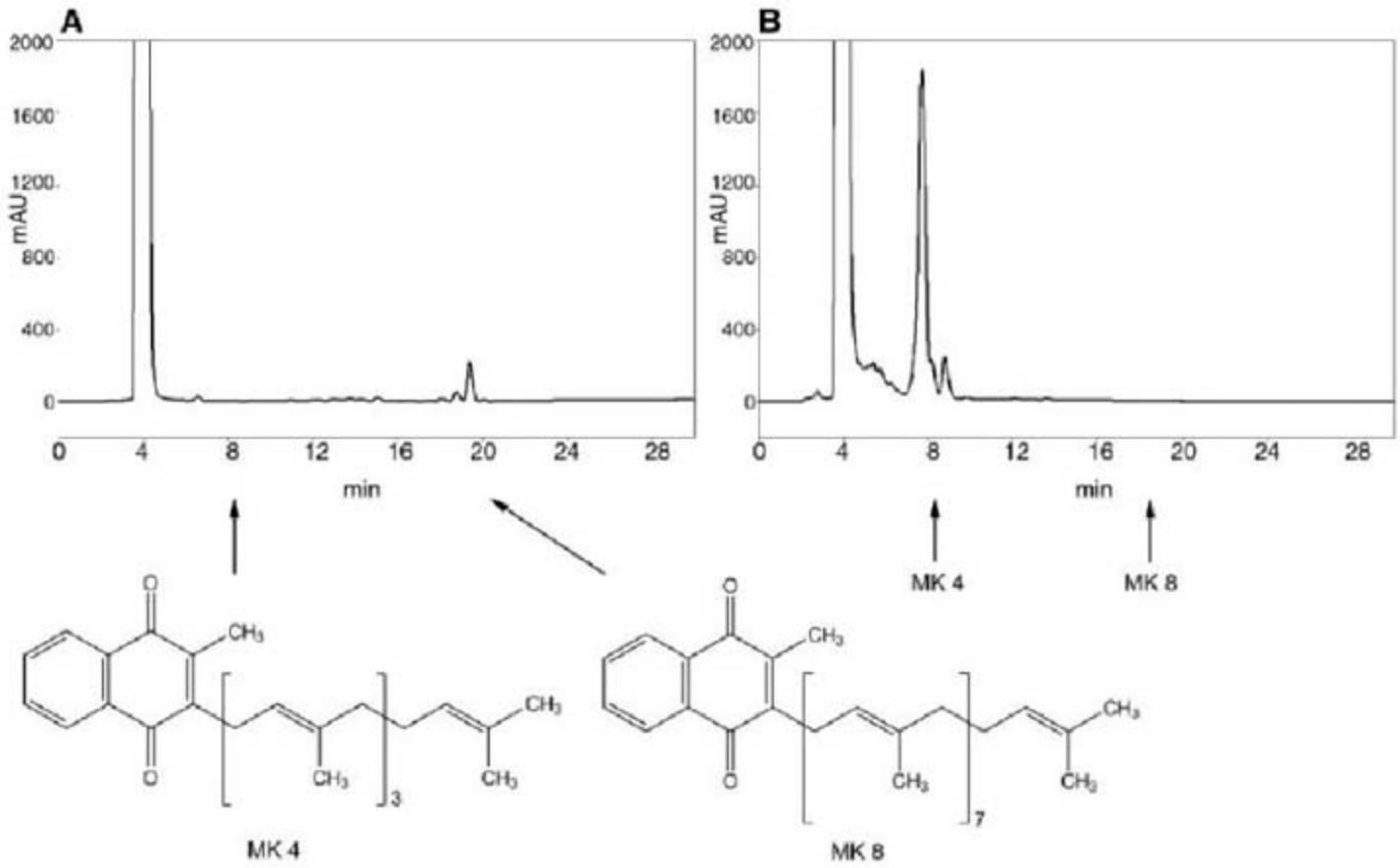

Fig. 3. HPLC analyses of MKs extracted from disruptants. The disruptants were cultivated in the presence of MK 4 (having a C20 prenyl side chain). After cultivation, the MKs were extracted with ethyl acetate and evaporated in vacuo. The obtained materials were analyzed by reverse-phase HPLC. The wild-type (**A**) and the SCO4506-disruptant (**B**) are shown as examples. The SCO4506-disruptant contained only MK4 added into the medium, in contrast to the wild type that had MK8 usually found in *S. coelicolor*. HPLC analyses of MKs extracted from the other disruptants were shown in fig. S2.

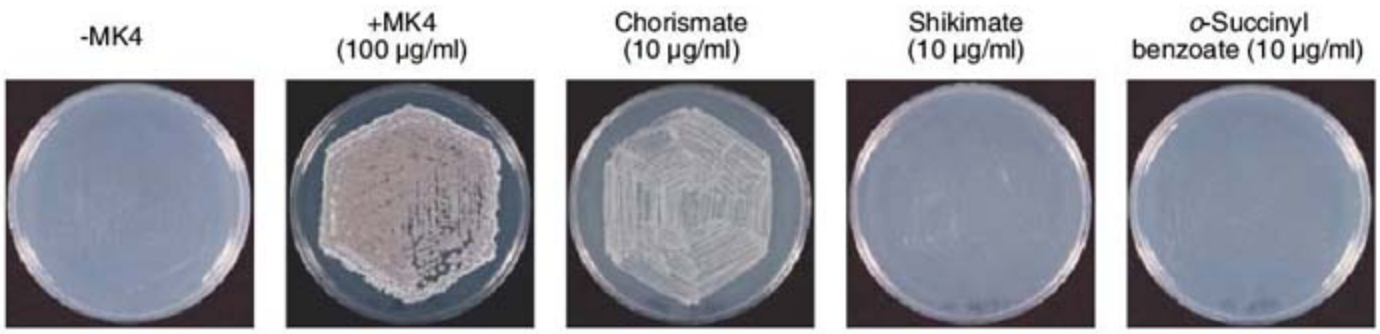

Fig. 4. One of 26 mutants obtained by mutagenic treatment required chorismate for its growth. The mutant was spread onto a yeast extract–malt extract (YEME) plate and a YEME plate containing MK 4, chorismate, shikimate, or *o*-succinylbenzoate. After cultivation at 30°C for 1 week, photographic images were taken of each plate. The mutant could grow only in the presence of chorismate, which suggests that it lacked functional chorismate synthase or shikimate kinase. Because the reaction catalyzed by the former enzyme is irreversible, the alternative pathway branches at chorismate.

SCO4506- and SCO4327-disruptants as converters (fig. S12).

In the next step, we isolated an intermediate from the culture broth of the SCO4326 mutant, which was purified as above and its structure determined as cyclic DHFL (Fig. 1) (figs. S13 to S17).

As a small amount of DHFL accumulated in the culture broth of the SCO4550-disruptant, we predicted that it catalyzed the reaction adjacent to SCO4327. An in vitro enzyme assay was prepared using the recombinant TTHA1092, which contained an ortholog of SCO4550 in *T. thermophilus* HB8. However, we did not detect the formation of cyclic DHFL. Additional enzymes and/or cofactors, and optimized assay conditions, may be necessary.

Recombinant TTHA1568 was prepared to provide an ortholog of SCO4326 in *T. thermophilus* HB8 to convert cyclic DHFL into the next intermediate. A product was obtained and was confirmed to be 1,4-dihydroxy-6-naphthoate by LC-MS (fig. S18); this was previously demonstrated to be an intermediate in the alternative pathway (*13*).

Because the alternative pathway appeared to branch at chorismate with the SCO4506 enzyme, and an examination of the structure of futalosine indicates that the nucleoside moiety is derived from inosine, plus the fact that a tracer experiment (*13*) has implicated a C2 unit from pyruvate or phosphoenolpyruvate between chorismate and inosine forming the C6' and C7' positions of futalosine, we tested the ability of the recombinant enzyme TTHA0803 (an ortholog of SCO4506 in *T. thermophilus* HB8) to catalyze the formation of futalosine. However, we did not detect futalosine, although 3-(1-carboxyvinyloxy) benzoate and m-hydroxybenzoate were formed from chorismate in the absence and presence of flavin mononucleotide (FMN), respectively.

We have succeeded in outlining an alternative pathway for the biosynthesis of MK in microorganisms by a combination of bioinformatics and biochemical experiments. We confirmed the occurrence of the alternative pathway among bacteria and found it (see SOM Text) in several Gram negatives and Archaea, notably in chlamydia and spirochetes. The alternative pathway was distributed only in prokaryotes and was absent in eukaryotes, including lower ones such as fungi, yeasts, and protists. Because humans and commensals, such as lactobacilli, lack this alternative pathway, it is an attractive target for the development of chemotherapeutics. We also searched microorganisms that have both the alternative pathway and the classical pathway or that have both the ubiquinone pathway and the alternative pathway. However, we were not able to find such bacteria among microorganisms whose genome analysis has been completed.

References and Notes

1. R. Bentley, R. Maganathan, *Microbiol. Rev.* **46**, 241 (1982).
2. R. Meganathan, *Vitam. Horm.* **61**, 173 (2001).
3. E. C. Cranenburg, L. J. Schurgers, C. Vermeer, *Thromb. Haemost.* **98**, 120 (2007).
4. S. M. Plaza, D. W. Lamson, *Altern. Med. Rev.* **10**, 24 (2005).
5. D. W. Lamson, S. M. Plaza, *Altern. Med. Rev.* **8**, 303 (2003).
6. S. D. Bentley *et al.*, *Nature* **417**, 141 (2002).
7. I. Borodina, P. Krabben, J. Nielsen, *Genome Res.* **15**, 820 (2005).
8. M. D. Collins *et al.*, *J. Gen. Microbiol.* **100**, 221 (1977).
9. J. F. Tomb *et al.*, *Nature* **388**, 539 (1997).
10. J. Parkhill *et al.*, *Nature* **403**, 665 (2000).
11. S. W. Marcelli *et al.*, *FEMS Microbiol. Lett.* **138**, 59 (1996).
12. C. W. Moss *et al.*, *J. Clin. Microbiol.* **28**, 395 (1990).
13. H. Seto *et al.*, *J. Am. Chem. Soc.* **130**, 5614 (2008).
14. A. Henne *et al.*, *Nat. Biotechnol.* **22**, 547 (2004).
15. F. R. Blattner *et al.*, *Science* **277**, 1453 (1997).
16. F. Kunst *et al.*, *Nature* **390**, 249 (1997).
17. M. Ikeda, S. Nakagawa, *Appl. Microbiol. Biotechnol.* **62**, 99 (2003).
18. S. T. Cole *et al.*, *Nature* **393**, 537 (1998).
19. S. F. Altschul *et al.*, *J. Mol. Biol.* **215**, 403 (1990).
20. D. A. Hopwood *et al.*, Gene Manipulation of Streptomyces, a Laboratory Manual (John Innes Foundation, Norwich, UK, 1985).
21. Materials and methods are available as supporting material on *Science* Online.
22. P. Macheroux *et al.*, *Planta* **207**, 325 (1999).
23. N. Hosokawa *et al.*, *Chem. Pharm. Bull. (Tokyo)* **47**, 1032 (1999).

24. This work was supported in part by a Grant-in-Aid for Scientific Research (B) to S.H. and by a Grant-in-Aid for Scientific Research on Priority Areas "Applied Genomics" from the Ministry of Education, Culture, Sports, Science and Technology of Japan, the Urakami Foundation, and the Skylark Food Science Institute to T.D. Author contributions: T.H., H.S., and T.D. conceived and designed the experiments; T.H., K.F., J.I., H.S., and T.D. performed the experiments; T.H., K.F., H.Y., N.I., H.S., and T.D. analyzed the data; and H.S. and T.D. wrote the paper. The DNA sequences determined and characterized in this study have been deposited in the DDBJ, EMBL, and GenBank data banks as follows: SCO4506, AB447888; SCO4327, AB447889; SCO4550, AB447890; SCO4326, AB447891; TTHA0556, AB447892; TTHA1568, AB447893.

Supporting Online Material

www.sciencemag.org/cgi/content/full/321/5896/1670/DC1
Materials and Methods
SOM Text
Figs. S1 to S18
Tables S1 to S4

13 May 2008; accepted 24 July 2008
10.1126/science.1160446

An Inhibitor of FtsZ with Potent and Selective Anti-Staphylococcal Activity

David J. Haydon,[1] Neil R. Stokes,[1]* Rebecca Ure,[1] Greta Galbraith,[1] James M. Bennett,[1] David R. Brown,[1] Patrick J. Baker,[2] Vladimir V. Barynin,[2] David W. Rice,[2] Sveta E. Sedelnikova,[2] Jonathan R. Heal,[3] Joseph M. Sheridan,[3] Sachin T. Aiwale,[4] Pramod K. Chauhan,[4] Anil Srivastava,[4] Amit Taneja,[4] Ian Collins,[1] Jeff Errington,[1,5] Lloyd G. Czaplewski[1]

FtsZ is an essential bacterial guanosine triphosphatase and homolog of mammalian β-tubulin that polymerizes and assembles into a ring to initiate cell division. We have created a class of small synthetic antibacterials, exemplified by PC190723, which inhibits FtsZ and prevents cell division. PC190723 has potent and selective in vitro bactericidal activity against staphylococci, including methicillin- and multi-drug–resistant *Staphylococcus aureus*. The putative inhibitor-binding site of PC190723 was mapped to a region of FtsZ that is analogous to the Taxol-binding site of tubulin. PC190723 was efficacious in an in vivo model of infection, curing mice infected with a lethal dose of *S. aureus*. The data validate FtsZ as a target for antibacterial intervention and identify PC190723 as suitable for optimization into a new anti-staphylococcal therapy.

Bacterial cell-division proteins, in particular FtsZ, offer unexploited and attractive targets for antibacterial drug discovery because they are essential and widely conserved throughout bacteria (*1*, *2*). During cell division, FtsZ undergoes guanosine 5′-triphosphate (GTP)–dependent polymerization to form the Z ring at the mid-cell. FtsZ recruits other proteins that together drive cell division and the formation of new cell poles (*3*). FtsZ is a distant structural and functional relative of mammalian β-tubulin (*4*–*6*), which is a well-exploited target for anticancer therapy (*6*). This suggests that the protein superfamily is amenable to inhibitor development and may provide structural insights to assist the rational design of FtsZ ligands. Several compounds that block bacterial cell division and/or inhibit the biochemical activity of the FtsZ protein in vitro (*7*–*13*) have been reported; however, so far none has demonstrated efficacy in models of infection or has entered clinical evaluation or use.

3-Methoxybenzamide (3-MBA) ($C_8H_9NO_2$, relative molecular mass of 151.16) (fig. S1) is a small ligand that has been reported to target FtsZ and inhibit cell division in the Gram-positive bacterium *Bacillus subtilis*, resulting in a filamentous morphology (*7*). Although 3-MBA has

[1]Prolysis, Begbroke Science Park, Oxfordshire OX5 1PF, UK. [2]Department of Molecular Biology and Biotechnology, University of Sheffield, Sheffield S10 2TN, UK. [3]Prosarix, Newton Hall, Cambridge CB22 7ZE, UK. [4]Jubilant Chemsys, B-34, Sector-58, Noida 201301, India. [5]Institute for Cell and Molecular Biosciences, Faculty of Medical Sciences, Newcastle University, Newcastle upon Tyne NE2 4HH, UK.

*To whom correspondence should be addressed. E-mail: neil.stokes@prolysis.com

a weak antibacterial potency, it is a small and efficient ligand with on-target activity and is able to penetrate the bacterial cell. It therefore provided a good starting point for a fragment-based approach to antibacterial drug discovery. A medicinal chemistry program was undertaken, first to determine the structure-activity relationships of the benzamide and then to explore and extend the methoxy group. The antibacterial activity of, and the microscopic cell morphology caused by, each derivative was measured to direct the iterative rounds of synthetic chemistry (*14*). Analysis of more than 500 analogs yielded a compound, PC190723 ($C_{14}H_8ClF_2N_3O_2S$, relative molecular mass of 355.75) (Fig. 1A), that inhibited cell division and had a vastly improved potency. PC190723 was constructed from substituted benzamide and thiazolopyridine moieties joined by an ether linkage.

PC190723 had potent antibacterial activity against *B. subtilis* as well as all strains and species of staphylococci that were tested [minimal inhibitory concentration (MIC) in the range of 0.5 to 1.0 μg/ml], including a methicillin-resistant *Staphylococcus aureus* (MRSA) strain and a multi-drug–resistant *S. aureus* (MDRSA) isolate that is resistant to many of the major classes of antibiotics (Table 1). The potency of PC190723 was more than 2000 times greater than that of 3-MBA against *S. aureus* (table S1). PC190723 was inactive against a range of other Gram-positive and Gram-negative pathogenic bacteria and did not inhibit the growth of yeast or human hepatocytes (Table 1). In a bacterial survival assay, concentrations of PC190723 equivalent to or greater than the MIC caused a reduction in viable *S. aureus* cell numbers of more than three logarithms within 24 hours (fig. S2), which was consistent with a bactericidal mode of action.

The in vivo efficacy of PC190723 was demonstrated in a murine septicaemia model of staphylococcal infection. A single subcutaneous (SC) or intravenous (IV) administration of PC190723 at 30 mg/kg resulted in a 100% survival of mice inoculated intraperitoneally with a potentially lethal dose of *S. aureus*, as compared with a 0% survival for the group receiving no compound (Fig. 1B). For both routes of administration, dose-dependent efficacy was observed, and the 50%-effective doses (ED_{50}) were 7.3 and 10.2 mg/kg for SC and IV administration, respectively. PC190723 was also efficacious when administered intraperitoneally (ED_{50} of 3.1 mg/kg) (fig. S3).

To verify the mode of action of the compound, *S. aureus* FtsZ was cloned, overexpressed, and purified, and an in vitro assay was developed to demonstrate that PC190723 directly inhibited the GTPase activity of FtsZ in a concentration-dependent manner with an inhibitory concentration (IC_{50}) of 55 ng/ml (Fig. 2A). A green fluorescent protein (GFP)–FtsZ construct (*11*) in *B. subtilis* was used to show that, after PC190723 exposure, FtsZ was distributed as discrete foci throughout the elongated cell, indicating mislocalization (Fig. 2B). This contrasts with other inhibitors of FtsZ, which cause the dissipation of FtsZ assembly (*9*, *11*). Treating rod-shaped *B. subtilis* or spherical *S. aureus* with PC190723 caused the elongation or enlargement, respectively, of the cells (Fig. 2, C and D). In a time-course experiment, PC190723 caused the maximal enlargement of *S. aureus* cells within 2 hours of exposure, which preceded the reduction in cell viability observed in the time-kill study (fig. S4).

Spontaneous PC190723-resistant *S. aureus* American Type Culture Collection (ATCC) 29213 mutants were isolated at compound concentrations equivalent to eight times the agar MIC or higher at a frequency of 2×10^{-8}, which is consistent with a single-gene–product target for PC190723 (*15*), and without further optimization would be suitable for use as a component in a combination therapy. The *ftsZ* gene of the mutants was sequenced, and each was found to contain an amino acid change in FtsZ at one of six residues: R191, G193, G196, V214, N263, and G266, most frequently at G196. It is possible that the resistance to PC190723 by the spontaneously isolated mutants is due to a secondary mutation(s) in proteins other than FtsZ. To test this, an engineered site-directed mutant of *B. subtilis* carrying only a mutation in FtsZ at G196 was created, which reduced its susceptibility to PC190723 (table S1). Mutations at R191, G193, and G266 conferred PC190723 dependency on *S. aureus*, in that the strains failed to grow in the absence of compound, suggesting that these mutant forms of FtsZ cannot function without having compound bound and providing further evidence of a direct interaction in vivo (fig. S5). Spontaneous mutations in residue A47, which was identified in 3-MBA–resistant *B. subtilis* mutants (*7*), were not isolated. A site-directed mutant of *B. subtilis* carrying the A47P mutation was created and, although it showed reduced susceptibility to 3-MBA, remained susceptible to PC190723 (table S1). Taken together, the biochemical, cytological, and genetic data confirm that PC190723 directly blocks FtsZ activity to prevent septum formation and cell division.

An alignment of FtsZ and tubulin protein sequences revealed that several of the PC190723-resistant mutations in FtsZ coincided with the residues of tubulin that form the binding site for the taxanes (*4*–*6*) (fig. S6). This suggests a common mode of ligand-target interaction between

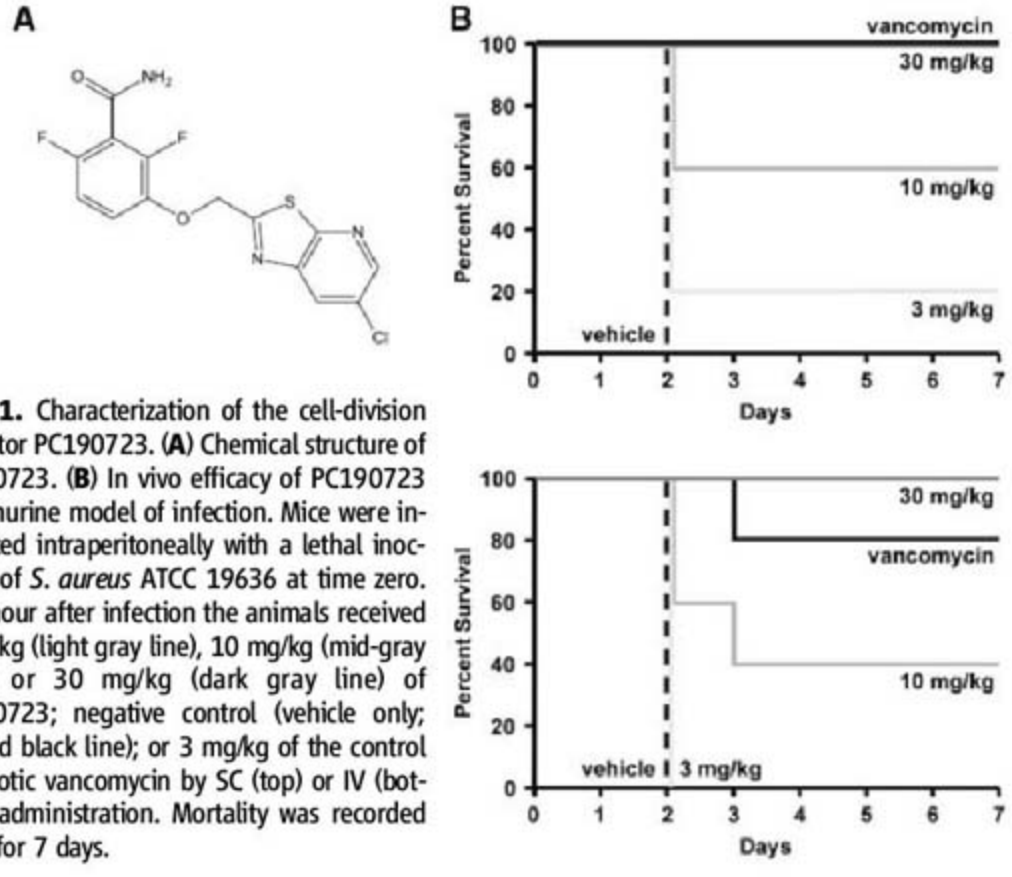

Fig. 1. Characterization of the cell-division inhibitor PC190723. (**A**) Chemical structure of PC190723. (**B**) In vivo efficacy of PC190723 in a murine model of infection. Mice were inoculated intraperitoneally with a lethal inoculum of *S. aureus* ATCC 19636 at time zero. One hour after infection the animals received 3 mg/kg (light gray line), 10 mg/kg (mid-gray line), or 30 mg/kg (dark gray line) of PC190723; negative control (vehicle only; dashed black line); or 3 mg/kg of the control antibiotic vancomycin by SC (top) or IV (bottom) administration. Mortality was recorded daily for 7 days.

Table 1. Microbiological profile of PC190723.

Organism and genotype	MIC (μg/ml)
B. subtilis	1
S. aureus	1
S. aureus (MRSA)	1
S. aureus (MDRSA)*	1
S. epidermidis	1
S. haemolyticus	0.5
S. hominis	1
S. lugdunensis	1
S. saprophyticus	1
S. warneri	1
Enterococcus faecalis	>64
Escherichia coli	>64
Haemophilus influenzae	>64
Pseudomonas aeruginosa	>64
Streptococcus pneumoniae	>64
Saccharomyces cerevisiae	>64
HepG2 (IC_{50})	>64

*Resistant to methicillin, oxacillin, ampicillin, gentamicin, erythromycin, penicillin, azithromycin, amikacin, amoxicillin/clavulanic acid, cephalothin, clindamycin, ceftriaxone, imipenem, lincomycin, streptomycin, perfloxacin, rifampin, and neomycin.

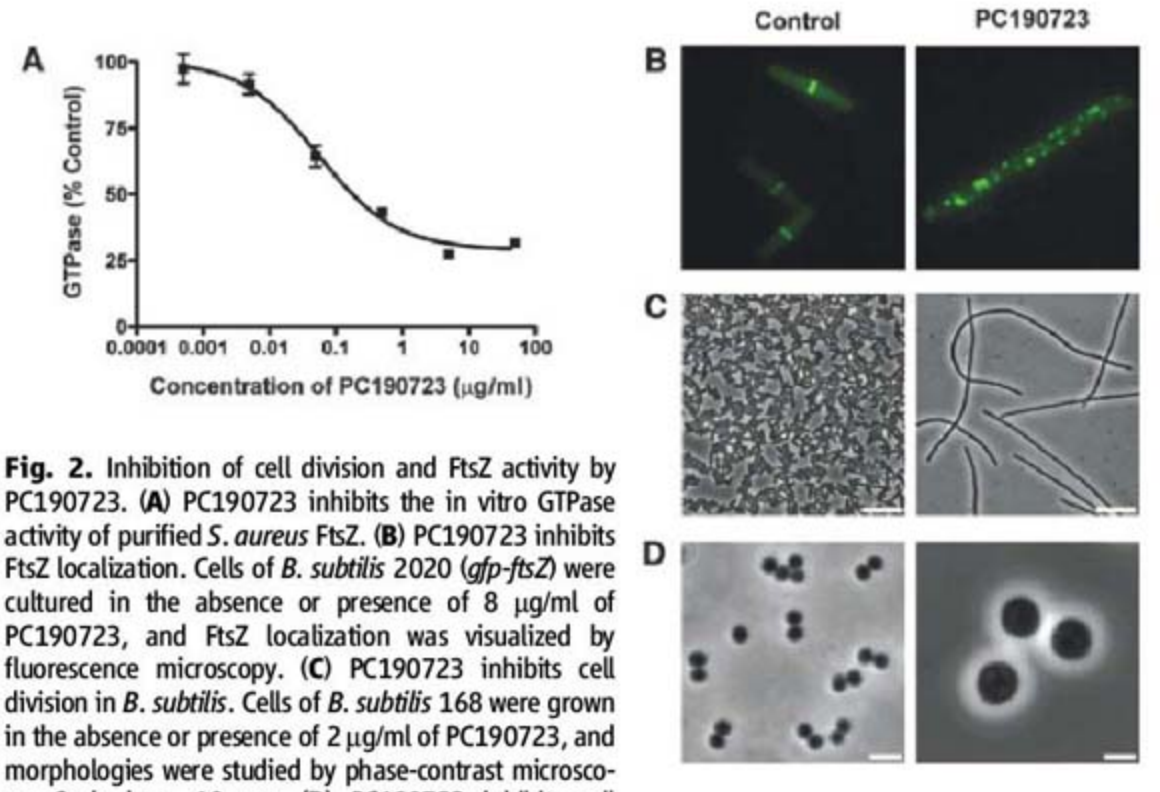

Fig. 2. Inhibition of cell division and FtsZ activity by PC190723. (**A**) PC190723 inhibits the in vitro GTPase activity of purified *S. aureus* FtsZ. (**B**) PC190723 inhibits FtsZ localization. Cells of *B. subtilis* 2020 (*gfp-ftsZ*) were cultured in the absence or presence of 8 μg/ml of PC190723, and FtsZ localization was visualized by fluorescence microscopy. (**C**) PC190723 inhibits cell division in *B. subtilis*. Cells of *B. subtilis* 168 were grown in the absence or presence of 2 μg/ml of PC190723, and morphologies were studied by phase-contrast microscopy. Scale bars, 10 μm. (**D**) PC190723 inhibits cell division in *S. aureus*. Cells of *S. aureus* ATCC 29213 were grown in the absence or presence of 2 μg/ml of PC190723, and morphologies were studied by phase-contrast microscopy. Scale bars, 2 μm.

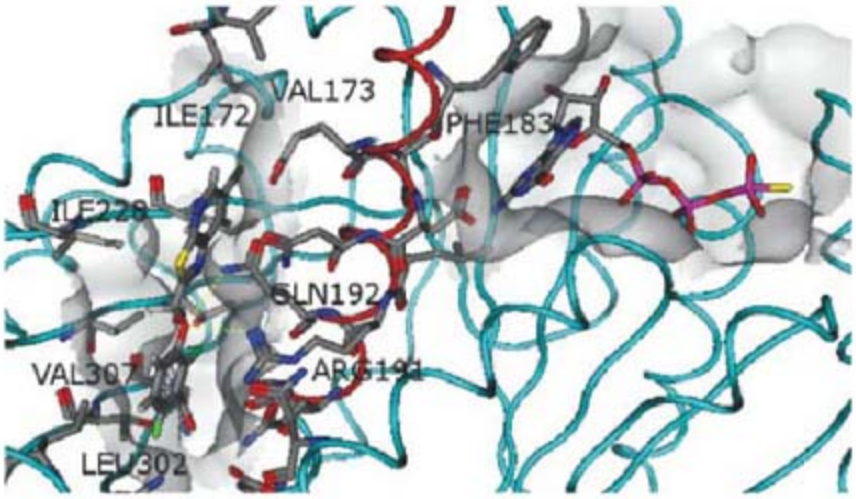

Fig. 3. Interaction of PC190723 with FtsZ. Model of a section of the FtsZ protein showing the position of the proposed binding site of PC190723 (left) relative to the nucleotide-binding site (right). The side chains of residues forming the putative binding pocket are labeled and are shown in ball-and-stick representation. The protein backbone is shown as a light blue ribbon. H7 is highlighted in red. In this model, hydrogen bonds are formed between the phenoxy ether of PC190723 and R191 and Q192 (dashed yellow lines). Blue, nitrogen; yellow, sulphur; gray, carbon; red, oxygen.

the evolutionarily related cytoskeletal elements of prokaryotes and eukaryotes. However, unlike Taxol, PC190723 did not enhance or inhibit tubulin polymerization in vitro (fig. S7). Further, Taxol did not inhibit cell division in bacteria (fig. S8).

A 1.7 Å crystal structure of *B. subtilis* FtsZ apo-form was used to identify a potential binding site(s) for 3-MBA and PC190723. The highest docking score positioned the ligands in a cleft (Fig. 3 and fig. S9) between helix seven (H7) and the C-terminal domain (*16*). The benzamide is predicted to bind in the cleft adjacent to amino acid residues R191, Q192, N263, V307, and T309. The thiazolopyridine portion of PC190723 is predicted to bind in a hydrophobic channel formed by amino acid residues I172, E185, N188, I228, and I230. All of the PC190723-resistant mutations (fig. S6) are in or adjacent to the residues comprising the docking site proposed by the modeling. This region is not part of the target's nucleotide-binding site. The core helix (H7) forms part of the Taxol-binding site in tubulin and has been proposed to act as a lever that can alter the interdomain orientations in tubulin and FtsZ (*4*, *5*, *17*). Interaction of PC190723 with H7 could contribute to the observed inhibition of GTPase activity and FtsZ polymerization. The docking model could also explain the species specificity of these benzamide compounds. Susceptible organisms have a valine at position 307. In nonsusceptible species, an arginine or histidine is present at this position (fig. S6). These larger polar residues partially occlude the cleft. In support of this hypothesis, substituting V307 for an arginine or histidine reduced the susceptibility of *B. subtilis* to 3-MBA and PC190723 (table S1).

PC190723 is representative of a new class of potent small-molecule antibacterial compounds that kill bacterial cells by inhibiting the essential protein FtsZ. In addition to their therapeutic potential, PC190723 and analogs may also be useful reagents for further studies on the biology of FtsZ and bacterial cell division. The potency of PC190723 against drug-resistant *S. aureus*, its efficacy in in vivo models of infection, and its structural and physicochemical properties (table S3) (*18*) make it an excellent candidate for optimization into a therapy to treat staphylococcal infection.

References and Notes

1. W. Vollmer, *Appl. Microbiol. Biotechnol.* **73**, 37 (2006).
2. R. L. Lock, E. J. Harry, *Nat. Rev. Drug Discov.* **7**, 324 (2008).
3. J. Errington, R. A. Daniel, D.-J. Scheffers, *Microbiol. Mol. Biol. Rev.* **67**, 52 (2003).
4. J. Löwe, L. A. Amos, *Nature* **391**, 203 (1998).
5. E. Nogales, S. G. Wolf, K. H. Downing, *Nature* **391**, 199 (1998).
6. K. H. Downing, *Annu. Rev. Cell Dev. Biol.* **16**, 89 (2000).
7. Y. Ohashi *et al.*, *J. Bacteriol.* **181**, 1348 (1999).
8. J. Wang *et al.*, *J. Biol. Chem.* **278**, 44424 (2003).
9. D. N. Margalit *et al.*, *Proc. Natl. Acad. Sci. U.S.A.* **101**, 11821 (2004).
10. T. Läppchen, A. F. Hartog, V. A. Pinas, G.-J. Koomen, T. den Blaauwen, *Biochemistry* **44**, 7879 (2005).
11. N. R. Stokes *et al.*, *J. Biol. Chem.* **280**, 39709 (2005).
12. H. Ito *et al.*, *Microbiol. Immunol.* **50**, 759 (2006).
13. C. Paradis-Bleau, M. Beaumont, F. Sanschagrin, N. Voyer, R. C. Levesque, *Bioorg. Med. Chem.* **15**, 1330 (2007).
14. Materials and methods are available as supporting material on *Science* Online.
15. A. J. O'Neill, I. Chopra, *Expert Opin. Invest. Drugs* **13**, 1045 (2004).
16. M. A. Oliva, D. Trambaiolo, J. Löwe, *J. Mol. Biol.* **373**, 1229 (2007).
17. L. A. Amos, J. Löwe, *Chem. Biol.* **6**, R65 (1999).
18. C. A. Lipinski, F. Lombardo, B. W. Dominy, P. J. Feeney, *Adv. Drug Deliv. Rev.* **23**, 3 (1997).
19. We thank various colleagues for assistance and advice and S. Ruston for support. This work was funded by investments from L. Clay and East Hill Management (Boston, MA, USA), The Wellcome Trust under the Seeding Drug Discovery Initiative, and a grant (AppGen55) in applied genomics from the UK Biotechnology and Biological Sciences Research Council and the UK Department of Trade and Industry. D.J.H., N.R.S., R.U., G.G., J.M.B., D.R.B., I.C., and L.G.C. are or have been paid employees of Prolysis. In addition, each has been offered share options in the company. J.E. founded Prolysis and retains an equity stake (in terms of shares issued) in the organization. He is the chief scientific officer and a director of Prolysis, and for this part-time role he is paid as a consultant. All other coauthors (that is, those not affiliated with Prolysis) do not declare any conflicts of interest. The evaluation of compound activity in vivo was performed by MDS Pharma Services. Compounds are the subject of patent application PCT/GB2007/001012. The atomic coordinates and structure factors of *B. subtilis* FtsZ have been deposited with the Protein Data Bank under the accession numbers 2vxy and r2vxysf. The sequences of the *ftsZ* wild-type and mutant strains have been deposited in GenBank with the accession numbers EU914258 to EU914264.

Supporting Online Material

www.sciencemag.org/cgi/content/full/321/5896/1673/DC1
Materials and Methods
Figs. S1 to S10
Tables S1 to S3
References

2 May 2008; accepted 28 July 2008
10.1126/science.1159961

Suppression of Cotton Bollworm in Multiple Crops in China in Areas with Bt Toxin–Containing Cotton

Kong-Ming Wu,[1]† Yan-Hui Lu,[1] Hong-Qiang Feng,[1] Yu-Ying Jiang,[2] Jian-Zhou Zhao[1]*

Transgenic cotton that has been engineered to produce insecticidal toxins from *Bacillus thuringiensis* (Bt) and so to resist the pest cotton bollworm (*Helicoverpa armigera*) has been widely planted in Asia. Analysis of the population dynamics of *H. armigera* from 1992 to 2007 in China indicated that a marked decrease in regional outbreaks of this pest in multiple crops was associated with the planting of Bt cotton. The study area included six provinces in northern China with an annual total of 3 million hectares of cotton and 22 million hectares of other crops (corn, peanuts, soybeans, and vegetables) grown by more than 10 million resource-poor farmers. Our data suggest that Bt cotton not only controls *H. armigera* on transgenic cotton designed to resist this pest but also may reduce its presence on other host crops and may decrease the need for insecticide sprays in general.

Transgenic crops carrying insecticides have become an important tool for insect pest management worldwide and, in 2007, were grown on a total of 42.1 million ha, accounting for about 37% of all the transgenic crops (*1*). One of these, Bt cotton, produces insecticidal toxins from *Bacillus thuringiensis* (Bt) and occupied 14 million ha worldwide and 3.8 million ha in China in 2007 (*1*). Bt cotton can suppress populations of a target pest with a narrow host range, e.g., pink bollworm (*Pectinophora gossypiella*) (*2*), but its long-term and wider ecological consequences are unknown.

The cotton bollworm, *Helicoverpa armigera*, is one of the most serious insect pests of cotton, corn, vegetables, and other crops throughout Asia. There are four generations of *H. armigera* per year in northern China. In general, wheat is the main host crop of first-generation *H. armigera* larvae, and cotton, corn, peanuts, soybeans, and vegetables are the major hosts for subsequent generations (*3*). Because of its long-distance migrations between provinces and dispersal among different host crops, provincewide outbreaks of *H. armigera* on cotton and other crops were common in the early 1990s in China (*3*). Bt cotton was first approved for commercial use in 1997 in China and remains the only Bt crop registered. By 2001, Bt cotton had been extensively planted, especially in northern China, which resulted in increased yields and decreased use of insecticides (*4*).

We conducted long-term and large-scale field monitoring of *H. armigera* during 1992–2007 in multiple crops in six provinces (Hebei, Shandong, Jiangsu, Shanxi, Henan, and Anhui), covering 38 million ha of farmland in northern China (fig. S1), in which 3 million ha of cotton and 22 million ha of other host crops (corn, peanuts, soybeans, and vegetables) were cultivated annually by more than 10 million small farmers. Our results indicated that both the egg density of *H. armigera* on cotton and the larval density on other major host crops were negatively correlated with the number of years after the introduction of Bt cotton in the period of 1997–2006 (Figs. 1 and 2). Before Bt cotton commercialization, the *H. armigera* population was fairly high on cotton and other host crops over the period from 1992 to 1996. However, population density of *H. armigera* was drastically reduced with the introduction of Bt cotton, especially during the period from 2002 to 2006 (table S1). Using stepwise regression, we evaluated the contribution of temperature, rainfall, and deployment of Bt cotton on the population density of *H. armigera* in six provinces (Table 1). For all six provinces in northern China, Bt cotton acreage correlated best with the reduction in *H. armigera* populations (Table 1). For the second and third generations, the deployment of Bt cotton contributed more to the reduction of *H. armigera* density than temperature and rainfall during 1997–2006 and was the key factor for its long-term suppression in all the six provinces of northern China (R^2 = 0.41 to 0.91, $P < 0.05$; Table 1). These results indicate that the regional occurrence of *H. armigera* on cotton and other major host crops in northern China was suppressed by the deployment of Bt cotton.

We also sampled *H. armigera* in cotton fields from 1998 to 2007 at Langfang Experiment Station in Hebei Province (*5*). The densities of eggs on Bt and non-Bt cotton and larvae on non-Bt cotton were negatively associated with the number of years after Bt cotton commercialization (R^2 = 0.52 to 0.63, $P < 0.05$). The population density of *H. armigera* can be described by the linear regression model (Fig. 3). The data also showed that the densities of *H. armigera* eggs were not significantly different between Bt and non-Bt cotton over the period of 1998–2007 ($P >$ 0.05) (Fig. 3A). However, larval densities on non-Bt cotton were significantly higher than those on Bt cotton from 1998 to 2006 ($P < 0.05$) (Fig. 3B), with an exception in 2007 when the pop-

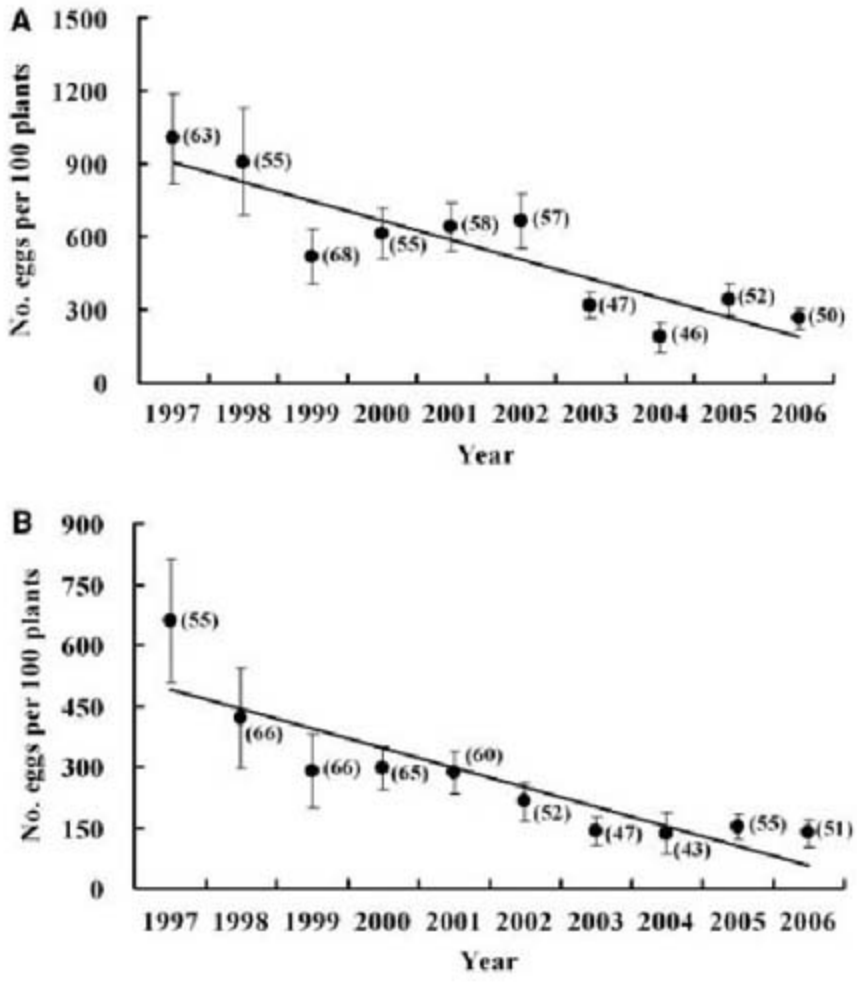

Fig. 1. Egg densities of *H. armigera* from 1997 to 2006 on cotton in northern China. (**A**) Relation between egg density of the second generation (•) and planting year of Bt cotton. Linear model of egg density (black line), $y = 157{,}076.05 - 78.21x$, $F = 32.16$, df = 1,549, $P < 0.0001$, $R^2 = 0.06$. (**B**) Relation between egg density of the third generation (•) and planting year of Bt cotton. Linear model of egg density (black line), $y = 94{,}644.36 - 47.15x$, $F = 26.42$, df = 1,558, $P < 0.0001$, $R^2 = 0.05$. Data are means ± SEM. Values in parentheses are the numbers of sampling sites for each year.

[1]State Key Laboratory for Biology of Plant Diseases and Insect Pests, Institute of Plant Protection, Chinese Academy of Agricultural Sciences, Beijing, 100193, People's Republic of China. [2]National Agro-Technical Extension and Service Center, Beijing, 100026, People's Republic of China.

*Present address: Pioneer Hi-Bred International, Inc., Johnston, IA 50131, USA.

†To whom correspondence should be addressed. E-mail: kmwu@ippcaas.cn

ulation density was low and larval density was not significantly different between the two treatments ($P > 0.05$). Using Bt cotton also reduced the duration of *H. armigera*'s oviposition period on cotton, because of decrease of moth density. Three peaks of egg density, representing the second, third, and fourth generations, respectively, were detected each year from 1998 to 2000, and in recent years, there was only one oviposition peak evident in the second generation, and no evident peak in generations 3 or 4 (fig. S2). The abundance of each generation and the peak duration of the third and fourth generations decreased linearly as Bt cotton commercialization proceeded through 1998 to 2007 (fig. S3). Thus, all data indicate that the commercial use of Bt cotton in northern China was associated with long-term areawide suppression of *H. armigera* after 10 years.

Regional control of *H. armigera* in multiple crops in China has been attained in recent years through the use of Bt cotton. Our results suggest that Bt cotton led to reduced populations of *H. armigera* not only on cotton but also on other host crops. This may be because cotton usually is the main host for the moths of the first generation to lay eggs and acts as the source of the subsequent generations on other host crops (*6*). Bt cotton kills most of the larvae of the second generation and, accordingly, works as a dead-end trap crop for *H. armigera* population. Interest in trap cropping, a promising agroecological approach for insect pest control, has increased considerably for modern agriculture (*7*, *8*), but few trap crops were used on such a large scale as that of Bt cotton in northern China, which shows that Bt crop can have a great advantage to expand the traditional view of a trap crop. This dependence on Bt cotton might also contribute to a reduction in both occurrence of *H. armigera* and the need for insecticide sprays in non-Bt host crops such as corn, soybeans, peanuts, and vegetables.

However, a major challenge for planting Bt cotton for pest control is the potential for insects to evolve resistance to Bt. Continuous monoculture of varieties that express the same Bt toxin could select for resistance, particularly when the amount of Bt toxin decreases as the plants age (*9*, *10*). A promising resistance management strategy entails the use of plants with a high dose of toxin in combination with the maintenance of "refuge" crops that encourage proliferation of Bt-susceptible insects within the pest population (*11*–*13*). To this end, the U.S. Environmental Protection Agency requires that each cotton farm set aside some land for cotton that does not produce Bt if farmers plant transgenic Bt cotton producing Cry1Ac toxic protein (*14*–*16*). Although successful in the United States (*17*), this strategy is difficult to implement in China because of the challenges associated with educating and monitoring millions of small

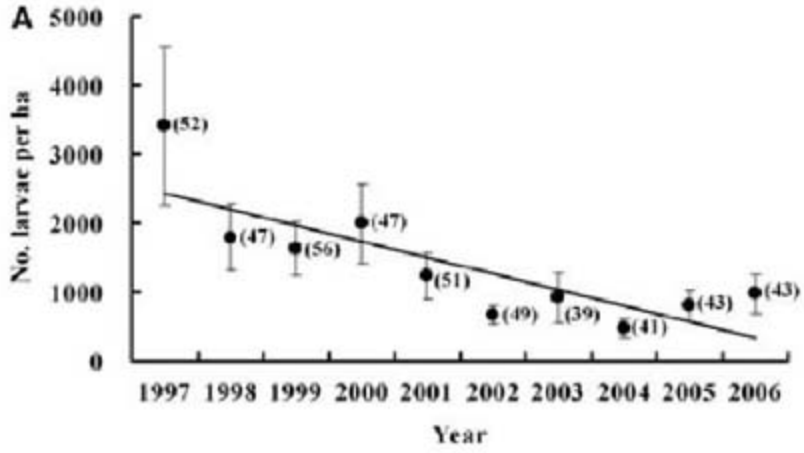

Fig. 2. Larval densities of *H. armigera* from 1997 to 2006 on corn, peanuts, soybeans, and vegetables in northern China. (**A**) Relation between larval density of the second generation (•) and planting year of Bt cotton. Linear model of larval density (black line), $y = 480{,}293.95 - 239.28x$, $F = 16.50$, df = 1,466, $P = 0.0001$, $R^2 = 0.03$. (**B**) Relation between larval density of the third generation (•) and planting year of Bt cotton. Linear model of larval density (black line), $y = 551{,}611.74 - 274.83x$, $F = 21.45$, df = 1,462, $P < 0.0001$, $R^2 = 0.04$. Data are means ± SEM. Values in parentheses are the numbers of sampling sites for each year.

Table 1. Effects of temperature, rainfall, and deployment of Bt cotton on the population density of *H. armigera* in northern China. Stepwise regression analysis was used for analyzing the association between population density (egg density on cotton or larval density on other host crops) of *H. armigera* and temperature (Temp.), rainfall, and deployment of Bt cotton. *F*, generation; R^2, coefficient of determination. Only variables from which the regression coefficient met the criteria of $P < 0.05$ are shown. NS, without significant effects ($P > 0.05$) on population density. + and − represent positive and negative associations between the population density and the factors, respectively. *$P < 0.05$; **$P < 0.01$.

Province	*F*	Egg density of *H. armigera* in cotton fields				Larval density of *H. armigera* on other major host crops			
		Regression coefficient			R^2	Regression coefficient			R^2
		Temp.	Rainfall	% Bt cotton		Temp.	Rainfall	% Bt cotton	
Hebei	2nd	NS	NS	−1.2224*	0.4392*	+0.1767*	NS	−2.4917**	0.8672**
	3rd	NS	NS	−2.1250**	0.7868**	NS	NS	−2.3092**	0.7216**
Shandong	2nd	NS	NS	−1.2932**	0.6023**	+0.1482*	NS	−1.4253**	0.7561**
	3rd	NS	NS	−1.8528*	0.4508*	NS	NS	−1.5658**	0.6724**
Jiangsu	2nd	NS	NS	−1.5974*	0.5617*	NS	NS	−2.3208**	0.6073**
	3rd	NS	NS	−1.2019*	0.4079*	NS	NS	−2.5182**	0.7124**
Shanxi	2nd	NS	−0.0080*	−3.1825**	0.8537**	NS	NS	−3.5959**	0.6308**
	3rd	NS	−0.0023*	−4.3043**	0.9145**	NS	NS	−5.3844*	0.5342*
Henan	2nd	NS	NS	−1.9166**	0.7431**	NS	NS	−1.5024**	0.6065**
	3rd	NS	NS	−1.0534*	0.5236*	NS	NS	−1.8253**	0.6017**
Anhui	2nd	NS	NS	−2.8418*	0.4876*	NS	NS	−2.8676*	0.4568*
	3rd	NS	NS	−2.1755*	0.5831*	NS	NS	−2.2374*	0.4809*
Northern China	2nd	NS	NS	−1.5425**	0.6675**	NS	NS	−1.7971**	0.7866**
	3rd	NS	NS	−2.1414**	0.8973**	NS	NS	−2.2161**	0.8794**

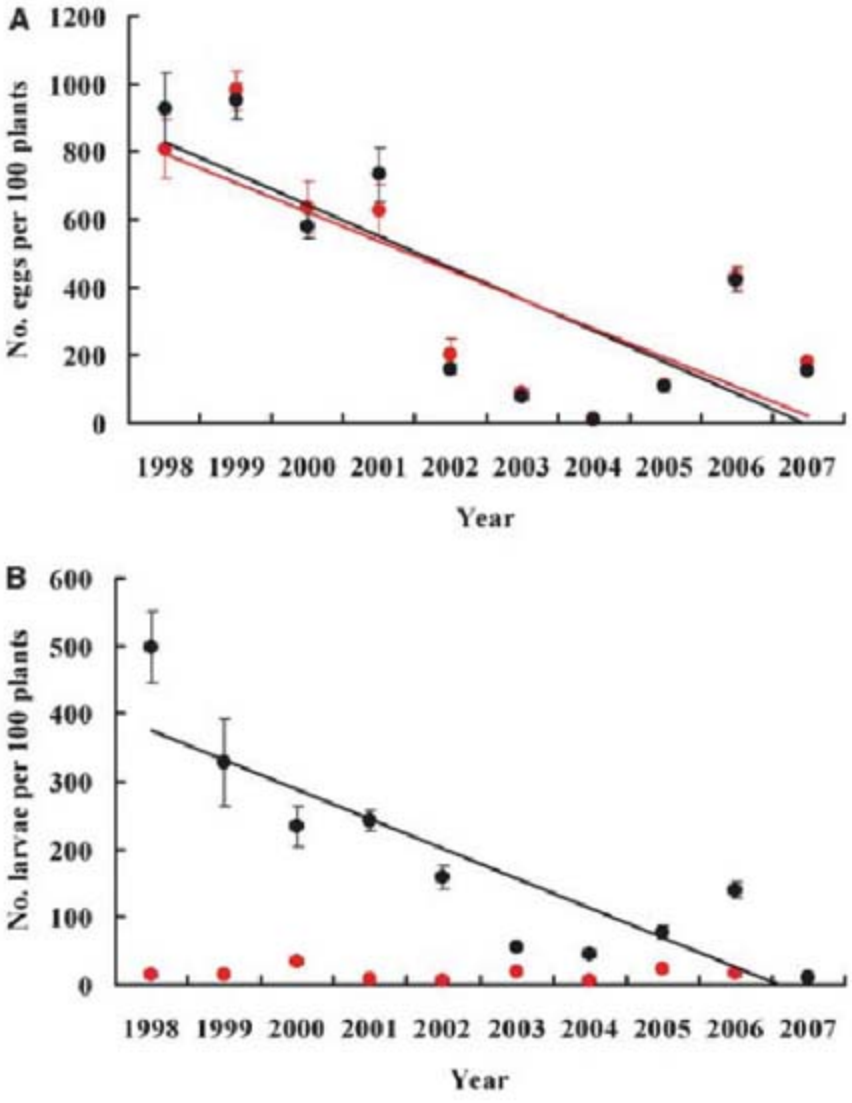

Fig. 3. Egg and larval densities of *H. armigera* on cotton at Langfang site, Hebei Province, China, from 1998 to 2007. (**A**) Relation between egg density on Bt cotton (red circles) and non-Bt cotton (black circles) and planting year of Bt cotton. Linear model on Bt cotton (black line), $y = 185{,}476.90 - 92.42x$, $F = 69.05$, df = 1,58, $P < 0.0001$, $R^2 = 0.54$. Linear model on non-Bt cotton (red line), $y = 171{,}365.94 - 85.37x$, $F = 62.59$, df = 1,58, $P < 0.0001$, $R^2 = 0.52$. (**B**) Relation between larval density on Bt cotton (red circles) and non-Bt cotton (black circles) and survey years. Linear model on non-Bt cotton (black line), $y = 87{,}107.86 - 43.41x$, $F = 97.56$, df = 1,58, $P < 0.0001$, $R^2 = 0.63$. Data are means ± SEM. There are six samples for each point in the graphs.

farmers. In China, a multiple cropping system consisting of soybeans, peanuts, corn, and vegetables is common. These crops also serve as hosts for *H. armigera*, and, because they do not express Bt toxin, they serve as refuges for nonresistant insects (*10*). Because cotton is not the only host crop, Bt cotton comprises about 10% of the major host crops in any province or throughout northern China. This accidental approach to refuge management appears to have, so far, warded off the evolution of resistance (*10*). Nevertheless, as a result of decreased spraying of broad-spectrum pesticides for controlling cotton bollworm in Bt cotton fields, mirids have recently become key pests of cotton in China (*18*, *19*). Therefore, despite its value, Bt cotton should be considered only one component in the overall management of insect pests in the diversified cropping systems common throughout China.

References and Notes

1. C. James, "Global status of commercialized biotech/GM Crops: 2007" (ISAAA Briefs No. 37, International Service for the Acquisition of Agri-biotech Applications, Ithaca, NY, 2007).
2. Y. Carrière *et al.*, *Proc. Natl. Acad. Sci. U.S.A.* **100**, 1519 (2003).
3. K. M. Wu, Y. Y. Guo, *Annu. Rev. Entomol.* **50**, 31 (2005).
4. J. Huang, S. Rozelle, C. Pray, Q. Wang, *Science* **295**, 674 (2002).
5. Materials and methods are available as supporting material on *Science* Online.
6. K. Wu, Y. Guo, S. Gao, *J. Econ. Entomol.* **95**, 832 (2002).
7. H. M. T. Hokkanen, *Annu. Rev. Entomol.* **36**, 119 (1991).
8. A. M. Shelton, F. R. Badenes-Perez, *Annu. Rev. Entomol.* **51**, 285 (2006).
9. B. E. Tabashnik, A. J. Gassmann, D. W. Crowder, Y.Carrière, *Nat. Biotechnol.* **26**, 199 (2008).
10. K. Wu, *J. Invertebr. Pathol.* **95**, 220 (2007).
11. F. Gould, *Annu. Rev. Entomol.* **43**, 701 (1998).
12. A. M. Shelton, J. Z. Zhao, R. T. Roush, *Annu. Rev. Entomol.* **47**, 845 (2002).
13. B. E. Tabashnik, T. J. Dennehy, Y. Carrière, *Proc. Natl. Acad. Sci. U.S.A.* **102**, 15389 (2005).
14. F. Gould *et al.*, *Proc. Natl. Acad. Sci. U.S.A.* **94**, 3519 (1997).
15. F. Gould, *Nat. Biotechnol.* **18**, 266 (2000).
16. Environmental Protection Agency, *Pesticide News Story: EPA Approves Natural Refuge for Insect Resistance Management in Bollgard II Cotton*; www.epa.gov/oppfead1/cb/csb_page/updates/2007/bollgard-cotton.htm.
17. Y. Carrière *et al.*, *Pest Manag. Sci.* **61**, 327 (2005).
18. K. Wu, W. Li, H. Feng, Y. Guo, *Crop Prot.* **21**, 997 (2002).
19. Y. H. Lu *et al.*, *Crop Prot.* **27**, 465 (2008).

20. This research was supported by 973 Projects Grant (2007CB109204) from the Ministry of Science and Technology of China and the National Natural Science Foundation of China (30625028). We thank A. M. Shelton (Cornell University) and two anonymous referees for comments and suggestions.

Supporting Online Material

www.sciencemag.org/cgi/content/full/321/5896/1676/DC1
Materials and Methods
Figs. S1 to S3
Table S1
References
Data Files S1 to S7

15 May 2008; accepted 8 August 2008
10.1126/science.1160550

Can Catch Shares Prevent Fisheries Collapse?

Christopher Costello,[1]* Steven D. Gaines,[2] John Lynham[3]†

Recent reports suggest that most of the world's commercial fisheries could collapse within decades. Although poor fisheries governance is often implicated, evaluation of solutions remains rare. Bioeconomic theory and case studies suggest that rights-based catch shares can provide individual incentives for sustainable harvest that is less prone to collapse. To test whether catch-share fishery reforms achieve these hypothetical benefits, we have compiled a global database of fisheries institutions and catch statistics in 11,135 fisheries from 1950 to 2003. Implementation of catch shares halts, and even reverses, the global trend toward widespread collapse. Institutional change has the potential for greatly altering the future of global fisheries.

Although the potentially harmful consequences of mismanaged fisheries were forecast over 50 years ago (*1*, *2*), evidence of global declines has only been seen quite recently. Reports show increasing human impacts (*3*) and global collapses in large predatory fishes (*4*) and other trophic levels (*5*) in all large marine ecosystems (LMEs) (*6*). It is now widely believed that these collapses are primarily the result of the mismanagement of fisheries.

One explanation for the collapse of fish stocks lies in economics: Perhaps it is economically optimal to capture fish stocks now and invest the large windfall revenues in alternative assets, rather than capturing a much smaller harvest on a regular basis. Although this remains a theoretical possibility for extremely slow-growing species

[1]Bren School of Environmental Science and Management, 4410 Bren Hall, University of California, Santa Barbara, CA 93106, USA. [2]Marine Science Institute, University of California, Santa Barbara, CA 93106, USA. [3]Department of Economics, University of California, Santa Barbara, CA 93106, USA.

*To whom correspondence should be addressed. E-mail: costello@bren.ucsb.edu

†Present address: Department of Economics, University of Hawaii at Manoa, 2424 Maile Way, Honolulu, HI 96822, USA.

(*7*), it remains rare in reality. A recent study reports that under reasonable economic parameterization, extinction is suboptimal (even with low growth rates) and that biomass under economically optimal harvest is larger than that under maximum sustainable yield (*8*).

If global fisheries contain large potential profits [perhaps a present value of $1 trillion (*9*)], yet the profits are only realized if the fisheries are managed sustainably, why are actively managed fisheries systematically overexploited? The answer lies in the misalignment of incentives. Even when management sets harvest quotas that could maximize profits, the incentives of the individual harvester are typically inconsistent with profit maximization for the fleet. Because individuals lack secure rights to part of the quota, they have a perverse motivation to "race to fish" to outcompete others. This race can lead to poor stewardship and lobbying for ever-larger harvest quotas, creating a spiral of reduced stocks, excessive harvests, and eventual collapse.

Examining specific cases, Beddington *et al.* (*10*), Hilborn *et al.* (*11*), Grafton *et al.* (*12*), and Griffith (*13*) argue that rights-based fisheries reforms offer promising solutions. Rather than only setting industry-wide quotas, fishermen are allocated individual rights. Referred to as catch shares or dedicated access privileges, these rights can be manifest as individual (and tradable) harvest quotas, cooperatives, or exclusive spatial harvest rights; the idea is to provide—to fishermen, communities, or cooperatives—a secure asset, which confers stewardship incentives. Most readily implemented within national jurisdictions (that is, inside 200 miles), some international agreements attempt to serve a similar function in international waters. Although both theory and empirical evidence suggest a robust link between catch shares and economic performance of a fishery (*14*, *15*), the link with ecological performance is more tenuous. Even so, Sanchirico and Wilen (*16*) argue that "It is widely believed and supported by anecdotal evidence that once fishers have a financial stake in the returns from sensible investment in sustainable practices, they are more easily convinced to make sacrifices required to rebuild and sustain fisheries at high levels of economic and biological productivity." A recent report provides examples consistent with this widely held belief (*17*). We tested the hypothetical causal link between the global assignment of catch shares and fisheries sustainability.

Whereas individual fishing rights have been implemented on small spatial scales in traditional cultures for millennia, the adoption rate in major fisheries has accelerated since the late 1970s. To test the efficacy of catch shares, we assembled a global database of 11,135 commercial fisheries and determined which fisheries had instituted catch shares from 1950 to 2003. We matched this institutional database to the same harvest database (*18*) used to assess fisheries collapse by Worm *et al.* (*6*). Our objective is to answer the question: Can catch shares prevent fisheries collapse?

In their widely cited contribution, Worm *et al.* (*6*) correlate the species richness of LMEs with fisheries collapse. They define a fishery as collapsed in year t if the harvest in year t is <10% of the maximum recorded harvest up to year t. Using this definition, ~27% of the world's fisheries were collapsed in 2003. Extrapolating this trend into the future, Worm *et al.* (*6*) find that 100% of the world's fisheries could be collapsed by 2048. Although this highly controversial projection (*19*) captured most of the attention from this article, a larger focus of the work was the role of ecosystem biodiversity in preventing collapse. Fisheries in more biodiverse regions were less likely to be collapsed at any given point in history. Unfortunately, however, this greater resilience to human exploitation does not change the ultimate conclusion. Biodiversity does not prevent collapse; it merely delays it.

In our analysis, we expanded beyond the characteristics of the ecosystem to consider the characteristics of the regulating fisheries institutions, simultaneously controlling for the ecosystem, genus, and other covariates. To assemble our catch-share database, we searched the published literature and government reports, interviewed experts on global fisheries, and vetted our final database with a diverse array of researchers. In total, we identified 121 fisheries managed using catch shares—defined as variations on individual transferable quotas (ITQs)—by 2003 (*20*). These work by allocating a dedicated share of the scientifically determined total catch to fishermen, communities, or cooperatives. This provides a stewardship incentive; as the fishery is better managed, the value of the shares increases. By analyzing the data at the fishery level [rather than the aggregate level, as in (*6*)], we facilitate inclusion of fisheries institutions as independent variables in our model specification.

We adopt the Worm *et al.* (*6*) definition of collapse. Although a better measure would be based on stock (*21*), no systematic database of global fish biomass exists. This collapse metric may overestimate the frequency of collapsed fisheries (*22*), which creates a conservative test for the benefits of catch shares. Sensitivity analyses that

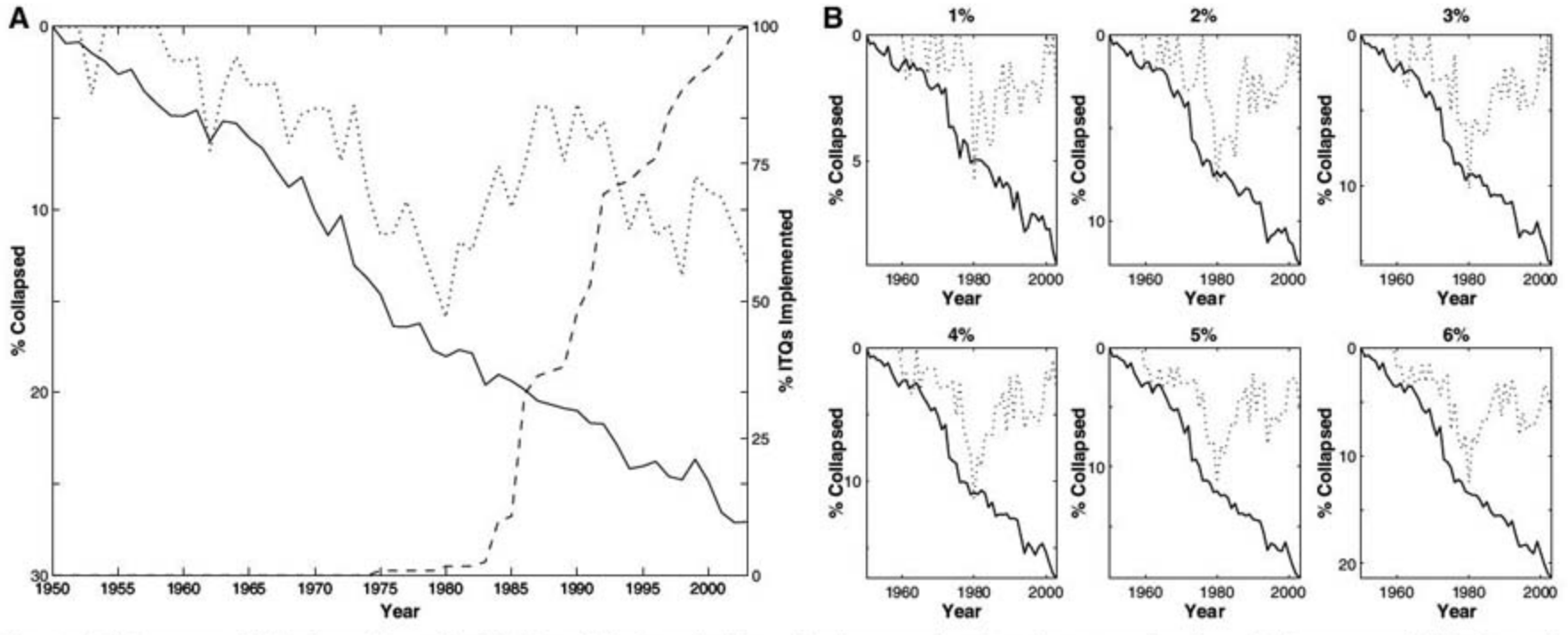

Fig. 1. (**A**) Percent of fisheries collapsed with (dotted line) and without (solid line) ITQ management using the Worm *et al.* (*6*) collapse threshold (10% of historical maximum). The number of ITQ fisheries increases through time (right y axis and dashed line), and the rate of implementation has been accelerating. (**B**) Percent of fisheries collapsed with (dotted line) and without (solid line) ITQ management using more conservative collapse thresholds: 1 to 6% of historical maximum catch.

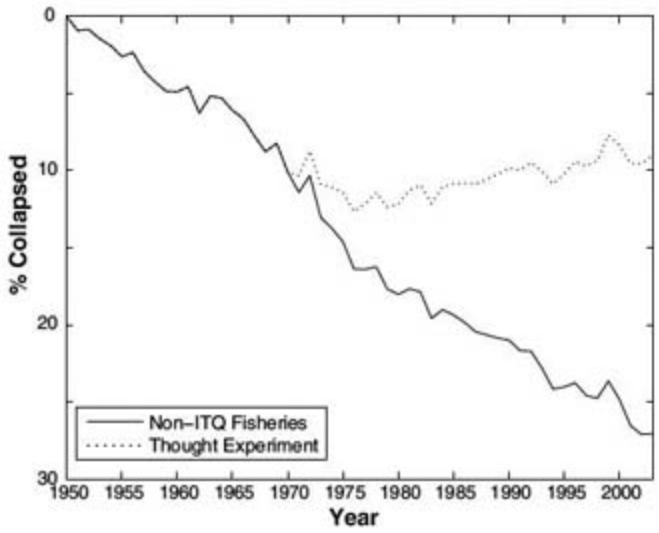

Fig. 2. Simulation of trend in fisheries collapse if all non-ITQ fisheries switched to ITQs in 1970 (dotted line), compared with the actual trend (solid line). The thought experiment assumes that the annual ITQ benefit counterbalances the global trend toward complete collapse, which is consistent with the observed trends in actual ITQs (Table 1). Fluctuations in the simulation arise from estimated interannual variability.

Table 1. Fishery-specific analyses of ITQ benefits. Each fishery is treated as a time series of collapse, with some fisheries converting to ITQ during the interval. Propensity score matching (*25*) controls for the effects of LME, genus, or species to further isolate biases that may arise from the particular places and fisheries where ITQs have been implemented. Columns 2 to 5 provide regression model results for four different propensity score models. Rows 2 and 3 provide the regression coefficients and SEs (in parentheses). Fisheries without ITQ management had an average annual percentage change of 0.54. For all comparisons, the annual benefit of ITQs roughly counters the current rate of decline in other fisheries (*23*). All estimated coefficients are statistically significant at the 1% level.

Parameter used to match fisheries	None	LME	Genus	Species
Percent ITQ difference (SE)	−7.06	−7.41	−6.79	−6.87
	(0.49)	(0.428)	(0.443)	(0.441)
Annual percent ITQ effect (SE)	−0.49	−0.37	−0.54	−0.51
	(0.136)	(0.137)	(0.136)	(0.139)

consider alternative thresholds for collapse and address other potential biases yield unchanged or stronger conclusions (*23*).

By 2003 the fraction of ITQ-managed fisheries that were collapsed (dotted line in Fig. 1A) was about half that of non-ITQ fisheries (solid line in Fig. 1A). Accelerated adoption of ITQs began in the late 1970s (dashed line and right *y* axis in Fig. 1A). In the preadoption period, would-be ITQ fisheries were on trajectories toward collapse, similar to non-ITQ fisheries. In the adoption period, the two curves diverge as ITQs are increasingly adopted (*24*). This disparity grows over time (*23*).

Demonstrating statistically a causal linkage between rights-based management and fisheries sustainability is complicated by three competing effects. First, the number of ITQ fisheries is growing, and new ITQ fisheries are drawn from a global pool with an ever-increasing fraction of collapsed fisheries. Random selection from this global pool could mask some benefits of rights-based management. Second, the conversion of fisheries to ITQs may involve a biased selection. For example, ITQs may be implemented disproportionately in fisheries that are already less collapsed, possibly giving a misleading perception of benefits from rights-based management. Finally, there may be temporal benefits of an ITQ (for instance, the longer an ITQ is in place in a given fishery, the less likely that fishery is to collapse). All of these mechanisms would lead to differences between ITQ and non-ITQ fisheries, but only the last mechanism implies a benefit from the management change.

An initial regression of the data in Fig. 1 suggests that implementing an ITQ reduces the probability of collapse by 13.7 percentage points (*23*). Because ITQs have been disproportionately implemented in a few global ecosystems such as Alaska, Iceland, New Zealand, and Australia (*25*), regional or taxonomic biases could generate misleading results. To account for potential selection bias, we used a variety of estimation strategies: (i) We restricted the sample to only those ecosystems or taxa that have experienced ITQ management. (ii) We used propensity score methods to match ITQ fisheries to appropriate control fisheries (*26*). (iii) We used fixed-effects estimation to identify the benefit of ITQs within each fishery.

The results are remarkably similar across all specifications and estimation techniques (*23*). The propensity score results are summarized in Table 1. Consistent with Fig. 1, ITQ fisheries perform far better than non-ITQ fisheries. Switching to an ITQ not only slows the decline toward widespread collapse, but it actually stops this decline. Each additional year of being in an ITQ (row 2 of Table 1) offsets the global trend (0.5% increase) of increasing collapse in non-ITQ fisheries (*23*). Other estimation techniques suggest even larger benefits. For example, fishery fixed-effects results suggest that ITQs not only halt the trend in global collapse, but they may actually reverse it (*23*).

Although bioeconomic theory suggests that assigning secure rights to fishermen may align incentives and lead to significantly enhanced biological and economic performance, evidence to date has been only case- or region-specific. By examining 11,135 global fisheries, we found a strong link: By 2003, the fraction of ITQ-managed fisheries that were collapsed was about half that of non-ITQ fisheries. This result probably underestimates ITQ benefits, because most ITQ fisheries are young.

The results of this analysis suggest that well-designed catch shares may prevent fishery collapse across diverse taxa and ecosystems. Although the global rate of catch-share adoption has increased since 1970, the fraction of fisheries managed with catch shares is still small. We can estimate their potential impact if we project rights-based management onto all of the world's fisheries since 1970 (Fig. 2). The percent collapsed is reduced to just 9% by 2003; this fraction remains steady thereafter. This figure is a marked reversal of the previous projections.

Despite the dramatic impact catch shares have had on fishery collapse, these results should not be taken as a carte blanche endorsement. First, we have restricted attention to one class of catch shares (ITQs). Second, only by appropriately matching institutional reform with ecological, economic, and social characteristics can maximal benefits be achieved. Nevertheless, these findings suggest that as catch shares are increasingly implemented globally, fish stocks, and the profits from harvesting them, have the potential to recover substantially.

References and Notes

1. H. S. Gordon, *J. Polit. Econ.* **62**, 124 (1954).
2. A. Scott, *J. Polit. Econ.* **63**, 116 (1955).
3. B. S. Halpern *et al.*, *Science* **319**, 948 (2008).
4. R. A. Myers, B. Worm, *Nature* **423**, 280 (2003).
5. J. B. C. Jackson *et al.*, *Science* **293**, 629 (2001).
6. B. Worm *et al.*, *Science* **314**, 787 (2006).
7. C. W. Clark, *J. Polit. Econ.* **81**, 950 (1973).
8. R. Q. Grafton, T. Kompas, R. W. Hilborn, *Science* **318**, 1601 (2007).
9. Our calculations are based on those of Sanchirico and Wilen (*16*). Using a disount rate of 9%, the present value of global fisheries is ($90 billion)/(0.09) = $1 trillion.
10. J. R. Beddington, D. J. Agnew, C. W. Clark, *Science* **316**, 1713 (2007).
11. R. Hilborn, J. M. Orensanz, A. M. Parma, *Philos. Trans. R. Soc. London Ser. B* **360**, 47 (2005).
12. R. Q. Grafton *et al.*, *Can. J. Fish. Aquat. Sci.* **63**, 699 (2006).
13. D. Griffith, *Front. Ecol. Environ.* **6**, 191 (2008).
14. R. Newell, J. Sanchirico, S. Kerr, *J. Environ. Econ. Manage.* **49**, 437 (2005).
15. R. Q. Grafton, D. Squires, K. J. Fox, *J. Law Econ.* **43**, 679 (2000).
16. J. N. Sanchirico, J. E. Wilen, *Int. J. Global Environ. Issues* **7**, 106 (2007).

17. D. Festa, D. Regas, J. Boomhauer. *Issues Sci. Tech.* **Winter**, 75 (2008).
18. Database (2007 version) of global fisheries catches of the Sea Around Us Project (Fisheries Centre, University of British Columbia, Vancouver, Canada). This database is based on a consolidation of several major data sources such as the FAO capture fisheries and its regional bodies, the International Council for the Exploration of the Seas STATLANT database, and the Northwest Atlantic Fisheries Organization, as well as data provided from the Canadian, United States, and other governments.
19. F. Hölker *et al.*, *Science* **316**, 1285 (2007).
20. Other forms of property rights may induce similar incentives. For example, territorial user right fisheries and community concessions provide localized incentives to steward the stock. These institutions were not counted as catch shares because they typically occur on a much smaller spatial scale than the LME catch data.
21. K. de Mutsert, J. H. Cowan Jr., T. E. Essington, R. Hilborn, *Proc. Natl. Acad. Sci. U.S.A.* **105**, 2740 (2008).
22. M. J. Wilberg, T. J. Miller, *Science* **316**, 1285 (2007).
23. See supporting online material for details.
24. The divergence between ITQ and non-ITQ fisheries is even more pronounced for less conservative definitions of collapse; i.e. 1 to 6% of historical maximum catch (Fig. 1B).
25. The LMEs with at least one fishery managed using an ITQ by 2003 are the California Current, Gulf of Alaska, Humboldt Current, Iceland Shelf, New Zealand Shelf, Scotian Shelf, Southest Australian Shelf, Southeast U.S. Continental Shelf, Southwest Australian Shelf, and West-Central Australian Shelf.
26. P. R. Rosenbaum, D. B. Rubin, *Biometrika* **70**, 41 (1983).
27. We thank the Paul G. Allen Family Foundation for generous financial support; the Sea Around Us Project for making the catch data publicly available; C. Wong and T. Kidman for helping to compile the database; B. Hansen for helpful comments; and J. Prince, K. Bonzon, and J. Toth for assisting with verifying the catch-share database.

Supporting Online Material

www.sciencemag.org/cgi/content/full/321/5896/1678/DC1
Materials and Methods
SOM Text
Figs. S1 and S2
Tables S1 to S5
References

22 April 2008; accepted 19 August 2008
10.1126/science.1159478

Parasite Treatment Affects Maternal Investment in Sons

T. E. Reed,[1,2*] F. Daunt,[2] M. E. Hall,[3†] R. A. Phillips,[4] S. Wanless,[2] E. J. A. Cunningham[1]

Parasitism can be a major constraint on host condition and an important selective force. Theoretical and empirical evidence shows that maternal condition affects relative investment in sons and daughters; however, the effect of parasitism on sex ratio in vertebrates is seldom considered. We demonstrate experimentally that parasitism constrains the ability of mothers to rear sons in a long-lived seabird, the European shag *Phalacrocorax aristotelis*. The effect contributes to the decline in offspring survival as the breeding season progresses and hence has important population-level consequences for this, and potentially other, seasonal breeders.

One key ecological factor influencing the condition of parents, and therefore the potential fitness of dependent offspring, is parasitism (*1*). In sexually dimorphic species, offspring of the larger sex often require higher nutritional investment and are more vulnerable to changes in parental condition (*2*). Moreover, sex allocation theory predicts that parents in good condition should bias investment toward offspring of the sex that stands to gain more from extra resources provided at critical developmental stages (*3*). We provide experimental evidence that parasites can constrain the ability of mothers, in particular, to rear offspring of the more expensive sex. This contributes to differential mortality of sons and daughters as the breeding season progresses and could explain the seasonal decline in offspring survival that is commonly observed in this and many other seasonal breeders.

Populations of the European shag *Phalacrocorax aristotelis* frequently suffer from severe infections of gastro-intestinal parasites, in particular anisakid nematodes [*Contracaecum rudolphi* and *Anisakis simplex* (*4*)]. Although their effects are usually sublethal, these parasites compete with the host for nutrients and trigger costly immune responses (*5*) that may impair host breeding success. Shag chicks must be provisioned in the nest for ~50 days by both parents. Male-biased broods require more food than female-biased broods, and male nestlings grow faster, attain higher peak masses at fledging, and are about 20% larger than females as adults (*4*).

We experimentally manipulated parasitism levels in breeding adults just before chick hatching by treating both male and female parents with a broad-spectrum antiparasite drug (ivermectin), which removes gut parasites and prevents reinfection over a period of ~6 weeks and hence for most of the chick-rearing period. Throughout the laying period, nests were randomly allocated to either a treatment group, in which both parents were treated with ivermectin (n = 34 nests), or a control (untreated) group in which parents were exposed to natural levels of parasitism (n = 83 nests). Treated and control nests were matched for laying date, ensuring an equal spread of laying dates in each group spanning the natural range (~6 weeks). The survival of sons was higher when their parents had been treated (Fig. 1A) [generalized linear mixed model

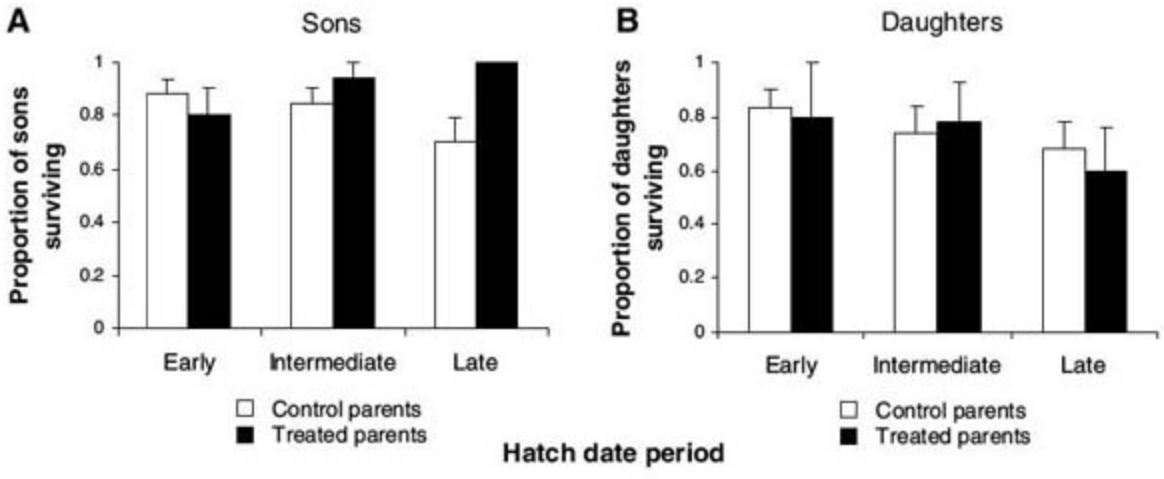

Fig. 1. Differential effect of ivermectin treatment on survival of sons (**A**) and daughters (**B**), and interaction with hatch date. Black bars represent chicks from treated parents, and white bars chicks from control parents. Hatch dates are grouped into early, intermediate and late periods, based on thirds of the distribution and corresponding roughly to 2-weekly intervals. The decline in the survival of sons is not apparent when their parents have been treated. Parasite treatment did not appear to affect the success of rearing daughters. Overall, parasitism in parents accounted for ~37% of the natural seasonal decline in chick survival. Data are means ± SEM. Effect sizes and statistics from logistic regression are given in the text.

[1]Institute of Evolutionary Biology, University of Edinburgh, Edinburgh EH9 3JT, UK. [2]NERC Centre for Ecology and Hydrology, Bush Estate, Penicuik, Midlothian EH26 0QB, UK. [3]Environmental and Evolutionary Biology, Institute of Biomedical and Life Sciences, University of Glasgow, Glasgow G12 8QQ, UK. [4]British Antarctic Survey, Natural Environment Research Council, High Cross, Madingley Road, Cambridge CB3 0ET, UK.

*To whom correspondence should be addressed. E-mail: tomreed@u.washington.edu

†Present address: Centre for Ecology and Conservation, School of Biosciences, University of Exeter, Cornwall Campus, Penryn, Cornwall TR10 9EZ, UK.

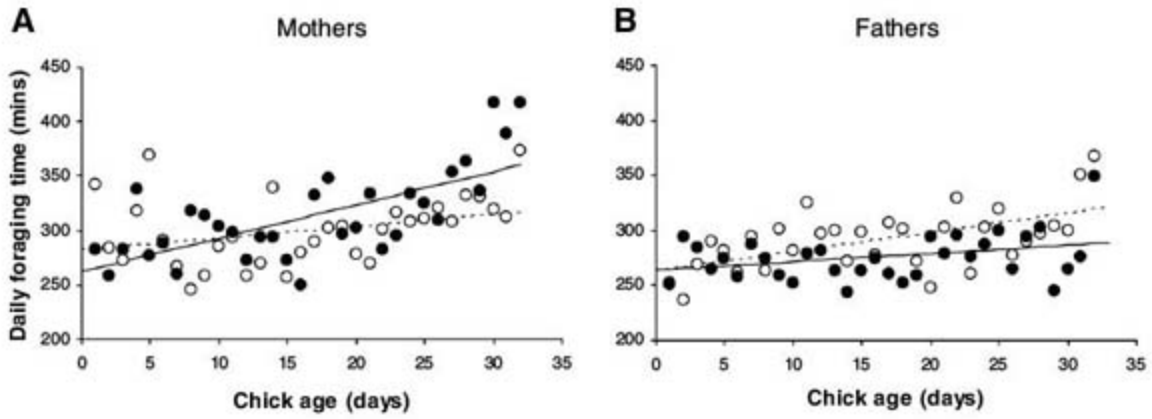

Fig. 2. Effect of the dosing procedure on average time spent foraging each day by mothers (**A**) and fathers (**B**) as chicks get older. Treated parents in both cases are represented by closed circles with a solid line showing the effect, and untreated (control) parents are indicated by open circles and a dashed line. The *x* axes show the age of the oldest chick in nests where the foraging effort of the parents was measured, and data points represent the mean daily time spent foraging by parents at each of these ages (day 0 is the day the first chick hatched). Mothers increased their foraging effort when treated with ivermectin, but fathers appeared to reduce theirs. Linear effects are best fits from the mixed-effects models, and statistics and sample sizes are given in the text.

(GLMM): treatment × chick sex interaction, $\chi^2 = 7.92$, $P = 0.005$; treated: 90.7 ± 4% (SEM) surviving; controls: 81 ± 4% surviving]. This was not the case for daughters (Fig. 1B) (treated: 71 ± 9% surviving; controls: 76 ± 5% surviving).

Parasitism can have population-level consequences. Like many birds, European shags that breed later in the season show reduced breeding success. In our study population, breeding 3 weeks after the population mean resulted in a 21% reduction in breeding success (GLMM of chick survival, date effect: $b = -0.123 \pm 0.032$, $\chi^2 = 15.34$, $P < 0.001$), mainly due to poorer survival of male chicks (decline in male survival: $b = -0.162 \pm 0.038$; female survival: $b = -0.078 \pm 0.038$; $\chi^2 = 5.70$, $P = 0.025$). However, following ivermectin treatment, the decline in offspring survival was significantly reduced in the group with treated parents compared with the control group (GLMM: treatment × hatch date interaction, $\chi^2 = 4.25$, $P = 0.039$; decline in controls: $b = -0.139 \pm 0.065$, treated: $b = -0.088 \pm 0.031$). This effect was driven by the increased survival of male chicks from treated pairs (GLMM: treatment × hatch date × chick sex interaction, $\chi^2 = 8.85$, $P = 0.003$), such that declines were no longer apparent for sons (Fig. 1A).

To examine possible reasons why sons were reared more successfully by ivermectin-treated parents, we used activity loggers to compare the foraging performance of treated and untreated males and females. As chicks became older, parents increased their foraging effort, but the patterns were different for treated mothers and treated fathers (Fig. 2) [linear mixed effects model (LMM): treatment × parental sex × chick age interaction, $n = 14$ mothers, $n = 16$ fathers; $\chi^2 = 9.65$, $P = 0.002$]. Treated mothers spent more time foraging as their chicks became older relative to control mothers (Fig. 2A) (LMM for mothers only: treatment × chick age interaction, $\chi^2 = 6.27$, $P = 0.013$). Treated fathers, by contrast, tended to reduce their effort through the chick-rearing period relative to control fathers (Fig. 2B) (LMM for fathers only: treatment × chick age interaction, $\chi^2 = 2.80$, $P = 0.095$). Treated parents did not maintain body mass over the chick-rearing period any better than control parents (average mass lost by $n = 10$ treated birds, mothers and fathers combined, was 39.0 ± 37.9 g, and 23.3 ± 32.3 g for $n = 15$ control birds; $t = 0.311$, $P = 0.758$, no significant sex differences) and presumably were not allocating additional resources to themselves. The treated mothers, it seems, passed the nutritional benefits on to their sons. Treated fathers may have reduced their investment in the brood as a whole (and so spent less time foraging) in response to a perceived increase by their partners. The net effect, nevertheless, was an increase in the survival of sons from treated nests, suggesting that sons benefited from increased maternal investment regardless of any reduction in effort by their fathers.

Given that mothers suffering from infection struggle to rear sons, should they not then prioritize investment in daughters? If so, we would expect the daughters of control parents to survive better than sons. This pattern was observed in the first year of the study, but not the second year. Environmental conditions were poor in 2005, and productivity in the colony was low. As expected, survival of daughters was significantly higher (83 ± 9%) than that of sons (58 ± 11%) for untreated pairs in this year ($n = 27$ nests, $\chi^2 = 10.97$, $P = 0.003$). In contrast, conditions were much more favorable in 2006 (and overall productivity much higher), and untreated parents were more successful at rearing sons (survival of daughters = 74 ± 6%, survival of sons = 87 ± 4%, $n = 56$ nests, $\chi^2 = 6.58$, $P = 0.012$). When resources are limited, it appears that mothers preferentially invest in daughters, and only when conditions improve do they shift the balance of resources over to sons. The effect that parasitism has on parents' ability to rear sons may depend, therefore, on environmental quality, most obviously the availability of food.

We have shown that the costs of parasitism to mothers can have a differential effect on the survival of male and female chicks, large enough to induce a marked decline in chick production in the population during the breeding season. Parasite prevalence tends to increase as the season progresses (fig. S1), and hence late breeders may suffer higher burdens. Late breeders may be also more susceptible to infection or its associated costs (*6*), because they tend to be in poorer physiological condition, less experienced, and less capable of mounting effective immune responses (*7*). Previous studies have shown that maternal condition can be a key factor in determining primary offspring sex ratio in birds (*8*), and parasitism has many well-documented effects on primary sex ratio in invertebrates (*9*). Our study illustrates that parasitism may be a key factor in limiting secondary sex ratio, but the effects of parasitism and its interaction with maternal condition on primary sex ratio in wild bird populations remains untested. Untangling these potentially interacting effects remains a challenge, but it is clear that parasites can have a substantial impact on the relative success of rearing male and female offspring.

References and Notes

1. B. C. Sheldon, S. Verhulst, *Trends Ecol. Evol.* **11**, 317 (1996).
2. T. H. Clutton-Brock, S. D. Albon, F. E. Guinness, *Nature* **313**, 131 (1985).
3. R. L. Trivers, D. E. Willard, *Science* **179**, 90 (1973).
4. Supporting material is provided on *Science* Online.
5. I. G. Colditz, *Parasite Immunol.* **30**, 63 (2008).
6. A. P. Moller, P. Christe, J. Erritzoe, A. P. Meller, *Oikos* **83**, 301 (1998).
7. J. Moreno, A. de Leon, J. A. Fargallo, E. Moreno, *Oecologia* **115**, 312 (1998).
8. R. G. Nager, P. Monaghan, R. Griffiths, D. C. Houston, R. Dawson, *Proc. Natl. Acad. Sci. U.S.A.* **96**, 570 (1999).
9. R. Stouthamer, J. A. J. Breeuwer, G. D. D. Hurst, *Annu. Rev. Microbiol.* **53**, 71 (1999).
10. We thank M. Harris, M. Frederiksen, L. Kruuk, S. Reece, S. West, P. Monaghan, and A. Young for helpful discussion and A. Kiploks and M. Newell for invaluable field assistance. Thanks also to M. Melo, S. Preuss, and J. Pemberton (University of Edinburgh) and K. Griffiths and A. Adams (University of Glasgow) for help with molecular sexing; B. Craig and A. Meredith for advice on parasitology; and H.-P. Fagerholm, D. Gibson, and M. Blaxter for nematode identification. Special thanks to Scottish Natural Heritage for permission to work on the island and the Isle of May Bird Observatory for help maintaining the marked population of shags. This work was supported by a Principal's Studentship to T.E.R. from the University of Edinburgh, a fellowship to E.J.A.C. from the Royal Society, and a NERC CASE studentship to M.E.H. The Association for the Study of Animal Behaviour (ASAB) funded the logger work.

Supporting Online Material

www.sciencemag.org/cgi/content/full/1159466/DC1
SOM Text
Fig. S1
References

22 April 2008; accepted 24 July 2008
Published online 7 August 2008;
10.1126/science.1159466
Include this information when citing this paper.

Apoptotic Force and Tissue Dynamics During *Drosophila* Embryogenesis

Yusuke Toyama,[1] Xomalin G. Peralta,[1]* Adrienne R. Wells,[2] Daniel P. Kiehart,[2]† Glenn S. Edwards[1]†

Understanding cell morphogenesis during metazoan development requires knowledge of how cells and the extracellular matrix produce and respond to forces. We investigated how apoptosis, which remodels tissue by eliminating supernumerary cells, also contributes forces to a tissue (the amnioserosa) that promotes cell-sheet fusion (dorsal closure) in the *Drosophila* embryo. We showed that expression in the amnioserosa of proteins that suppress or enhance apoptosis slows or speeds dorsal closure, respectively. These changes correlate with the forces produced by the amnioserosa and the rate of seam formation between the cell sheets (zipping), key processes that contribute to closure. This apoptotic force is used by the embryo to drive cell-sheet movements during development, a role not classically attributed to apoptosis.

Morphogenesis is a biomechanical process whereby individual cells and cohorts of cells produce and respond to forces to generate the complex form of a developing multicellular organism (*1*). Dorsal closure during *Drosophila* embryogenesis (Fig. 1, A to C, fig. S1, and movie S1) is an example of a robust morphogenetic process that also is a model system for biological and biophysical investigations of epidermal fusion and wound healing (*2*–*6*). During dorsal closure, two lateral epithelial cell sheets advance to progressively cover an eye-shaped opening that is transiently occupied by the amnioserosa, an extraembryonic tissue. The dorsal-most row of cells in each epithelial sheet constitutes a distinct tissue, known as the leading edge of the lateral epidermis, which contains an actomyosin-rich cable or supracellular "purse string." As closure progresses, the leading edges approach each other and form seams at each canthus in a process known as zipping (*7*), in which a canthus is the structure at the anterior- and posterior-most ends of the dorsal opening. Dorsal closure is the consequence of synchronized cellular forces and processes. Active forces are generated by nonmuscle myosin II in each purse string and in the amnioserosa (*8*), and by a resistive force in the lateral epidermis (*2*, *4*). Synchronization is a consequence of an emergent property that correlates the rate of closure with zipping (*5*, *6*).

Apoptosis, or programmed cell death, has been extensively investigated [reviewed in (*9*)] and is an integral part of dorsal closure (*10*) and other developmental processes. Of particular relevance is the stereotypic sequence of events that characterizes apoptotic cells in epithelia, where delamination and apoptosis must be precisely coordinated so that dying cells are removed without

[1]Physics Department and Free Electron Laser Laboratory, Duke University, Durham, NC 27708, USA. [2]Department of Biology, Duke University, Durham, NC 27708, USA.

*Present address: Sandia National Laboratories, Albuquerque, NM 87185, USA.

†To whom correspondence should be addressed. E-mail: dkiehart@duke.edu (D.P.K.); edwards@fel.duke.edu (G.S.E.)

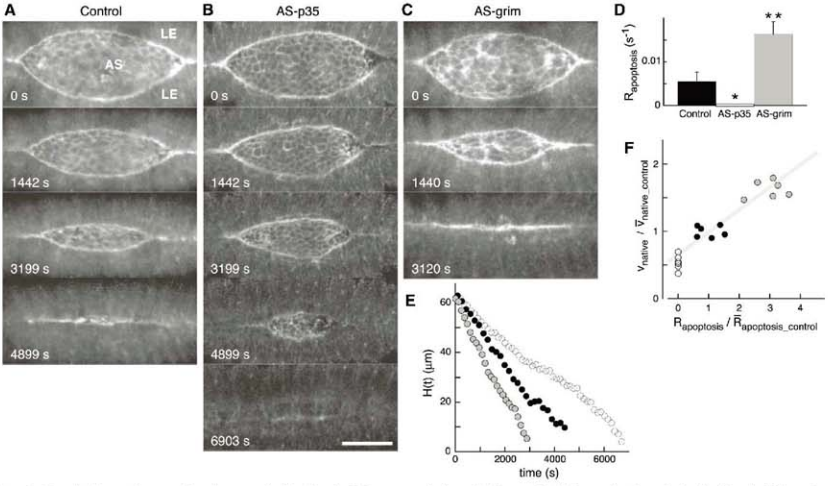

Fig. 1. Dorsal closure in control and apoptotically altered GFP-moe–expressing embryos. Confocal fluorescent images of **(A)** control, **(B)** AS-p35, and **(C)** AS-grim embryos are shown (AS, amnioserosa; LE, lateral epidermis). Anterior is to the left in all figures. Scale bar, 50 μm. **(D)** $R_{apoptosis}$ for control (black), AS-p35 (white), and AS-grim (gray) embryos; error bars indicate SD. A single or double asterisk indicates that the value is significantly different from the control value at $P < 0.05$ and $P < 0.01$, respectively. **(E)** Plot of $H(t)$ as a function of time for embryos that were shown in (A) to (C), respectively. **(F)** Correlation between v_{native} and $R_{apoptosis}$ (each normalized by the average value for control embryos as indicated by overbars, correlation coefficient $r = 0.941$).

compromising either the transepithelial or planar integrity of the tissue. In Madin-Darby canine kidney cell monolayers, an actomyosin ring forms within the apoptotic cell and a supracellular actomyosin purse string forms in the neighboring cells that surround this apoptotic cell (*11*). Contraction of these purse strings is reported to drive cell extrusion. In *Drosophila*, apoptosis occurs during stages 11 to 16 of embryogenesis [(*12*) and supporting online material (SOM) text]. After dorsal closure, the components of the amnioserosa cells are recycled through apoptosis (*10*). In addition, Kiehart *et al.* (*2*) observed that 13 out of 110 amnioserosa cells constricted their apical surfaces and dropped out of the epithelial plane and into the interior of the embryo during dorsal closure, suggesting the possibility of apoptosis. Here we show that apoptosis provides one-third to one-half of the net force that drives closure. This feature is in addition to the known roles of apoptosis, such as in eliminating supernumerary cells and maintaining homeostasis.

Through-focus (*Z*-stack) confocal images of dorsal closure in wild-type embryos that express the F-actin reporter [green fluorescent protein (GFP) fused to the actin-binding domain of moesin (GFP-moe) (*2*)] indicate that a subset of amnioserosa cells exhibits the hallmarks of apoptosis (Fig. 2). These include the constriction of their apical surfaces, their extrusion inward from the amnioserosa cell sheet, subsequent blebbing, and cell fragmentation. Five to seven cells that neighbor each apoptotic cell are distorted as part of this process (upper right-hand frame of Fig. 2A), thereby taking on a rosette geometry (*13*, *14*). These neighboring cells elongate toward the apoptotic cell to maintain a continuous dorsal surface as the apoptotic cell is extruded; contraction of both the apoptotic cell and the apoptotic supracellular purse string in the neighboring cells (*11*) may contribute to these cell shape changes, by which the surface area of these nearest-neighbor cells decreased by $27.3 \pm 8.6\%$ ($N = 52$ cells) relative to a $14.2 \pm 4.4\%$ ($N = 58$ cells) reduction in control amnioserosa cells ($P < 0.05$, SOM text). Figure 2B also indicates that the next-to–nearest-neighbor cells are distorted and are pulled toward the apoptotic cell. These observations demonstrate that the vast majority of the amnioserosa cells are directly influenced by the apoptotic process and exceed by a factor of 5 to 7 the number that actively undergo apoptosis before the completion of closure. This raises the possibility that the apoptotic process contributes to the force that favors closure. To test this hypothesis, we used the bipartite GAL4-UAS system, which allows tissue-specific and temporally specific gene expression (*15*), to inhibit or induce (enhance) apoptosis in the amnioserosa and then investigated the effects on the kinematics and dynamics of closure.

We inhibited the apoptotic process in amnioserosa cells only, by using a strong driver (c381-GAL4) to express an anti-apoptotic caspase suppressor (*p35*) responder [(*16*), hereafter referred to as AS-p35]. We induced (enhanced) apoptosis only in amnioserosa cells, by using a weaker driver, c825-GAL4 (*17*), to express a pro-apoptotic (*grim*) responder [(*18*), hereafter referred to as AS-grim]. These embryos also express GFP-moe to provide contrast for in vivo confocal microscopy. Complete genotypes and our choice of drivers are accounted for in (*19*). None of amnioserosa cells in AS-p35 embryos exhibited the hallmarks of apoptosis (movie S2), and the number of apoptotic cells increased in AS-grim embryos relative to controls. We measured the occurrence of apoptosis in amnioserosa cells and defined the rate of apoptosis, $R_{apoptosis} = n/\tau$, where n is the number of amnioserosa cells exhibiting the hallmarks of apoptosis observed during a time τ (SOM text). $R_{apoptosis}$ was increased from $5.5 \pm 2.1 \times 10^{-3}\ s^{-1}$ ($N = 6$ embryos) in controls (*19*) to $16.3 \pm 2.9 \times 10^{-3}\ s^{-1}$ ($N = 6$ embryos) in AS-grim

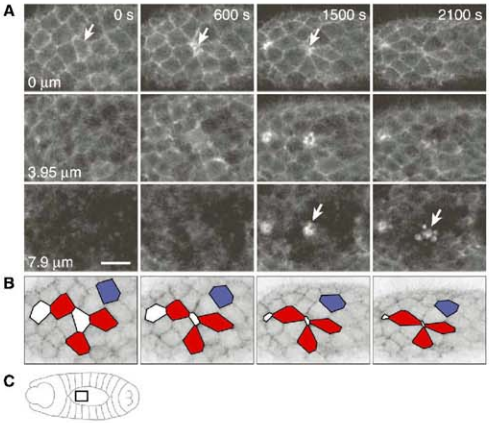

Fig. 2. Fate of apoptotic amnioserosa cells and the distortion of the surrounding cells in wild-type embryos. **(A)** Confocal sections through GFP-moe–expressing embryos, where rows indicate depth below the surface and columns indicate time (as shown). Accumulation of F-actin is evident on the surface of one amnioserosa cell at time 0 s (arrow). Contraction occurs between 0 and 1500 s (arrows). Cell extrusion is evident at all depths at 1500 s (arrows). Blebbing is evident 7.90 μm below the surface at 2100 s (arrow). Scale bar, 10 μm. **(B)** Color-enhanced reproduction of the surface images from (**A**). The red cells are pulled toward the apoptotic cells (white), rearrange their neighbor-neighbor configurations, and fill the gap. The blue cell does not change shape as dramatically but is distorted and pulled toward the apoptotic cell. **(C)** Schematic representation indicating the region of the amnioserosa imaged in (**A**) (not to scale).

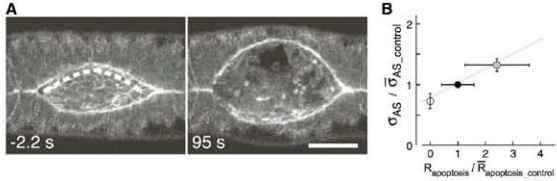

Fig. 3. Experimental determination of σ_{AS}. **(A)** Edge-cut protocol of a wild-type embryo expressing GFP-moe: Shown are the location of the edge cut (dashed line), which commenced at $t = 0$ s, and the morphology at the turning point. Scale bar, 50 μm. **(B)** Correlation between σ_{AS} and $R_{apoptosis}$ (each normalized by the average value for control embryos, $r = 0.997$). Points are average values for control (black), AS-p35 (white), and AS-grim (gray) embryos normalized by the average value for control embryos as indicated by overbars; error bars indicate SD.

embryos, and no apoptosis ($0.0 \pm 0.0 \times 10^{-3}$ s^{-1}, $N = 6$ embryos) was observed in AS-p35 embryos (Fig. 1D).

We observed three significant kinematic and dynamic consequences when apoptosis was either inhibited or induced. First, we quantified the rate of closure $v_{native} = dh/dt$ by measuring h as a function of time t, where h is the maximum distance from a purse string to the dorsal midline (fig. S2). v_{native} is the result of the net force exerted by the amnioserosa, lateral epidermis, and purse string on a leading-edge cell (*4*, *5*). v_{native} is reduced from 6.3 ± 0.6 nm/s ($N = 5$ embryos) in controls to 3.6 ± 1.1 nm/s ($N = 6$ embryos) in AS-p35 embryos and increased to 10.2 ± 0.8 nm/s ($N = 6$ embryos) in AS-grim embryos. Plots of H, the height from purse string to purse string at the maximum opening (fig. S2), versus t are well approximated as linear in all cases (Fig. 1, A to C, and E; and movies S3 to S5).

Second, mechanical jump experiments (*4*, *5*) were used to quantify changes in σ_{AS}, the force per unit of length produced by the amnioserosa on the leading edge under experimental conditions that either inhibit or induce apoptosis in the amnioserosa. A laser microbeam was used to rapidly dissect the amnioserosa away from one of the leading edges (the edge-cut protocol) [Fig. 3A and movie S6 (*19*)]. With the release of σ_{AS}, the leading edge recoils away from the dorsal midline to a turning point and closure eventually resumes. The initial recoil velocity, v_{recoil}, is directly proportional to σ_{AS} (SOM text). Taking the ratio of the measured $v_{recoil\_AS\text{-}p35}$ (or $v_{recoil\_AS\text{-}grim}$) to $v_{recoil\_GAL4\ control}$ yields the ratios

$$\frac{\sigma_{AS\_AS\text{-}p35}}{\sigma_{AS\_GAL4\ control}} \approx \frac{v_{recoil\_AS\text{-}p35}}{v_{recoil\_GAL4\ control}}, \quad \frac{\sigma_{AS\_AS\text{-}grim}}{\sigma_{AS\_GAL4\ control}} \approx \frac{v_{recoil\_AS\text{-}grim}}{v_{recoil\_GAL4\ control}} \quad (1)$$

where the GAL4 control genotype represents several distinct genotypes (*19*). v_{recoil} was 2373 ± 60 nm/s in controls ($N = 7$ embryos), 1727 ± 287 nm/s in AS-p35 embryos ($N = 5$ embryos, $P < 0.05$), and 3141 ± 246 nm/s in AS-grim embryos ($N = 6$ embryos, $P < 0.05$). Thus, in apoptosis-suppressed AS-p35 embryos, σ_{AS} is reduced by $29 \pm 9\%$, whereas in apoptosis-enhanced AS-grim embryos, σ_{AS} is increased by $32 \pm 7\%$, relative to controls. This indicates that about one-third of the force produced by the amnioserosa in wild-type embryos is attributable to apoptosis.

Third, we quantified changes in zipping due to inhibiting or inducing apoptosis by evaluating the change in the seam lengths $w_A(t)$ and $w_P(t)$ at the anterior (A) and posterior (P) canthi, respectively (fig. S2). Figure 4A plots the length $w_A(t) + w_P(t)$. Zipping is slower in AS-p35 embryos and faster in AS-grim embryos, relative to controls. Previously, we showed that [SOM text (*5*)]

$$\frac{dw_A}{dt} + \frac{dw_P}{dt} = \frac{k_{z,A}}{\tan\theta_{A,R}(t) + \tan\theta_{A,L}(t)} + \frac{k_{z,P}}{\tan\theta_{P,R}(t) + \tan\theta_{P,L}(t)} \quad (2)$$

where $k_{z,A}$ and $k_{z,P}$ are the zipping rate constants; $\theta_{A,R}$, $\theta_{A,L}$, $\theta_{P,R}$, and $\theta_{P,L}$ are angles defined by the dorsal midline and the segments of the purse strings that meet at each canthus; and R and L refer to the right and left sides of the essentially bilaterally symmetric embryo (fig. S2). Figure 4B and table S1 compare $k_{z,A}$ and $k_{z,P}$. At the anterior canthus, $k_{z,A}$ decreased by $40 \pm 23\%$ when apoptosis was inhibited. In contrast, at the posterior canthus, $k_{z,P}$ increased by $73 \pm 34\%$ when apoptosis was increased. Additionally inhibition of apoptosis decreased $k_{z,A}$ to $k_{z,P}$, and enhancement of apoptosis increased $k_{z,P}$ to $k_{z,A}$.

To investigate why changes in apoptosis might influence the zipping rate at each canthus, we quantified the distribution of $R_{apoptosis}$ in control, AS-p35, and AS-grim embryos (Fig. 4C). In controls, apoptosis occurs about five times more frequently in the anterior and middle thirds of the dorsal opening, relative to the posterior third. In AS-p35 embryos, there is a uniform absence of apoptosis throughout the dorsal opening. In AS-grim embryos, the occurrence of apoptosis is enhanced and distributed uniformly throughout the dorsal opening. Taken together, these observations indicate that the symmetry properties in the rate of apoptosis correlate with those of zipping (table S2).

Given these three kinematic and dynamic consequences, we considered next the correlations between normalized plots of v_{native} (Fig. 1F), σ_{AS} (Fig. 3B), and k_z (Fig. 4D) versus $R_{apoptosis}$ (SOM text). These figures demonstrate that v_{native}, σ_{AS}, and k_z are each strongly correlated with $R_{apoptosis}$ and are mutually correlated.

We conclude that during dorsal closure, delamination of the apoptosing amnioserosa cells produces forces that both facilitate cell extrusion and promote closure. This apoptotic force significantly contributes to σ_{AS}, and thus the dynamics of closure changed when the rate of apoptosis was altered. Our observations suggest directions for future research. It is well known that the disruption of cell-matrix interactions induces apoptosis in epithelial cells (*20*). Thus, we hypothesize that tension and apoptosis may contribute to a positive feedback mechanism that serves as a force regulator or rheostat.

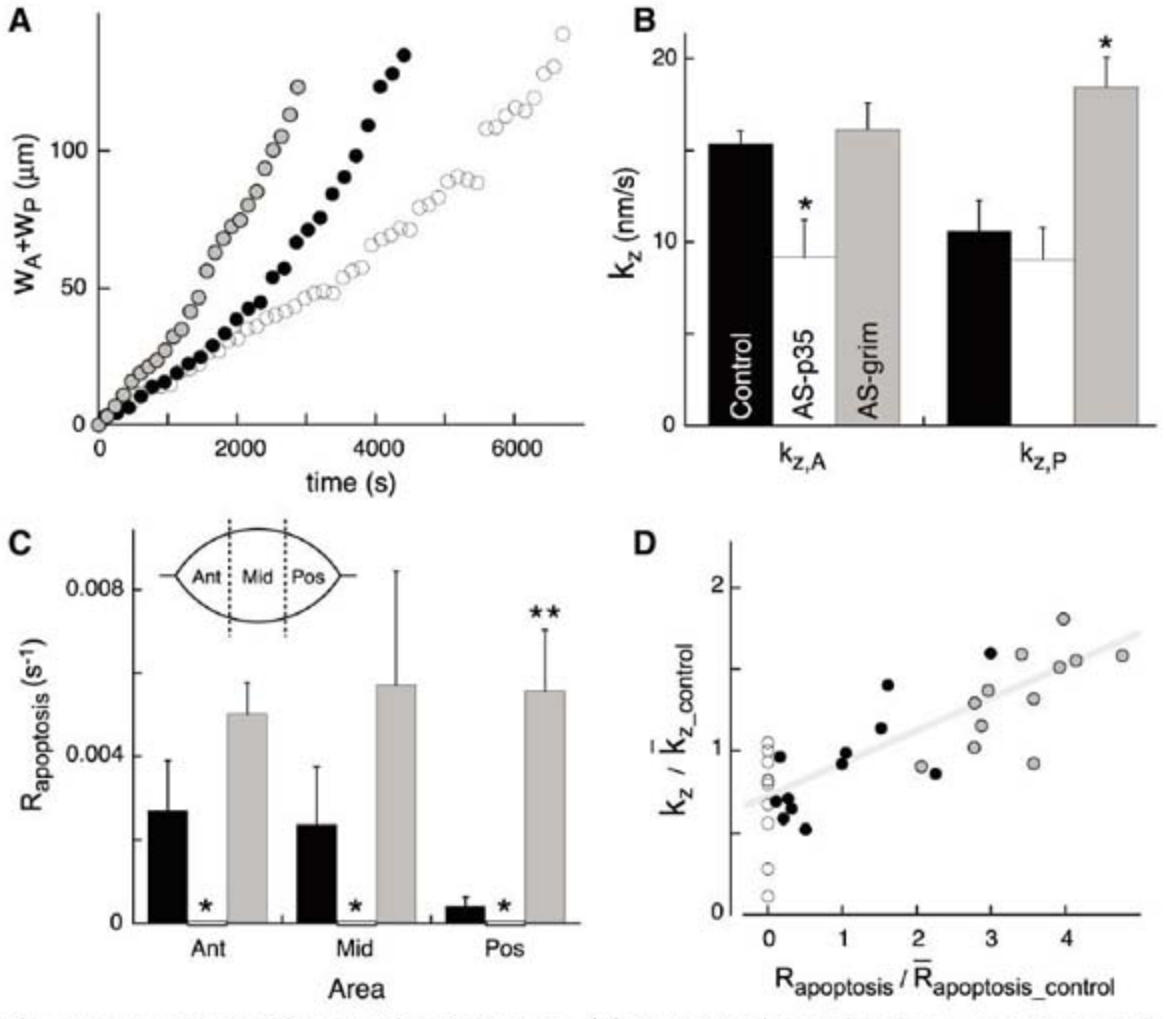

Fig. 4. Apoptosis contributes to the zipping rate. (**A**) Plot of total seam length $w_A + w_P$ for controls (black), AS-p35 (white), and AS-grim (gray) for the embryos shown in Fig. 1, A to C. (**B**) Histogram of $k_{z,A}$ and $k_{z,P}$ and (**C**) spatial distribution of $R_{apoptosis}$ in control (black), AS-p35 (white), and AS-grim (gray) embryos (*$P < 0.05$; **$P < 0.01$); error bars indicate SD. The dorsal opening was segmented by taking thirds of the canthus-to-canthus distance [inset in (C)]. (**D**) Correlation between k_z and $R_{apoptosis}$ [each normalized by the average value ($k_{z,A}$ and $k_{z,P}$ or $R_{apoptosis\_Ant}$ and $R_{apoptosis\_Pos}$) for controls as indicated by the overbars, $r = 0.802$].

Our results raise the possibility of a dynamic role for apoptosis in other morphogenic processes. Indeed, an apoptotic force has been proposed as part of the epithelial strand-pull theory in hair follicles (*21*). Although not all apoptotic processes are related to force generation, we anticipate that apoptotic forces may be important for epithelial fusion in processes such as the development of the adult abdomen of *Drosophila* (*22*). Moreover, we cannot rule out the possibility that apoptotic forces contribute to the tissue-sculpting processes that drive processes such as digit individualization and joint formation. An apoptotic force may also play a beneficial role during wound healing (*11*, *23*) as a source of mechanical tension that promotes tissue reconstruction. We propose that evolution efficiently uses all possible sources of forces for morphogenesis, and that apoptosis in the amnioserosa is one such force that is co-opted to help drive dorsal closure.

References and Notes

1. R. Keller, L. A. Davidson, D. R. Shook, *Differentiation* **71**, 171 (2003).
2. D. P. Kiehart, C. G. Galbraith, K. A. Edwards, W. L. Rickoll, R. A. Montague, *J. Cell Biol.* **149**, 471 (2000).
3. A. Jacinto, A. Martinez-Arias, P. Martin, *Nat. Cell Biol.* **3**, E117 (2001).
4. M. S. Hutson *et al.*, *Science* **300**, 145 (2003).
5. X. G. Peralta *et al.*, *Biophys. J.* **92**, 2583 (2007).
6. X. G. Peralta, Y. Toyama, D. P. Kiehart, G. S. Edwards, *Phys. Biol.* **5**, 015004 (2008).
7. A. Jacinto *et al.*, *Curr. Biol.* **10**, 1420 (2000).
8. J. D. Franke, R. A. Montague, D. P. Kiehart, *Curr. Biol.* **15**, 2208 (2005).
9. M. D. Jacobson, M. Weil, M. C. Raff, *Cell* **88**, 347 (1997).
10. B. H. Reed, R. Wilk, F. Schock, H. D. Lipshitz, *Curr. Biol.* **14**, 372 (2004).
11. J. Rosenblatt, M. C. Raff, L. P. Cramer, *Curr. Biol.* **11**, 1847 (2001).
12. J. M. Abrams, K. White, L. I. Fessler, H. Steller, *Development* **117**, 29 (1993).
13. J. T. Blankenship, S. T. Backovic, J. S. P. Sanny, O. Weitz, J. A. Zallen, *Dev. Cell* **11**, 459 (2006).
14. M. Tamada, T. D. Perez, W. J. Nelson, M. P. Sheetz, *J. Cell Biol.* **176**, 27 (2007).
15. A. H. Brand, N. Perrimon, *Development* **118**, 401 (1993).
16. R. J. Clem, M. Fechheimer, L. K. Miller, *Science* **254**, 1388 (1991).
17. L. Hrdlicka *et al.*, *Genesis* **34**, 51 (2002).
18. P. Chen, W. Nordstrom, B. Gish, J. M. Abrams, *Genes Dev.* **10**, 1773 (1996).
19. Materials and methods are available as supporting material on *Science* Online.
20. S. M. Frisch, H. Francis, *J. Cell Biol.* **124**, 619 (1994).
21. K. Stenn, S. Parimoo, S. Prouty, C. Chuong, in *Molecular Basis of Epithelial Appendage Morphogenesis*, C.-M. Chuong, Ed. (Landes Bioscience, Austin, TX, 1998), pp. 111–130.
22. N. Ninov, D. A. Chiarelli, E. Martin-Blanco, *Development* **134**, 367 (2007).
23. D. G. Greenhalgh, *Int. J. Biochem. Cell Biol.* **30**, 1019 (1998).

24. We thank S. Venakides, U. S. Tulu, and A. Rodiriguez-Diaz for useful discussions and A. Boury and R. Montangue for fly husbandry. This research was supported by NIH grant GM33830.

Supporting Online Material

www.sciencemag.org/cgi/content/full/321/5896/1683/DC1
Materials and Methods
SOM Text
Figs. S1 to S4
Tables S1 and S2
Movies S1 to S6
References

27 February 2008; accepted 30 July 2008
10.1126/science.1157052

Clusters of Hyperactive Neurons Near Amyloid Plaques in a Mouse Model of Alzheimer's Disease

Marc Aurel Busche,[1,4] Gerhard Eichhoff,[1,4] Helmuth Adelsberger,[1,4] Dorothee Abramowski,[2] Karl-Heinz Wiederhold,[2] Christian Haass,[3,4] Matthias Staufenbiel,[2] Arthur Konnerth,[1,4]* Olga Garaschuk[1,4]†

The neurodegeneration observed in Alzheimer's disease has been associated with synaptic dismantling and progressive decrease in neuronal activity. We tested this hypothesis in vivo by using two-photon Ca^{2+} imaging in a mouse model of Alzheimer's disease. Although a decrease in neuronal activity was seen in 29% of layer 2/3 cortical neurons, 21% of neurons displayed an unexpected increase in the frequency of spontaneous Ca^{2+} transients. These "hyperactive" neurons were found exclusively near the plaques of amyloid β–depositing mice. The hyperactivity appeared to be due to a relative decrease in synaptic inhibition. Thus, we suggest that a redistribution of synaptic drive between silent and hyperactive neurons, rather than an overall decrease in synaptic activity, provides a mechanism for the disturbed cortical function in Alzheimer's disease.

A progressive decrease in neuronal activity is an established feature of Alzheimer's disease (AD) (*1*, *2*). Even early stages of AD are associated with a decrease in the density of cortical synapses (*3*, *4*) and dendritic spines (*5*). Furthermore, results obtained in various animal models of the disease show amyloid β (Aβ)–mediated inhibition of synaptic currents (*6*–*8*), disruption of synaptic plasticity (*9*, *10*), as well as endocytosis of glutamate receptors (*8*, *11*–*15*). These findings are summarized in the synaptic failure hypothesis suggesting that "AD represents, at least initially, an attack on synapses" (*4*). To test this hypothesis under in vivo conditions, we explored activity of individual cortical neurons in a mouse model of AD. We used double-transgenic APP23xPS45 mice (fig. S1), which overexpress both β-amyloid precursor protein (APP_{Swe}) and mutant presenilin 1 [Gly^{384}→Ala^{384} mutation (G384A)] under the control of Thy-1 promoter (*16*). For the simultaneous in vivo visualization of amyloid plaques and cortical neurons (Fig. 1A), we used the multicell bolus loading technique (*17*). We sequentially injected the Ca^{2+} indicator dye Oregon Green 488 BAPTA-1 AM (OGB-1) and the fluorescent marker thioflavin S, known to label fibrillar amyloid deposits (*18*–*21*).

For the assessment of neural network function in APP23xPS45 mice, we analyzed the spontaneous ongoing cortical activity, which is known to be an important determinant of information processing in the brain (*22*–*26*). We simultaneously monitored spontaneously occurring somatic Ca^{2+} transients in many individual cells (Fig. 1, A and B). Such Ca^{2+} transients directly reflect firing of action potentials in neurons (*27*, *28*). In wild-type (WT, 6- to 10-month-old) mice, the pattern of ongoing activity was remarkably stable from cell to cell (Fig. 1, B and C) with a low mean frequency of Ca^{2+} transients (1.41 ± 0.04 transients/min, n = 564 cells). In APP23xPS45 mice of the same age, the pattern of activity was distinctly different from that in the WT control mice (Fig. 1, B to D). In the mutant mice, only 50% of the neurons were active in the normal frequency range, whereas the remaining neurons were at roughly equal proportions, either silent (showing no Ca^{2+} transients over 6-min-long recording periods) or hyperactive [showing transients at much higher frequencies (fig. S2)]. We observed a 16-fold increase in the fraction of hyperactive neurons and a threefold increase in the fraction of silent neurons. We detected no major differences in amplitude (37 ± 4% $\Delta F/F$, where F is fluorescence, and n = 564 cells in WT versus 39 ± 4% and n = 564 in APP23xPS45) or decay time constant (0.96 ± 0.02 s in WT versus 0.83 ± 0.01 s in APP23xPS45) of intracellular Ca^{2+} transients in WT and mutant mice.

[1]Institut für Neurowissenschaften, Technische Universität München (TUM), 80802 München, Germany. [2]Novartis Institutes for Biomedical Research, 4002 Basel, Switzerland. [3]Adolf-Butenandt-Institute, Department of Biochemistry, Laboratory for Neurodegenerative Disease Research, Ludwig-Maximilians-Universität, 80336 München, Germany. [4]Center for Integrated Protein Science, 81377 München, Germany.

*To whom correspondence should be addressed. E-mail: arthur.konnerth@lrz.tum.de

†Present address: Institute of Physiology II, Wilhelmstraße 27, 72074 Tübingen, Germany.

Next, we mapped the distribution of the three types of neurons in relation to the three-dimensionally nearest amyloid plaque (*16*). Hyperactive neurons were found only in close proximity (<60 μm) to the plaque border, whereas silent cells and cells with regular frequencies of Ca^{2+} transients were distributed throughout the cortex (Fig. 2, A and B). At increasing distances from the plaques, the proportion of silent cells gradually increased (Fig. 2C). To address the question of whether changes in neuronal activity pattern occur also in the absence of amyloid plaques, we studied predepositing APP23xPS45 mice (1.5 to 2 months of age; fig. S1, D to F). At this age the cortical activity was normal, without any difference in the amplitude, the kinetics, or the frequency of spontaneous Ca^{2+} transients (fig. S3). Furthermore, the behavioral performance was inconspicuous: At 2 months of age, APP23xPS45 mice performed normally when tested in the discriminatory water maze task [spatial memory test (*29*)] and in the Y maze [working memory test (*30*); fig. S4]. In contrast, 6- to 8-month-old Aβ-depositing mice showed a significantly reduced performance in both memory tests. In the water maze test, APP23xPS45 mice not only made fewer correct choices but also needed a significantly longer time for making a decision (fig. S4, A and B).

What are the mechanisms underlying neuronal hyperactivity in APP23xPS45 mice? The increased frequency of Ca^{2+} transients may be caused by spontaneous Ca^{2+} release from overfilled intracellular Ca^{2+} stores because the G384A mutation was shown to abolish the presenilin-mediated Ca^{2+} leak from intracellular Ca^{2+} stores (*31*). This Ca^{2+} leak is important to maintain the physiological filling state of the stores (*32*). However, we found that in 4/4 mutant mice the sodium channel blocker tetrodotoxin (TTX) completely and reversibly blocked all Ca^{2+} transients of hyperactive neurons, indicating that they were exclusively generated by action potential firing. This posed the next question of whether in hyperactive neurons there is an increased neuronal excitability leading to strong intrinsic firing or whether the Ca^{2+} transients are driven by synaptic activity. This question was answered by the observation that the Ca^{2+} transients of hyperactive neurons were completely abolished by the application of the ionotropic glutamate receptor blockers 6-cyano-7-nitroquinoxaline-2,3-dione (CNQX) and D,L-2-amino-5-phosphonovaleric acid (APV) (n = 7 cells in five mice) (Fig. 3A). The synaptic origin of the Ca^{2+} transients in hyperactive neurons was further supported by the finding that, in a given peri-plaque region, all neuronal Ca^{2+} transients were strictly correlated with the respective neuropil signals, known to reflect primarily the activity of presynaptic fibers (*27*) (Fig. 3, B and C; n = 6 experiments). The activity of hyperactive neurons surrounding a given plaque was correlated (Fig. 3, B and D). Importantly, the spontaneous as well as glutamate-induced Ca^{2+} transients detected in hyperactive neurons were very similar to those recorded in the "normal" neurons (figs. S5 and S6), indicating the absence of any major increase in intrinsic excitability in hyperactive neurons. Thus, a possible explanation for the neuronal hyperactivity may be an impairment of synaptic inhibition. In order

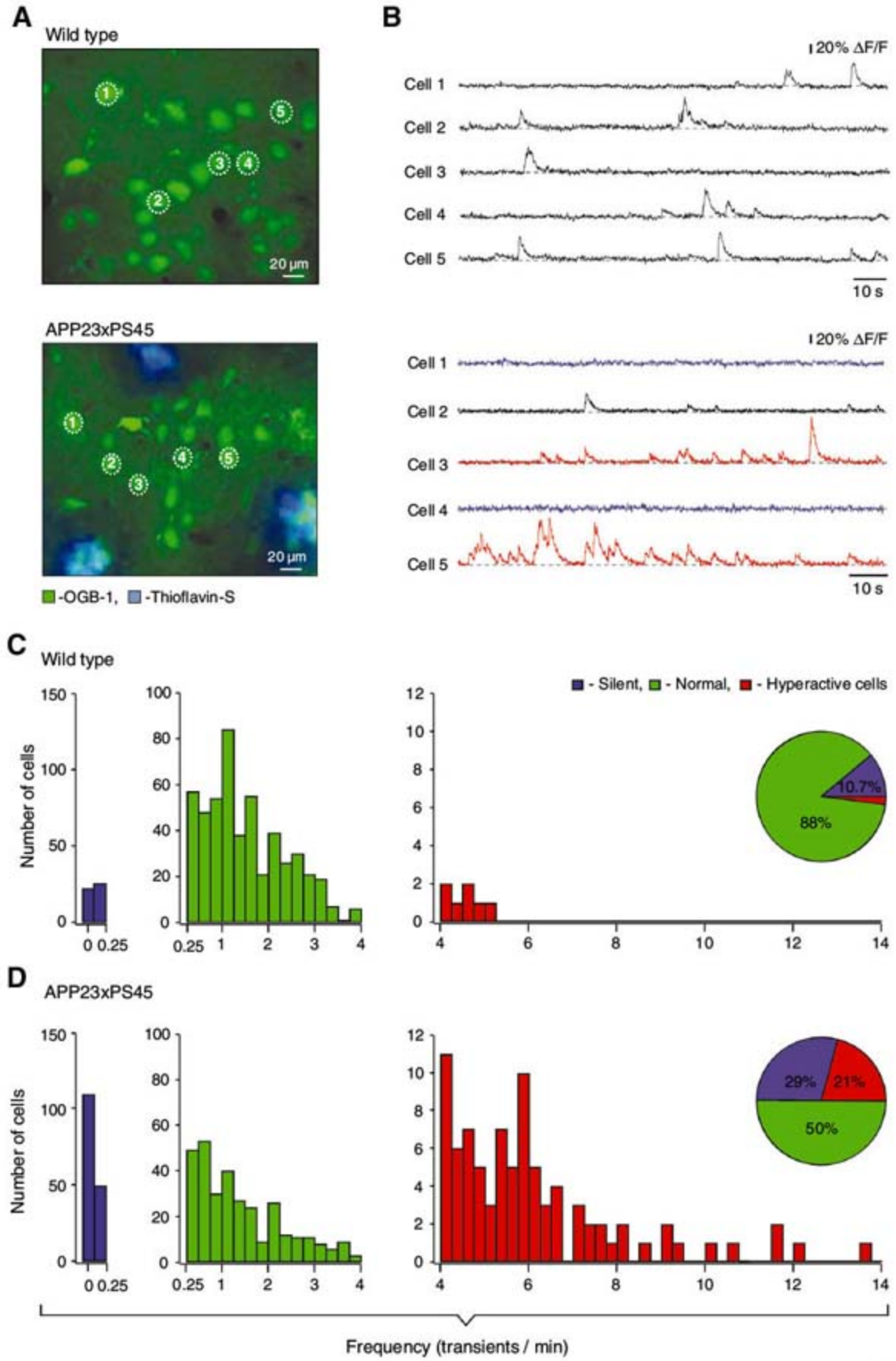

Fig. 1. Altered activity of layer 2/3 neurons in APP23xPS45 mice. (**A** and **B**) Spontaneous Ca^{2+} transients (B) recorded in vivo in the corresponding neurons of the frontal cortex shown in (A) in a WT (top) and a APP23xPS45 (bottom) mouse. Traces in (B) bottom are color-coded to mark neurons that were either inactive during the recording period (blue) or showed an increased frequency of Ca^{2+} transients (red). (**C** and **D**) Histograms showing the frequency distribution of Ca^{2+} transients in WT and APP23xPS45 mice (in both cases n = 564 cells). There is a substantial increase in the amount of silent and hyperactive neurons in APP23xPS45 mice. (Insets) Pie charts showing the relative proportion of silent, normal, and hyperactive neurons in WT (n = 10) and APP23xPS45 (n = 20) mice.

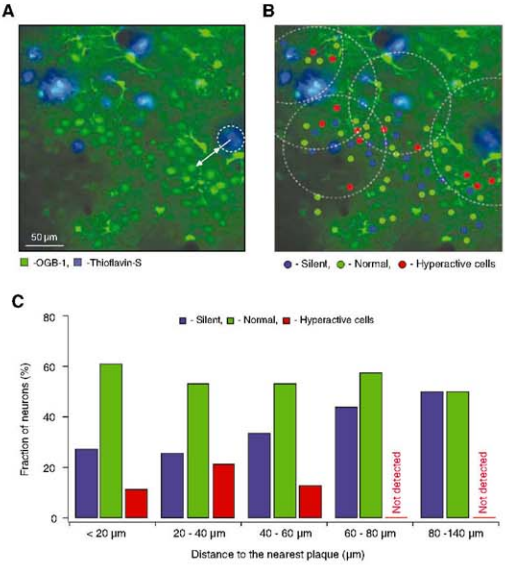

Fig. 2. Spatial distribution of silent and hyperactive neurons in APP23xPS45 mice. **(A)** Maximal projection image (100- to 130-μm depth) of layer 2/3 in the frontal cortex of an APP23xPS45 mouse. To measure the distance from the plaque to the recorded cell, we fitted the plaque with a circle and measured the distance (arrow) between the plaque border and the middle of the cell. The cortical area located above and below the imaged plane (55- to 175-μm depth) was also scanned to assure that plaques shown were nearest to the recorded neurons. **(B)** Activity map of this region with neurons color-coded according to the frequency of their Ca^{2+} transients. The broken line circles are centered at the respective plaques and delineate the area located less than 60 μm from the plaque border. **(C)** Bar graph showing the abundance of silent, normal, and hyperactive neurons at different distances from the border of the nearest plaque (n = 422 cells).

to test whether hyperactive neurons still receive synaptic inhibition, we locally applied diazepam, a benzodiazepine that increases the open probability of γ-aminobutyric acid type A ($GABA_A$) receptor channels. This treatment markedly reduced the activity of hyperactive neurons (from 6.10 ± 0.28 transients/min, n = 13 cells in five mice, to 1.52 ± 0.36 transients/min; Fig. 3, E and F). Application of the $GABA_A$ receptor antagonist gabazine increased the frequency of Ca^{2+} transients in all three types of neurons to the same level of 30 to 40 transients/min (Fig. 3, G and H). However, the relative frequency increase in hyperactive neurons (5.7-fold, n = 9 cells in four mice) was distinctly smaller compared with the frequency increase in normally active cells (16.3-fold, n = 13 cells in four mice). Thus, taken together, our results suggest that an impaired synaptic inhibition, rather than intracellular Ca^{2+} release from store signaling or intrinsic firing, underlies hyperactivity.

What are the mediator(s) of the synaptically driven neuronal hyperactivity? The list of candidate molecules includes (i) soluble Aβ42 oligomers accumulating in the vicinity of amyloid plaques (*33*, *34*) as well as (ii) different proinflammatory mediators released from activated microglia and astrocytes. The latter include cytokines, reactive oxygen species, complement factors, free radicals, and nitric oxide (*35*). These factors most likely cause an anatomical remodeling of both excitatory and inhibitory synaptic inputs that underlies the observed changes in neuronal function. Such a remodeling has been observed in two different mouse models of AD. In APP23 mice, axons of entorhinal (excitatory) neurons showed a hyperinnervation of the thalamic regions surrounding Aβ plaques (*36*), whereas in hAPP mice axonal sprouting of GABAergic interneurons was found in the hippocampal dentate gyrus (*37*).

In conclusion, the study of the in vivo function of individual cortical neurons in a mouse model of AD revealed an increase in neuronal activity in the direct vicinity of Aβ plaques. Not only do hyperactive neurons fire more frequently, they also do this in a correlated manner, thus increasing the risk for seizurelike activity. Indeed, AD patients are known to have an increased incidence of epileptic seizures (*38*, *39*), and spontaneous nonconvulsive seizures have been observed in the cortex and hippocampus of another AD mouse model (*37*). The hyperactive neurons are likely candidates to trigger this pathological activity. Besides, hyperactivity may contribute to the calcium overload recently observed in neurites surrounding Aβ plaques (*40*). Together with the silent neurons, which are distributed throughout the cortex, hyperactive neurons comprise up to 50% of neuronal population, revealing a substantial dysfunction of neuronal network in APP23xPS45 mice. A strict correlation was observed between the formation of amyloid plaques, the appearance of hyperactive neurons, and the impairment of the animal's learning capability. Furthermore, the peri-plaque regions appear to act like distinct functional compartments of the diseased mouse brain. These compartments are not only "reservoirs" of bioactive molecules, attracting and activating microglia as well as causing loss of dendritic spines and axonal dystrophies (*41*), they also modify the functional properties of neurons, making them hyperactive.

References and Notes

1. D. Provolovic, V. Van de Ven, A. T. Sack, K. Maurer, D. E. Linden, *Psychiatry Res.* **140**, 97 (2005).
2. D. H. Silverman *et al.*, *JAMA* **286**, 2120 (2001).
3. C. A. Davies, D. M. Mann, P. Q. Sumpter, P. O. Yates, *J. Neurol. Sci.* **78**, 151 (1987).
4. D. J. Selkoe, *Science* **298**, 789 (2002).
5. R. D. Terry *et al.*, *Ann. Neurol.* **30**, 572 (1991).
6. A. Y. Hsia *et al.*, *Proc. Natl. Acad. Sci. U.S.A.* **96**, 3228 (1999).
7. E. H. Chang *et al.*, *Proc. Natl. Acad. Sci. U.S.A.* **103**, 3410 (2006).
8. F. Kamenetz *et al.*, *Neuron* **37**, 925 (2003).
9. D. M. Walsh *et al.*, *Nature* **416**, 535 (2002).
10. J. S. Jacobsen *et al.*, *Proc. Natl. Acad. Sci. U.S.A.* **103**, 5161 (2006).
11. H. Hsieh *et al.*, *Neuron* **52**, 831 (2006).

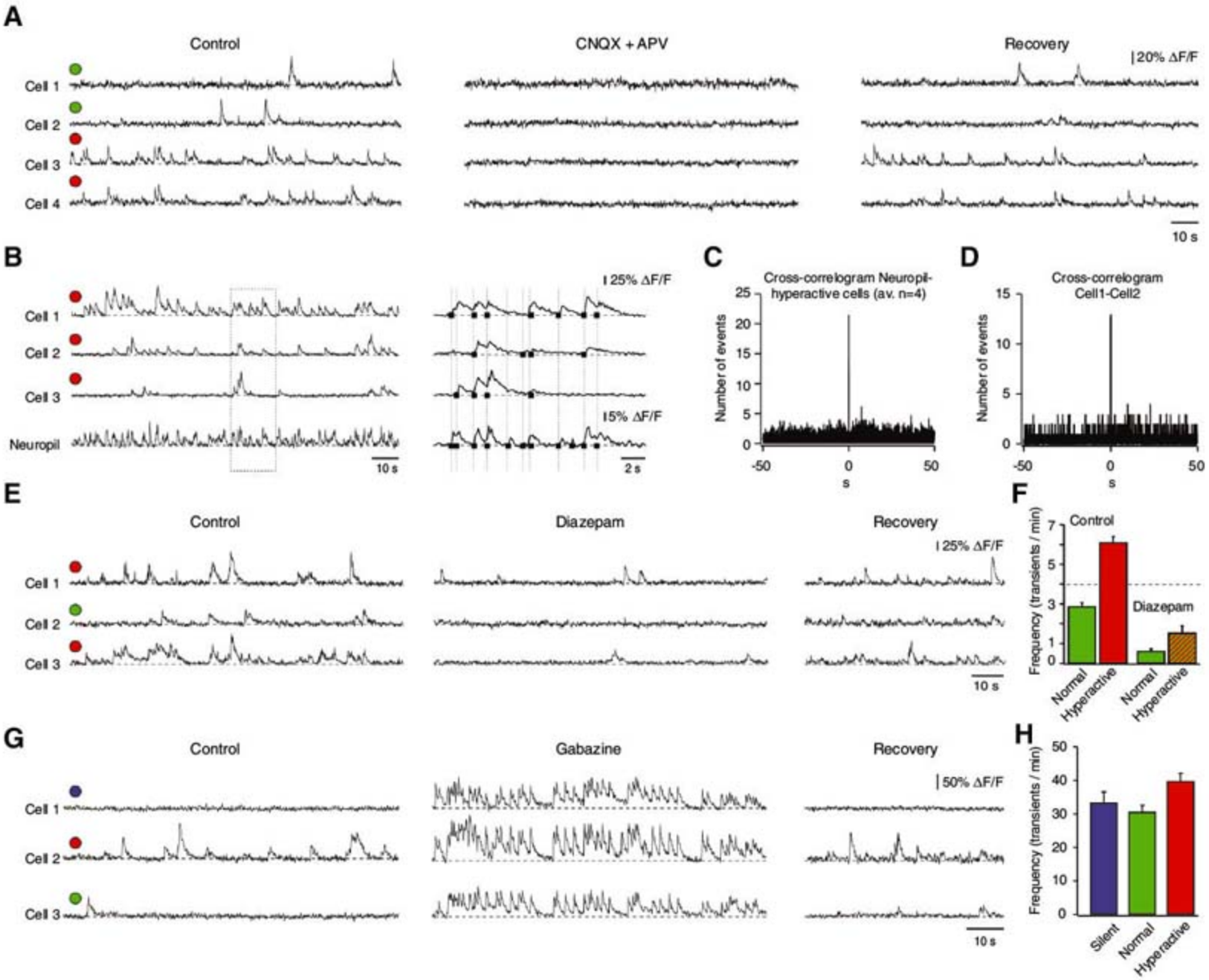

Fig. 3. Synaptic mechanisms of hyperactivity. (**A**) Spontaneous Ca^{2+} transients in layer 2/3 neurons before, during, and after a local iontophoretic application of CNQX and APV. Here and below, the colored circles indicate the type of neuron (blue, silent; green, normal; and red, hyperactive). (**B**) Activity pattern in a region with many hyperactive neurons. Each Ca^{2+} transient in the cell is correlated with a transient in the neuropil. Each black square marks the beginning of a Ca^{2+} transient. (**C** and **D**) Cross-correlograms of digitized traces showing that Ca^{2+} transients in individual hyperactive neurons are correlated with each other and with Ca^{2+} transients in the neuropil. (**E**) Spontaneous Ca^{2+} transients before, during, and after a local pressure application of diazepam. (**F**) Summary graph illustrating the effect of diazepam on the frequency of Ca^{2+} transients (n = 21 normal and 13 hyperactive neurons). (**G**) Spontaneous Ca^{2+} transients before, during, and after a local iontophoretic application of gabazine (60 s, 500 μM in the application pipette). (**H**) Summary graph illustrating the effect of gabazine on the frequency of Ca^{2+} transients (n = 6 silent, 13 normal, and 9 hyperactive neurons). Error bars in each panel represent SEM.

12. S. Oddo *et al.*, *Neuron* **39**, 409 (2003).
13. V. Nimmrich *et al.*, *J. Neurosci.* **28**, 788 (2008).
14. G. M. Shankar *et al.*, *J. Neurosci.* **27**, 2866 (2007).
15. E. M. Snyder *et al.*, *Nat. Neurosci.* **8**, 1051 (2005).
16. Materials and methods are available as supporting material on *Science* Online.
17. C. Stosiek, O. Garaschuk, K. Holthoff, A. Konnerth, *Proc. Natl. Acad. Sci. U.S.A.* **100**, 7319 (2003).
18. R. H. Christie *et al.*, *J. Neurosci.* **21**, 858 (2001).
19. J. Grutzendler, K. Helmin, J. Tsai, W. B. Gan, *Ann. N. Y. Acad. Sci.* **1097**, 30 (2007).
20. O. Garaschuk, R. I. Milos, A. Konnerth, *Nat. Protoc.* **1**, 380 (2006).
21. G. Eichhoff, M. A. Busche, O. Garaschuk, *Eur. J. Nucl. Med. Mol. Imaging* **35**, S99 (2008).
22. A. Arieli, A. Sterkin, A. Grinvald, A. Aertsen, *Science* **273**, 1868 (1996).
23. I. Ferezou, S. Bolea, C. C. Petersen, *Neuron* **50**, 617 (2006).
24. J. Anderson, I. Lampl, I. Reichova, M. Carandini, D. Ferster, *Nat. Neurosci.* **3**, 617 (2000).
25. D. Ji, M. A. Wilson, *Nat. Neurosci.* **10**, 100 (2007).
26. L. Marshall, H. Helgadottir, M. Molle, J. Born, *Nature* **444**, 610 (2006).
27. J. N. Kerr, D. Greenberg, F. Helmchen, *Proc. Natl. Acad. Sci. U.S.A.* **102**, 14063 (2005).
28. T. R. Sato, N. W. Gray, Z. F. Mainen, K. Svoboda, *PLoS Biol.* **5**, e189 (2007).
29. M. Arns, M. Sauvage, T. Steckler, *Behav. Brain Res.* **106**, 151 (1999).
30. O. Wirths, H. Breyhan, S. Schafer, C. Roth, T. A. Bayer, *Neurobiol. Aging* **29**, 891 (2008).
31. O. Nelson *et al.*, *J. Clin. Investig.* **117**, 1230 (2007).
32. H. Tu *et al.*, *Cell* **126**, 981 (2006).
33. R. Kayed *et al.*, *Science* **300**, 486 (2003).
34. C. Haass, D. J. Selkoe, *Nat. Rev. Mol. Cell Biol.* **8**, 101 (2007).
35. M. T. Heneka, M. K. O'Banion, *J. Neuroimmunol.* **184**, 69 (2007).
36. A. L. Phinney *et al.*, *J. Neurosci.* **19**, 8552 (1999).
37. J. J. Palop *et al.*, *Neuron* **55**, 697 (2007).
38. J. C. Amatniek *et al.*, *Epilepsia* **47**, 867 (2006).
39. D. A. Lozsadi, A. J. Larner, *Dement. Geriatr. Cogn. Disord.* **22**, 121 (2006).
40. K. V. Kuchibhotla *et al.*, *Neuron* **59**, 214 (2008).
41. M. Meyer-Luehmann *et al.*, *Nature* **451**, 720 (2008).

42. A.K. is a Carl-von-Linde Fellow of the Institute for Advanced Study of the TUM. We thank L. B. Cohen for comments on the manuscript. Supported by grants from the Deutsche Forschungsgemeinschaft (SFB 596, GA 654/1-1, and HO 2156/2-1) and the Helmholtz Gemeinschaft.

Supporting Online Material

www.sciencemag.org/cgi/content/full/321/5896/1686/DC1

Materials and Methods
Figs. S1 to S6
References

7 July 2008; accepted 19 August 2008
10.1126/science.1162844

Reward-Predictive Cues Enhance Excitatory Synaptic Strength onto Midbrain Dopamine Neurons

Garret D. Stuber,[1] Marianne Klanker,[2] Bram de Ridder,[1] M. Scott Bowers,[1] Ruud N. Joosten,[2] Matthijs G. Feenstra,[2] Antonello Bonci[1,3]*

Using sensory information for the prediction of future events is essential for survival. Midbrain dopamine neurons are activated by environmental cues that predict rewards, but the cellular mechanisms that underlie this phenomenon remain elusive. We used in vivo voltammetry and in vitro patch-clamp electrophysiology to show that both dopamine release to reward predictive cues and enhanced synaptic strength onto dopamine neurons develop over the course of cue-reward learning. Increased synaptic strength was not observed after stable behavioral responding. Thus, enhanced synaptic strength onto dopamine neurons may act to facilitate the transformation of neutral environmental stimuli to salient reward-predictive cues.

Dopamine (DA) neurons, originating in the ventral tegmental area (VTA) and substantia nigra and projecting to forebrain areas, are essential for the expression of goal-directed behaviors for both natural rewards and drugs of abuse (*1–3*). DA neurons are initially phasically activated by primary rewards such as food but shift their activation to reward-predictive stimuli after extended conditioning (*4*). Although DA signaling appears to be plastic, and can be modified by manipulating the contingency between conditioned stimuli and rewards (*5*), the cellular mechanisms that underlie this cue-reward learning remain unclear.

Long-term potentiation (LTP) and long-term depression (LTD) are hypothesized cellular mechanisms for learning and memory storage (*6*). Glutamatergic synapses onto DA neurons can express LTP (*7, 8*), LTD (*9–11*), and short-term plasticity (*7*). Furthermore, passive (*12–14*) or voluntary (*15*) exposure to cocaine can lead to long-lasting changes in synaptic function in DA neurons. Although excitatory synapses are highly plastic, it is unknown whether associative learning leads to synaptic alterations onto DA neurons.

Both the firing of VTA neurons and the release of DA are time-locked to receipt of unpredicted rewards as well as to conditioned stimuli that predict reward delivery (*16, 17*). However, the time course in which DA release develops to reward-predictive stimuli is poorly characterized. Thus, we used fast-scan cyclic voltammetry (FSCV) (figs. S1 and S2 and table S1) (*18*) to monitor rapid DA fluctuations in the nucleus accumbens (NAc) of rats during the acquisition of a cue-reward association in a Pavlovian conditioning task. Rats ($n = 8$) underwent single or multiple conditioning sessions ($n = 13$ total sessions) (*19*) in which the onset of a cuelight stimulus (CS) preceded the delivery of a sucrose pellet. Cue-reward learning was assayed by the development of conditioned approach behavior, in which rats make goal-directed nosepokes into the sucrose pellet receptacle during presentation of the CS (*20*).

Before the development of conditioned-approach behavior, NAc DA transients were time-locked to reward delivery and/or retrieval (Fig. 1A). During subsequent trials, in which cue-reward associations were formed, DA transients were typically observed in response to both reward and CS onset (Fig. 1, B and D). After acquisition of the cue-reward association, DA transients were predominantly time-locked to CS onset (Fig. 1, C and D). The onset of phasic DA release to the CS developed gradually, as seen in Fig. 1D and fig. S3, when voltammetric recordings were made in a representative rat over four consecutive conditioning sessions. Because cue-evoked DA release developed throughout learning, we examined whether DA release correlated with conditioned-approach behavior. Figure 1E and table S1 show that the ratio of the CS-related DA release to the reward-related DA release was significantly ($r^2 = 0.68$; $P = 0.0005$) correlated with number of CS nosepokes in a conditioning session (also see fig. S4). Furthermore, when rats displayed conditioned-approach behavior (>20 CS-directed nosepokes), and therefore learned the cue-reward association to some degree, CS-related DA was significantly higher compared with those sessions in which rats showed less conditioned approach [$t(11) = 2.94$; $P = 0.013$] (Fig. 1F).

Because conditioned DA release to reward-predictive stimuli developed as learning progressed, we hypothesized that alterations in synaptic strength onto DA neurons play a role in cue-reward learning. Using a similar behavioral paradigm as described above, adult rats were trained in one, three, or five daily sessions in which a 10-s tone/houselight conditioned stimulus predicted reward delivery (CS^+ group). A separate group of rats received the same exposure to the tone/houselight stimulus and sucrose, but these stimuli were not explicitly paired together (CS^- group) (Fig. 2A). Figure

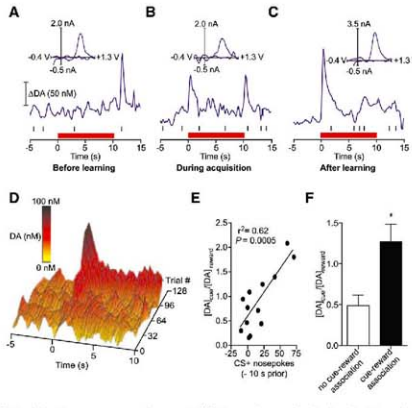

Fig. 1. Phasic DA release in the NAc to reward-predictive stimuli develops during learning. **(A to C)** Single-trial example traces of DA release during different stages of conditioning. Red horizontal bar indicates CS duration, which was followed by sucrose delivery (at 10 s). Black vertical ticks indicate nosepokes into the sucrose receptacle. Insets show background-subtracted cyclic voltammograms taken from the DA peak to the pellet delivery in (A) and from the DA peak to CS onset in (B) and (C). **(D)** The development of DA release in response to the CS in a single rat across four conditioning sessions each consisting of 32 trials. CS onset occurred at $t = 0$. **(E)** Nosepokes made during the CS period correlated with amount of $[DA]_{cue}/[DA]_{reward}$ across 13 behavioral sessions in $n = 8$ rats tested. **(F)** Bar graph of data in (E) showing that rats with the greatest conditioned-approach behavior to the CS showed significantly higher $[DA]_{cue}/[DA]_{reward}$.

[1]Ernest Gallo Clinic and Research Center, Department of Neurology, University of California, San Francisco, Emeryville, CA 94608, USA. [2]Netherlands Institute for Neuroscience, an Institute of the Royal Netherlands Academy of Arts and Sciences, Amsterdam, Netherlands. [3]Wheeler Center for the Neurobiology of Drug Addiction, University of California, San Francisco, San Francisco, CA 94143, USA.

*To whom correspondence should be addressed. E-mail: antonello.bonci@ucsf.edu

2B shows the acquisition of the cue-reward association over the course of five conditioning sessions for CS$^+$ rats and no acquisition for CS$^-$ rats. A two-way repeated measures analysis of variance (ANOVA) showed a significant increase in conditioned-approach behavior in the CS$^+$ rats versus the CS$^-$ rats over conditioning (conditioning x group interaction, $F_{4,208} = 5.12$; $P = 0.0006$). Post hoc tests revealed that early in conditioning (session 1), there was no significant difference in conditioned-approach behavior between CS$^+$ and CS$^-$ rats. However, by session 3, CS$^+$ rats developed significant conditioned approach to the CS, whereas unpaired CS$^-$ rats did not. By session 5, no further increase in conditioned approach was seen in the CS$^+$ rats, demonstrating that at this time, no new learning of the cue-reward association was occurring.

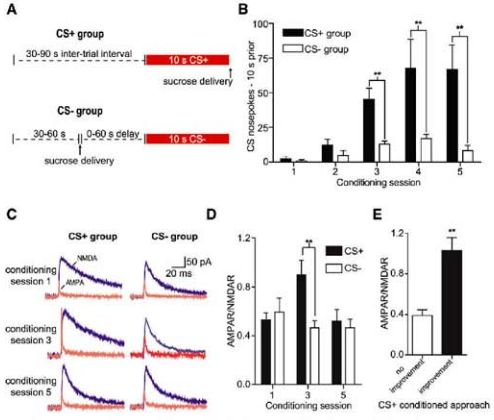

Fig. 2. Excitatory synaptic strength is transiently increased after the acquisition of a cue-reward association. **(A)** Schematic of the CS$^+$ and CS$^-$ behavioral paradigms. **(B)** Conditioned-approach behavior (CS nosepokes, 10 s prior) increased over five sessions in the CS$^+$ group but not in the CS$^-$ group. **(C)** Example traces of AMPAR- and NMDAR-mediated currents taken from CS$^+$ and CS$^-$ rats after (~1 hour) conditioning sessions 1, 3, or 5. **(D)** Average data showing that the AMPAR/NMDAR was transiently elevated only in CS$^+$ rats immediately after conditioning session 3. **(E)** Analysis of CS$^+$ data from sessions 3 through 5 showing that rats that showed a >30% increase in cue-directed nosepokes over the previous conditioning session displayed a significant increase in the AMPAR/NMDAR versus rats that did not show an increase in performance.

To explore whether changes in excitatory synaptic strength occurred at synapses onto DA neurons over the course of cue-reward learning, in vitro whole-cell patch clamp electrophysiological experiments were performed ~1 hour after CS$^+$ or CS$^-$ rats completed either the first, third, or fifth conditioning session. DA neurons in midbrain slices were voltage-clamped at +40 mV, and excitatory postsynaptic currents (EPSCs) were recorded before and after bath application of 50 μM of the NMDAR antagonist D-2-amino-5-phosphonopentanoate (AP5) to resolve both AMPA- and NMDA-mediated currents (fig. S5). The AMPAR/NMDAR was then computed to determine an index of excitatory synaptic strength onto DA neurons (*13*, *21*). The AMPAR/NMDAR was significantly increased in CS$^+$ rats over conditioning [$F_{(2,52)} = 4.08$, $P = 0.023$]. Example traces and averages in Fig. 2, C and D, show that the AMPAR/NMDARs were comparable in CS$^+$ and CS$^-$ rats after the first session of cue-reward pairing [CS$^+$: 0.53 ± 0.057, $n = 12$; CS$^-$: 0.59 ± 0.11, $n = 8$; $t(18) = 0.58$; $P = 0.57$]. However, after the third conditioning session, the AMPAR/NMDAR was significantly higher in CS$^+$ rats relative to CS$^-$ controls [CS$^+$: 0.90 ± 0.12, $n = 10$;

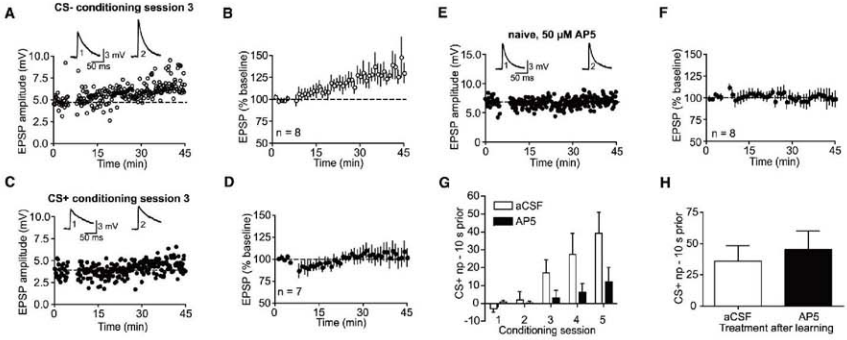

Fig. 3. NMDAR antagonism blocks LTP and cue-reward learning. **(A** and **B)** Example and average data showing that LTP was induced in cells taken from CS$^-$ rats after session 3. **(C** and **D)** Example and average data showing that LTP could not be induced in cells taken from CS$^+$ rats. **(E** and **F)** An example experiment and average data showing that NMDAR antagonism blocked the induction of LTP in cells taken from naïve rats. **(G)** Behavioral data showing NMDAR antagonism in the VTA blocked the acquisition of the cue-reward association. **(H)** Behavioral data showing that NMDAR antagonism had no effect on conditioned-approach behavior after learning had occurred.

CS : 0.46 ± 0.06, $n = 7$; $t(15) = 2.82$; $P = 0.013$] (Fig. 2, C and D). Once the cue-reward association was well established (after conditioning session 5), AMPAR/NMDARs in CS^+ and CS rats were again comparable [CS^+: 0.52 ± 0.09, $n = 11$; CS : 0.46 ± 0.07, $n = 10$; $t(19) = 0.46$; $P = 0.65$] (Fig. 2, C and D). Further analysis of the CS^+ trained rats show AMPAR/NMDARs were significantly higher in rats that showed a large improvement (>30% increase) in CS^+ nosepokes from the previous session [$t(14) = 4.57$; $P = 0.0004$] (Fig. 2E).

Postsynaptic increases in AMPAR or decreases in NMDAR number or function can lead to an elevated AMPAR/NMDAR. To determine which receptor subtype(s) was altered in DA neurons after learning, AMPA or NMDA was bath-applied onto CS^+ or CS midbrain slices immediately after conditioning session 3. AMPA-, but not NMDA-mediated current was elevated in cells from CS^+ versus CS rats (fig. S6). Consistent with this, AMPAR-mediated mEPSCs were increased in amplitude in cells from CS^+ rats relative to controls with no change in mEPSC frequency or paired-pulse ratio (fig. S7). Taken together, this suggests that increased excitatory synaptic strength associated with cue-reward learning is mediated by an increase in postsynaptic AMPAR function.

We next tested whether the induction of LTP at excitatory synapses onto DA neurons was altered in CS^+ rats after acquisition of the cue-reward association. LTP was then induced using a spike-timing-dependent plasticity protocol (*8*) (fig. S8). Experiments in naïve rats verified that this protocol was capable of inducing LTP in DA neurons from adult rats (fig. S8). An example cell in Fig. 3A and average data in Fig. 3B show that, in cells from CS rats after conditioning session 3, EPSP-AP pairing significantly increased the evoked EPSP amplitude to 131.2 ± 3.2% of baseline [averaged over $t = 40$ to 45 min of the experiment, $F_{(7,41)} = 8.43$, $P \leq 0.0001$]. In contrast, no change in EPSP amplitude was observed in cells recorded from CS^+ rats after session 3 [106.6 ± 1.4% baseline; $F_{(6,40)} = 0.71$, $P = 0.90$] (Fig. 3, C and D).

To determine whether NMDAR-mediated signaling was required for the expression of LTP at excitatory synapses onto DA neurons, the NMDAR antagonist, D-AP5, was bath-applied to slices taken from naïve rats while EPSPs were measured before and after LTP induction. An example cell in Fig. 3E and average data in Fig. 3F illustrate that bath application of 50 μM AP5 significantly blocked LTP induction at excitatory synapses on DA neurons [$F_{(7,43)} = 0.56$, $P = 0.98$].

An increase in the AMPAR/NMDAR (Fig. 2, C to E), as well as an occlusion of LTP (Fig. 3, C and D), was observed immediately after acquisition, suggesting that an LTP-like synaptic change in DA neurons may facilitate cue-reward learning. Because VTA LTP induction required NMDA receptors (Fig. 3, E and F), we examined whether NMDARs in the VTA were required for cue-reward learning. Thus, a separate group of rats were implanted with cannulae aimed at the VTA. After recovery from surgery, rats received microinjections of an artificial cerebrospinal fluid (aCSF) vehicle or 0.5 nmol/0.5 μl AP5 10 min before CS^+ conditioning sessions. Rats that received aCSF microinjections developed cue-reward associations over the course of five conditioning sessions (Fig. 3G) in a similar fashion to rats that did not undergo surgery (Fig. 2B). VTA NMDAR antagonism significantly impaired the acquisition of conditioned-approach behavior relative to aCSF-injected control rats [$F_{(105,1)} = 7.54$, $P = 0.007$] (Fig. 3G). Finally, rats previously injected with aCSF were microinjected with AP5 immediately before an additional conditioning session (conditioning session 6) to determine whether NMDAR antagonism may be modulating the expression of conditioned approach behavior instead of blocking learning. However, conditioned approach behavior after AP5 injection on session 6 was not altered relative to aCSF microinjections [$t(11) = 1.44$, $P = 0.18$] (Fig. 3H).

The release of DA in the NAc to reward-predictive stimuli developed throughout learning, as did changes in synaptic strength. Reward learning transiently enhanced excitatory synaptic strength in midbrain DA neurons as a result of increased currents through postsynaptic AMPARs, which are known to modulate the firing of DA neurons (*22*, *23*). Furthermore, neurons from CS^+ rats that acquired the cue-reward association did not show LTP, compared to naïve and CS rats where LTP could be induced. This suggests that, during the acquisition phase of cue-reward learning, excitatory synapses onto DA neurons may become maximally potentiated as a result of exposure to repeated cue-reward pairings. Both the induction of LTP and the development of conditioned approach behavior were blocked by VTA NMDAR antagonism, suggesting that NMDAR signaling in the VTA is crucial for the formation of cue-reward associations. VTA NMDAR antagonism blocks the acquisition of drug-induced conditioned place preference (*24*), and VTA extracellular glutamate levels are dramatically increased after exposure to drug-associated cues (*25*), suggesting an important role of VTA glutamatergic neurotransmission in modulating goal-directed behavior by conditioned stimuli.

The increase in synaptic strength onto DA neurons was only elevated immediately after the acquisition of cue-reward learning. At this time, rats typically exhibited the largest change in conditioned-approach behavior relative to previous sessions, implying that the transient increase in synaptic strength acts to facilitate learning but is not required for the long-term maintenance of cue-reward associations, because increased synaptic strength was not observed following stable behavioral responding. The persistent storage of cue-reward information may rely on the formation of new synapses or on plasticity in brain regions outside the VTA. These data are in stark contrast to increases in synaptic strength induced by drugs of abuse that can last for weeks after drug exposure (*15*) and may lead to maladaptive learning in which drug-associated cues are overvalued relative to cues that predict natural reinforcers. Therefore, the transient enhancement in synaptic strength after normal reward learning may transform neutral stimuli into reward-predictive stimuli, whereas the rescaling of synaptic strength after learning would allow for the formation of future cue-reward associations.

References and Notes

1. R. A. Wise, *Nat. Rev. Neurosci.* **5**, 483 (2004).
2. P. Di Ciano, B. J. Everitt, *Eur. J. Neurosci.* **19**, 1661 (2004).
3. I. A. Yun, K. T. Wakabayashi, H. L. Fields, S. M. Nicola, *J. Neurosci.* **24**, 2923 (2004).
4. W. Schultz, *J. Neurophysiol.* **80**, 1 (1998).
5. G. D. Stuber, R. M. Wightman, R. M. Carelli, *Neuron* **46**, 661 (2005).
6. R. C. Malenka, M. F. Bear, *Neuron* **44**, 5 (2004).
7. A. Bonci, R. C. Malenka, *J. Neurosci.* **19**, 3723 (1999).
8. Q. S. Liu, L. Pu, M. M. Poo, *Nature* **437**, 1027 (2005).
9. M. J. Thomas, R. C. Malenka, A. Bonci, *J. Neurosci.* **20**, 5581 (2000).
10. S. Jones, J. L. Kornblum, J. A. Kauer, *J. Neurosci.* **20**, 5575 (2000).
11. M. Mameli, B. Balland, R. Lujan, C. Luscher, *Science* **317**, 530 (2007).
12. S. L. Borgland, R. C. Malenka, A. Bonci, *J. Neurosci.* **24**, 7482 (2004).
13. M. A. Ungless, J. L. Whistler, R. C. Malenka, A. Bonci, *Nature* **411**, 583 (2001).
14. C. Bellone, C. Luscher, *Nat. Neurosci.* **9**, 636 (2006).
15. B. T. Chen *et al.*, *Neuron* **59**, 288 (2008).
16. P. N. Tobler, C. D. Fiorillo, W. Schultz, *Science* **307**, 1642 (2005).
17. J. J. Day, M. F. Roitman, R. M. Wightman, R. M. Carelli, *Nat. Neurosci.* **10**, 1020 (2007).
18. M. L. Heien, M. A. Johnson, R. M. Wightman, *Anal. Chem.* **76**, 5697 (2004).
19. Materials and methods are available as supporting material on *Science* Online.
20. J. J. Cheng, J. P. de Bruin, M. G. Feenstra, *Eur. J. Neurosci.* **18**, 1306 (2003).
21. R. C. Malenka, R. A. Nicoll, *Science* **285**, 1870 (1999).
22. X. F. Zhang, X. T. Hu, F. J. White, M. E. Wolf, *J. Pharmacol. Exp. Ther.* **281**, 699 (1997).
23. P. G. Overton, D. Clark, *Brain Res. Rev.* **25**, 312 (1997).
24. G. C. Harris, G. Aston-Jones, *Neuropsychopharmacology* **28**, 73 (2003).
25. Z. B. You, B. Wang, D. Zitzman, S. Azari, R. A. Wise, *J. Neurosci.* **27**, 10546 (2007).

26. We thank H. Fields, F. W. Hopf, P. Janak, and K. Tye for helpful comments and R. Sadler and L. Wang for technical assistance. This work was supported by DA021937 (G.D.S.), DA015096 (A.B.), funds from the State of California for medical research on alcohol and substance abuse through the University of California, San Francisco (A.B.), the Van Den Houtenfonds (M.G.F.), and the Netherlands Organisation for Scientific Research, NWO (M.G.F.).

Supporting Online Material

www.sciencemag.org/cgi/content/full/321/5896/1690/DC1
Materials and Methods
Figs. S1 to S8
Table S1
References

23 May 2008; accepted 15 August 2008
10.1126/science.1160873

Molecular Coupling of *Xist* Regulation and Pluripotency

Pablo Navarro,[1] Ian Chambers,[2] Violetta Karwacki-Neisius,[2] Corinne Chureau,[1] Céline Morey,[1] Claire Rougeulle,[1]* Philip Avner[1]*

During mouse embryogenesis, reversion of imprinted X chromosome inactivation in the pluripotent inner cell mass of the female blastocyst is initiated by the repression of *Xist* from the paternal X chromosome. Here we report that key factors supporting pluripotency—Nanog, Oct3/4, and Sox2—bind within *Xist* intron 1 in undifferentiated embryonic stem (ES) cells. Whereas *Nanog* null ES cells display a reversible and moderate up-regulation of *Xist* in the absence of any apparent modification of Oct3/4 and Sox2 binding, the drastic release of all three factors from *Xist* intron 1 triggers rapid ectopic accumulation of *Xist* RNA. We conclude that the three main genetic factors underlying pluripotency cooperate to repress *Xist* and thus couple X inactivation reprogramming to the control of pluripotency during embryogenesis.

In mammals, X inactivation is controlled by the X-linked gene *Xist*, which produces a non-coding RNA that coats the X chromosome in cis and triggers X inactivation (*1*). During the cleavage stages of the female preimplantation mouse embryo, X inactivation is imprinted and *Xist* is specifically expressed from the paternal inactive X chromosome (*2*–*4*). Although imprinted *Xist* expression is maintained in extra-embryonic tissues, in the pluripotent inner cell mass (ICM) of the blastocyst, *Xist* expression is extinguished and the paternal X chromosome reactivated (*3*, *4*). Subsequently, in the ICM-derived differentiating epiblast, monoallelic *Xist* expression is randomly up-regulated to establish random X inactivation. To date, the molecular mechanisms specifying X chromosome reprogramming in the ICM have not been defined.

Derived from the ICM, pluripotent embryonic stem (ES) cells express low levels of *Xist*. Upon differentiation, random X inactivation is established through monoallelic up-regulation of *Xist* in females but not in males. ES cells are therefore a suitable ex vivo model system for addressing how *Xist* is repressed in the pluripotent ICM. A major repressor of *Xist* RNA accumulation has already been characterized in ES cells: the antisense noncoding RNA *Tsix* (*5*). However, the paternally inherited invalidation of *Tsix* does not block the normal reactivation of the paternal X chromosome in the ICM (*6*), and *Xist* transcription remains repressed in *Tsix*-mutant undifferentiated ES cells (*7*–*9*). An as yet unknown ES cell–specific repressive activity must therefore be responsible for ensuring *Xist* down-regulation until cellular differentiation is initiated.

Given the tight correlation between *Xist* regulation and pluripotency observed in both the embryo and ES cells, the core transcription factors of the genetic circuitry underlying pluripotency—*Nanog* (*10*, *11*), *Oct3/4* (*12*), and *Sox2* (*13*)—may be involved in the transcriptional repression of *Xist*. In the ICM of the blastocyst, the reversion of X inactivation follows Nanog expression (*3*). In three independently generated *Nanog*-null ES cells [RCNβH-B(t), RCNTK(t), and TβC44cre6] (*14*), *Xist* is four- to sixfold up-regulated as compared with the RCN(t) and TβC44 control cell lines (Fig. 1A), whereas restoration of *Nanog* to RCNβH-B(t) by reparative homologous recombination is accompanied by efficient *Xist* repression [RCNβH-B(t)-Rescue] (Fig. 1A). Thus, *Nanog* and *Xist* expression are inversely correlated in ES cells. *Xist* up-regulation is rapidly established 48 hours after the induction of *Nanog* deletion and does not involve *Tsix* down-regulation (fig. S1), indicating that *Xist* might be a direct target of Nanog.

[1]Institut Pasteur, Unité de Génétique Moléculaire Murine, CNRS, URA2578, F-75015, Paris, France. [2]Medical Research Council (MRC) Centre Development in Stem Cell Biology, Institute for Stem Cell Research, School of Biological Sciences, University of Edinburgh, MRC EH9 3JQ, Edinburgh, UK.

*To whom correspondence should be addressed. E-mail: rougeull@pasteur.fr (C.R.); pavner@pasteur.fr (P.A.)

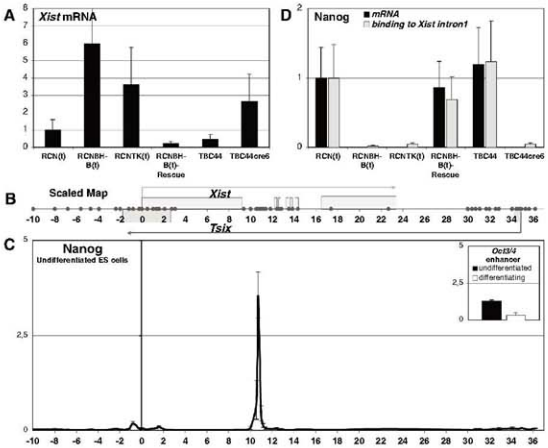

Fig. 1. Nanog binds *Xist* intron 1 to down-regulate *Xist* expression. (**A**) Relative expression levels of *Xist* in different *Nanog* mutants: RCN(t) (*Nanog*$^{+/+}$), RCNβH-B(t) (*Nanog*$^{-/-}$), RCNTK(t) (*Nanog*$^{-/-}$), RCNβH-B(t)-Rescue (*Nanog*$^{+/-}$), TβC44 (*Nanog*$^{+/-}$), and TβC44cre6 (*Nanog*$^{-/-}$). *Xist* RNA levels in RCN(t) were set to one (values and error bars are mean ± SD, $N = 5$). The difference in *Xist* RNA levels between *Nanog* expressing and not expressing cells is statistically significant ($P < 0,0001$, unpaired t test, $N = 15$). (**B**) Map of the *Xist*/*Tsix* locus. *Xist* exons, gray; *Tsix* exons, white. Each primer pair used in the ChIP assay is indicated by a black dot. The coordinate of the primer pair overlapping the *Xist* transcription initiation site was set as the origin of the x axis (0 kb). (**C**) Profile of Nanog binding across the *Xist*/*Tsix* region in undifferentiated female ES cells (LF2 cell line). (Inset) Result obtained in parallel experiments at the ES cell–specific *Oct3/4* enhancer (*25*). Both graphs show the percentage of immunoprecipitation (% IP) obtained after normalization to the input (values and error bars are mean ± SD, $N = 4$). (**D**) Analysis of *Nanog* mRNA expression ($N = 5$) and ChIP signal at *Xist* intron 1 in *Nanog*-null ES cells [$N = 4$ for RCN(t) and RCNβH-B(t), $N = 2$ for all other cell lines]. The level of *Nanog* mRNA was calculated and presented as in (A). The relative levels of binding were calculated by dividing the % IP obtained in each cell line with the primer pair providing the maximal value in (C) by that measured in RCN(t) (set to one, all values and error bars are mean ± SD).

Chromatin immunoprecipitation (ChIP) (*15*) has demonstrated that Nanog is associated with the first intron of the *Xist* gene in both female and male undifferentiated ES cells (Fig. 1, C and D), but not in differentiating ES cells, mouse embryonic fibroblasts (fig. S2), or the three *Nanog*-null ES cell lines (Fig. 1D). As expected, Nanog binding to *Xist* intron 1 DNA is restored in RCNβH-B (t)-Rescue (Fig. 1D) and is unchanged in the *Tsix*-truncated ES cell line Ma2L (*16*) (fig. S3A). We conclude that Nanog displays the appropriate characteristics of the oft-looked-for, ES cell–specific repressor of *Xist* transcription. However, the four- to sixfold up-regulation of *Xist* detected in *Nanog*-null cells is considerably below that generally associated with X inactivation induction in differentiating wild-type (WT) female ES or *Tsix*-mutant male ES cells (1000-fold, fig. S3B). This suggests the existence of additional factors whose repressive activity would remain unaffected by *Nanog* invalidation. Prime candidates are the pluripotency-associated transcription factors Oct3/4 and Sox2, whose binding sites overlap substantially with those of Nanog (*17*, *18*).

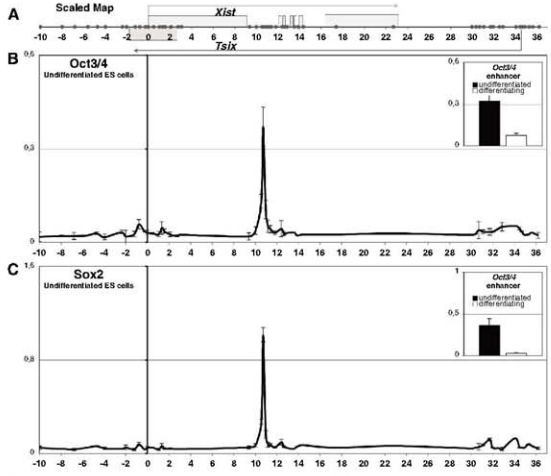

Fig. 2. Direct binding of Oct3/4 and Sox2 to *Xist* intron 1. **(A)** Map of the *Xist*/*Tsix* locus. Binding of Oct3/4 **(B)** and Sox2 **(C)** across *Xist*/*Tsix* in undifferentiated female ES cells (LF2 cell line), obtained and presented as in Fig. 1 (values and error bars are mean ± SD, $N = 4$).

Similarly to Nanog, Oct3/4 and Sox2 bind within *Xist* intron 1 DNA in undifferentiated WT and *Tsix*-truncated ES cells (Fig. 2 and figs. S2 and S3A). In *Nanog*-null ES cells, both Oct3/4 and Sox2 remain bound to *Xist* intron 1 DNA (fig. S4), supporting the idea that Oct3/4 and Sox2 prevent complete up-regulation of *Xist* in *Nanog*-null cells. To analyze *Oct3/4* function, we took advantage of the *Oct3/4*-null male ES cell line ZHBTc4 (*19*), in which *Oct3/4* expression is sustained from a tetracycline (Tc)–repressible transgene. Tc treatment triggers rapid silencing of *Oct3/4* (Fig. 3A) and induces differentiation (fig. S5A). Accordingly, *Nanog*, *Sox2*, and *Tsix* are progressively down-regulated from 48 hours of Tc treatment (Fig. 3A). In contrast, *Xist* is consistently up-regulated after 24 hours of Tc treatment (Fig. 3A), reaching levels

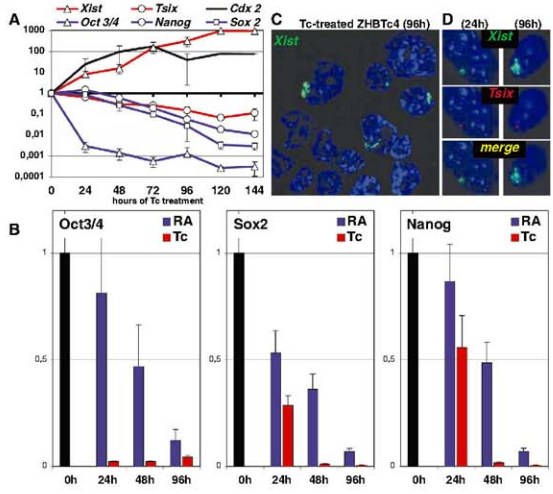

Fig. 3. Inappropriate *Xist* up-regulation in male ES cells upon drastic silencing of *Oct3/4*. **(A)** Time-course variation of gene expression upon addition of Tc to the male ZHBTc4 ES cell line. The graph shows the ratio of expression levels between Tc-treated and untreated ZHBTc4 cells, after standardization to *ArpoP0* mRNA levels. The results were plotted on a log10-scale *y* axis (values and error bars are mean ± SD, $N = 4$). **(B)** Binding of Oct3/4, Sox2, and Nanog in undifferentiated (set here to one) and differentiating ZHBTc4 cells treated with either RA or Tc (values are mean ± SD, $N = 3$). **(C)** RNA-FISH analysis of *Xist* (L510 probe, green) on 4′,6′-diamidino-2-phenylindole–stained (blue) nuclei after 4 days of treatment with Tc. **(D)** RNA-FISH analysis of *Xist* (L510 probe, green) and *Tsix* (E17 probe, red) after 24 and 96 hours of Tc treatment.

similar to those observed in differentiating female ES cells (fig. S6A) and indicating that Oct3/4 represses *Xist*. The lack of *Xist* up-regulation in ZHBTc4 cells differentiated by retinoic acid (RA) in the absence of Tc excludes the occurrence of anomalous up-regulation of *Xist*, unlinked to *Oct3/4* silencing, in differentiating ZHBTc4 cells (fig. S5, D and E). The rapid silencing of Oct3/4 triggered by Tc induces the loss of Oct3/4 from *Xist* intron 1 DNA within 24 hours, and after 48 hours, this is followed by the loss of Sox2 and Nanog binding (Fig. 3B). In contrast, during the first 48 hours of exposure to RA, Oct3/4, Sox2, and Nanog binding persists (Fig. 3B). This indicates that the major increase of *Xist* expression observed in Tc-treated ZHBTc4 cells is a consequence of the premature loss of binding, not only of Oct3/4 but also of Sox2 and Nanog. The three factors therefore act synergistically to repress *Xist*.

Ectopic accumulation of *Xist* RNA is observed in a fraction of the Tc-treated ZHBTc4 cell population that maximally reaches 10% after 96 hours of treatment ($N > 200$ counted nuclei) (Fig. 3C). The marked up-regulation of *Xist* may therefore concern only a limited subpopulation of Tc-treated ZHBTc4 ES cells (fig. S6). Because *Tsix* blocks *Xist* RNA accumulation during differentiation (*5*), the rare Tc-treated ZHBTc4 cells accumulating *Xist* RNA could have prematurely extinguished *Tsix* transcription. This would indicate that *Tsix*, and not *Xist*, is the primary target of Oct3/4, Sox2, and Nanog. However, *Xist* up-regulation [like that of *Cdx2*, a known target of *Oct3/4* (*20*)] is established as early as 24 hours post-Tc treatment ($P = 0.0098$, paired t test, $N = 4$ independent experiments) and precedes *Tsix* down-regulation, whose expression remains unaffected during the first 24 hours of treatment ($P = 0.1678$, paired t test, $N = 4$). In addition, RNA–fluorescence in situ hybridization (FISH) revealed that 92 and 36% of the *Xist*-positive Tc-treated cells still display a *Tsix* signal after 24 ($N = 118$) and 96 hours ($N = 182$) of treatment (Fig. 3D). Thus, *Xist* repression by Oct3/4, Sox2, and Nanog is probably not a secondary consequence of their direct action on *Tsix*. In agreement with this, the loss of these three factors in *Tsix*-truncated cells is accompanied by *Xist* up-regulation (fig. S3B), demonstrating that *Tsix* is not required for the repression of *Xist* mediated by Nanog, Oct3/4, and Sox2. The spatial association of *Xist* intron 1 DNA with the *Xist* promoter in ES cells [but not with the *Tsix* promoter (*21*)] further indicates that *Xist* is the direct target of Nanog, Oct3/4, and Sox2.

The heterogeneity of *Xist* RNA accumulation after Tc addition might alternatively be linked to Nanog mosaicism (*14*). Indeed, ~20% of undifferentiated ES cells are Nanog-negative at any given time (*14*), and *Xist* is partially derepressed in such cells (fig. S7). Ectopic *Xist* activation upon acute *Oct3/4* extinction in Tc-treated cells could be restricted to this Nanog-negative fraction. This predicts that the Nanog-negative subpopulation of female ES cells would be naturally primed for the initiation of X inactivation on differentiation. In agreement, *Xist* up-regulation systematically occurs in Nanog-negative WT female ES cells after 48 hours of differentiation (fig. S8).

Ectopic *Xist* up-regulation in male ES cells in which Nanog, Oct3/4, and Sox2 binding is individually or collectively manipulated (Figs. 1 and 3), together with the correlation at the single cell–level between Nanog-Oct3/4 extinction and *Xist* RNA accumulation in differentiating WT female ES cells (fig. S8), demonstrates that Nanog, Oct3/4, and Sox2 are critical ES cell–specific repressors of *Xist* acting synergistically to couple X inactivation regulation to pluripotency. Because in the ICM (from which ES cells are derived) the paternal X is reactivated (*3*, *4*), we propose that these three critical regulators of pluripotency play a direct and pivotal role in X chromosome reprogramming through their mediation of a transient repression of *Xist* (fig. S9). This proposal argues against the prevalent view that reversion of Xp inactivation in the ICM is a reflection of more global reprogramming events occurring at this stage in support of pluripotency (*4*, *22*). In female primordial germ cells (PGCs), X reactivation is initiated by the extinction of *Xist* RNA immediately after reexpression of *Nanog* (*23*, *24*). Because the expression of *Oct3/4* and *Sox2* also characterizes pluripotent PGCs (*22*), we speculate that Nanog, Oct3/4, and Sox2 may also be directly involved in X chromosome reprogramming during PGC development. Deciphering whether the molecular triggers of pluripotency play a direct function in other pluripotency-associated epigenetic processes will shed light on how genetic and epigenetic mechanisms interact together to ensure the appropriate progression of embryonic development.

References and Notes

1. K. Ng, D. Pullirsch, M. Leeb, A. Wutz, *EMBO Rep.* **8**, 34 (2007).
2. K. D. Huynh, J. T. Lee, *Nature* **426**, 857 (2003).
3. W. Mak *et al.*, *Science* **303**, 666 (2004).
4. I. Okamoto, A. P. Otte, C. D. Allis, D. Reinberg, E. Heard, *Science* **303**, 644 (2004), published online 11 December 2003; 10.1126/science.1092727.
5. J. T. Lee, N. Lu, *Cell* **99**, 47 (1999).
6. S. Kalantry, T. Magnuson, *PLoS Genet.* **2**, e66 (2006).
7. P. Navarro, S. Pichard, C. Ciaudo, P. Avner, C. Rougeulle, *Genes Dev.* **19**, 1474 (2005).
8. S. Vigneau, S. Augui, P. Navarro, P. Avner, P. Clerc, *Proc. Natl. Acad. Sci. U.S.A.* **103**, 7390 (2006).
9. P. Navarro, D. R. Page, P. Avner, C. Rougeulle, *Genes Dev.* **20**, 2787 (2006).
10. I. Chambers *et al.*, *Cell* **113**, 643 (2003).
11. K. Mitsui *et al.*, *Cell* **113**, 631 (2003).
12. J. Nichols *et al.*, *Cell* **95**, 379 (1998).
13. S. Masui *et al.*, *Nat. Cell Biol.* **9**, 625 (2007).
14. I. Chambers *et al.*, *Nature* **450**, 1230 (2007).
15. Materials and methods are available as supporting material on *Science* Online.
16. S. Luikenhuis, A. Wutz, R. Jaenisch, *Mol. Cell. Biol.* **21**, 8512 (2001).
17. L. A. Boyer *et al.*, *Cell* **122**, 947 (2005).
18. Y. H. Loh *et al.*, *Nat. Genet.* **38**, 431 (2006).
19. H. Niwa, J. Miyazaki, A. G. Smith, *Nat. Genet.* **24**, 372 (2000).
20. H. Niwa *et al.*, *Cell* **123**, 917 (2005).
21. C. L. Tsai, R. K. Rowntree, D. E. Cohen, J. T. Lee, *Dev. Biol.* **319**, 416 (2008).
22. M. A. Surani, K. Hayashi, P. Hajkova, *Cell* **128**, 747 (2007).
23. M. de Napoles, T. Nesterova, N. Brockdorff, *PLoS One* **2**, e860 (2007).
24. M. Sugimoto, K. Abe, *PLoS Genet.* **3**, e116 (2007).
25. J. L. Chew *et al.*, *Mol. Cell. Biol.* **25**, 6031 (2005).

26. We thank D. Colby for technical assistance, members of our laboratories for stimulating discussion, and A. Smith for the gift of the ZHBTc4 ES cell line. P.N., C.C., C.R., and P.A. were supported by recurrent funding from the CNRS and the Institut Pasteur, contracts 05-JCJC-0166-01 and 07-BLAN-0047-01 from the Agence Nationale de Recherche, and funding from the EU Epigenome Network of Excellence. Research in I.C.'s laboratory was supported by the Wellcome Trust, the Juvenile Diabetes Research Foundation, and the Biotechnological and Biological Sciences and Medical Research Councils of the UK.

Supporting Online Material

www.sciencemag.org/cgi/content/full/321/5896/1693/DC1
Materials and Methods
Figs. S1 to S10
References

27 May 2008; accepted 14 August 2008
10.1126/science.1160952

qPCR—MAKING OLDER TECHNOLOGY NEW AGAIN

Scientists want more from quantitative polymerase chain reactions, including more sensitivity and specificity. In addition, researchers seek new applications of this technology, such as simplifying it for point-of-care uses. As described here, a range of new products make all of these wishes come true. **by Mike May**

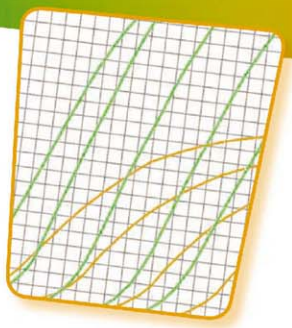

In Belfast, David Coulson, a postdoctoral research fellow at **Queen's University,** takes postmortem brain samples. The samples come from people who suffered from neurodegenerative diseases. Then, Coulson uses qPCR (quantitative PCR, also know as real-time PCR) to study the expression levels of various genes from the samples. "The biggest challenge in qPCR," says Coulson, "is the analysis of the data, rather than the technique itself."

In particular, Coulson points out that normalizing qPCR data typically relies on reference genes. Ideally, these genes get expressed at constant levels, which makes them a scale of sorts for comparing the expression levels of other genes. However, says Coulson, "Certain genes that have been called reference genes are not necessarily good references." For example, a reference gene that varies in expression introduces errors in later analysis. So before applying qPCR to comparative expression levels, researchers must validate their reference genes.

In the May 6, 2008, issue of *BMC Molecular Biology,* Coulson and his colleagues reported on applying qPCR to postmortem brain samples from people with Alzheimer's disease, Parkinson's disease, or dementia with Lewy bodies. From this work, Coulson points out that genes validated as reference genes for some disease might not work in others. "You can't predict how a disease process could affect the reference genes," Coulson says. To keep track of reference genes, Coulson and his colleagues now use qBase*Plus* from **Biogazelle** in Belgium. Coulson says that this software "actually checks the stability of the reference genes as part of the downstream analysis of qPCR data."

Like Biogazelle, many other companies hope to make qPCR more robust and easier to use. Doing that will demand improvements in reference genes and other characteristics of this research tool. As Sandrine Miller, product manager for qPCR at **Invitrogen** in Carlsbad, California, says, "This is a nice technology and one that has been in the market for some time now." She adds, "Today, the main challenges for qPCR are sensitivity and specificity. For example, researchers might want to detect as little of a pathogen as possible or discover rare genes that other techniques can't find." Miller also sees scientists looking for higher throughput from qPCR. In fact, most qPCR users want the same three things: sensitivity, specificity, and higher throughput.

> "Most qPCR users want the same three things: sensitivity, specificity, and higher throughput."

Old and New Techniques

Although the TaqMan approach to qPCR emerged in the early 1990s, companies keep putting this relatively old technique to work on new problems. Earlier this year, for instance, **Applied Biosystems** in Foster City, California—a company that was recently acquired by Invitrogen—introduced its TaqMan MicroRNA arrays. These provide array-based qPCR. "Lots of researchers want to know which miRNAs are involved in a disease or a biological process of interest," says Iain Russell,

Look for these **Upcoming** Articles
Lab on a Chip/Microfluidics — November 7
Cell Signaling — December 5

Inclusion of companies in this article does not indicate endorsement by either AAAS or Science, *nor is it meant to imply that their products or services are superior to those of other companies.*

product manager of consumables at Applied Biosystems. "So we are working to put together workflows and products that provide data for many targets in parallel." The TaqMan Human MicroRNA Array v1.0, for instance, includes 365 different miRNA assays.

Applied Biosystems also aims qPCR at mRNA. "We've used our algorithms to make about 800,000 mRNA assays," says Jon Sherlock, the company's TaqMan array product manager. That large number of assays helps researchers study a range of genes in parallel. To make the process even easier and more efficient, Applied Biosystems developed its TaqMan Express Plates. "Users can go online and select the genes of interest," says Sherlock. "Then, we put them on a 96-well reaction plate that users just put in their own instrument." He says that this product will make large experiments more accessible to a wider number of researchers. "Our Express Plates can also be used to validate microarray results," Sherlock says.

It's not just about looking at more genes or more miRNAs, though, because tools from Applied Biosystems also focus on using smaller samples. "Using large amounts of tissue tends to mask local effects," explains Sherlock. "Looking at smaller samples provides more accurate results, especially for more localized effects."

As scientific questions move toward smaller samples, researchers want to examine differences between smaller pieces, down to cells or even organelles. This leads to the study of single-cell heterogeneity. "The simplest example of this is genetic differences from one cell to another," says Frank Feist, executive director for the Munich-based **Advalytix** business at **Olympus.** Such variations could be used in many ways, including telling scientists more about disease. For example, Advalytix's customers focus on immunology, stem cells, and oncology. "They're trying to see if the degree of heterogeneity has clinical relevance," says Feist, "and there is a strong hypothesis that it is relevant."

Single-cell heterogeneity could be unveiled with qPCR. In the past, however, qPCR lacked the sensitivity to work with single cells, which are also difficult to handle. Advalytix's AmpliGrid slide improves qPCR sensitivity and makes it easy to handle single cells, according to Feist. "The AmpliGrid's flat glass surface contains 48 lithographically defined reaction sites that each hold a single 1-microliter drop within a hydrophobic ring," explains Feist. "Researchers deposit single cells into these reaction sites using flow cytometry, laser capture microscopy, or micromanipulation with up to 100 percent accuracy." Then, researchers perform the reverse transcription step of the qPCR reaction on the AmpliGrid, which Feist says "improves sensitivity of the overall qPCR reaction because the inert glass surface does not absorb any template and the 1-microliter volume makes it stochastically more likely for template and polymerase to react." After reverse transcription, the product is diluted and further analyzed with standard qPCR.

CREDIT: ©ISTOCKPHOTO.COM/DRA_SCHWARTZ

Cross-Platform Products

For any scientific technology, it can be difficult to combine the right parts from various companies. In some cases, scientists simply purchase both the platform and reagents from one vendor. On the other hand, mixing vendors might create better performance in some situations. For instance, Invitrogen developed its new EXPRESS qPCR Supermix reagents for high performance on virtually all qPCR instruments. In addition, Invitrogen's SuperScript VILO cDNA synthesis kit—included in the EXPRESS qRT-PCR reagents—was developed to provide greater sensitivity and linearity in qRT-PCR. "VILO uses SuperScript III in a novel formulation to extend the linearity of synthesis and generate four-fold greater yields of cDNA—enabling the end-users to use more cDNA in their downstream qPCR reaction without inhibition and giving much earlier detection in qRT-PCR, typically at least two cycles earlier," says Miller.

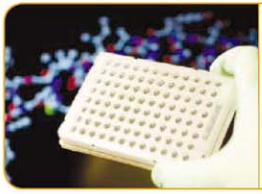

"We want to push qPCR toward point of care."

Agilent Technologies' Stratagene Products Division located in La Jolla, California, also makes reagents for qPCR, such as its new Brilliant II Fast reagents. "It runs much faster," says David Kerry, **Stratagene's** product manager for genomics. "Standard qPCR runs take 65 to 90 minutes, depending on the gene, the size, et cetera. Using Brilliant II Fast, a standard 40 cycles can be performed in as little as 48 minutes." Such an increase in speed might not matter much with small experiments. "However, if you're looking to perform hundreds if not thousands of reactions, the extra time can add up," says Kerry. "Therefore, the faster you perform the reactions, the faster you can get to the results that you want to investigate."

Faster reactions also mean better productivity. Rachel Formosa, Stratagene's product line manager for genomics, says, "In surveys we've done of customers, we've found that about 70 percent of qPCR instruments have four or more users, so they want others getting done quickly." The Brilliant II Fast reagents also help researchers follow the results of a run more quickly. "With Brilliant II," says Formosa, "you start seeing the gene of interest in qPCR three to four cycles earlier than with other reagents. That's a 10-fold difference in detection."

Reagents for qPCR come in various forms. **Integrated DNA Technologies (IDT)** in Coralville, Iowa, for example, recently released its Ultramer long oligonucleotides, which can be used with qPCR. John Havens, IDT's business development manager, says, "These DNA oligomers can be made with 60–200 bases, and they are fully quality-control tested with electrospray mass spectroscopy. This makes sure that the product has the right identity, as measured by mass with an accuracy of plus or minus 0.02 percent."

Havens points out that such oligomers make useful positive controls for qPCR. "You could synthetically make one continued >

Featured Participants

Advalytix
www.advalytix.com

Agilent Technologies
www.agilent.com

Applied Biosystems
www.appliedbiosystems.com

Biogazelle
www.biogazelle.com

Integrated DNA Technologies
www.idtdna.com

Invitrogen
www.invitrogen.com

Olympus Corporation
www.olympus-global.com

Promega
www.promega.com

Q Chip
www.q-chip.com

Queen's University
www.queensu.ca

Stratagene, An Agilent Technologies Division
www.stratagene.com

of these to represent the target of interest in a genomics sample to verify that your reactions are working properly," he says. Moreover, a researcher could make Ultramers with slight variations at specific points to see if that impacts the results from qPCR. "This would make sure that allele-specific qPCR is designed correctly," explains Havens. If researchers want to test a string of variations, IDT will provide Ultramers in 96-well plates. Getting such long oligos, though, does increase the price per base when compared to the price of shorter oligos, since the technology for making the Ultramers is more costly.

When needed, Ultramers can also be made as dual-labeled probes. IDT will make these with a fluorophore on each end or with a fluorophore on one end and a quencher on the other.

Increasing the Take

To increase the amount and quality of information gathered with qPCR, researchers also want multiplexing. "When you look at the expression of single genes in individual tubes," says Ilgar Abbaszade, strategic marketing manager for gene and protein sciences at **Promega** in Madison, Wisconsin, "you can get errors in comparing them because of differences in the reagent concentrations in the different tubes due to pipetting mistakes, for example. You can even get differences based on the location of the well, because of slight differences in heating and cooling conditions in the different wells." If the expression levels of different genes can be measured in the same tube—multiplexed—then some of those errors can be minimized. "More than 35 percent of the people I ask say that they want to multiplex, but only a few of them do it," says Abbaszade.

To help more scientists multiplex qPCR, Promega commercialized its Plexor qPCR System. "It is as simple as the dye-based systems," says Abbaszade, "but at the same time it is as specific as probe-based assays." Promega also provides software that helps customers design multiplexed qPCR assays. "This software is free on our website," says Abbaszade, "and it's free even for people who don't use Plexor. The software helps scientists design primers that work in the same tube with no interference." Then, customers can order the primers that they designed. Abbaszade adds that this system should work with any genes.

Multiplexing qPCR could also be used to make more-powerful diagnostic tools. "You could combine the expression data from several genes, and use that to develop tests to diagnose certain diseases," Abbaszade says. "Multiplexed qPCR assays could also, for example, help to evaluate the potency of stem-cell lines, and that usually depends on the expression level of more than one gene. Researchers could use Plexor to combine that all in one test."

Sometimes, applications of qPCR depend more on simplicity than anything else. For instance, if a company wants to use qPCR to develop a product that could be used by a wide range of people—including ones with no training in molecular biology—the qPCR process must be as easy and foolproof as possible. In Cardiff, Wales, scientists at **Q Chip** make that kind of qPCR tool. This company developed a proprietary system that "lets us make microspheres that are all the same size and have the same content," says Jo Daniels, Q Chip's chief scientific officer. "It's a reliable way to make very uniform spheres from any polymer."

This company's ReaX product is a bead—about a thousand micrometers in diameter—that includes qPCR assays. "This product stabilizes the contents of the beads," says Daniels. "It also makes it so that basically anyone can do qPCR. You just need the DNA, and the beads can be analyzed with any kit on any platform." The Q Chip beads come in plates, and a user just pulls back the strip across the wells, and pipettes in the DNA.

In fact, extending qPCR to new users is part of the point behind Q Chip. "We want to push qPCR toward point of care," says Mark Barry, Q Chip's chief executive. "There will be lots of applications in the future for clinicians, soldiers, et cetera, who will need easy-to-use and reliable assays, and ReaX provides just that." Q Chip also provides its proprietary MicroPlant for companies that want to use Q Chip's technology to make their own ReaX products. "By using Q Chip's MicroPlant under license," says Barry, "companies can manufacture their own beads and assays."

Overall, new qPCR tools—from turning up the capabilities of TaqMan to developing entirely new products, such as reagents or beads—make this technology faster, simpler, and more sensitive. That already makes qPCR more powerful in the lab, and it could eventually end up in the clinic, too.

Mike May is a publishing consultant for science and technology.

DOI: 10.1126/science.opms.p0800028

Real-Time PCR Detection

The CFX96 real-time polymerase chain reaction (PCR) system builds on the power and flexibility of the C1000 thermal cycler, adding an easy-to-install interchangeable reaction module. The instrument features a 3.3°C per second average ramp rate, a patent-pending reduced-mass sample block, a 10-second settling time, and high-speed performance. The system produces results in less than 30 minutes. A thermal gradient feature optimizes reactions in a single experiment. Reliable results can be obtained with sample volumes as low as 10 µl. Powerful, intuitive software helps accelerate every step in research, from getting started to getting results.

Bio-Rad Laboratories
For information 877-246-7231
www.bio-rad.com

DNA from Mammalian Tissue

The Agencourt DNAdvance System is a kit for DNA isolation and extraction from mammalian tissue samples. The kit incorporates the patented SPRI (solid phase reversible immobilization) paramagnetic bead-based nucleic acid purification technology. The kit can be automated on the Beckman Coulter Biomek NXP and FXP workstations to process three 96-well plates in about 75 minutes without the use of organic solvents, vacuum filtration, or centrifugation. A typical application is the use of knockout mice for genotyping studies: DNA extraction from a mouse tail can be difficult, but this kit provides a streamlined process that maximizes yields.

Beckman Coulter/Agencourt
For information 978-867-2962
wwww.agencourt.com

Plasmid DNA Screening

Toothpick-PCR allows for the rapid release of plasmids from transformed bacteria for screening by polymerase chain reaction (PCR). It does not require the user to grow bacteria, perform minipreps, or purify the plasmid DNA. The kit also does not use ethidium bromide, so eliminates the problems associated with this stain.

G-Biosciences/Genotech
For information 314-991-6034
www.GBiosciences.com

Plasmid Miniprep Kit

The GenElute 96-Well Plasmid Miniprep Kit provides rapid generation of transfection-grade plasmid from bacterial cultures. Suitable for a variety of pharmaceutical and biotechnology research applications, the kit rapidly purifies plasmid DNA with high viral titers. The kit can recover up to 10 µg of high-copy plasmid DNA per well from 1.3 ml of harvested bacterial culture in less than 50 minutes. The purified plasmid DNA is suitable for a wide variety of molecular biology applications, including cloning, restriction digestion, in vitro transcription and translation, and sequencing. The kit is compatible with automated liquid handling workstations and offers a vacuum-manifold–based manual protocol.

Sigma-Aldrich
For information 800-521-8956
www.sigma-aldrich.com

DNA Purification with Inhibitor Removal

This line of nucleic acid isolation products is optimized for troublesome samples, and features a patent-pending technology that removes enzymatic inhibitors from any sample, including soil, stool, water, environmental, and plant. Highly pure DNA or RNA can be isolated with fast and easy spin columns or capture columns. Even previously unusable archived DNA samples that still contain contaminants after being purified using other products or techniques can be cleaned up and eluted inhibitor-free.

Mo Bio Laboratories
For information 800-606-6246
www.mobio.com/IRT

DNA Analyzer

The Spartan DXT DNA analyzer now includes a second (red) channel for optical detection that permits scientists to test for two genetic markers simultaneously in the same reaction tube. It also enables scientists to run internal controls to confirm that an assay is working properly. The new feature provides users with improved diagnostic capabilities for their on-demand DNA testing applications, including real-time polymerase chain reaction. The two-channel instrument is just as portable as the single-channel DX version, sharing the same footprint. Scientists have validated the Spartan DX for applications such as testing for herpes simplex virus in pediatric meningitis and vancomycin-resistant enterococci, an antibiotic-resistant "superbug."

Spartan Bioscience
For information 613-866-8803
www.spartanbio.com

Electronically submit your new product description or product literature information! Go to **www.sciencemag.org/products/newproducts.dtl** for more information.

Newly offered instrumentation, apparatus, and laboratory materials of interest to researchers in all disciplines in academic, industrial, and governmental organizations are featured in this space. Emphasis is given to purpose, chief characteristics, and availability of products and materials. Endorsement by *Science* or AAAS of any products or materials mentioned is not implied. Additional information may be obtained from the manufacturer or supplier.